# Slantwise Convection: Climatology, Numerical Modeling, and Parameterization

Ting-Chen Chen

陳亭蓁

Department of Atmospheric and Oceanic Sciences

McGill University

Montreal, Canada

June 2021

A thesis submitted to McGill University in partial fulfillment of the requirements for the degree of Doctorate of Philosophy in Atmospheric Sciences.



2021/06/14

# ACKNOWLEDGMENTS

I would like to express deep gratitude to my supervisor, Prof. Peter Yau, and co-supervisor, Prof. Daniel Kirshbaum. From them, I have learned so much about doing research, critical thinking and academic writing. I also thank them for supporting me in attending conferences, giving me the freedom to explore my research interests and to design projects while providing insightful guidance when I feel lost. This thesis is also benefited from the valuable comments given by my thesis committee members and examiners, Prof. Kerry Emanuel, Prof. John Gyakum, Dr. Stephane Belair, and Prof. Yi Huang.

I thank all members and staff in the Department of Atmospheric and Oceanic Sciences. They made all the courses, academic workshops, and social events insightful and enjoyable. A particular word of gratitude is due to Molly Menzel, Dalrin Ampritta, Eric Lai, Matthew Henry, Charles Brunette, Chris McCray, Kirsten Feng, Sisi Chen, Eyad Atallah, Eric Bembenek, Devendra Pal, Paloma Borque, Ali Asaadi, Konstantinos Menelaou, Natalie Gervasi, Kyle Gorkowski, Jagdeep Sodhi, Daniel Tootill, Kevin Bloxam, Meng-Tze Lee, Yan-Ting Chen, and Michael Rollings for being wonderful friends and offering all kinds of support throughout the past years. I am also grateful for all McGill Taiwanese Graduate Student Association members for enriching my life here, especially Jennifer Ho, who welcomed me when I first arrived in Canada. I also deeply appreciate my old friends overseas, in particular Jhao-Yu Chen, Yu-Jung Chen, Yi-Ying Wu, and Yen-Ting Chang, who have been supporting me even before this journey started.

It would have not been possible to finish this Ph.D. without my dearest friends, Andrés Pérez, Sonja Drueke, Yu-Chen Wang, and Francesco Ragone. They have not only shared wise advice about research and life, brought me great joy, but most importantly, gotten me through tough times. Finally, I am forever indebted to my beloved family in Taiwan, who unconditionally supported my decision to pursue a Ph.D. on the other side of the world.

# STATEMENT OF ORIGINALITY

The following elements of the thesis show original scholarship and represent distinct contributions to knowledge:

- In Chapter 2, the global climatology of slantwise convection is investigated. This study is the first attempt to explore the probability of slantwise convection within cyclones and the evolution of slantwise convection potential (versus upright convection potential) during the lifetime of explosive and non-explosive cyclones.

- In Chapter 3, an in-line package for retrieving all the budget terms of prognostic variables ($u$, $v$, $w$, $\theta$) is implemented in the Weather Research and Forecasting (WRF) model (v3.8.1) and is made publicly available. This package facilitates an accurate budget analysis with a 99th percentile residual always smaller than 0.1% of the net tendency term. A quantitative comparison of the accuracy using this in-line method and other commonly-used post-processing methods is also shown.

- In Chapter 4, the explicit representation of pure slantwise convection at various model grid spacings is investigated under a 2D idealized, non-hydrostatic framework. With the in-line retrieval tool shown in Chapter 3, this study is one of a few that provides a comprehensive momentum budget analysis for the free slantwise convection evolution and identifies the dynamical processes that dominate its associated grid-spacing sensitivity.

- In Chapter 5, a modified version of a parameterization scheme for slantwise convection is proposed, implemented in the WRF model, and evaluated. The performance of this scheme is tested for two test cases: an idealized pure slantwise convection case and a real-data simulation.

# CONTRIBUTION OF AUTHORS

Chapters 2, 3, and 4 are all published articles in the refereed journals *Journal of Atmospheric Sciences*, *Geoscientific Model Development*, and *Quarterly Journal of the Royal Meteorological Society*, respectively. Chapter 5 has been submitted to *Journal of Atmospheric Sciences*. All four articles are co-authored by Prof. Man-Kong (Peter) Yau and Prof. Daniel J. Kirshbaum, who provided supervision throughout my doctoral studies. For each article, I conducted the research and the analysis, produced the figures, and wrote the manuscripts. Both Prof. Man-Kong (Peter) Yau and Prof. Daniel J. Kirshbaum assisted with editing the manuscripts and gave guidance and suggestions.

# ABSTRACT

The representation of atmospheric convection is one of the most critical problems in numerical weather prediction (NWP) and general circulation models (GCMs). While this issue has been an active research area for decades, a specific type of convection, slantwise convection, has received considerably less attention than its more common counterpart, upright convection. Slantwise convection results from the release of conditional symmetric instability (CSI), which can exist in a conditionally (vertically) stable environment. Therefore, the neglect may induce uncertainties in the weather and climate forecasts because the characteristic width scale of slantwise convection (∼50 km) may not be entirely grid-resolvable, and most current operational convective parameterization schemes ignore slantwise convection. With an ultimate goal of filling in the gap related to slantwise convection representation in the NWP and GCMs, this Ph.D. thesis investigates three fundamental aspects of slantwise convection: climatology, explicit representation at varying model grid spacing, and parameterization.

The first step of this project is to assess the importance of slantwise convection from a climatological perspective using long-term global reanalysis data. Consistent with past observational studies, slantwise convection is statistically favored the most in winter over the westernmost oceanic regions where strong vertical wind shear and midlatitude storms prevail. The probability of potential slantwise convection occurrence within cyclones increases with the concurrent intensification rate of the storm, e.g., 30% for averaged and 57% for rapidly-intensifying cyclones, respectively. The release of slantwise convective available potential energy (SCAPE) also coincides with the sharp deepening phase in the life cycle of explosive cyclones.

In the second part of the study, we investigate the sensitivity of slantwise convection to horizontal grid resolution under a 2D idealized framework. An in-line retrieval tool for momentum budget analysis is implemented and utilized in the Weather Research and Forecasting (WRF) model to aid the physical interpretation of simulated results with horizontal grid spacing ($\Delta y$) varying between 1 and 40 km. It is found that the large-scale impacts associated with slantwise convection, such as the precipitation, vertical momentum transport, and SCAPE evolutions, converge numerically when $\Delta y$ is reduced to $\leq 5$ km. Dynamically, 5 km is needed to realistically release the small-scale conditional instabilities embedded in the mesoscale slantwise updraft as they can energize the circulation and enhance the large-scale CSI neutralization.

Finally, given the climatological importance of slantwise convection and that the associated critical features may not be adequately represented in large-scale models, a parameterization scheme for slantwise convection is implemented in WRF. The performance of the scheme is tested first for the 2D idealized setup in the second part of the study, and its application in a real-data case that exhibited potential for slantwise convection is showcased. The scheme helps to improve the quantitative precipitation forecast for both cases. Comparing the coarse-gridded simulations ($\Delta y = 40$ km) with and without the additional slantwise convection parameterization scheme, the former exhibits a larger extent of CSI neutralization, generating stronger grid-resolved updrafts and producing greater amounts of precipitation, all in better agreement with the fine-gridded reference simulations.

# RÉSUMÉ

La représentation de la convection atmosphérique est l'un des problèmes les plus importants de la prévision météorologique et des modèles de circulation générale (GCMs). Bien qu'il s'agisse d'un domaine de recherche actif depuis des décennies, un type spécifique de convection, la convection oblique, a reçu moins d'attention que la convection verticale. La convection oblique résulte de la libération de l'instabilité symétrique conditionnelle (CSI), qui peut exister dans un environnement conditionnellement (verticalement) stable. Négliger la convection oblique peut contribuer aux incertitudes des prévisions météorologiques et climatiques puisque l'échelle caractéristique de la convection oblique ($\sim$50 km) n'est pas entièrement résolue, et la plupart des paramétrisations actuelles ne prennent pas en compte la convection oblique. Afin de remédier au problème de représentation de la convection oblique dans la prévision météorologique et les GCMs, cette thèse explore trois aspects de la convection oblique: la climatologie, la représentation explicite à différents espacements de grille, et la paramétrisation.

La première étape de ce projet consiste à évaluer l'importance de la convection oblique d'un point de vue climatologique en utilisant des données de réanalyse globale. Conformément aux études d'observation antérieures, la convection oblique est davantage présente en hiver dans les régions océaniques les plus à l'ouest, où un fort gradient vertical du vent existe et où les tempêtes de moyenne latitude prédominent. La probabilité d'occurrence potentielle de convection oblique dans les cyclones augmente avec leur taux d'intensification, p. ex.: 30% pour les cyclones moyens et 57% pour les cyclones à intensification rapide. La libération de l'énergie potentielle disponible dû à la convection oblique (SCAPE) coïncide également avec l'approfondissement soudain dans le cycle de vie des cyclones explosifs.

Dans la deuxième partie de l'étude, nous étudions la sensibilité de la convection oblique à la résolution horizontale de la grille d'un modèle idéalisé 2D. Nous implémentons un outil

d'analyse du budget dynamique dans le modèle Weather Research and Forecasting (WRF) afin de faciliter l'interprétation physique des simulations avec un espacement horizontal de la grille ($\Delta y$) variant entre 1 et 40 km. Les impacts à grande échelle associés à la convection oblique, tels que la précipitation, le transport de quantité de mouvement vertical et les évolutions de SCAPE, convergent numériquement lorsque $\Delta y$ est réduit à $\leq$ 5 km. De manière dynamique, un espacement de 5 km est nécessaire pour simuler de manière réaliste la libération d'instabilités conditionnelles dû aux courants ascendants obliques à méso-échelle, car elles peuvent dynamiser la circulation et améliorer la neutralisation du CSI à grande échelle.

Enfin, étant donné l'importance climatologique de la convection oblique et que les caractéristiques critiques qui y sont associées ne sont pas correctement représentées dans les modèles ayant une résolution spatiale de plus de 5 km, une paramétrisation pour la convection oblique est implémenté dans le modèle WRF. La paramétrisation est d'abord testée avec la configuration idéalisée 2D présentée dans la deuxième partie de cette étude, puis nous effectuons une application avec des données réelles pour une situation présentant un potentiel de convection oblique. La paramétrisation aide à améliorer la prévision quantitative des précipitations pour les études idéalisées et réelles. En comparant les simulations à plus basse résolution ($\Delta y$ = 40 km) avec et sans le schéma de paramétrisation, nous montrons que l'introduction d'une paramétrisation pour la convection oblique augmente la neutralisation du CSI, générant des courants ascendants plus forts et produisant de plus grandes quantités de précipitations, en meilleur accord avec les simulations de référence à mailles fines.

# Contents

# List of Figures

# List of Tables

# Chapter 1

# Introduction

## 1.1 Background and motivation

Atmospheric convection plays a vital role in the Earth's climate system. On the local scale, it can give rise to precipitation and different forms of severe weather, and on the global scale, it constitutes a significant component of the general circulation for heat, moisture, and energy redistribution. Therefore, for numerical weather/climate modeling, the representation of convection is critical and can significantly affect the accuracy of simulations. In particular, because the atmospheric states are simulated by models solving the governing equations on discrete grids, subgrid convective processes may be poorly- or un-resolved. In those cases, they need to be collectively parameterized in terms of the prognostic variables on grid scale (Arakawa, 1993). This is termed the convective parameterization problem, and it plays a crucial component in the large-scale numerical weather prediction (NWP) and general circulation models (GCMs). Despite significant progress in convective parameterization, a specific type of convection, slantwise convection, remains inadequately explored.

Slantwise convection, as implied by its name, tilts with height due to the combination of

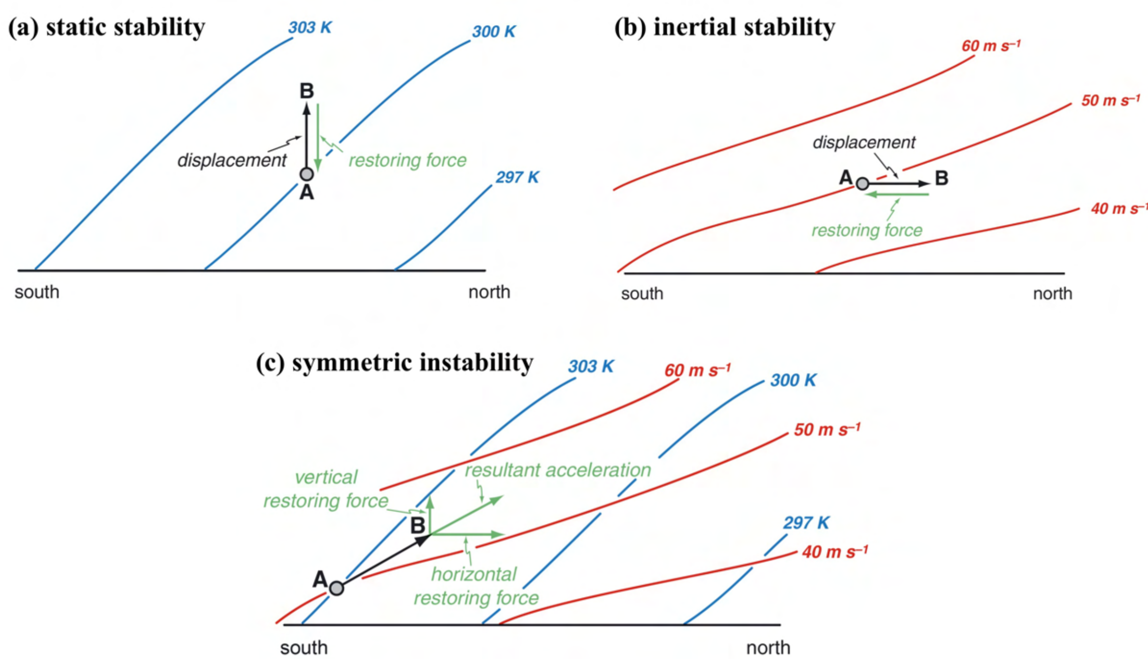


**Fig. 1.1**: Schematic plots for (a) static stability, (b) inertial stability, and (c) symmetric instability. Red and blue lines are surfaces of constant geostrophic absolute momentum and potential temperature (or saturation equivalent potential temperature for saturated flows), respectively. A tube of air is displaced from position A toward position B [From Markowski and Richardson (2010)].

the buoyancy force and inertial force in the vertical and horizontal directions, respectively. Such forces are associated with the release of conditional symmetric instability (CSI), an extended combination of conditional (gravitational/static) and inertial instabilities but can exist without the latter two. In other words, the atmosphere can be stable for both vertical and horizontal displacements of air parcels but unstable for a slantwise displacement, still generating deep clouds and precipitation (Fig. 1.1). The net acceleration is directed in a cross-section along the horizontal temperature gradient with relatively small variations in its perpendicular dimension (hence "symmetric" about the local temperature gradient). Therefore, precipitation associated with the CSI release is often characterized by elongated bands aligned with the thermal wind but sometimes can deviate by $< 15°$ on radar imagery (Fig. 1.2) (e.g., Schultz and Schumacher, 1999). Readers are referred to Chapter 2.2.1. for the measures to identify CSI and assess slantwise convection.

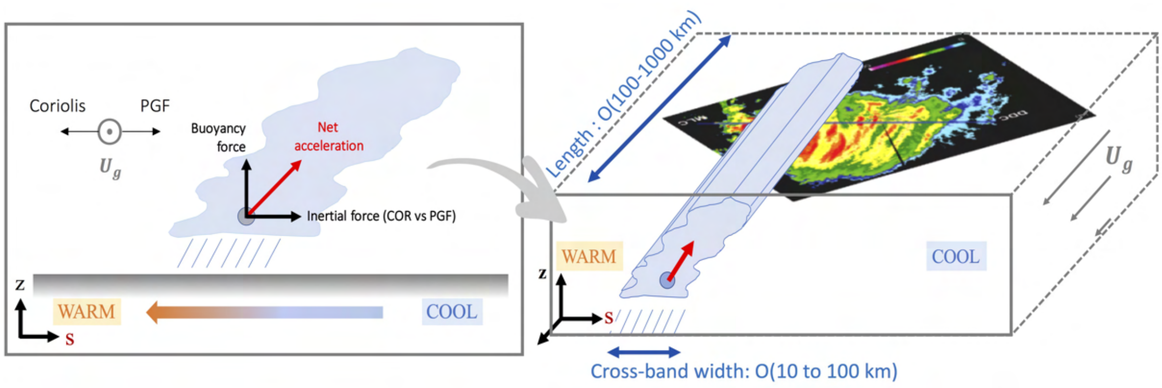


**Fig. 1.2**: Schematic plots for the 2D and 3D view of slantwise convection. The radar reflectivity image for precipitation bands likely associated with CSI is taken from Markowski and Richardson (2010).

Observational evidence of slantwise convection is often found in baroclinic flows, especially over the frontal zones in extratropical cyclones[†]. Despite detailed studies on its theoretical (e.g., Ooyama, 1966; Hoskins, 1974; Emanuel, 1994), observational (e.g., Reuter and Yau, 1990, 1993; Thorpe and Clough, 1991; Browning et al., 2001a), and numerical (e.g., Huang, 1991; Innocentini and Neto, 1992; Persson and Warner, 1991, 1993, 1995) perspectives, slantwise convection is often neglected in the NWP and GCM cloud/convection representation problem. The relatively scant attention on slantwise rather than upright convection is due mainly to the latter's more dominant global presence, larger growth rate, and stronger updrafts. In addition, the understanding about the climatological characteristics of slantwise convection is lacking. Most past studies concerned limited geographical areas and synoptic timescales for single events, and only a few recent studies using the long-term reanalysis data have shown statistically that CSI release could be common over the midlatitude oceans in winter (Ma, 2000; Glinton et al., 2017). Therefore, slantwise convection is worthy of further study, particularly in its association with midlatitude weather

[†]Note that slantwise convection can occur in pre-frontal regions that are associated with anticyclonic environmental flows.

systems, from a global perspective.

If slantwise convection is indeed important on a climatological basis, a follow-up question is whether it can be adequately represented in NWP models and GCMs. For different physical processes, there are different lower bounds on model resolution (usually a range instead of a specific value) for explicit representations, beyond which they should be parameterized. Generally, models running at a horizontal grid spacing smaller than 4 km are considered "convection-permitting" (Arakawa et al., 2011; Prein et al., 2015), but the model resolution that allows explicit representation of slantwise convection is likely to differ and has not been well explored. The quasi-linear banded structure of slantwise convection has two characteristic horizontal scales: the cross-band width ranges from 50 to 500 km, and the along-band length can extend longer, i.e., several hundred to a few thousand kilometers (e.g., Emanuel, 1983a; Chou and Thorpe, 1993). Given its mesoscale characteristics, slantwise convection may be partially resolved in present global NWP models running at relatively fine grid spacings O(10 km). However, if the circulations are only partially resolved (in the gray zone for slantwise convection), they may still introduce errors because the most unstable mode for slantwise convection, and its interaction with embedded upright convection, may not be adequately realized. To fully address these concerns, it is imperative to explore the impacts of varying model grid spacings on slantwise convection simulation and investigate how significantly the inadequate representation may impact the large-scale environment.

For coarse-gridded NWP models and GCMs with insufficient resolution to resolve slantwise convection (e.g., model grid length shorter than one-fourth the typical band width), parameterization is required. Despite the development of various cumulus/convective parameterization schemes (CPS) since the 1960s (e.g., Kuo, 1965; Manabe et al., 1965; Arakawa and Schubert, 1974; Anthes, 1977; Betts and Miller, 1986; Tiedtke, 1989; Kain and Fritsch, 1990; Emanuel, 1991), most of the currently-employed CPS only target upright convection by relating it to moist gravitational instability (Stensrud, 2007). Such design omits potential contributions from the release of CSI and may underestimate the convective activity.

There have been numerous calls for parameterizing slantwise convection in the refereed literature (e.g., Emanuel, 1983a; Innocentini and Neto, 1992; Persson and Warner, 1993; Balasubramanian and Yau, 1995; Schultz and Schumacher, 1999). However, as of this date, only a few slantwise convective parameterization schemes exist (e.g., Thorpe, 1986; Nordeng, 1987; Chou and Thorpe, 1993; Ma, 2000). While implementing these schemes has shown potential improvement in forecasts of precipitation, midlatitude jet, and cyclone developments in a few studies (e.g., Lindstrom and Nordeng, 1992; Balasubramanian and Yau, 1995; Ma, 2000), none of these schemes are applied in current operational NWP and GCMs. Studies on evaluating the necessity and the impacts of including slantwise convective parameterizations remain lacking. As CPS has been identified as one of the major sources of bias for GCMs (e.g., Zhao, 2014; Zhao et al., 2016), we believe the inclusion of the missing physics related to slantwise convection may help to improve the predictive skills of these models. As a first step, further studies are required to justify the benefits and validity of parameterizing slantwise convection.

## 1.2 Research questions and dissertation outline

The purpose of this dissertation is to fill existing gaps in the study of slantwise convection and parameterization by focusing on three aspects: climatology (Chapter 2), explicit representation at varying model grid spacings (Chapter 3 and 4), and parameterization (Chapter 5). The structure and research questions associated with each chapter are as follows:

- **Chapter 2**: To assess the climatological likelihood of slantwise convective occurrence, 6-h global ERA-Interim reanalysis data are analyzed over January 1979–December 2015. In addition to the seasonality and global distribution of slantwise convection potential, the focus is also on a quantitative evaluation of its association with the observed precipitation and cyclone activities (e.g., frequency, location, and intensification rate). Key research questions explored here include:

- Where, when, and how frequently does slantwise convection occur?
- How robust is its association with midlatitude weather systems?
- How does the susceptibility to slantwise convection evolve within the life cycle of storms?

■ As Chapter 2 suggests the importance of slantwise convection, further questions are raised:

- Can slantwise convection be adequately represented in NWP/climate models?
- At which resolution can pure slantwise convection be explicitly resolved, and beyond which resolution does slantwise convection require parameterization?

As a step toward addressing the above questions, we conduct idealized simulations of unforced slantwise convection with the Weather Research and Forecasting (WRF) model and investigate the sensitivity to different horizontal model grid spacings ranging from 40 to 1 km. The investigations are presented in Chapter 3 and 4. Specifically,

**Chapter 3**: To identify the dynamics underlying the simulated slantwise convection, momentum budget analysis is conducted. While post-processing analysis usually contains large residual (errors) and may hinder an accurate physical interpretation, we develop an in-line retrieval method to extract all the momentum tendency terms directly from the WRF model during its integration. This chapter describes the motivation for utilizing this in-line retrieval method, its detailed implementation in WRF, and its advantages over other post-processing methods.

**Chapter 4**: Using the in-line retrieval tool from Chapter 3 to facilitate an accurate momentum budget analysis, we shift the focus back to the investigation of explicit representation of slantwise convection at various grid spacings. In particular, this chapter provides a physical discussion on the dynamics during the development of an unforced, isolated slantwise convection and the sensitivity to the model grid spacing.

- **Chapter 5**: The need to parameterize slantwise convection is justified from Chapters 2 and 4 for models lacking sufficient grid resolution. In Chapter 5, a slantwise convective parameterization scheme is implemented (modified based on Ma 2000) and tested using the WRF model. The performance of this slantwise convection scheme is evaluated for both an idealized test case (same as in Chapter 4) and a real-data case simulation.

- **Chapter 6**: This chapter summarizes the main contributions of this dissertation. Future works needed in this research area are also given.

# Chapter 2

# Climatology of slantwise convection

To determine whether slantwise convection is climatologically significant, this chapter examines the global likelihood of slantwise convection and its association with the observed weather systems using the ERA-interim reanalysis data set. The goal is to identify where, when, and how frequently slantwise convection is likely to occur. Moreover, since past observational studies often found slantwise convection in association with cyclones, this work provides an novel investigation on how the probability of and potential for slantwise convection evolve at different stages of cyclones' lifetime, respectively.

This chapter consists of the following published article:

Chen, T.-C., M. K. Yau, and D. J. Kirshbaum, 2018: Assessment of conditional symmetric instability from global reanalysis data. *J. Atmos. Sci.*, **75**, 2425–2443, https://doi.org/10.1175/JAS-D-17-0221.1

Footnotes with a superscript symbol "†" indicate editorial notes added for clarifications, which are not shown in the original published article.

# Assessment of Conditional Symmetric Instability from Global Reanalysis Data

TING-CHEN CHEN, M. K. YAU, AND DANIEL J. KIRSHBAUM

*Department of Atmospheric and Oceanic Sciences, McGill University, Montreal, Quebec, Canada*



## Abstract

Slantwise convection, the process by which moist symmetric instability is released, has often been linked to banded clouds and precipitation, especially in frontal zones within extratropical cyclones. Studies also suggest that the latent heat release associated with slantwise convection can lead to a spinup of surface frontogenesis[†], which can enhance the rapid intensification of extratropical cyclones. However, most of these studies considered only local areas or short time durations. In this study, we provide a novel statistical investigation of the global climatology of the potential occurrence of slantwise convection, in terms of conditional symmetric instability, and its relationship with precipitating systems. Using the 6-hourly ERA-Interim, two different indices are calculated, namely, slantwise convective available potential energy (SCAPE) and vertically integrated extent of realizable symmetric instability (VRS), to assess the likelihood of occurrence of slantwise convection around the globe. The degree of association is quantified between these indices and the observed surface precipitation as well as the cyclone activity. The susceptibility of midlatitude cyclones to slantwise convection at different stages of their life cycle is also investigated.

[†]Note that latent heating may act either frontogenetically or frontolytically.

As compared to the nonexplosive cyclone cases, the time evolution of SCAPE and VRS within rapidly deepening cyclones exhibit higher values before, and a more significant drop after, the onset of rapid intensification, supporting the idea that the release of symmetric instability might contribute to the intensification of storms.

## 2.1 Introduction

Moist symmetric instability (SI) is an important mesoscale process in the atmosphere (Bennetts and Hoskins, 1979; Emanuel, 1983a). Slantwise convection, the process by which moist SI is released, has been associated with banded clouds and precipitation, especially in frontal zones within extratropical cyclones (e.g., Emanuel, 1983b; Reuter and Yau, 1993; Balasubramanian and Yau, 1994a; Thorpe and Emanuel, 1985; Glinton et al., 2017, hereafter G17). This quasi-two-dimensional circulation is found mostly in regions with strong baroclinicity and vertical wind shear, oriented along an axis roughly parallel to the direction of the thermal wind (e.g., Seltzer et al., 1985). The width of the bands ranges from 50 to 500 km and the length varies considerably with cases, but with a general order of several hundred kilometers (e.g., Emanuel, 1983a; Huang, 1991).

The concept of symmetric instability represents an extension of static/gravitational instability and inertial instability, with the former related to the buoyancy force and the latter arising from the imbalance of the pressure gradient and inertial (e.g., centrifugal or Coriolis) forces. The term "symmetric" refers to the two-dimensional nature (with no variation in the direction of the thermal wind vector, here taken as the $x$ direction) of the hypothetical system used to derive the instability condition. In a statically and inertially stable environment, the slantwise displacement of an air tube aligned with the $x$ axis may become unstable if the potential temperature surfaces are sloped more steeply than the geostrophic absolute momentum surfaces in the $y$–$z$ plane (see Chapter 3.4 in Markowski and Richardson, 2010, for a schematic illustration). In that event, an air tube displaced along the latter surfaces would accelerate away from its original position under the power of the buoyancy force. For a moist atmosphere, a similar condition for potential symmetric instability applies when the potential temperature is replaced by the equivalent potential temperature, and conditional symmetric instability (CSI) results when the potential temperature is replaced by the saturation equivalent potential temperature (Schultz and Schumacher, 1999).

Moreover, analogous to how convective available potential energy (CAPE) can be used to estimate the strength of upright convection, slantwise CAPE (SCAPE), defined as the maximum kinetic energy that can be released by a lifted air tube (instead of an air "parcel" for CAPE) along a slanted trajectory, can be used to estimate the maximum strength of slantwise convection. Through the release of CSI, an adjustment takes place that eliminates the environmental SCAPE. A slantwise conditionally neutral state then results with the saturated equivalent potential temperature surfaces parallel to the absolute momentum surfaces. This slantwise neutral state is often observed in mature convective systems in baroclinic environments (e.g., Emanuel, 1983b; Kuo et al., 1991; Reuter and Yau, 1990, 1993).

In addition to its association with precipitation bands, CSI has also been linked to the explosive development of extratropical cyclones. From the analysis of sounding observations, Reuter and Yau (1993) found that, 12 h before the rapid intensification of a cyclone, the boundary layer ahead of the cyclone track was neutral or slightly stable for upright convection but unstable for slantwise convection. Sometime later, deep convective plumes were observed near the surface low center at the stage of explosive cyclogenesis. Numerical modeling studies have shown that the release of latent heat in slantwise convection may increase the rate of surface frontogenesis (e.g., Thorpe and Emanuel, 1985). By conducting numerical experiments with and without a parameterization for slantwise convection, Balasubramanian and Yau (1994a) found that simulated midlatitude cyclogenesis is sharper with the inclusion of slantwise convection, and that the onset of the rapid spinup coincides with the formation of a bent-back warm front, which is spatially overlapped with the maximum geostrophic vorticity.

Consistent results were obtained by Kuo et al. (1991) in a numerical simulation of a rapidly intensifying extratropical marine cyclone. They found that the heaviest simulated precipitation takes place over the warm frontal region where the pressure rapidly drops and the maximum latent heating is observed. The conjunction of diabatic process and the frontal upglide motion creates a positive feedback loop, reinforcing the low-level frontogenesis. However, the association between slantwise convection potential and explosive cyclogenesis is not always obvious. Shutts (1990a,b) examined the prestorm condition for eight cyclones simulated by the Met Office's fine-mesh model, finding that large SCAPE (over 1000 J kg$^{-1}$) appears in two out of five explosive cyclogeneses and one out of three nonexplosive cases. Some uncertainty in the relationship between slantwise convection and midlatitude cyclogenesis may relate to the inability of numerical models to explicitly describe this convection with limited grid resolution (Shutts, 1990a,b). Also, the SCAPE diagnoses in Shutts (1990a,b) were only shown at a specific analysis time for each case, so it is unclear how SCAPE evolves over the life cycle of the developing cyclones.

Whereas previous work on CSI and banded precipitation were mostly case studies, G17 examined the climatologies of SCAPE and a metric called vertically integrated extent of realizable symmetric instability (VRS), a measure to quantify the "releasable" CSI [see more in Section 2.2.1(2)], over the North Atlantic and European region using the ERA-Interim data. They found that, at any given time in winter, there is an approximately 20% chance that slantwise convection is occurring somewhere over the western North Atlantic Gulf Stream region. When slantwise convection occurs, the maximum vertical extent in each air column over which the CSI is likely to be released has an averaged cumulative depth of 1 km and above. To quantify the contribution of CSI to the climatological precipitation, they first calculated the Pearson correlation coefficient between the daily averaged CAPE or SCAPE and the corresponding 24-h accumulated precipitation from the Hadley Centre U.K. precipitation (HadUKP) dataset, both of which were first averaged over the United Kingdom, and obtained a climatological (January 1979– December 2010) value of 0.21 and 0.43, respectively. This result indicates that the contribution of slantwise convection to the precipitation in the United Kingdom may be significant. For the larger North Atlantic and European region, the ERA-Interim precipitation data were used. They found that the correlation between precipitation and SCAPE is around 0.05–0.1 higher than between precipitation and CAPE across most of the North Atlantic Gulf Stream region and the central North Atlantic, with a peak difference of up to 0.15 near the eastern U.S. coastline in winter, autumn, and spring.

Whereas ample evidence exists that CSI is an important mechanism for the formation or enhancement of some banded convective systems, most of the literature has focused on limited geographic extent at synoptic time scales. A global analysis of thermal stratification by Korty and Schneider (2007) found that the frequency of convectively (upright and/or slantwise) neutral air masses is common not only in the tropics but also in oceanic regions around the midlatitude storm tracks, and Zamora et al. (2016) showed similar patterns in global climate models. To our knowledge, Ma (2000) was the first to produce a global climatology of SCAPE, using the ERA-15 data for 1979–1993. While he suggested that moderate SCAPE may strongly influence precipitation in midlatitude oceans in the winter hemisphere, the links between the two were not quantified. The aim of this study is twofold. The first goal is to investigate the susceptibility of the atmosphere to CSI around the globe using a more recent, updated reanalysis dataset that covers a longer time span than that considered by Ma (2000). Second, we statistically quantify the association between slantwise convection potential and the related observed weather phenomena, such as precipitation and cyclone frequency as well as intensification rate. Some of the analysis is similar to G17 but extended to the global domain.

The organization of the paper is as follows. In Section 2.2, the global reanalysis dataset used in this study, the indices for the assessment of CSI, and the reanalysis-based precipitation and cyclone data for the comparison are introduced. Results are shown in Section 2.3, connecting the climatology of slantwise convection potential with its correlation to the precipitation and cyclone activity. Finally, Section 2.4 presents the summary.

## 2.2 Data and methods

The assessment of CSI over the globe is conducted using the global reanalysis dataset ERA-Interim, from the European Centre for Medium-Range Weather Forecasts (ECMWF). The spatial resolution is $0.75° \times 0.75°$ on 37 vertical levels from 1000 up to 1 hPa, and the temporal resolution is every 6 h over the period January 1979–December 2015. Caveats on the usage of reanalysis data include the inadequacy of its resolution in resolving CSI and the lack of a slantwise convective parameterization in the production of such products. Nevertheless, G17 mentioned that CSI can still be ultimately released via the convection scheme if CSI is converted to conditional instability, a process suggested by a few studies (e.g., Xu, 1986; Gray et al., 2011). Glinton (2013) compared the VRS climatology between ERA-Interim and the CSI-release-permitting Met Office Unified Model (MetUM), version 7.3, run over the North Atlantic and European region (NAE) (with approximately 12-km horizontal grid spacing) and concluded that CSI release can still be quantified to some extent using ERA-Interim. Furthermore, there is evidence to suggest that, despite the coarse resolution, patterns of saturation potential vorticity consistent with slantwise convective adjustment are present in global models (Zamora et al., 2016).

### 2.2.1 Assessment of symmetric instability

There are several measures to assess different types of symmetric instability (Schultz and Schumacher, 1999). Here, we utilize two different indices, mainly related to CSI, to identify the potential occurrence of slantwise convection. These indices are calculated every 6 h and their long-term averages are presented. The surface pressure field is used to exclude the data below Earth's surface (e.g., over high terrain).

#### (1) SCAPE

SCAPE represents the maximum potential energy that can be released during the lifting of a hypothetical air tube along a sloping trajectory. Along with SCAPE, CAPE is also calculated to gain insight into the relative occurrence of upright convection and slantwise convection all over the globe. Note that the calculations of CAPE and SCAPE can be sensitive to different assumptions. Here, the pseudoadiabatic ascent of a parcel from the lowest 50-hPa mixed layer above the surface is assumed, and ice-phase transitions are not considered. CAPE, the vertically integrated positive buoyancy of the parcel, is defined as the vertical integral of positive temperature difference between the parcel and its surrounding environment:

$$\mathrm{CAPE} = \int_{\mathrm{LFC}}^{\mathrm{LNB}} [R_{\mathrm{d}}(T_{\mathrm{vt}} - T_{\mathrm{ve}})] d(-\mathrm{ln}p), \tag{2.1}$$

where $T_{\mathrm{vt}}$ and $T_{\mathrm{ve}}$ are the virtual temperature of the lifted air and of the environment, respectively, and $R_{\mathrm{d}}$ is the gas constant for dry air. The above integral yields positive values between the level of free convection (LFC) and the level of neutral buoyancy (LNB) of the lifted parcel.

The theoretical maximum available potential energy for slantwise convection, SCAPE, is diagnosed by evaluating the integrand in (2.1) on a geostrophic absolute momentum surface, $M = u_g - fy$, where $f$ is the Coriolis parameter, $u_g$ is the geostrophic flow, and $y$ is defined as 90° counterclockwise of the thermal wind. This integral is confined to the layer over which the temperature difference between the mixed-layer air tube and the surrounding environment, during the lifting along the $M$ surface, is positive. The lower and upper limits are defined as the level of free slantwise convection (LFSC) and the level of slantwise neutral buoyancy (LSNB), respectively:

$$\mathrm{SCAPE} = {}_M\int_{\mathrm{LFSC}}^{\mathrm{LSNB}} [R_\mathrm{d}(T_\mathrm{vt} - T_\mathrm{ve})] d(-\ln p). \tag{2.2}$$

Note that the environmental temperature in the above formula is measured along the $M$ surface on which the air tube is lifted. In a shallow barotropic atmosphere, $M$ surfaces are oriented vertically and thus the above formula for SCAPE becomes identical to the one for CAPE. Hence, the difference between SCAPE and CAPE can be regarded as the contribution from baroclinicity.

For computational efficiency, we adopt an estimated formula for SCAPE that can be obtained in each vertical column (Emanuel, 1983b):

$$\mathrm{SCAPE} = \int_{\mathrm{LFSC}}^{\mathrm{LSNB}} [R_\mathrm{d}(T_\mathrm{vt} - T_\mathrm{ve}) + \frac{1}{2}\frac{f}{\eta}\frac{d(u-u_0)^2}{d(-\ln p)}] d(-\ln p), \tag{2.3}$$

where $u$ is the horizontal wind component in the direction of the thermal wind and is assumed to be close to geostrophic[†], $u_0$ is the initial $u$ of the lifted tube, and $\eta$ is the absolute geostrophic vorticity, here defined as $f - \frac{\partial u}{\partial y}$ on pressure levels. The first term shown in (2.3) represents the gravitational contribution to the potential energy, defined as the static term, while the second term indicates the contribution from the inertial force (i.e., the symmetric term). Note that there are several assumptions contained in (2.3). First, the vertical shear is assumed to be nearly unidirectional. Second, the component

[†]This assumption is not valid for strongly curved flow.

of the flow in the direction of the column-averaged shear at each level is assumed to be close to geostrophic. Last, at each level, the horizontal gradients of $M$ are assumed to be constant between the initial location of the lifted tube and the sloped $M$ surface along which the air tube is hypothetically lifted. The first assumption is approximately valid for two-dimensional systems, such as the frontal zones of extratropical cyclones. Previous work investigating the validity of two-dimensional theory for three-dimensional flows has indicated that a time-scale separation must be assumed between a relatively rapid time scale for ascent and a slower time scale for the evolution of the flow (e.g., Gray and Thorpe, 2001). The second assumption is generally satisfied in baroclinic systems. The validity of the third assumption was discussed in Emanuel (1983b). He showed that this condition is frequently met for large-scale flows for which the Rossby number is small. Furthermore, a comparison between our calculated SCAPE using (2.3) and the results shown in G17, in which (2.2) is used, exhibits very similar SCAPE distribution within cyclones (not shown), suggesting that this simplification is likely to have little impact on our results.

While CAPE has been widely used in both research applications and operational centers to diagnose the potential occurrence of severe convective weather or precipitating events (e.g., Brooks et al., 2003; Marsh et al., 2007; Subrahmanyam et al., 2015), it is proposed in G17 that SCAPE can be a superior index for this purpose since it not only includes the available potential energy associated with moist static instability (CAPE) but also accounts for the presence of moist symmetric instability. Their analyses over the United Kingdom and North Atlantic support this notion. In the present study, comparison of the correlation coefficient between SCAPE and CAPE with precipitation analysis is extended to the entire globe.

**(2) VRS**

While SCAPE provides a measure of the likelihood of moist convection (including both upright and slantwise) from the perspective of maximum available energy, such energy can only be released if a lifting mechanism exists to bring the air to its LFSC. Based on an ingredient-based methodology for forecasting deep, moist convection, three ingredients are required: instability, moisture, and lift (e.g., Schultz and Schumacher, 1999). Following this idea, Dixon et al. (2002) developed the VRS diagnostic measure. Building on Dixon et al. (2002), Morcrette (2004), and G17, here we define VRS as the maximum continuous thickness in each air column where the following conditions are met simultaneously:

(i) Nearly saturated conditions. A moderate threshold of RH $>$ 90% is chosen in this study based on the systematic analysis of the impacts of relative humidity criteria on the VRS calculation in Glinton (2013).

(ii) Upward motion.

(iii) The presence of negative (positive) saturated geostrophic potential vorticity, $\mathrm{MPV}_{\mathrm{g}}^*$, in the Northern (Southern) Hemisphere:

$$f\mathrm{MPV}_{\mathrm{g}}^* < 0, \quad \text{where} \quad \mathrm{MPV}_{\mathrm{g}}^* = \frac{1}{\rho}[\nabla \times \boldsymbol{V}_{\mathbf{g}} + f\hat{\boldsymbol{z}}] \cdot \nabla\theta_e^*, \tag{2.4}$$

where $\rho$ is the air density, $\boldsymbol{V}_{\mathbf{g}}$ is the geostrophic wind vector, $f$ is the Coriolis parameter, and $\theta_e^*$ is the saturation equivalent potential temperature. By defining the $y$ axis as 90° counterclockwise of the column-averaged thermal winds, the geostrophic wind $u_{\mathrm{g}}$ as the scalar component in the direction of the $x$ axis at each layer, and by expanding $\mathrm{MPV}_{\mathrm{g}}^*$ in pressure coordinates together with invoking the hydrostatic approximation, we obtain

$$\begin{aligned}\mathrm{MPV}^*_{\mathrm{g}} &= g[-\frac{\partial u_{\mathrm{g}}}{\partial p}\frac{\partial \theta^*_e}{\partial y} - (f - \frac{\partial u_{\mathrm{g}}}{\partial y})\frac{\partial \theta^*_e}{\partial p}] \\ &= g[-\frac{\partial M}{\partial p}\frac{\partial \theta^*_e}{\partial y} - (-\frac{\partial M}{\partial y})\frac{\partial \theta^*_e}{\partial p}] \\ &= -g[\nabla_p \theta^*_e \times \nabla_p M] \cdot \hat{\boldsymbol{x}}.\end{aligned}$$

Note that (2.4) is equivalent to the aforementioned necessary condition of symmetric instability that the (saturated equivalent) potential temperature surfaces are sloped more steeply than the geostrophic absolute momentum surfaces in a vertical cross-section normal to the thermal wind (see Section 2.1).

(iv) The absence of both conditional (static/gravitational) instability and inertial instability, that is, $\frac{\partial \theta^*_e}{\partial z} > 0$ and $f\eta_{\mathrm{g}} > 0$, where $\eta_{\mathrm{g}} = f - \frac{\partial u_{\mathrm{g}}}{\partial y}$, respectively.

The fourth condition is added to exclude the contributions of inertial and static instability, and thus the combination of the third and fourth conditions defines the existence of pure CSI. The identification of SI based on geostrophic potential vorticity can be rewritten in terms of another frequently used measure, the Richardson number ($Ri$), defined as the ratio of the stratification to the vertical geostrophic wind shear (e.g., Stone, 1966, 1967, 1971; Hoskins, 1974; Seltzer et al., 1985; Reuter and Yau, 1990; Dixon et al., 2002; O'Neill and Kaspi, 2016). For the necessary condition of CSI, (2.4) is also equivalent to

$$\frac{\eta}{f} Ri_{\mathrm{m}} < 1, \tag{2.5}$$

where the moist Richardson number $Ri_{\mathrm{m}} \equiv N^2_{\mathrm{m}}/V^2_{\mathrm{g}z} = [f(\frac{\delta z}{\delta y})_{M_{\mathrm{g}}}]/[\eta(\frac{\delta z}{\delta y})_{\theta^*_e}]$, $N_{\mathrm{m}}$ is the saturated buoyancy frequency and $V_{\mathrm{g}z}$ is the vertical geostrophic wind shear.

It can be deduced that large CSI requires a strong horizontal temperature gradient (and thus strong vertical wind shear outside the equatorial region) along with weak static and inertial stability (i.e., small $Ri_{\mathrm{m}}$). Our calculation of VRS is based near the surface, or 1000 hPa, and extends up to 200 hPa, so it has an upper bound of 800 hPa in depth. To compare with the climatology of cyclone tracks [see Section 2.2.2(2)], we only evaluate the VRS during the time period when both the ERA-Interim data and cyclone track data are available (January 1979–December 2008).

Note that there might be a degree of uncertainty in the geostrophic potential vorticity calculation near the equator since the geostrophic balance is not applicable there. Finally, we reiterate that the presence of SCAPE and/or VRS is a necessary but not sufficient condition for slantwise convection to be the locally dominant fluid-dynamical process.

### 2.2.2 Reanalysis-based data

To evaluate the relation between CSI and related weather phenomena, we utilize the reanalysis-based data as proxies of the real observations and compare their precipitation and cyclone activity analyses with the indices introduced above.

#### (1) PRECIPITATION

Given that upward motions cause condensation of water within clouds, vigorous moist convection with strong updrafts often gives rise to heavy precipitation. Because CAPE can be used to estimate the maximum upward motion that results from the buoyancy force (or the release of static instability), it is well correlated with the observed precipitation distribution in areas where deep convection dominates the precipitation climatology, especially when the analysis is conducted over a large spatial area and time period (e.g., Monkam, 2002; Subrahmanyam et al., 2015).

Estimates of cumulative precipitation over a given time period vary with the forecast initialization time, and some studies have suggested that the cumulative precipitation forecast over 12–24 h (the start of the forecast is defined as 0 h) is preferable to avoid model spinup over the first several hours of integration (e.g., Hawcroft et al., 2016). In contrast, some studies suggested that the 0–12-h forecast agrees best with other independent global precipitation estimates from the Global Precipitation Climatology Project (GPCP; Adler et al., 2003) and the Climate Prediction Center (CPC) Merged Analysis of Precipitation (CMAP; Xie and Arkin, 1997; Kallberg, 2011). Here, the 0–12-h forecast is chosen and the monthly average is computed. Studies have found that the ERA-Interim precipitation exhibits close agreement with these observational analyses on the monthly time scale (e.g., Simmons et al., 2010; Bromwich et al., 2011; Dee et al., 2011). However, biases and uncertainties also exist in the observational analyses, especially over the oceans, mountainous regions, and polar areas (e.g., Adler et al., 2003).

In contrast to the instantaneous correlations between CAPE/SCAPE and precipitation conducted by G17, we examine the correlations of monthly means. This approach, which was chosen for computational efficiency, is based on the assumption that temporal means of instantaneous correlations can be captured by correlations of monthly means. As will be seen, the similarities between our findings and those of G17 over their common region suggest that this assumption is reasonably valid.

### (2) CYCLONES

The cyclone data used in this study are obtained from Serreze (2009), which comprise a 50-yr record of cyclone statistics for the Northern Hemisphere from January 1958 to December 2008. In this dataset, cyclone locations are detected by applying the updated tracking algorithm of Serreze et al. (1997) to the sea level pressure fields from the NCEP–NCAR reanalysis[†] at 6-h intervals. Cyclogenesis (cyclolysis) is identified at the time of the first (last)

[†]The acronyms "NCEP" and "NCAR" stand for National Centers for Environmental Prediction and National Center for Atmospheric Research, respectively. This reanalysis dataset has a spatial resolution of 2.5×2.5 degrees (NCEP/National Weather Service/NOAA/U.S. Department of Commerce, 1994; Kistler

appearance of a closed 1-hPa isobar. To account for the latitudinal variation in geostrophic wind for a unit pressure gradient, sea level pressure tendency values are adjusted by multiplying a latitude-dependent factor, $\sin\phi_{\mathrm{ref}}/\sin\phi$, where $\phi_{\mathrm{ref}}$ is a reference latitude of 60°N following Sanders and Gyakum (1980) and Serreze (1995) and $\phi$ is the latitude at each point (Serreze et al., 1997). While inconsistency might exist when applying different cyclone detection algorithms to different reanalysis data, here we neglect such potential impacts and target the most robust cyclone systems and discard some spurious ones associated with the reduction of surface pressure to sea level pressure over high topography.

Therefore, cyclones that lasted for short durations ($<$ 36 h) and those remained nearly stationary (i.e., the cyclone center shifts less than 3° among their first, mid-lifetime, and last observation) are eliminated in this study. We also identify cases with explosive cyclogenesis by examining whether they experienced a central surface pressure drop of more than 24 hPa within 24 h[†] at some point during their lifetime (Sanders and Gyakum, 1980).

## 2.3 Results

### 2.3.1 Global distribution of CAPE and SCAPE

Before analyzing the climatological SCAPE, the seasonal distribution of 37-yr-averaged CAPE over the globe is first examined (Fig. 2.1a–d). The basic patterns are consistent with previous climatologies (e.g., Ma, 2000; Riemann-Campe et al., 2009; G17), although uncertainty exists in peak values, especially over the terrain. The largest CAPE values lie between 30°N and 30°S focusing near the intertropical convergence zone (ITCZ) where

et al., 2001). Such a coarse resolution may not be able to resolve the smaller-scale cyclones and may result in some time lags between the detected and the actual peak intensifying stage of the cyclones. However, we assume that these limitations do not significantly affect our results.

[†]This threshold is defined at a reference latitude of 60°N. Therefore, the minimum rate of central-pressure drop for explosive cyclogenesis at, say 30°N, is only 14 hPa per 24 hours.

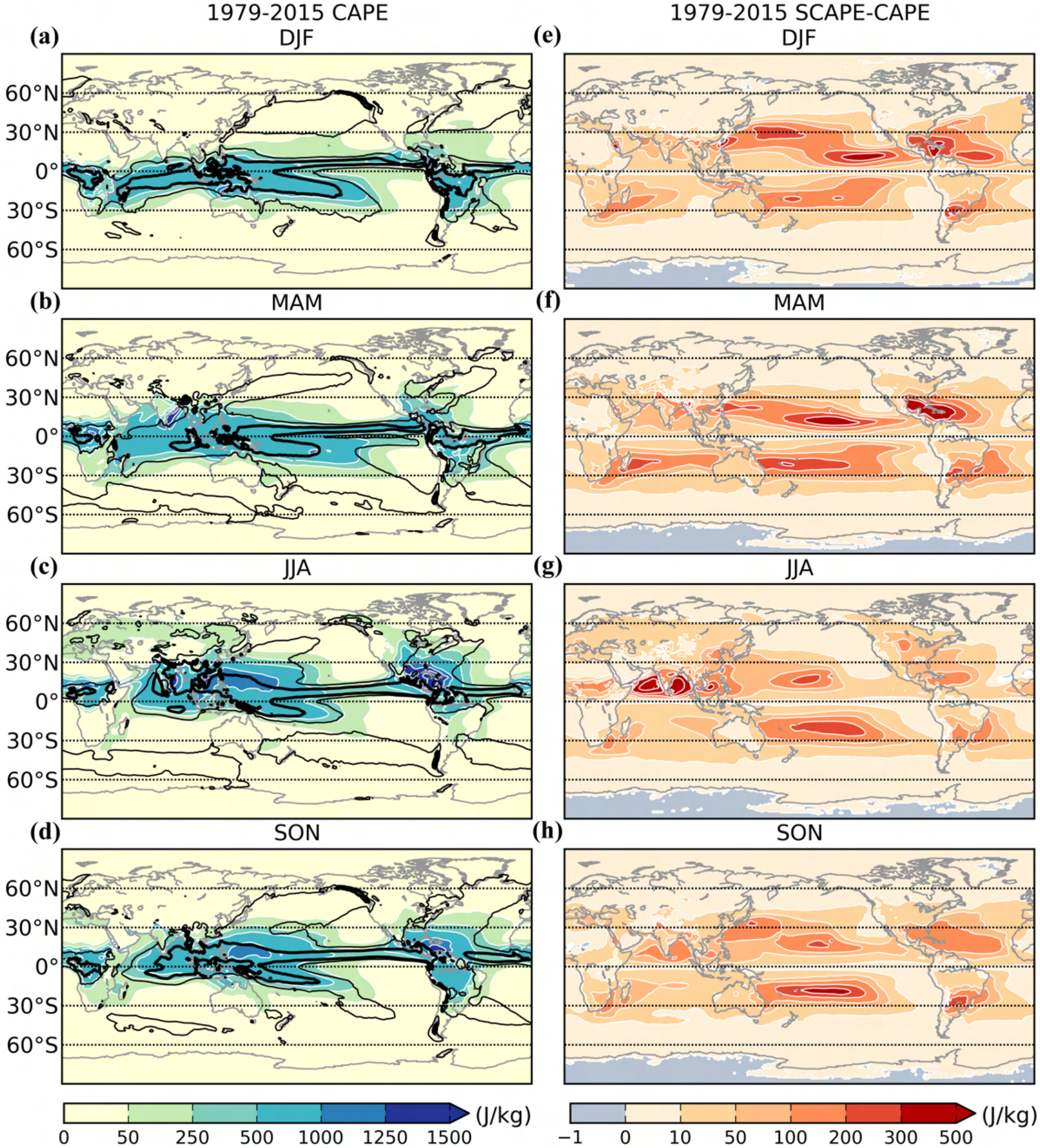


**Fig. 2.1**: The 37-yr-averaged global distribution of CAPE (shaded; J kg$^{-1}$) and precipitation [thin (thick) black contour indicates 3 (8) mm day$^{-1}$] for (a) DJF, (b) MAM, (c) JJA, and (d) SON during 1979–2015. (e)–(h) As in (a)–(d), respectively, but for the difference of SCAPE and CAPE, $\gamma_s$ (shaded; J kg$^{-1}$).

warm and humid air prevails. Regional CAPE maxima are also observed over the Gulf of Mexico, the Amazon basin in South America, the southwestern North Pacific, the Bay of Bengal, and the Congo River basin in Africa†, especially in June–August (JJA). The climatologically averaged CAPE ranges from 0 to 1800 J kg$^{-1}$, and the interannual CAPE standard deviation has a general magnitude of 100–500 J kg$^{-1}$. The standard deviation distribution is similar to the long-term-average CAPE distribution (not shown), indicating that areas with larger averaged CAPE also exhibit larger temporal variations. The seasonal variation of CAPE is more clearly illustrated in zonally averaged latitudinal profiles in Fig. 2.2a. As the maximum shifts to the Southern Hemisphere following the seasonal change from JJA to December–February (DJF), its value decreases as well, mainly because of the reduced land coverage in the Southern Hemisphere. The absolute maximum is located in the Northern Hemisphere rather than the Southern Hemisphere over all seasons except DJF.

The global distributions of the mean and standard deviation of SCAPE, as well as their zonally averaged profiles, are all similar to those of CAPE, except for slightly wider north–south extents. Figure 2.1e–h displays the global distribution of SCAPE minus CAPE, $\gamma_\mathrm{s}$. The spatial distribution of $\gamma_\mathrm{s}$ is consistent with the results of Ma (2000). The values of $\gamma_s$ reach as high as 500 J kg$^{-1}$, and large patches exceeding 100 J kg$^{-1}$ are widespread over the oceans between 5° and 40°N and between 5° and 30°S, where warm and humid air coincides with substantial vertical wind shear. Such subtropical patches of positive $\gamma_\mathrm{s}$ are observable in all seasons and they extend farther northward in the North Atlantic and North Pacific Oceans in DJF when the strongest vertical wind shear is observed (e.g., Chapter 6.1 in Holton, 2004). A local extremum in $\gamma_\mathrm{s}$ is observed in the northern Indian Ocean in JJA, associated with the prevailing low-to-mid-level monsoon that con-

†These regions are also associated with dominant monsoon systems (e.g., Wang and Ding, 2008; Zhou et al., 2016).

tributes greatly to the symmetric term of (2.3) over that area. Over the Antarctica region, small but negative $\gamma_s$ often arises from a negative symmetric term ($M$ slightly decreases with height) in the low layers. The zonally averaged $\gamma_s$ displays a bimodal distribution (Fig. 2.2b), which largely does not shift in latitude with season but stays maximized in the subtropical and the lower midlatitude regions (Fig. 2.1e–h). The peak values of zonally averaged $\gamma_s$ are located near 14°N and 20°S.

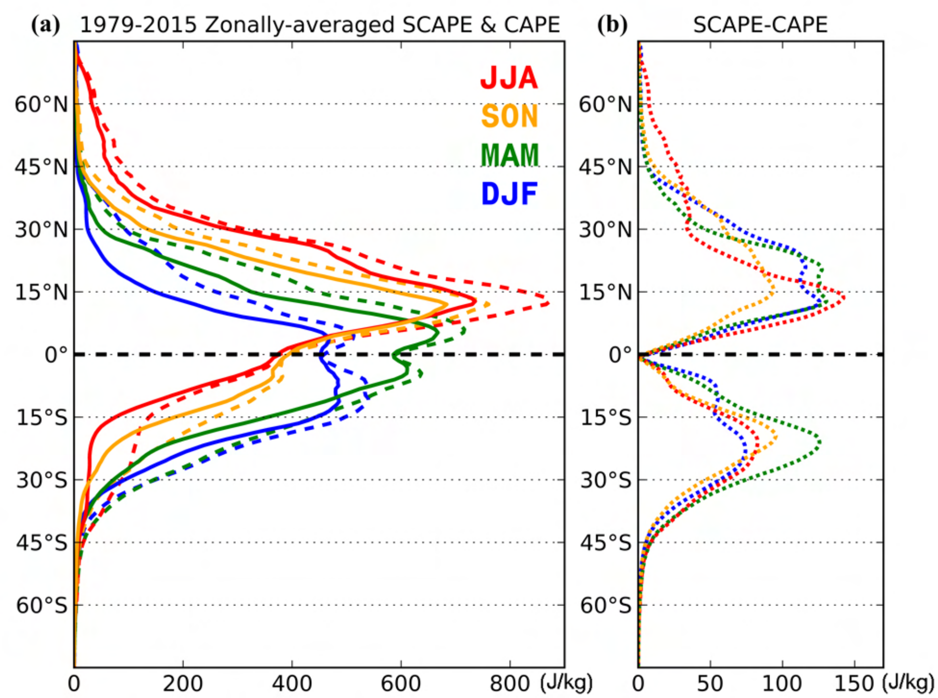


**Fig. 2.2**: (a) Zonal averages of CAPE (solid lines) and SCAPE (dashed lines) for JJA (red), SON (yellow), MAM (green), and DJF (blue) during 1979–2015. The calculation is made only when the value of CAPE (SCAPE) is greater than zero. (b) As in (a), but for the difference of SCAPE and CAPE. The calculation is made only when the difference is greater than zero.

### 2.3.2 Correlation of SCAPE and precipitation

The large coincidence of precipitation and the CAPE distribution in tropical areas lends support to the predominant role of upright convection in the tropics (Fig. 2.1a–d). However, there is some precipitation (with an average of $> 3$ mm day$^{-1}$) in the midlatitude Pacific and Atlantic Oceans [extending poleward and eastward from 30°N (30°S) of the western part of the ocean to 60°N (60°S)] coinciding with small or zero CAPE. Such inconsistency between CAPE and precipitation may be partially associated with the neglect of slantwise convection.

To quantify their associations, the correlation between the monthly averaged CAPE or SCAPE and the corresponding monthly precipitation during the period of January 1979–December 2015 at each grid point is calculated to obtain correlation maps for four different seasons. It should be borne in mind that neither CAPE nor SCAPE should be expected to correlate perfectly with precipitation, because these parameters neglect important effects such as water loading and entrainment processes, and because nonconvective processes (e.g., orographic lifting and symmetrically stable portions of baroclinic systems) also produce precipitation.

The correlation between CAPE and precipitation (Fig. 2.3a–d) is generally positive globally with local peak values of above 0.9 in subtropical areas in every season and in the Arctic area during winter. While the annual-mean CAPE is very small in the Arctic (Fig. 2.1), persistent negative anomalies of both CAPE and precipitation (relative to the annual mean) give rise to a large correlation over that time. Over the tropical and subtropical regions, this correlation generally exceeds 0.6 except over a nearly horizontal thin band along the equator, where the largest precipitation ($> 8$ mm day$^{-1}$) is observed. This result is consistent with G17 in that, climatologically, CAPE has a stronger (weaker) association with precipitation in areas with light to moderate (heavy) precipitation. Specifically, while

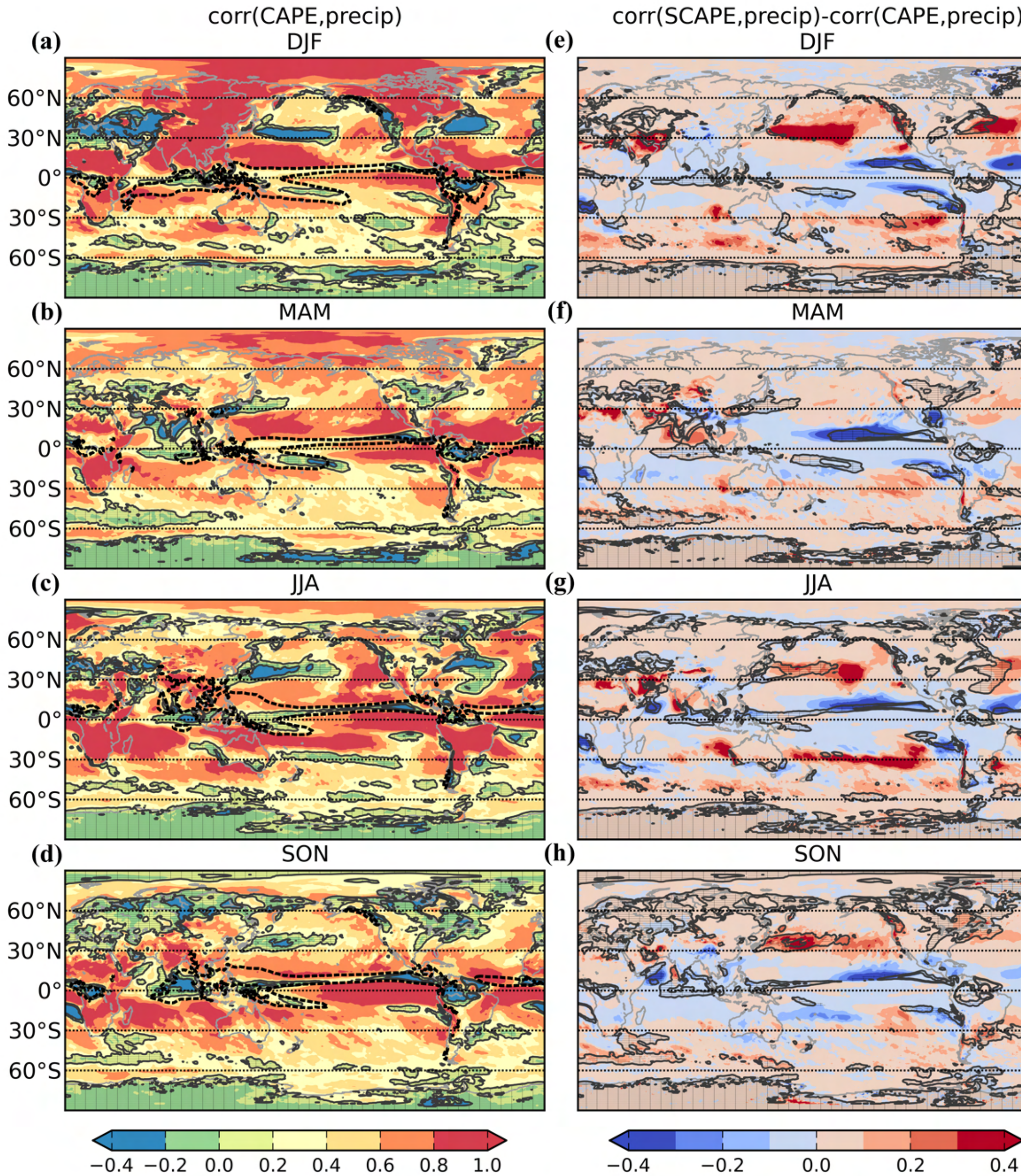


**Fig. 2.3**: The 37-yr-averaged correlation between CAPE and precipitation for (a) DJF, (b) MAM, (c) JJA, and (d) SON during 1979–2015. Black dashed contour encloses the areas with precipitation average > 8 mm day$^{-1}$. Areas without the hatching indicate correlations between CAPE and precipitation that are significantly significant from zero at the 95% confidence level. (e)–(h) As in (a)–(d), respectively, but for the correlation between SCAPE and precipitation minus the one between CAPE and precipitation. Areas without the hatching indicate correlations between SCAPE and precipitation that are statistically significant from zero at the 95% confidence level.

the infrequent instances of large CAPE in climatologically dry regions tend to coincide with periods of heavier precipitation, the nearly continuous large CAPE in climatologically humid regions does not always coincide with precipitation. In the midlatitudes, negative correlations ($< -0.3$) are frequently observed in the westernmost parts of North Atlantic and North Pacific, especially in DJF and JJA. Detailed analyses suggest that during DJF, moderate rainfall is still observed in these areas, but CAPE is generally smaller than its average value. The situation reverses in JJA when mostly positive CAPE fails to coincide with the occasional light rain (not shown).

Some such inconsistencies are ameliorated when SCAPE is used. Figure 2.3e–h displays the difference of precipitation correlation using SCAPE from the one using CAPE. Qualitatively consistent with the results shown in G17 for the North Atlantic and European region, SCAPE shows a higher correlation than CAPE with precipitation mainly in the midlatitudes. However, over the central to eastern tropical Pacific, SCAPE strongly exceeds CAPE yet the precipitation is only moderate (Fig. 2.1). A significantly higher ($> 0.3$) correlation difference is found mostly in midlatitude oceans around 30°–40°N (30°–40°S), particularly in DJF (JJA), suggesting that the precipitation contributed by slantwise convection is especially important over that area during the winter months. Note that these correlation coefficients are higher than those of G17, possibly because of our use of monthly means rather than 6-hourly diagnostics for correlation calculation. In terms of the domain average, both SCAPE and CAPE exhibit correlation coefficients on the order of 0.4–0.5 and slightly smaller values of 0.3 over land (Table 2.1). By performing the Student's $t$ test, the correlation coefficients between CAPE (or SCAPE) and precipitation are generally found to be significantly different from zero at the 95% confidence level for a two-tailed test. In general, SCAPE provides the greatest improvement over CAPE in precipitation correlation in subtropical and midlatitude areas, with an annual average correlation coefficient difference of 0.06. Such enhancement is maximized in DJF and JJA, with correlation coefficient differences of 0.08 and 0.06, respectively. Among all the ocean basins, the North Pacific and North Atlantic exhibit the highest domain-averaged correlation coefficients between SCAPE and precipitation, with annual values of 0.51 and 0.52, respectively. The other domain-averaged correlation coefficients over different areas and during different seasons are summarized in Table 2.1.

**Table 2.1**: Correlation between SCAPE and precipitation and its difference from the correlation between CAPE and precipitation. Values averaged over different domains and for different seasons are also calculated. The averaged correlation coefficients between CAPE or SCAPE and precipitation (prec) are all statistically significant at the 95% confidence level for a two-tailed test.

| | Corr(SCAPE, prec) | | | | | Corr(SCAPE, prec)−Corr(CAPE, prec) | | | | |
|---|---|---|---|---|---|---|---|---|---|---|
| | Annual | DJF | MAM | JJA | SON | Annual | DJF | MAM | JJA | SON |
| Global | 0.42 | 0.47 | 0.44 | 0.43 | 0.37 | 0.02 | 0.03 | 0.01 | 0.02 | 0.02 |
| Tropics | 0.53 | 0.55 | 0.51 | 0.57 | 0.52 | -0.03 | -0.03 | -0.04 | -0.03 | -0.03 |
| Subtropics midlatitudes | 0.46 | 0.49 | 0.46 | 0.48 | 0.44 | 0.06 | 0.08 | 0.04 | 0.06 | 0.05 |
| Land | 0.34 | 0.44 | 0.33 | 0.37 | 0.25 | 0.02 | 0.02 | 0.02 | 0.02 | 0.02 |
| North Pacific Ocean | 0.51 | 0.58 | 0.53 | 0.48 | 0.50 | 0.02 | 0.07 | -0.04 | 0.01 | 0.02 |
| North Atlantic Ocean | 0.52 | 0.54 | 0.63 | 0.48 | 0.50 | 0.04 | 0.06 | 0.02 | 0.01 | 0.03 |
| South Pacific Ocean | 0.47 | 0.42 | 0.45 | 0.53 | 0.53 | 0.03 | 0.02 | 0.01 | 0.05 | 0.01 |
| South Atlantic Ocean | 0.42 | 0.36 | 0.43 | 0.44 | 0.44 | 0.03 | 0.03 | 0.03 | 0.04 | 0.03 |
| Indian Ocean | 0.47 | 0.53 | 0.39 | 0.53 | 0.44 | 0.03 | 0.04 | 0.03 | 0.03 | 0.01 |

*Tropics cover 20°N–20°S; Subtropics midlatitudes cover regions 20°–60°.

## 2.3.3 Global distribution of fractional SCAPE residual and VRS

### (1) FRACTIONAL SCAPE RESIDUAL

The poorer correlation of SCAPE, relative to CAPE, with precipitation in the central to eastern Pacific (i.e., the large residual term $\gamma_s$ does not correspond to large precipitation there) suggests that upright convection may dominate in those areas despite the increased symmetric instability. This suggests a different way to gauge the relative importance of upright convection and slantwise convection. Thus, as an alternative to the absolute magnitude of the difference between SCAPE and CAPE, we define a fractional SCAPE residual as follows:

$$f_{\mathrm{s}} = \frac{\gamma_{\mathrm{s}}}{\mathrm{SCAPE}} = \frac{\mathrm{SCAPE} - \mathrm{CAPE}}{\mathrm{SCAPE}}. \tag{2.6}$$

The value of $f_{\mathrm{s}}$ ranges from 0 to 1. When SCAPE $\approx$ CAPE (i.e., the atmosphere is close to barotropic or the vertical geostrophic wind shear is nearly 0), $f_{\mathrm{s}} \approx 0$ and the area is favorable for upright convection. On the other hand, in regions with $f_{\mathrm{s}}$ close to 1, CSI dominates over conditional (static) instability, which is more favorable for pure slantwise convection.

Figure 2.4a–d shows the 37-yr average of $f_{\mathrm{s}}$ in four different seasons. Slantwise convection, in terms of $f_{\mathrm{s}}$, is favored the most in the midlatitude western North Pacific with an averaged $f_{\mathrm{s}}$ of above 0.7 in DJF. Note that while the average value is less than 1, there are many instances when $f_{\mathrm{s}}$ equals to 1, especially in subtropical and midlatitude areas between 15° and 45°N and between 15° and 45°S. In an environment where CSI and conditional (static) instability coexist (termed ”convective symmetric instability”; i.e., CAPE>0 and SCAPE>CAPE), mechanisms for the development of rainbands likely differ from pure upright or slantwise convection because the two types of instability may manifest on different scales and interact (Schultz and Schumacher, 1999). The present climatology suggests that convective-symmetric instability, in terms of intermediate values for $f_{\mathrm{s}}$, is rather common in subtropical and midlatitude areas.

Over much of the globe, the distribution of $f_{\mathrm{s}}$ generally follows the distribution of the vertical wind shear (Fig. 2.4e–h), indicating that slantwise convection is more likely to occur in areas where vertical wind shear, and thus horizontal baroclinicity (via thermal wind balance outside the equatorial region) is stronger. However, $f_{\mathrm{s}}$ is much smaller over land than over ocean even with strong vertical wind shear (e.g., over eastern Asia in DJF

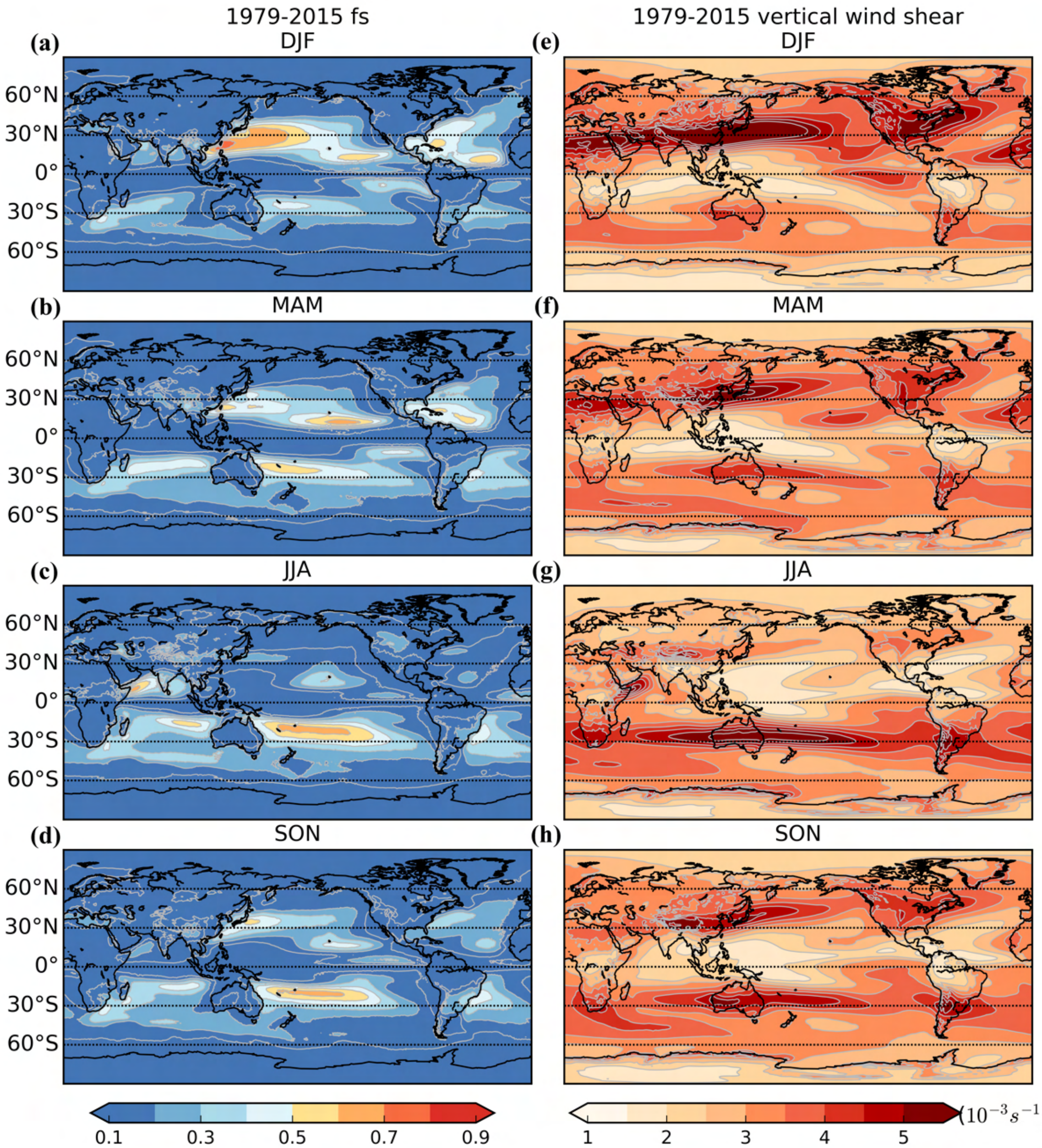


**Fig. 2.4**: The 37-yr-averaged $f_s$ [see (2.6) in the text] for (a) DJF, (b) MAM, (c) JJA, and (d) SON during 1979– 2015. (e)–(h) As in (a)–(d), respectively, but for the vertically averaged (pressure weighted) wind shear from 200 to 900 hPa (or at the first level above the surface if the surface lies above 900 hPa).

as well as over Australia in JJA). This finding arises in part because both SCAPE and CAPE are small there due to limited moisture content over land, particularly over complex terrain, during the winter season. Compared to the distribution of $\gamma_s$, the peak $f_s$ shifts slightly toward higher latitudes. This is because CAPE (and thus SCAPE) is generally larger in lower-latitude regions, which increases the denominator of (2.6) and thus reduces $f_s$. Recall that SCAPE is composed of both a static and symmetric term [see (2.3)], hence, in areas with moderate $\gamma_s$ and relatively large SCAPE, the symmetric term resulting from baroclinicity is still small relative to the static term (i.e., small $f_s$). Such areas are thus more likely to experience upright convection rather than slantwise convection (e.g., the Indian Ocean in JJA and the southeastern part of the North Pacific in DJF; Figs. 2.1e, g and 2.4a, c).

**(2) VRS**

Figure 2.5a–d illustrates the global 30-yr-averaged VRS and frequency of its occurrence for four different seasons. The average is conditional upon the VRS being greater than zero (i.e., it omits instances of zero VRS) and the frequency is defined by the cumulative duration when VRS $>$ 0 divided by the total time. On the long term average, the releasable moist symmetric instability generally has a continuous depth of 80–110 hPa in the subtropics and midlatitudes. The spatial patterns of both the averaged VRS and the VRS frequency of occurrence show high similarities to those shown in G17 over the North Atlantic and European region. Large long-term averaged VRS of above 110 hPa in depth are observed over the westernmost North Pacific and North Atlantic Oceans, the Rocky Mountains, and the southeastern part of the North Atlantic Ocean in DJF (Fig. 2.5a) and over Asia and along 30°S of the South Pacific Ocean in JJA (Fig. 2.5c). Generally, the bottom of the VRS layer lies at a lower height over the ocean (850–700 hPa) than over terrain ($\sim$600 hPa) in the midlatitudes (Fig. 2.5e–h).

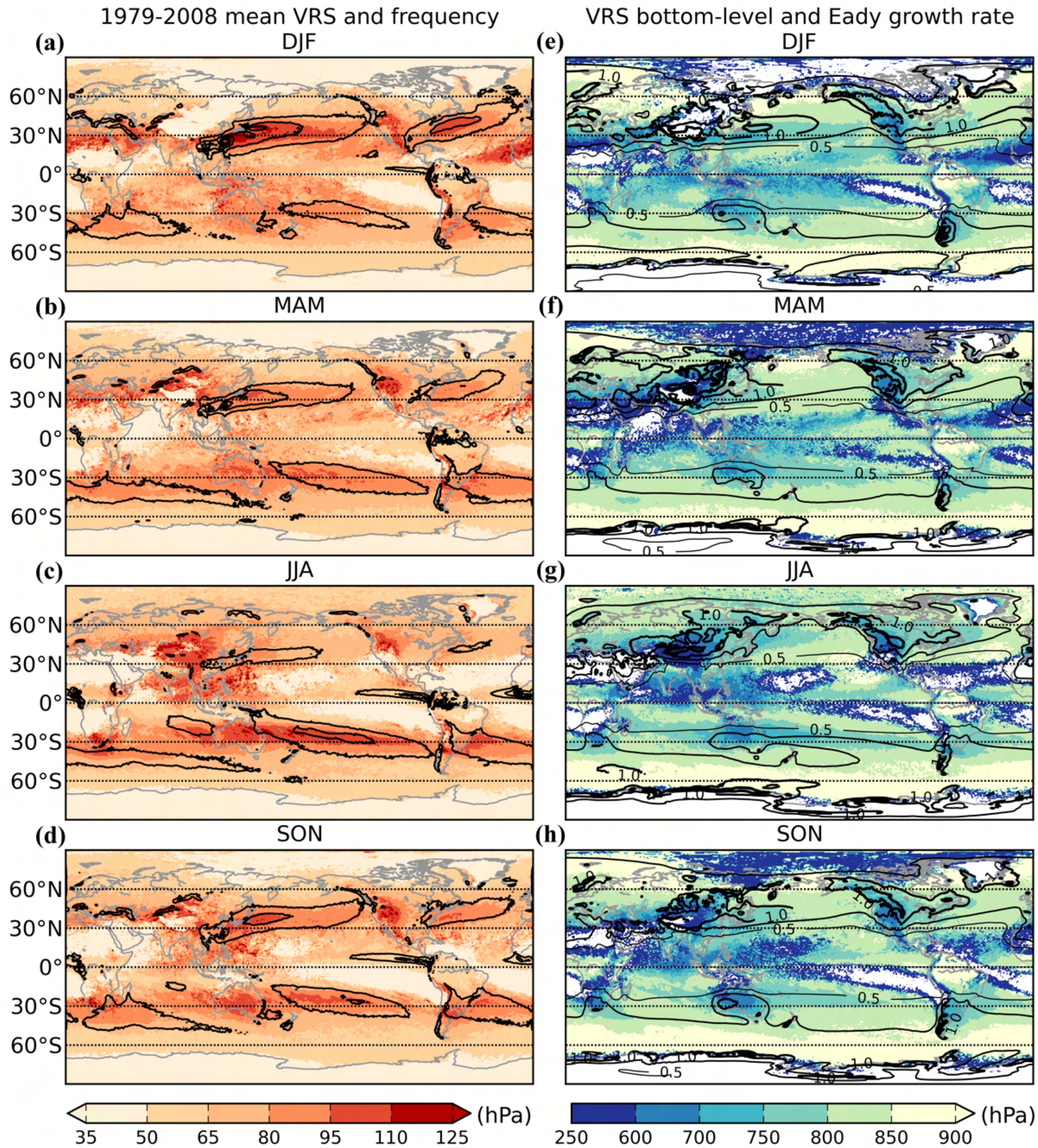


**Fig. 2.5**: The 30-yr-averaged VRS (shaded; hPa) and frequency of occurrence (contours; starting at 2%; interval: 4%) for (a) DJF, (b)MAM, (c) JJA, and (d) SON during 1979–2008. The average is made only when VRS is greater than zero. (e)–(h) As in (a)–(d), respectively, but for the bottom level of VRS (shaded; hPa) where VRS>0 and the vertically averaged (pressure weighted) maximum Eady growth rate from 200 to 900 hPa or near the surface (contours; starting at 0.5 day$^{-1}$; interval: 0.25 day$^{-1}$).

The frequency of VRS occurrence agrees well with the distribution of $f_\mathrm{s}$, and both resemble the climatological midlatitude storm tracks [e.g., Figs. 2a and 4a in Bengtsson et al. (2006); Fig. 1 in Tamarin and Kaspi (2017)]. This finding is consistent with G17's result for the North Atlantic. For the Northern Hemisphere, VRS more frequently occurs in the oceanic region downstream of the continents under midlatitude westerlies, such as over the northwestern Pacific and northwestern Atlantic with a peak frequency of over 15% and about 10%, respectively, of the total time in DJF. Note that our value over the North Atlantic is somewhat smaller than the 20% shown in G17. As for the Southern Hemisphere, the VRS frequency distribution between 10° and 40°S is more zonally symmetric as a result of the larger coverage of ocean than in the Northern Hemisphere. In all, regions with large VRS and high frequency of occurrence, such as the northwestern Pacific and northwestern Atlantic during DJF, March–May (MAM), and September–November (SON), as well as the midlatitude South Pacific and Atlantic in JJA, represent favorable environments for moist slantwise convection.

As mentioned in Section 2.2.1(2), CSI is more likely to exist in environments with strong wind shear and weak static stability, the combination of which tends to yield strong baroclinic instability. Thus, we also examine the climatology of the maximum Eady growth rate (Eady, 1949):

$$\sigma = 0.31\frac{|f|}{N}\left|\frac{\partial \boldsymbol{V}}{\partial z}\right|, \tag{2.7}$$

where $N$ is the dry Brunt–Väisälä frequency, and $\boldsymbol{V}$ is the horizontal wind vector. We calculate this quantity at each level and then obtain the pressure-weighted average from 200 to 900 hPa (or, at the first level above the surface if the surface lies above 900 hPa). Indeed, the result shows that deep and/or frequent VRS (Fig. 2.5a–d) coincide with the areas of strongest baroclinic instability (Fig. 2.5e–h).

However, while the conditionally averaged VRS have comparable magnitudes over land

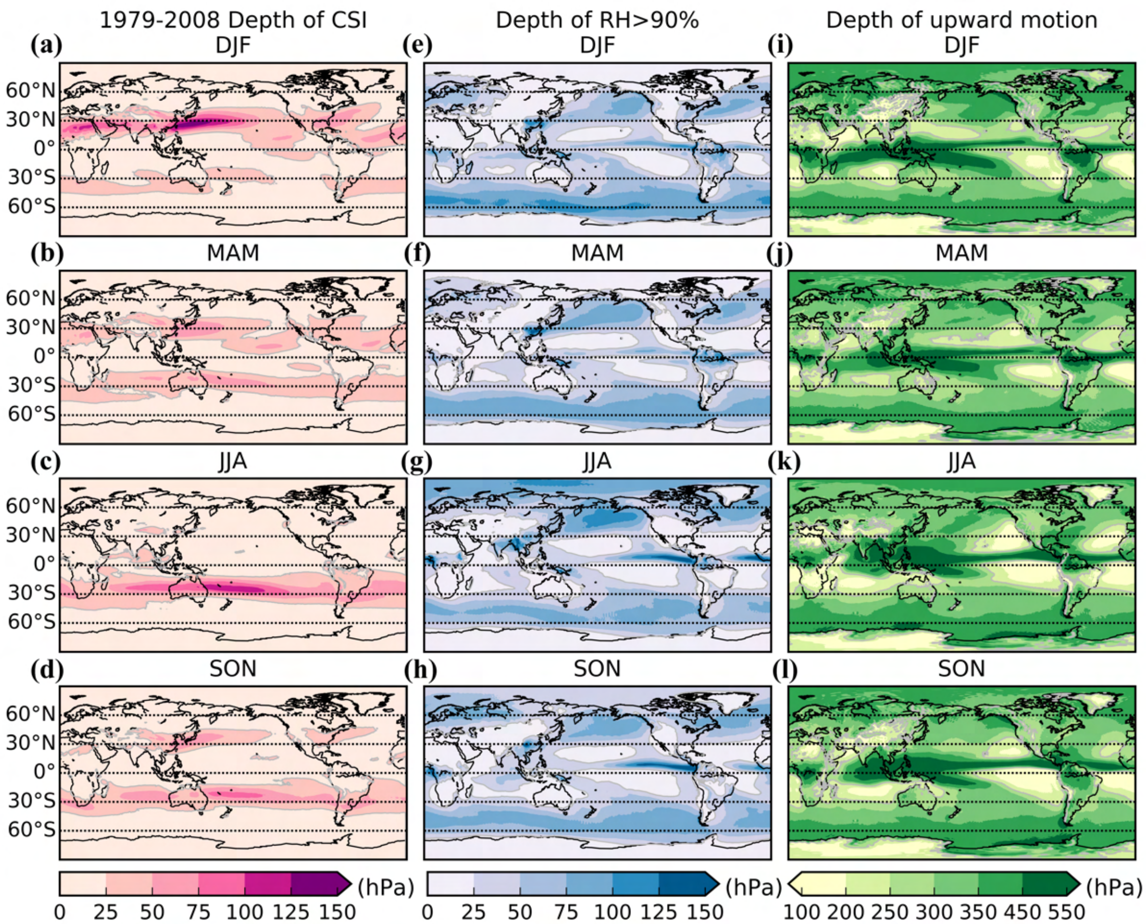


**Fig. 2.6**: The 30-yr-averaged maximum continuous air depth of the existence of CSI (shaded; hPa) for (a) DJF, (b) MAM, (c) JJA, and (d) SON during 1979–2008. (e)–(h) As in (a)–(d), respectively, but for the depth of RH > 90% (shaded; hPa). (i)–(l) As in (a)–(d), respectively, but for the depth of upward motion (shaded; hPa).

and over ocean, it is found that the VRS frequency tends to be much lower over land than over the oceans even with a similar strength of the peak baroclinic instability (over 1 day$^{-1}$). To address this issue, all three components of VRS are investigated separately (Fig. 2.6). While the maximum continuous air depth of CSI is slightly larger in the western ocean basins than over the eastern part of continents, likely related to the stronger baroclinicity over western oceanic boundary currents, the overall distribution is more zonally symmetric than that for the other two components of VRS. The maximum continuous depths of the layers with RH> 90% and positive vertical motion both exhibit much stronger land–ocean contrasts in every season. Layers above the midlatitude ocean with RH> 90% are generally deeper than those above the adjacent midlatitude land, by around 50 hPa. Except for the ITCZ area, where upright convection is dominant, the vertical motion over the ocean is also deeper (> 50 hPa in depth) than that over adjacent land. Two additional calculations of VRS are conducted, each of which excludes the criteria of RH> 90% or upward motion (not shown). It is found that the maximum continuous depth where only CSI and RH> 90% are considered (regardless of the presence of upward motion) shows higher resemblance to our original definition of VRS, suggesting that given the existence of CSI, the long-standing, vertically extended moisture over the ocean likely plays a decisive role in promoting the frequent existence of VRS there.

### 2.3.4 Instantaneous features of slantwise convection events

Detailed examination shows that, instantaneously, positive VRS is manifested as mesoscale cellular clusters or curved bands propagating eastward with a maximum horizontal length scale of order 1000 km and a peak depth of around 350 hPa. To look more closely at the detailed distribution of $f_s$ and VRS for individual events, three observational cases associated with slantwise convection (Emanuel, 1983b; Reuter and Yau, 1990; G17) are briefly revisited here (Fig. 2.7). Although $f_s$ and VRS do not necessarily overlap with each other at any given instant, they both correspond well to the regions where moderate or heavy precipitation occurred along/near the fronts. The location of fronts generally coincides with the areas of heaviest precipitation and horizontal wind shifts, with the warm fronts extending eastward of the surface low and the cold fronts extending south-southwestward. As shown here, although the distribution of these two parameters within a given cyclone is case dependent, both the warm front (Fig. 2.7b,c; see Figs. 11 and 12 in Reuter and

Yau 1990) and the cold front (Fig. 2.7a,c; see Fig. 3a in Emanuel 1983b and Fig. 2 in G17) are possible areas for slantwise convection. Interested readers can refer to the above-cited studies for the detailed discussion on the distribution of slantwise convection over the warm and/or cold frontal areas (in particular, G17 examined seven cases and presented the synthesis in schematic form in their Fig. 3).

### 2.3.5 Correlation of VRS and cyclone activity

The high resemblance between cyclone tracks (Fig. 2.8a–d) and VRS (Fig. 2.5a–d) motivates a quantification of the correlation between the two (Fig. 2.8e–h). This comparison focuses on the Northern Hemisphere where the cyclone data (Serreze, 2009) are available. The general seasonal variation of cyclone frequency broadly agrees with that of VRS occurrence frequency, with a highest maximum value of 3.2 month$^{-1}$ in both the North Pacific and North Atlantic basins in DJF and a lowest maximum frequency of around 2 month$^{-1}$ over these same regions in JJA. The correlation between VRS and cyclone frequency is calculated using their monthly averages from January 1979 to December 2008. Figure 2.8e–h shows that the correlation coefficient between VRS and cyclone frequency is generally positive over the entire Northern Hemisphere with a rather small domain average of 0.09, and among all the seasons, DJF and JJA feature relatively higher correlation coefficients of 0.12 and 0.17, respectively (Table 2.2). The other domain-averaged correlation coefficients during different seasons are summarized in Table 2.2. Locally, relatively high correlation coefficients of above 0.6 can be observed in regions where cyclones are less frequent (e.g., the eastern coast of northeastern Asia in DJF and the Middle East, the eastern North Pacific Ocean, and the southern North Atlantic Ocean in JJA). Although the null hypothesis of zero correlation cannot be ruled out at the 95% confidence level, the general positive correlation coefficient suggests that moist slantwise convection has a higher (lower) occur-

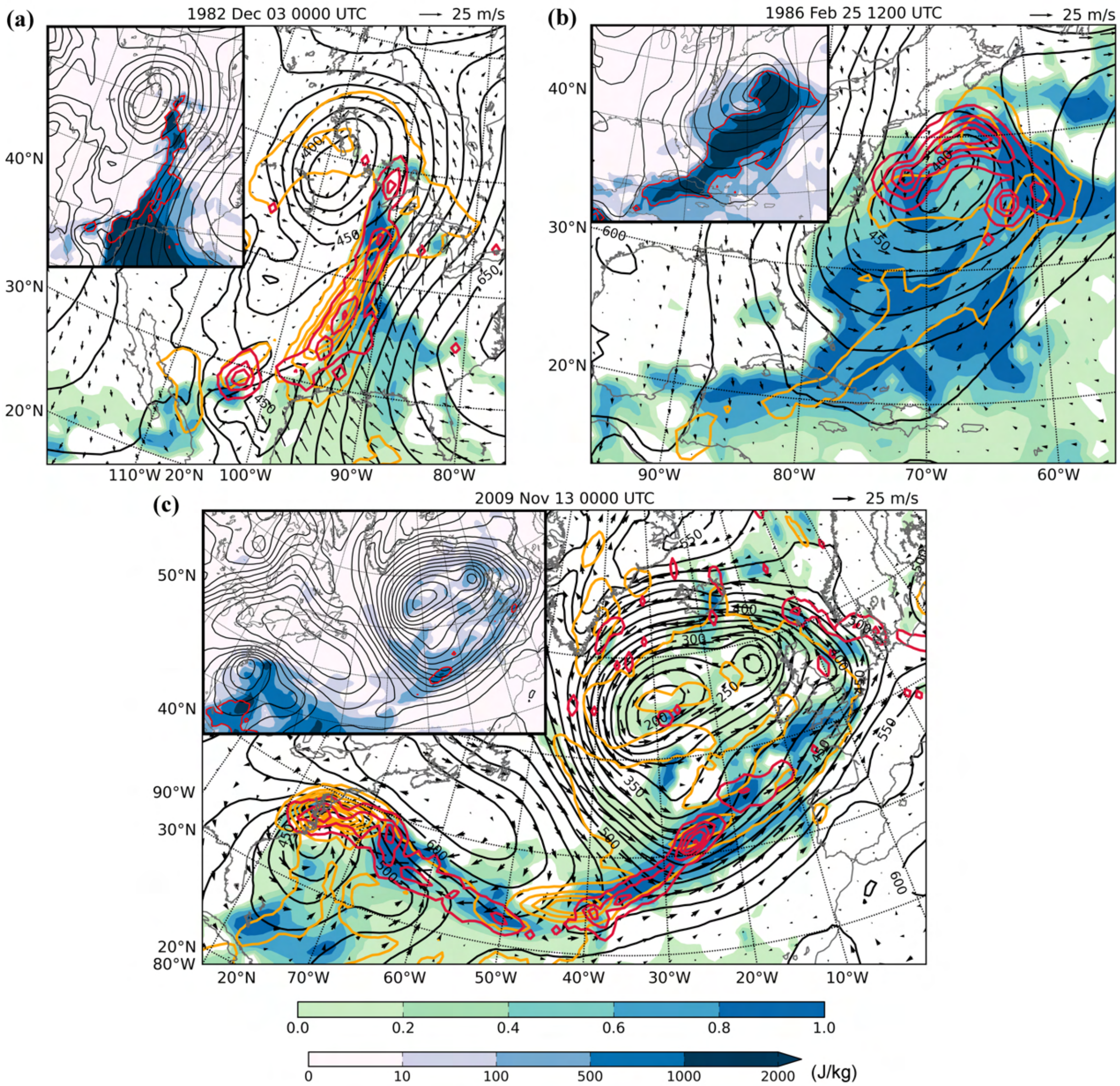


**Fig. 2.7**: Snapshots of slantwise convection cases analyzed in (a) Emanuel (1983b), (b) Reuter and Yau (1990), and (c) G17. SCAPE (shaded in the inset panels; J kg$^{-1}$) and $f_s$ (shaded in the main panels), ERA-Interim 6-h accumulated precipitation (yellow contours; starting at 2 mm; interval: 10 mm), VRS (red contours in the main panels; starting at 10 hPa; interval: 50 hPa), and 950-hPa wind (vectors; m s$^{-1}$) and geopotential height (black contours; m). The red contours in the inset panels bounds where SCAPE is 400 J kg$^{-1}$ larger than CAPE.

rence over the areas with more (less) cyclone activity and where the background baroclinic instability is stronger (weaker).

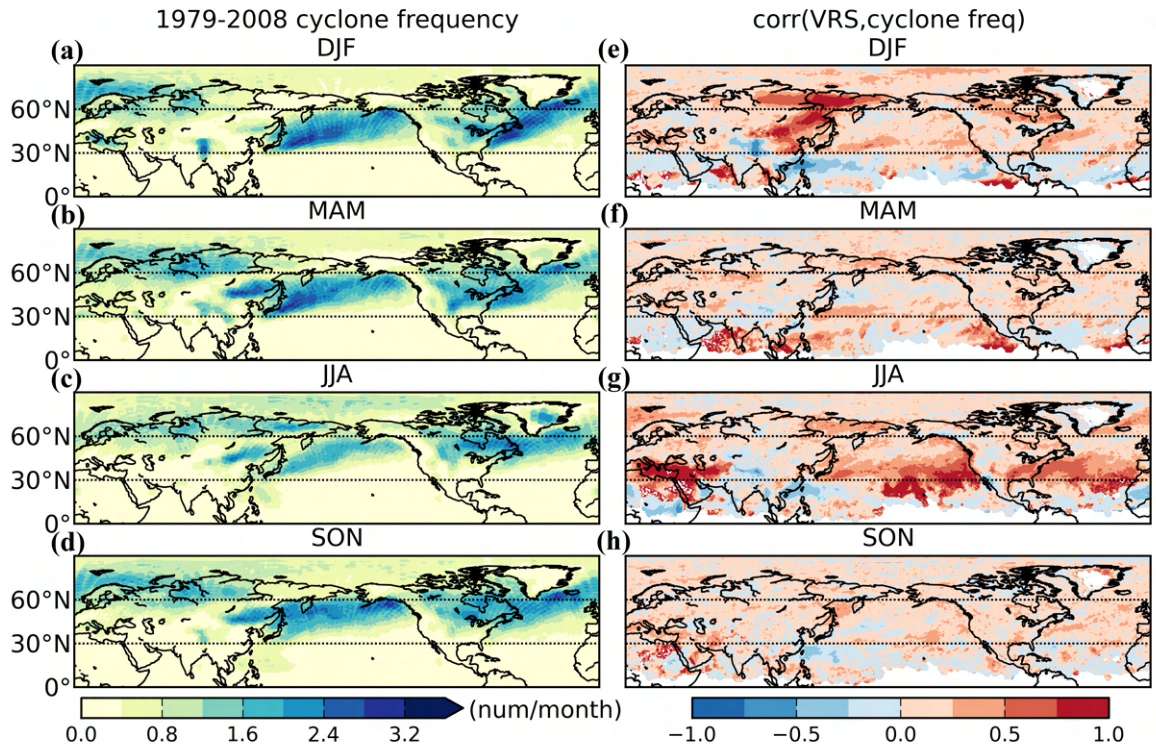


**Fig. 2.8**: The 30-yr-averaged cyclone frequency (shaded; month$^{-1}$) for (a) DJF, (b) MAM, (c) JJA, and (d) SON during 1979–2008. (e)–(h) As in (a)–(d), respectively, but for the correlation between VRS and cyclone frequency. The blank areas are where the standard deviation of either VRS or cyclone frequency equals zero.

A related question that merits exploration is how often are cyclones associated with slantwise convection? We calculate the observed numbers of cyclones that contain nonzero VRS within a 300-km radius of a cyclone center and divided them by the total observational number of cyclones [note for a cyclone with a lifetime of 5 days, the observational number is $5 \times 4$ (4 observations per day)$= 20$ instead of 1], which gives a 30% probability of CSI release (VRS>0) given the existence of a cyclone. In other words, at a given time, 30% of the observed cyclones are likely exhibiting slantwise convection near their core. Considering that slantwise convection may not exist for the whole life cycle of each cyclone, the calculation is further partitioned into different categories based on the observed intensification rate of the cyclones for each time step. Despite the increasing margin of error (yet still small with values $< 1.2\%$) due to decreasing sample size, the probability of VRS $> 0$ increases with the intensification rate of the cyclones (Fig. 2.9).While the chance for cyclones in the weakening stage to exhibit slantwise convection is less than 30%, cyclones undergoing rapid intensification (central pressure drops equal to or more than 24 hPa day$^{-1}$) have a greater than 57% chance of being associated with slantwise convection.

### 2.3.6 Time evolution of CSI within explosive and nonexplosive cyclones

It was just shown that the susceptibility of the atmosphere to slantwise convection exhibits a strong relationship to the intensification rate of the cyclone. To further investigate this issue, the averaged time evolutions of SCAPE, CAPE, and VRS around the center of the cyclones from 1979 to 2008 are presented in Fig. 2.10, along with the averaged intensity change of the cyclones. The analysis is conducted separately for explosive and nonexplosive cyclones, and a comparison between them is then performed.

**Table 2.2**: Correlation coefficients between VRS and cyclone frequency for different domains and different seasons during January 1979–December 2008. Boldface values are statistically significant at the 95% confidence level for a two-tailed test.

| | Annual | DJF | MAM | JJA | SON |
|---|---|---|---|---|---|
| Northern Hemisphere | 0.09 | 0.12 | 0.10 | 0.17 | 0.09 |
| Tropics | 0.03 | 0.06 | 0.19 | 0.04 | 0.07 |
| Subtropics and midlatitudes | **0.11** | 0.12 | 0.09 | **0.25** | 0.10 |
| Land | 0.08 | 0.17 | 0.08 | 0.13 | 0.10 |
| North Pacific Ocean | 0.10 | 0.07 | 0.14 | **0.25** | 0.07 |
| North Atlantic Ocean | **0.10** | 0.08 | 0.09 | **0.27** | 0.10 |

For each cyclone that underwent explosive development during its lifetime, the onset of the rapid intensification is identified as 0 h, and then the associated SCAPE, CAPE, and VRS at different times (with an interval of 6 h) are calculated by averaging over a circular domain with a radius of 300 km around the cyclone center. As shown in Fig. 2.10b, slight buildups of SCAPE and VRS are observed 36–12 h before the onset, which are followed by significant drops during the rapid deepening stage. As cyclones reach their peak intensity (at +30 h in Fig. 2.10a), the two values decrease to a minimum and remain low for the following 30 h. Note that the buildup and the drop of VRS slightly lag those of SCAPE, suggesting that the environment first becomes thermodynamically susceptible to CSI, and a few hours later the layers with releasable CSI develop and/or deepen (thus increasing VRS) because of intensifying vertical motion. The evolution of CAPE, on the other hand, does not show such a strong sensitivity to the phase of cyclone evolution.

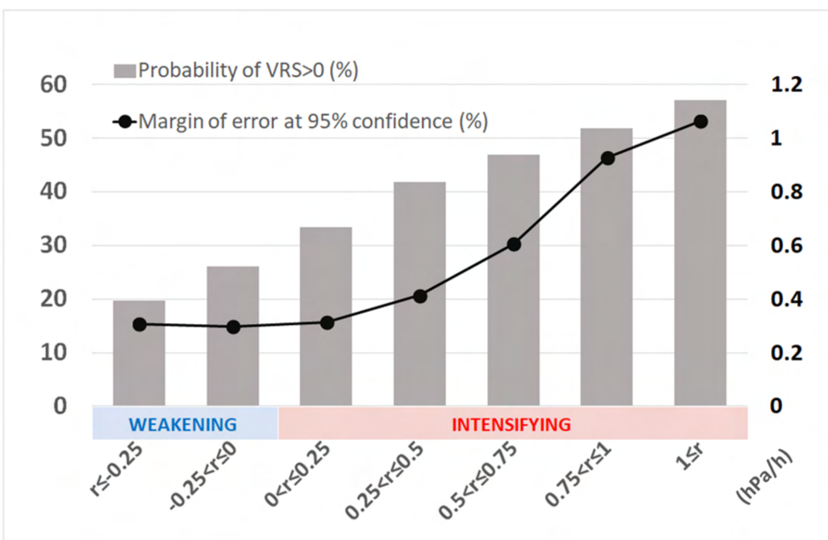


**Fig. 2.9**: Probability of slantwise convection occurrence potential given the existence of cyclones with different intensification rates $r$, defined by the decrease of central pressure per hour. Positive (negative) values ($r$) indicate the cyclones are undergoing intensification (weakening) at that time. The black curve (corresponding to the value on the right $y$ axis) is the margin of error at the 95% confidence level (%).

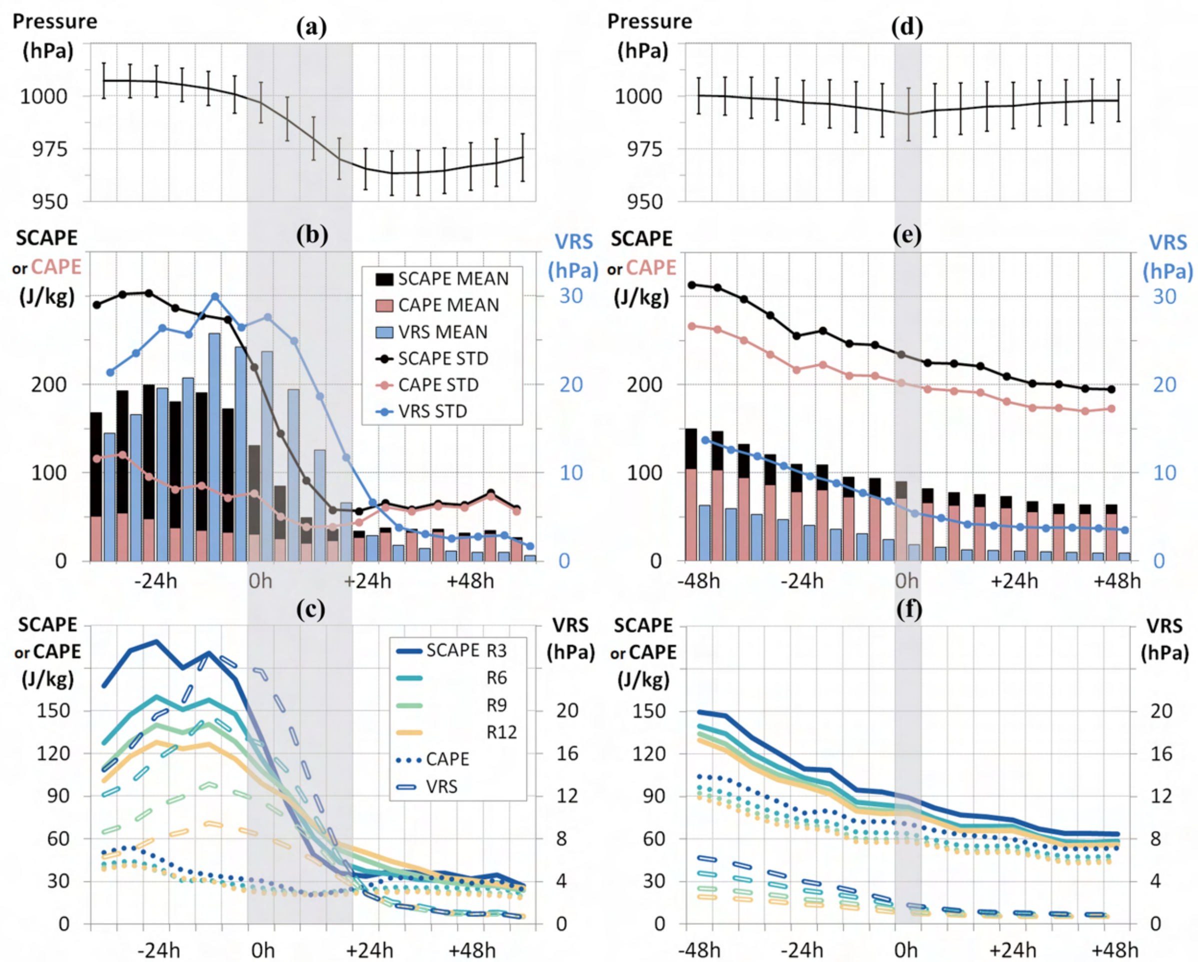


**Fig. 2.10**: (a) Averaged time evolution of central sea surface pressure[†](curve and error bars denote the standard deviation among all the cases); (b) SCAPE (black bars), CAPE (pink bars), and VRS (blue bars) averaged within a radius of 300 km around each center of explosive cyclones in the Northern Hemisphere during 1979–2008. Standard deviation for SCAPE and VRS among all the cases are denoted in dash–dotted curves. (c) Averaged SCAPE (solid), CAPE (dotted), and VRS (dashed) using different selected radii ranging from 300 km (R3) to 1200 km (R12). The gray shading denotes the period of rapid intensification (RI) and 0 h is defined as the onset of the RI in each cyclone. (d)–(f) As in (a)–(c), respectively, but for nonexplosive cyclones, and 0 h is defined as the time while reaching the peak intensity.

The standard deviations of both SCAPE and VRS are even larger than their averaged values, indicating a large uncertainty among different explosive cases. Such a large vari-

[†]Correction: should be sea-level pressure.

ability is expected given the large variability in the sizes and the structures of cyclones and the different synoptic environments of the different cases. Nevertheless, the mean evolution of these indices provides a general picture that the cyclones become increasingly symmetrically unstable prior to their rapid intensification and then release this instability during the rapid deepening phase through vigorous slantwise convection. By the time that peak intensity is reached, the likelihood of slantwise convection drops to a minimum as the atmosphere is almost fully neutralized to slantwise displacements. This averaged evolution is consistent with that found in several observational case studies (e.g., Emanuel, 1983b; Shutts, 1990b,a; Reuter and Yau, 1993), providing support that a slantwise moist adjustment takes place within explosive cyclones, especially during their intensifying stage.

The time evolutions of SCAPE, CAPE, and VRS for nonexplosive cyclones in Fig. 2.10e show that, unlike in the explosive cases, all three indices exhibit a gradual decrease before these cyclones reach their peak intensity, and the rate of decrease becomes even smaller thereafter. After the intensification of the cyclone, VRS reduces to as low a value as that in explosive cases but SCAPE and CAPE do not reduce as much, suggesting that the maximum available energy is not entirely released, possibly because of the lack of deep-layer humidity and/or large-scale ascent in nonexplosive cases. Also, despite large standard deviations, the magnitudes of SCAPE and VRS (but not CAPE) are smaller than those observed in explosive cases on average.

Considering slantwise convection can occur along the cold-frontal system that extends farther away from the center, a sensitivity test on the selected radius, ranging from 300 to 1200 km, is conducted (Fig. 2.10c, f). While the averaged values of these indices decrease with selected radius, their overall trends do not change significantly.

The contrasting evolution of these indices between explosive and nonexplosive cases indicates that the intensity of slantwise convection may vary strongly with the cyclone intensification rate. During the deepening period, explosive cyclones tend to have more active (with larger decrease of SCAPE but not CAPE) and deeper (with larger VRS) slantwise convection than nonexplosive cases, and the associated enhancement of latent heat release lends support to the notion that slantwise convection can promote an intensification of the cyclones.† Furthermore, the increasing slantwise convection potential at early stages in explosive cyclones may play a key role in determining whether rapid intensification subsequently occurs. The potentially important role of slantwise convection on the life cycle of explosive cyclones suggested by this analysis is a topic that merits further investigation.

## 2.4 Summary

The purpose of this study is to understand the climatology of slantwise convection over the entire globe, which has not been extensively presented in the literature. Two indices, slantwise convective available potential energy (SCAPE) and vertically integrated extent of realizable symmetric instability (VRS), are calculated to assess the climatology of conditional symmetric instability using the 37-yr ERA-Interim dataset. Furthermore, the correlation of the slantwise convection potential and properties of observed weather systems, such as precipitation and cyclone activity, are also investigated statistically.

The spatial distribution of the 37-yr seasonal-averaged SCAPE, and the seasonal variation of its zonal average, are similar to those of CAPE except for a wider north–south extent. CAPE has been widely used as a diagnostic tool for assessment of the potential for deep convection (e.g., Brooks et al., 2003; Marsh et al., 2007; Subrahmanyam et al., 2015). G17 showed that the correlations of SCAPE with precipitation generally exceed those of CAPE with precipitation over subtropical and midlatitude areas in the North At-

†While possible mechanisms have been proposed as to how slantwise convection in the frontal zone may reinforce the development and intensification in *some* cyclones (e.g., Kuo et al., 1991; Balasubramanian and Yau, 1994a), the existence of these mechanisms cannot be identified from our analysis due to the coarse spatial and temporal resolution. Furthermore, we clarify that the three-dimensional distribution of the latent heating can either decrease or strengthen the cyclone development, depending on how it is distributed with respect to the cyclone center.

lantic and European regions. This study extends a similar analysis to the whole globe, verifying that, in general, SCAPE correlates with precipitation more strongly than CAPE in a climatological content since it accommodates both upright convection and slantwise convection. Both CAPE and SCAPE feature statistically significant domain-averaged correlation coefficients of around 0.4–0.5 with precipitation. Generally, SCAPE exhibits a higher correlation with precipitation than CAPE, in particular over subtropical and midlatitude areas with a 0.06-higher domain-averaged correlation coefficient annually. Locally, SCAPE has >0.3-higher correlation coefficients with precipitation than CAPE in the North Pacific and North Atlantic basins during December–February (DJF), indicating the importance of slantwise convection to precipitation there. In contrast, SCAPE shows a lower correlation with precipitation than does CAPE in some tropical regions, possibly because upright convection is still dominant in areas of large CAPE. Furthermore, thermal wind balance is not valid in the tropics and thus slantwise convection is less likely to be relevant there considering the theoretically 2D nature of symmetric instability.

Compared to the absolute difference of SCAPE and CAPE, the fractional residual term, $f_{\mathrm{s}} = (\mathrm{SCAPE} - \mathrm{CAPE})/\mathrm{SCAPE}$, helps more clearly to identify the relative importance of upright convection and slantwise convection. Tropical areas are dominated by upright convection (with $f_{\mathrm{s}}$ near zero) in almost every season. By contrast, there is a high chance of the coexistence of upright and slantwise convection (with intermediate values of $f_{\mathrm{s}}$) in subtropical and midlatitude regions. Areas of strong vertical wind shear, such as over the midlatitude western oceanic boundary currents, favor slantwise convection (with higher $f_{\mathrm{s}}$). In particular, the northwestern Pacific Ocean and the 10°–30°S band of the South Pacific Ocean exhibit the highest likelihoods of pure slantwise convection in terms of $f_{\mathrm{s}}$ in DJF and in June–August (JJA), respectively.

Another index for the assessment of releasable conditional symmetric instability, VRS, is also examined and extended globally to provide a complementary perspective of moist slantwise convective potential. Unlike SCAPE, which encompasses both static and moist symmetric instability, the definition of VRS explicitly excludes static instability and thus only considers moist symmetric instability. Herein, the VRS is a measure of the maximum continuous air thickness where conditional symmetric instability, moisture, and vertical motion coexist. The climatological distributions of VRS frequency and $f_s$ share large similarities, specifically that the air over the midlatitude westernmost oceans (i.e., storm-track regions) is the most susceptible to slantwise convection due to strong baroclinicity, partly strengthened by the western oceanic boundary currents, and abundant moisture. The instantaneous VRS can exceed 350 hPa and has a rather sparse horizontal distribution, manifesting either as cellular clusters or in bands stretching over several hundred kilometers, likely associated with frontal systems. The climatologically averaged depth of VRS peaks at 110 hPa, generally with the bottom level between 850 and 700 hPa. G17 observed a close correspondence of the VRS spatial structure with the North Atlantic storm track. Consistent with that result, the present study finds that the seasonal distribution of VRS frequency resembles the seasonal cyclone frequency in both the North Atlantic and North Pacific. Although the Northern Hemisphere–averaged correlation coefficient between VRS and cyclone frequency does not pass the 95% confidence level, the positive value of 0.11 averaged over subtropics and midlatitudes in the Northern Hemisphere is statistically significant. A novel finding of this study is that the probability of CSI release (VRS $> 0$) is 30% given the existence of a cyclone and increases with the intensification rate of cyclones. A cyclone undergoing rapid intensification has a greater-than-57% chance of exhibiting slantwise convection.

Finally, the evolution of slantwise convection potential during the life cycles of explosive and nonexplosive cyclones has been investigated for the first time. A clear separation between explosive and nonexplosive cases was found. While for explosive cyclones, both VRS and SCAPE (but not CAPE) increase from 36 to 12 h prior to the onset of their rapid intensification and then decrease sharply thereafter, the nonexplosive cases exhibit a much gentler decreasing rate of VRS and SCAPE during the entire period of interest. Thus, not only does slantwise convection have a higher chance to occur in those explosive cases at the peak deepening stage, it is also expected to be more active (with a larger release of SCAPE but not CAPE) and deeper (with a larger VRS), which may contribute to the rapid intensification by releasing additional latent heat. After the cyclones reach their peak intensity, the atmosphere is modified to a nearly slantwise neutral state with low SCAPE–CAPE and VRS in both the explosive and nonexplosive cases.

**Acknowledgments.** The research reported here has been supported by the NSERC/Hydro-Quebec Industrial Research Chair program. We thank Morgan E. O'Neill, Suzanne Gray, and one anonymous reviewer for their valuable comments and suggestion that helped to improve this study.

# Chapter 3

# Numerical modeling: in-line retrieval of budget analysis

Chapter 2 confirms the importance of slantwise convection in midlatitudes, raising a question as to whether the current NWP and GCMs can adequately represent it? As an attempt to answer this question, we conduct numerical simulations of slantwise convection and investigate its explicit representation at different horizontal grid spacing.

Momentum budget analysis is used to identify various dynamical processes in governing the flow evolution and grid-spacing sensitivity. To avoid large residual hindering the physical interpretation, we first develop an in-line retrieval method to extract all the budget terms during the model integration to guarantee an accurate budget analysis. This chapter introduces such an in-line retrieval tool and its advantages over other post-processing methods. Note that this article deals with technical development, and readers who wish to focus on the results of slantwise convection simulations are referred to Chapter 4.

This work consists of the following published article:

Chen, T.-C., M.-K. Yau and D. J. Kirshbaum, 2020: Towards the closure of momentum budget analyses in the WRF (v3.8.1) model, *Geosci. Model Dev.*, **13**, 1737-1761, `https://doi.org/10.5194/gmd-13-1737-2020`

Footnotes with a superscript "†" indicate editorial notes added for clarifications.

# Towards the closure of momentum budget analyses in the WRF (v3.8.1) model

TING-CHEN CHEN, MAN-KONG YAU, AND DANIEL J. KIRSHBAUM

*Department of Atmospheric and Oceanic Sciences, McGill University, Montreal, Quebec, Canada*



## Abstract

Budget analysis of a tendency equation is widely utilized in numerical studies to quantify different physical processes in a simulated system. While such analysis is often post-processed when the output is made available, it is well acknowledged that the closure of a budget is difficult to achieve without temporal and/or spatial averaging. Nevertheless, the development of errors in such calculations has not been systematically investigated. In this study, an in-line budget retrieval method is first developed in the WRF v3.8.1 model and tested on a 2D idealized slantwise convection case with a focus on the momentum equations. This method extracts all the budget terms following the model solver, which gives a high accuracy, with a residual term always less than 0.1% of the tendency term. Then, taking the in-line values as truth, several off-line budget analyses with different commonly used simplifications are performed to investigate how they may affect the accuracy of the estimation of individual terms and the resultant residual. These assumptions include using a lower-order advection operator than the one used in the model, neglecting grid staggering, or following a mathematically equivalent but transformed format of the governing

equations. Errors in these post-processed analyses are found mostly over the area where the dynamics are the most active, thus impairing the subsequent physical interpretation. A maximum 99th percentile residual can reach $> 50\%$ of the concurrent tendency term, indicating the danger of neglecting the residual term as done in many budget studies. This work provides general guidance not only for budget diagnoses with the WRF model but also for minimizing the errors in post-processed budget calculations.

## 3.1 Introduction

The atmosphere is a complex system with different scales of motion. Its dynamics are governed by a set of fluid equations based on the fundamental laws of physics. Although the equation set cannot be solved analytically, numerical models can be used to simulate the observed weather and climate systems to improve our understanding of the atmosphere. Due to the complexity and nonlinearity of the numerical models, budget analysis is often employed to interpret the results by quantifying the contribution of each term (i.e., physical process) in a tendency equation that governs the evolution of a certain quantity in the simulated system. The accuracy of a given budget analysis can be estimated from the residual term, defined as the difference between the tendency term on the left-hand side (lhs) of the equation and the summation of all the forcing terms on its right-hand side (rhs). Budget analysis has been performed on diverse properties (e.g., momentum, temperature, water vapor, vorticity) of many systems on various scales, including the Madden–Julian oscillation (MJO; e.g., Kiranmayi and Maloney, 2011; Andersen and Kuang, 2012), tropical cyclones (e.g., Zhang et al., 2000; Rios-Berrios et al., 2016; Huang and Montgomery, 2018), squall lines (e.g., Sanders and Emanuel, 1977; Gallus and Johnson, 1992; Trier et al., 1998), supercell thunderstorms (e.g., Lilly and Jewett, 1990), and so on.

Despite the popularity of the budget analysis, it is generally acknowledged that, in model post-processing analysis, obtaining a closed budget with a negligible residual is difficult (e.g., Kanamitsu and Saha, 1996) and has been accomplished mostly in time- or domain-averaged budget calculations (e.g., Lilly and Jewett, 1990; Balasubramanian and Yau, 1994a; Arnault et al., 2016; Kirshbaum et al., 2018; Duran and Molinari, 2019). Even in the case of averaged budgets, the residual term that contains non-explicitly diagnosed physics can be larger than the tendency term (e.g., Liu et al., 2016), and many studies simply do not display the residual, making the proper interpretation of the budget analysis difficult.

The "residual analysis method" is sometimes utilized to obtain an indirect estimation of the physical processes that are hard to diagnose or are unresolved in a set of analysis or observational data. In such cases, a non-negligible residual is sometimes used to gain insight into such processes. However, as just discussed, the residual term also contains the inaccuracies associated with the calculations within the budget analysis (e.g., Kornegay and Vincent, 1976; Abarca and Montgomery, 2013). It is thus unclear whether the unresolved physics in such data sets do indeed comprise the main component of the residual without considering the contributions of other sources of errors in the budget calculation (Kuo and Anthes, 1984). Whereas it is almost impossible to separate the subgrid-scale, unresolved processes from other errors in reanalysis or observational data (e.g., Hodur and Fein, 1977; Lee, 1984), the focus of this study is on numerical model data where the local tendency and all the associated resolved and parameterized physics can be obtained from the model. Thus, the residual term in this study specifically refers to errors in the budget calculation.

To reduce the residual, an in-line budget analysis that extracts all the terms of a prognostic equation directly from the model during its integration is generally the most accurate. However, the procedure has been reported only in a few studies (e.g., Zhang et al., 2000; Lehner, 2012; Moisseeva, 2014; Moisseeva and Steyn, 2014; Potter et al., 2018; see Appendix A for a summary and comparison among these works). Most other studies still conduct the off-line or post-processing budget analysis when the output is made available after the model integration. Some specific suggestions have been given in the past regarding how to reduce the error of post-processed budget analysis. For example, Lilly and Jewett (1990) emphasized the importance of evaluating terms using the same differencing scheme, grid stretching, and grid staggering as that used in the simulation model. However, it is uncertain whether these rules have been widely followed, and how much of a reduction in residual can be obtained with this approach.

In some post-processed budget analyses, transformed equations with different assumptions from those in the model are used and naturally lead to errors in the budget results. On the other hand, even when the same form of the equations is followed, errors can still arise from multiple sources during the post-processing. Some errors are inherent in the time discretization scheme of the model, some are traced to the numerical methods in solving the temporal or spatial derivatives with finite differencing (e.g., Kuo and Anthes, 1984), and others might emerge during the interpolation or extrapolation from model grids to analysis grids (e.g., Lilly and Jewett, 1990). While the tendency term is often the result of a few cancelations among competing forcing terms, the seemingly non-dominant terms may be as important as the large forcing terms in determining the sign and the value of the tendency. Thus, an incorrect estimation of even a small term may result in a residual with magnitude comparable to the tendency term, hindering the subsequent physical interpretation.

A few models, such as the Cloud Model 1 (CM1; Bryan and Fritsch, 2002) and the High Resolution Limited Area Model (HIRLAM; Undén et al., 2002), include in-line budget diagnoses that users can choose to include in the model output. However, many other commonly used models [e.g., Fifth-Generation NCAR/Penn State Mesoscale Model (MM5; Grell and Stauffer, 1994),Weather Research and Forecasting Model (WRF; Skamarock et al., 2008), the Advanced Regional Prediction System (ARPS; Xue et al., 2000, 2001), and the Regional Atmospheric Modeling System (RAMS; Pielke et al., 1992)] do not have this capability. In this study, we develop an in-line momentum budget retrieval tool in the Advanced Research WRF model, one of the most widely used numerical weather prediction models. During the period 2011–2015, there were on average 510 peer-reviewed journal publications involving WRF per year (Powers et al., 2017). Given the widespread use of WRF for both real-case and idealized modeling, such a budget tool may prove useful in numerous applications. In our budget diagnosis, each contributing term is extracted during the model integration and stored as a standard output. In so doing, we essentially solve the prognostic variables as done in the model so that the two sides of the tendency equation are always in balance regardless of the output time interval. By taking the results from the in-line budget analysis as truth, we then perform several different post-processing budget analyses with commonly made simplifications or a different format of equation. Comparisons between the post-processed budgets and the in-line/true values are made to investigate the potentially large errors in each forcing term and the resultant residuals.

## 3.2 Model and numerical setup

### 3.2.1 Model and momentum equations

The WRF configuration used in this study is a two dimensional [($y$, $z$); no variation in the $x$ direction], fully compressible, non-hydrostatic, and idealized version of the Advanced Research WRF model, version 3.8.1 (Skamarock et al., 2008). Here we briefly revisit the parts that are relevant to the momentum budget analysis. The governing equations in the WRF model are cast on a terrain-following dry hydrostatic pressure coordinate. This vertical coordinate, $\eta$, is defined as

$$\eta = (p_{\mathrm{dh}} - p_{\mathrm{dh\_top}})/\mu_{\mathrm{d}},$$

where $p_{\mathrm{dh}}$ is the hydrostatic pressure of the dry air and $\mu_{\mathrm{d}}$ represents the mass of the dry air per unit area in the column; $\mu_{\mathrm{d}} = p_{\mathrm{dh\_sfc}} - p_{\mathrm{dh\_top}}$ where $p_{\mathrm{dh\_sfc}}$ and $p_{\mathrm{dh\_top}}$ indicate the values of $p_{\mathrm{dh}}$ at the surface and the top of the dry atmosphere, respectively.

To ensure conservation properties, the model equations are formulated in flux form, with the prognostic variables coupled with $\mu_{\mathrm{d}}$. The flux-form momentum components are defined as

$$U = \mu_{\mathrm{d}} u, \quad V = \mu_{\mathrm{d}} v, \quad W = \mu_{\mathrm{d}} w, \quad \Omega = \mu_{\mathrm{d}} \frac{\mathrm{d}\eta}{\mathrm{d}t},$$

where $u$, $v$, and $w$ are the two horizontal and vertical velocities, respectively. Note that the dry-mass-coupled velocities ($U$, $V$ , $W$) on coordinates ($x$, $y$, $z$) have units of pascal meter per second, and the dry-mass-coupled vertical velocity on $\eta$ coordinate, $\Omega$, has a unit of pascal per second. For the idealized 2D case on an $f$ plane as in this study, the momentum equations in the WRF model are written as

$$\underbrace{\frac{\partial V}{\partial t}}_{\substack{V\text{ tendency}}} = \underbrace{-\nabla \cdot (\boldsymbol{V} v)}_{\substack{\text{advection}\\ \text{ADV}}} \underbrace{-\mu_{\mathrm{d}} \alpha \frac{\partial p}{\partial y} - \frac{\alpha}{\alpha_{\mathrm{d}}} \frac{\partial p}{\partial \eta} \frac{\partial \phi}{\partial y}}_{\substack{\text{horizontal pressure gradient force}\\ \text{PGF}}} \underbrace{-fU}_{\substack{\text{Coriolis}\\ \text{COR}}} \underbrace{-(\frac{vW}{r_{\mathrm{e}}})}_{\substack{\text{curvature}\\ \text{CUV}}} + \underbrace{P_V}_{\substack{\text{remaining}\\ \text{(parameterized)}\\ \text{physics}}} + \text{res}, \tag{3.1}$$

$$\underbrace{\frac{\partial W}{\partial t}}_{\substack{W\text{ tendency}}} = \underbrace{-\nabla \cdot (\boldsymbol{V} w)}_{\substack{\text{advection}\\ \text{ADV}}} + \underbrace{g(\frac{\alpha}{\alpha_{\mathrm{d}}} \frac{\partial p}{\partial \eta} - \mu_{\mathrm{d}})}_{\substack{\text{net vertical pressure gradient}\\ \text{and buoyancy force}\\ \text{PGFBUOY}}} \underbrace{+(\frac{uU + vV}{r_{\mathrm{e}}})}_{\substack{\text{curvature}\\ \text{CUV}}} + \underbrace{P_W}_{\substack{\text{remaining}\\ \text{(parameterized)}\\ \text{physics}}} + \text{res}, \tag{3.2}$$

where

$$-\nabla \cdot (\boldsymbol{V} a) = -\frac{\partial (Ua)}{\partial x} - \frac{\partial (Va)}{\partial y} - \frac{\partial (\Omega a)}{\partial \eta} \tag{3.3}$$

is the flux-form advection, $p$ is the full pressure with inclusion of vapor, $\phi$ is the geopotential, $f$ is the Coriolis parameter, $r_{\mathrm{e}}$ is the mean earth radius, and $\alpha$ and $\alpha_{\mathrm{d}}$ are the full and dry-air specific volume, respectively. In our selected microphysics scheme (Thompson et al., 2008), six hydrometeors are included, and thus $\alpha = \alpha_{\mathrm{d}}(1 + q_{\mathrm{v}} + q_{\mathrm{c}} + q_{\mathrm{r}} + q_{\mathrm{i}} + q_{\mathrm{s}} + q_{\mathrm{g}})^{-1}$, where $q_{\mathrm{v}}$, $q_{\mathrm{c}}$, $q_{\mathrm{r}}$, $q_{\mathrm{i}}$, $q_{\mathrm{s}}$, $q_{\mathrm{g}}$ are the mixing ratios for water vapor, cloud, rain, ice, snow, and graupel, respectively. The rhs forcing terms for the $V$ tendency include the flux-form advection (ADV), horizontal pressure gradient force (PGF), Coriolis force (COR), vertical (earth-surface) curvature (CUV), and the remaining physics ($P_V$). For the $W$ tendency, the rhs forcings contain the flux-form advection (ADV), net force between the vertical pressure gradient and buoyancy (PGFBUOY), curvature effect (CUV), and the remaining physics ($P_W$). The remaining physics may include diffusion, damping processes, and other parameterized physics, depending on the model setup. Note that for closing the budget analysis, all the known physics processes that come into play should be explicitly written in the equation and be diagnosed or directly retrieved from the model. The residual (res) is added on the last rhs term in (3.1) and (3.2) to represent the imbalance between the two sides of the equation during budget analysis, but it is not part of the original equations solved in the model.

To develop an in-line budget retrieval tool, it is important to understand how these prognostic variables are advanced in the WRF model. Governing equations are first recast to perturbation forms with respect to a dry hydrostatically balanced reference state that is a function of height only (defined at initialization) to reduce truncation errors and machine rounding errors. Specifically, variables of $p$, $\phi$, $\alpha_{\mathrm{d}}$, and $\mu_{\mathrm{d}}$ are separated into reference and perturbation components, e.g., $p(x, y, \eta, t) = \bar{p}(z) + p'(x, y, \eta, t)$. The introduction of these perturbation variables only changes the expressions for the rhs terms PGF and PGFBUOY in (3.1) and (3.2), which will not be shown here for simplicity. Readers can refer to Skamarock et al. (2008, their Chapter 2.5) for more details. Based on Skamarock et al. (2008), Fig. 3.1 summarizes the WRF integration strategy. The integration is wrapped by a third-order Runge–Kutta (RK3) scheme, in which the prognostic variables (generalized as $\Phi$ here) are advanced from $t$ to $t + \Delta t$ given their corresponding partial differential equations, $\frac{\partial\Phi}{\partial t} = F(\Phi)$, following a three-step strategy:

$$\begin{aligned} \Phi^* &= \Phi^t + \frac{\Delta t}{3} F(\Phi^t), \\ \Phi^{**} &= \Phi^t + \frac{\Delta t}{2} F(\Phi^*), \\ \Phi^{t+\Delta t} &= \Phi^t + \Delta t F(\Phi^{**}), \end{aligned} \tag{3.4}$$

where $\Delta t$ is the model integration time step and $F$, the large-step forcing, represents the summation of all the rhs terms of (3.1) and (3.2) excluding the residual. Although the parameterized forcings stay fixed from step one to three as most of the parameterization schemes are called only once at the first RK3 step, the rest of the non-parameterized forcings and thus the total $F$ are changed with the updated $\Phi^*$ and $\Phi^{**}$ at the second and third RK3 step. Within each RK3 step, a subset of integration with a relatively smaller time step is embedded to accommodate high-frequency modes for numerical stability (Wicker and Skamarock, 2002; Klemp et al., 2007; Skamarock et al., 2008). A maximum number of small steps in one model integration step can be specified by the user. To improve accuracy in the temporal solver, the variables being advanced in this small-step integration are the temporal perturbation fields, defined by the deviation from their more recent RK3 predictors: $\Phi'' = \Phi - \Phi^{t*}$, where $\Phi^{t*} = \Phi^t, \Phi^*$ and $\Phi^{**}$ for the first, second, and third RK3 step, respectively. Thus, the perturbation momentum equations to be solved are driven by the large-step forcings and the small-step [sometimes referred as "acoustic-step" although it deals with both acoustic and gravity wave modes (e.g., Klemp et al., 2007; Skamarock et al., 2008)] corrections:

$$\begin{aligned}\underbrace{\frac{\partial V''}{\partial t}}_{V''\text{ tendency}} = & \underbrace{\left[\underbrace{-\nabla\cdot(\boldsymbol{V}v)}_{\text{ADV}}\underbrace{-\mu_{\mathrm{d}}\alpha\frac{\partial p}{\partial y}-\frac{\alpha}{\alpha_{\mathrm{d}}}\frac{\partial p}{\partial \eta}}_{\text{PGF}}\underbrace{-fU}_{\text{COR}}\underbrace{-\left(\frac{vW}{r_{\mathrm{e}}}\right)}_{\text{CUV}}+P_V\right]^{t*}}_{\text{large-step forcings }(F)} \\ & \underbrace{-\frac{\alpha^{t*}}{{\alpha_{\mathrm{d}}}^{t*}}\left[{\mu_{\mathrm{d}}}^{t*}\left({\alpha_{\mathrm{d}}}^{t*}\frac{\partial p''^{\tau}}{\partial y}+{\alpha_{\mathrm{d}}}''^{\tau}\frac{\partial \bar{p}}{\partial y}+\frac{\partial \phi''^{\tau}}{\partial y}\right)+\frac{\partial \phi^{t*}}{\partial y}\left(\frac{\partial p''}{\partial \eta}-\mu''_{\mathrm{d}}\right)^{\tau}\right]}_{\text{small-step modes (ACOUS)}},\end{aligned} \tag{3.5}$$

$$\begin{aligned}\underbrace{\frac{\partial W''}{\partial t}}_{W''\text{ tendency}} = & \underbrace{\left[\underbrace{-\nabla\cdot(\boldsymbol{V}w)}_{\text{ADV}}+\underbrace{g\left(\frac{\alpha}{\alpha_{\mathrm{d}}}\frac{\partial p}{\partial \eta}-\mu_{\mathrm{d}}\right)}_{\text{PGFBUOY}}+\underbrace{-\left(\frac{uU+vV}{r_{\mathrm{e}}}\right)}_{\text{CUV}}+P_W\right]^{t*}}_{\text{large-step forcings }(F)} \\ & \underbrace{+g\overline{\left\{\left(\frac{\alpha^{t*}}{{\alpha_{\mathrm{d}}}^{t*}}\right)\left[\frac{\partial}{\partial \eta}\left(C\frac{\phi''}{\partial \eta}\right)+\frac{\partial}{\partial \eta}\left(\frac{{c_{\mathrm{s}}}^2}{\alpha^{t*}}\frac{\Theta''}{\Theta^{t*}}\right)-{\mu_{\mathrm{d}}}''\right]\right\}}^{\tau}}_{\text{small-step modes (ACOUS)}},\end{aligned} \tag{3.6}$$

where $\tau$ indicates the time in the small-step integration, and $C$ as well as ${c_s}^2$ are sound-wave-related terms (Chapter 3.1.2 in Skamarock et al., 2008). Here we leave out the details regarding the small-step terms that are irrelevant to the in-line budget retrieval. Note that the overbar in (3.6) indicates a forward-in-time averaging operator for the small-step modes to damp instabilities associated with vertically propagating sound waves (see Eq. (3.19) in Skamarock et al., 2008).

Equations (3.5) and (3.6) are the ones used to integrate the prognostic momentum fields in the WRF model. For each RK3 step, after the total large-step forcing $F$ is determined, $V''$ and $W''$ are defined and advanced within the small-step scheme by a loop that adds $F$ multiplied by a time interval, $\Delta\tau$ (varies with different RK3 steps; Fig. 3.1), and the small-step forcing (ACOUS). After the small-step integration loop ends, $V$ and $W$ are then recovered from their temporal perturbation fields and moved forward to the next RK3 step.

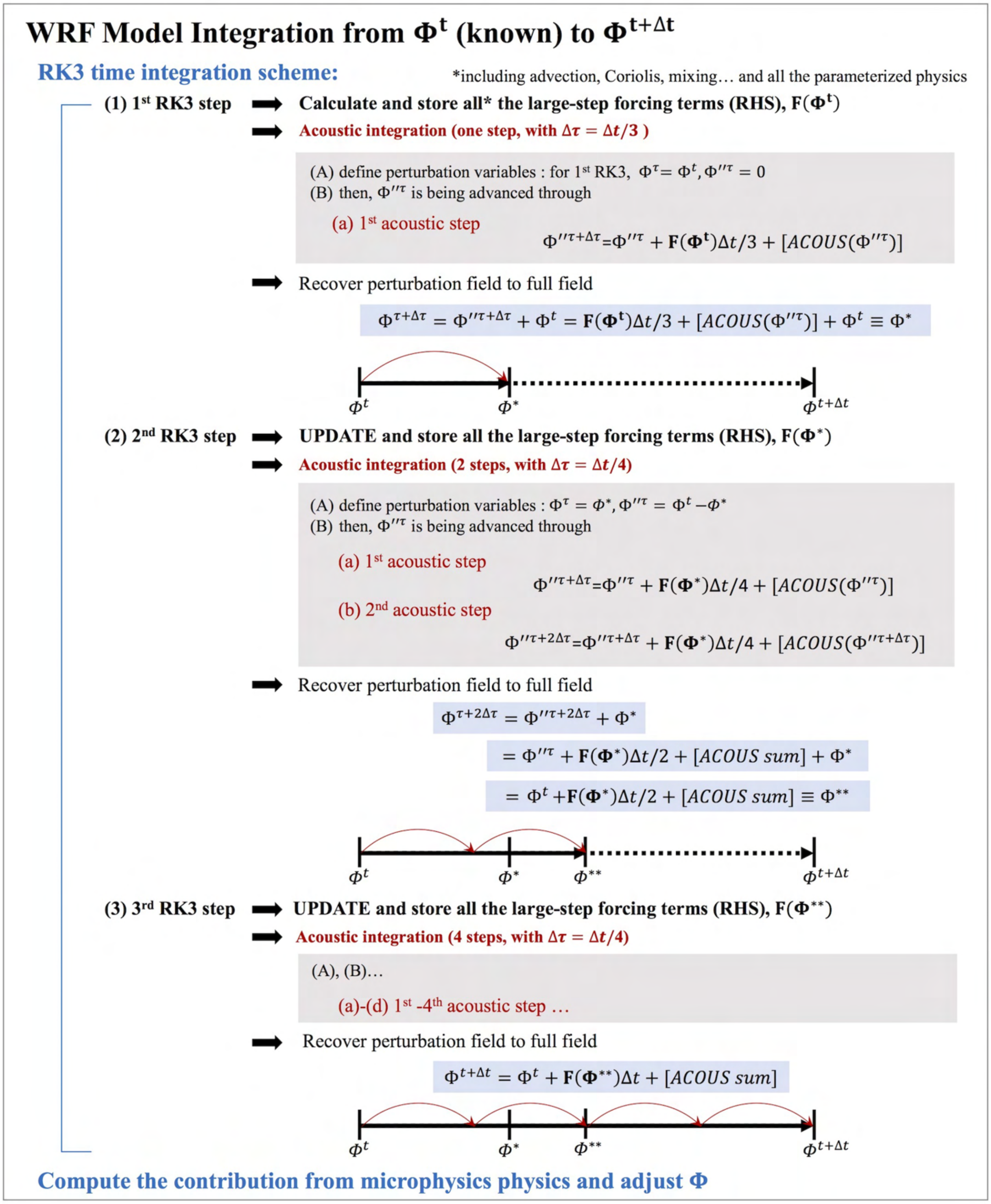


**Fig. 3.1**: The time integration strategy for advancing a state variable (generalized as $\Phi$) in the WRF model based on Skamarock et al. (2008). In this given example, four acoustic steps are specified for one integration time.

While it is not relevant to the momentum equations discussed here, for some variables directly contributed by the microphysics scheme, the associated contribution should be considered after the RK3 integration loop ends as the microphysics are integrated externally using an additive time splitting (Chapter 3.1.4 in Skamarock et al., 2008).

### 3.2.2 Experimental setup

The main discussion of this study will focus on a 2D ($y$, $z$) idealized simulation of slantwise convection. This process releases conditional symmetric instability (CSI), which can be idealized by assuming no flow variations along the direction of thermal winds (denoted as the $x$ direction in our setup). The initial field consists of a thermally balanced uniform westerly wind shear in $x$. This baroclinic environment contains no conditional (gravitational) instability, no inertial stability, and no dry symmetric instability but does contain some CSI. A two-dimensional bubble containing perturbations of potential temperature and zonal wind is added to initiate convection[†] and a slanted secondary circulation ($v$, $w$). See Appendix B for more details about the experimental setup. The domain size is 1600 and 16 km in the $y$ and $z$ direction, respectively, with a horizontal grid length of 10 km and 128 vertical layers. The model integration time step is 1 min. For simplicity, the only parameterization used is the Thompson microphysics scheme (Thompson et al., 2008). In addition, the upper-level implicit Rayleigh vertical velocity damping (damp_opt=3) is also activated (Chapter 4.4.2 in Skamarock et al., 2008). The former does not directly contribute to the momentum fields (although it can affect the momentum field indirectly through density and pressure variations), and the latter, contained in $P_W$ in (3.2) and (3.6), affects only the $W$ momentum budget. No subgrid turbulence scheme is used (diff_opt=0). The WRF model offers different orders of advection operators, and the default third- and fifth-order operators are selected for the vertical and horizontal in this case, respectively.

[†]slantwise convection.

Most of the subsequent analyses and discussion are based on this slantwise convection case with a 10 km grid length unless specified otherwise. Two other simulations, one of which uses the same setup but with an increased horizontal resolution of 2 km, will be discussed in Section 3.4.

Figure 3.2 shows the 48 h evolution of the 99th percentiles of $v$ and $w$ (hereafter the lowercase indicates that the calculation uses the uncoupled momentum field) and their tendencies. For the 10 km case, the horizontal velocity reaches its peak in about 20 h, a few hours after the vertical velocity reaches its maximum, and then undergoes a weakening. Both $v$ and $w$ tendencies are maximized at around 15 h. To understand the evolution of the associated flow dynamics, a momentum budget analysis serves as a natural choice. However, as a preliminary step prior to carrying out such analysis, we focus only on the technical discussion of the budget analysis methodology. The physical interpretation of the motion is beyond the current scope and will be presented in a subsequent paper.

## 3.3 Methodology and results

### 3.3.1 In-line momentum budget analysis

For the in-line budget analysis, all the terms are retrieved directly from the model for all the integration time steps, and therefore they represent the "instantaneous" terms that act over the specified short integration time window. For the large-step forcing, the WRF model accumulates all forcing terms at the beginning of each RK3 step. To separate them, we simply take the difference before and after WRF calls the subroutine for each large-step forcing, store their values separately, and output only the values at the third RK3 step (the total forcing is $F(\Phi^{**}\Delta t)$ as shown in Fig. 3.1). As for the contribution of the small-step modes, they are obtained by accumulating over all the small steps in the third RK3 step

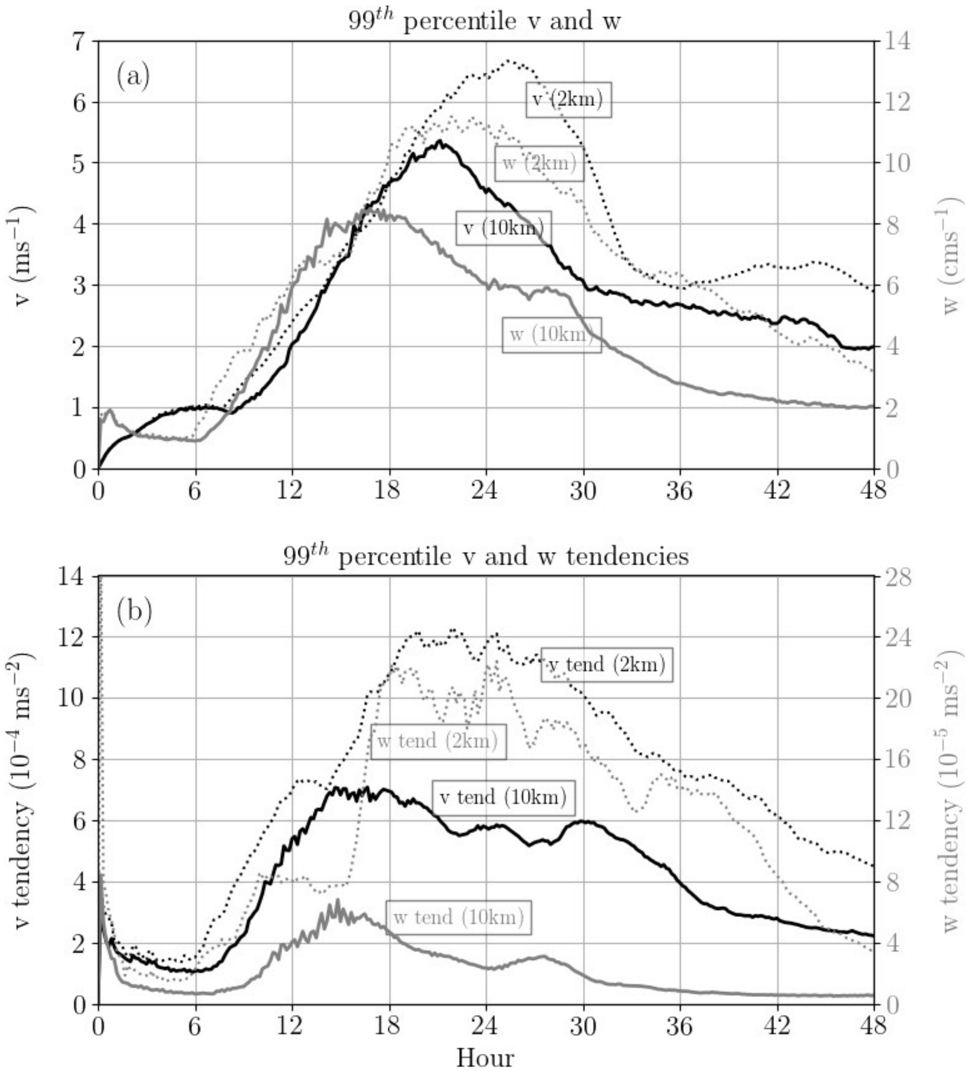


**Fig. 3.2**: Evolutions of the 99th percentiles of (a) horizontal velocity, $v$ (black; axis on the left), and vertical velocity, $w$ (gray; axis on the right) in the simulation of slantwise convection. Panel (b) is the same as (a) but for their tendencies (black and gray lines for $v$ and $w$ tendencies, respectively). Solid lines are for the 10 km simulation, while the dotted ones are for the 2 km case.

(ACOUS sum shown in Fig. 3.1). It is worth noting that (3.6) is a vertically implicit equation that couples with the geopotential tendency equation (Skamarock et al., 2008; Klemp et al., 2007). A tri-diagonal equation for the vector $W$ (involving three grid points in the vertical direction) is thus solved (Satoh, 2002). This means that $W$ (the scalar at a given grid point) is not advanced by linear additions in the small-step or acoustic scheme. To ensure the closure of the in-line retrieval budget, we simply take the total changes that are contributed by the implicit solver in the acoustic scheme as small-step modes of $W$ in the third RK3 step. Note that this way does not violate the original $W$ equation in (3.6). The contribution from these accumulated small-step modes in the $V$ and $W$ tendency budgets are combined with their large-step PGF and PGFBUOY, respectively, as they share the same mathematical expressions. Finally, we add the in-line calculation for the tendency term outside of the RK3 integration loop, after the microphysics scheme:

$$\frac{\partial \Phi^{t+\Delta t}}{\partial t} \equiv \frac{\Phi^{t+\Delta t} - \Phi^{t}}{\Delta t} \tag{3.7}$$

where $\Delta t$ is the model integration time step and $\Phi$ represents $V$ or $W$ (coupled momentum; hereafter the momentum tendency with capital $V$ or $W$ refers to the lhs term derived for the budget analysis). The values of $\Phi$ at times $t$ and $t+\Delta t$, the latter denoted by superscripts, are termed the current and predicted states, respectively. Note that while variables of momentum tendencies (specifically named "ru_tend, rv_tend and rw_tend") can be directly outputted from the WRF model by modifying the registry file, these variables do not necessarily represent the actual momentum changes that consider all the physical (e.g., microphysics, small-step modes) and non-physical processes (e.g., damping) but only the summation of all the large-step forcings.

Figures 3.3 and 3.4 present the results of the in-line budget analysis for horizontal momentum and vertical momentum, respectively, at three selected times (6, 12, and 16 h). To demonstrate the momentum changes in a common physical unit (velocities; meter per second), every term of the flux-form budget equation shown in this paper is divided by the dry-air mass, ${\mu_\mathrm{d}}^{t+\Delta t}$ (so that, for example, the $V$ tendency has a unit of meter per second squared). The magnitude of the $V$ tendency intensifies during this period with local maxima on the order of $10^{-4}$ to $10^{-3}$ m s$^{-2}$ (Fig. 3.3). Two forcing terms, PGF and COR, are a few times larger than the ADV term but generally offset each other, making the ADV term of comparable importance in determining the tendency. The CUV term for $V$ tendency is generally small and thus not shown in Fig. 3.3. The residual, obtained from (3.1) with $P_V$ equal to 0, is always smaller than $10^{-7}$ m s$^{-2}$ during the entire 48 h simulation (not shown). To understand how the peak error evolves with time and to avoid reaching misleading conclusions based on one or more outlying values, the evolution of the 99th percentile magnitude of the residual term is shown. Figure 3.5 shows that it reaches a value of about $7 \times 10^{-9}$ m s$^{-2}$ around 15 h. Recall that the 99th percentile

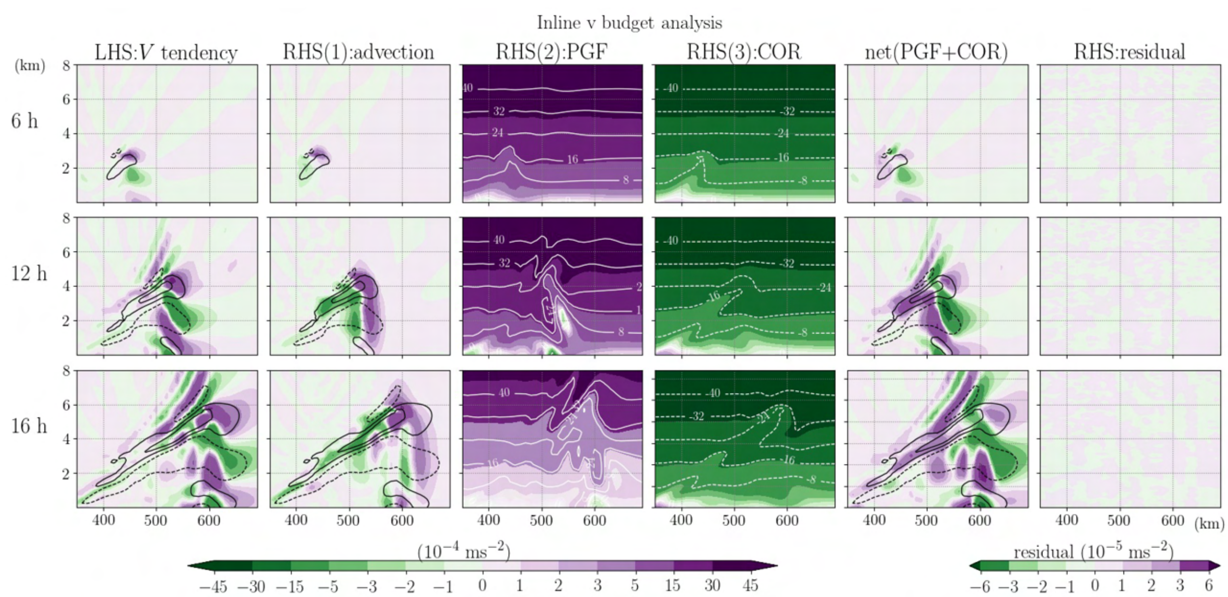


**Fig. 3.3**: In-line budget analysis of horizontal momentum, $V$, with each term extracted directly from the model. In each row, the shading in each subplot from the left to right shows the term of $V$ tendency, flux-form advection (ADV), horizontal pressure gradient force (PGF), Coriolis force (COR) (white contours indicate the values exceeding the color bar), PGF+COR, and residual [(3.1); $P_V$ is 0 and the generally small curvature term (CUV) is not shown]. All terms are divided by $\mu_{\mathrm{d}}$ and thus have units of meters per second squared. The black contours indicate the horizontal velocity $v$ of 2 and 6 m s$^{-1}$ (positive and negative values shown in solid and dashed lines, respectively). Each row from top to bottom illustrates the budget analysis at 6, 12, and 16 h, respectively.

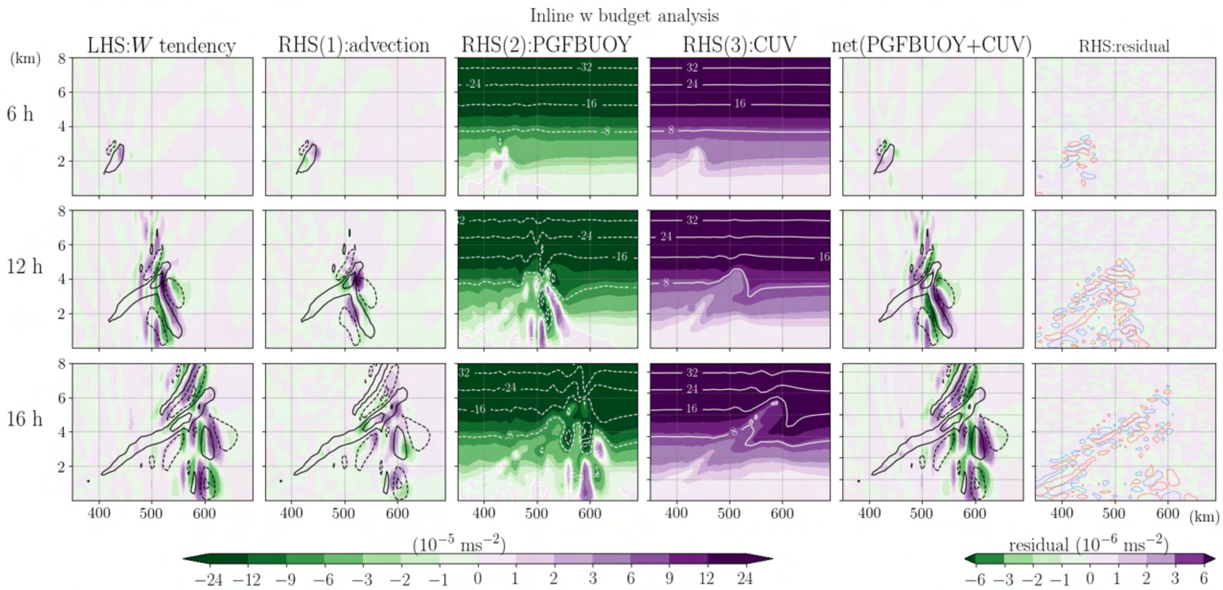


**Fig. 3.4**: In-line budget analysis of vertical momentum, $W$, with each term extracted directly from the model. In each row, the shading in each subplot from the left to right shows the term of $W$ tendency, advection (ADV), net vertical pressure gradient and buoyancy force (PGFBUOY), curvature (CUV) (white contours indicate the values exceeding the color bar), PGFBUOY+CUV, and residual [(3.2); $P_W$ is considered but not shown here]. All terms are divided by $\mu_\mathrm{d}$ and thus have units of meters per second squared. The black contours indicate the vertical velocity $w$ of 5 and 15 cm s$^{-1}$ (positive and negative values shown in solid and dashed lines, respectively). The red (blue) contours shown in the rightmost column, laid on top of the residual (shading), indicate the small-step components of PGFBUOY with a positive (negative) value of $3 \times 10^{-4}$ m s$^{-2}$. Each row from top to bottom illustrates the budget analysis at 6, 12, and 16 h, respectively.

magnitude of the simulated $v$ tendency has a peak of $7 \times 10^{-4}$ m s$^{-2}$ (Fig. 3.2b). Thus, the relative magnitude of the 99th percentile residual is about 0.001% of the 99th percentile tendency term during the peak intensifying stage. Compared to the $V$ tendency, the $W$ tendency exhibits narrower features in the horizontal direction (Fig. 3.4) with an overall smaller magnitude in every term. The two largest forcings, PGFBUOY and CUV, usually have opposite signs, so their combined effect is on the same order as the ADV and the $W$ tendency term. While the contribution from the upper-layer vertical velocity damping is not shown in Fig. 3.4, it is included as part of the rhs ($P_W$) of (3.2) when calculating the

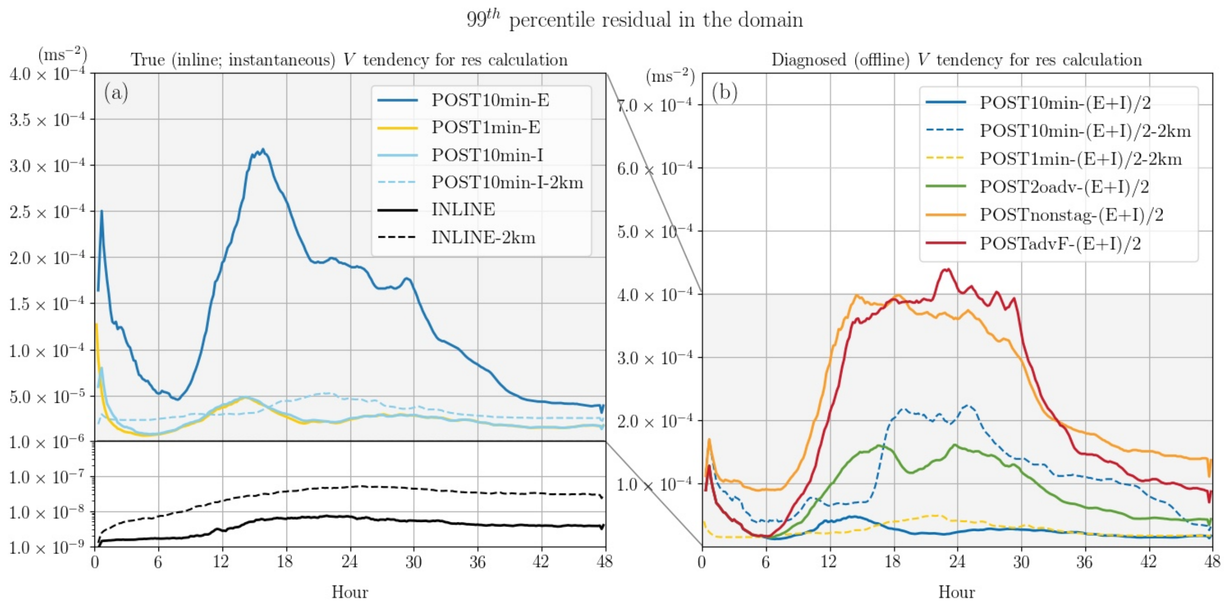


**Fig. 3.5**: Evolution of the 99th percentile of the residual magnitude (meters per second squared) of the horizontal momentum $V$ budget analysis. For the residual calculation, (a) uses the true $V$ tendency (derived during the integration of the model) and (b) uses the post-diagnosed $V$ tendency (3.8) as the lhs term. Different colors indicate different post-processed methods for estimating the rhs forcing terms. The residuals obtained from the in-line budget retrieval are in black. Solid and dashed lines are for the 10 km run and 2 km run, respectively.

residual for the in-line budget analysis. The residual in the in-line $W$ budget is generally 4 orders of magnitude smaller than its tendency term. The 99th percentile residual for $W$ budget is about $2 \times 10^{-10}$ m s$^{-2}$, around 0.0003% of the 99th percentile $w$ tendency during the peak intensifying stage of the convection (not shown).

## 3.3.2 Post-processed momentum budget analyses

### (1) Key features and methodologies

In contrast to extracting terms directly from the model during its integration, most of the studies in which the momentum budget analysis is conducted use the model output files after the completion of the integration. Note that since the sub-output time-step information is not available between successive outputs, only the large-step forcing terms can be estimated in these post-processed budget analyses. Generally, the neglect of the acoustic or small-step modes is expected to have little impact on the results as the high-frequency modes are often considered meteorologically insignificant. However, it is mentioned in Klemp et al. (2007) and Skamarock et al. (2008) that the WRF small-step integration scheme includes not only the acoustic-wave but also some gravity-wave modes, which may not be insignificant. These gravity-wave modes form during the small-step integration due to the designated terms that are required for acoustic wave propagation and "Consequently, in this vertical coordinate (i.e., terrain-following hydrostatic pressure coordinate), the terms governing the acoustic and gravity wave modes are intermingled to the extent that it does not appear feasible to evaluate any of the gravity wave terms on the large time steps, even if one desired to do so" (Klemp et al., 2007).

Most of the studies did not reveal the complete details about how their analysis was done, so we cannot presume their methodologies and the possible errors. However, a few simplifications commonly made in the post-processed budget analyses may introduce errors that result in deviations from the simulated results and thus a significant residual. Below we revisit the relevant features of the WRF model that should be considered and discuss how they might affect the post-processed budget if they are ignored. Then, the results are shown for different post-processed budget analyses with different simplifications (Table 3.1). The aim herein is to identify these potential errors hidden in the budget calculation and show how severely they affect the resulting interpretation.

**(a) Diagnosed tendency** In a post-processed budget analysis, the tendency term of a given variable is approximated by the difference between the value of this variable at two successive output times divided by the output time interval. Thus, the accuracy may be sensitive to the output time interval. The value at the predicted state has a form of

$$\left.\frac{\partial \Phi^{t+\Delta t}}{\partial t}\right|_{\text{diagnosed}} \approx \frac{\Phi^{t+\Delta t} - \Phi^{t+\Delta t-\Delta t_{\text{output}}}}{\Delta t_{\text{output}}}. \tag{3.8}$$

If the output interval is longer than the model integration time step, the diagnosed tendency would deviate from the model prediction of the instantaneous tendency. To increase the accuracy, the output time interval $\Delta t_{\text{output}}$ needs to be similar to the integration time step $\Delta t$.

**Table 3.1**: A summary of all different approaches for the post-processed horizontal momentum budget analysis that are applied to the model output after the integration finishes.

| | Form of the equation | Output time interval | Order of (vertical; horizontal) advection operators | Forcing terms diagnosed using the explicit or implicit method | Calculated on C staggering grids |
|---|---|---|---|---|---|
| Slantwise convection simulation with a grid length of 10 km and integration time step of 1 min | | | | | |
| POST10min-E | Flux | 10 min | 3; 5 | Explicit | Yes |
| POST1min-E | Flux | 1 min | 3; 5 | Explicit | Yes |
| POST10min-I | Flux | 10 min | 3; 5 | Implicit | Yes |
| POST10min-(E+I)/2 | Flux | 10 min | 3; 5 | Average of explicit and implicit | Yes |
| POST2oadv-(E+I)/2 | Flux | 10 min | 2; 2 | Average of explicit and implicit | Yes |
| POSTnonstag-(E+I)/2 | Flux | 10 min | 3; 5 | Average of explicit and implicit | No |
| POSTadvF-(E+I)/2 | Advective | 10 min | 3; 5 | Average of explicit and implicit | Yes |
| Slantwise convection simulation with a grid length of 2 km and integration time step of 10 s | | | | | |
| POST10min-I-2km | Flux | 10 min | 3; 5 | Implicit | Yes |
| POST10min-(E+I)/2-2km | Flux | 10 min | 3; 5 | Average of explicit and implicit | Yes |
| POST1min-(E+I)/2-2km | Flux | 1 min | 3; 5 | Average of explicit and implicit | Yes |
| Squall line simulation with a grid length of 25 0m and integration time step of 3 s | | | | | |
| POST3sec-E | Flux | 3 s | 3; 5 | Explicit | Yes |

**(b) Spatial discretization on the C staggered grid** For computational efficiency and accuracy, WRF utilizes a C-grid staggering system (Arakawa and Lamb, 1977). This staggering system is pertinent to the numerical solution for spatial derivatives. For most of the spatial derivatives other than advection (e.g., the pressure gradient force), the second order finite difference operator is used in the WRF model. For example, the y derivative of variable $\Phi$ is calculated using the discrete operator:

$$\frac{\partial \Phi}{\partial y_{i,j,k}} = \frac{1}{\Delta y}\left(\Phi_{i,j+\frac{1}{2},k} - \Phi_{i,j-\frac{1}{2},k}\right). \tag{3.9}$$

The index $(i, j, k)$ corresponds to a location with $(x, y, \eta) = (i\Delta x, j\Delta y, k\Delta\eta)$, where $\Delta x$, $\Delta y$ and $\Delta\eta$ are the grid lengths in the two horizontal and vertical directions (can be vertically stretched), respectively. The same expression applies for the $x$ or the $\eta$ derivatives. Grid staggering implies that different variables may be located on different grids, i.e., shifted by a half-grid point from the others as illustrated in Fig. 3.6. Depending on what variable the spatial derivatives are intended for, (3.9) should be carried out on the corresponding grid, which is not necessarily the same as the $\Phi$ grid. For example, for the $V$ tendency,

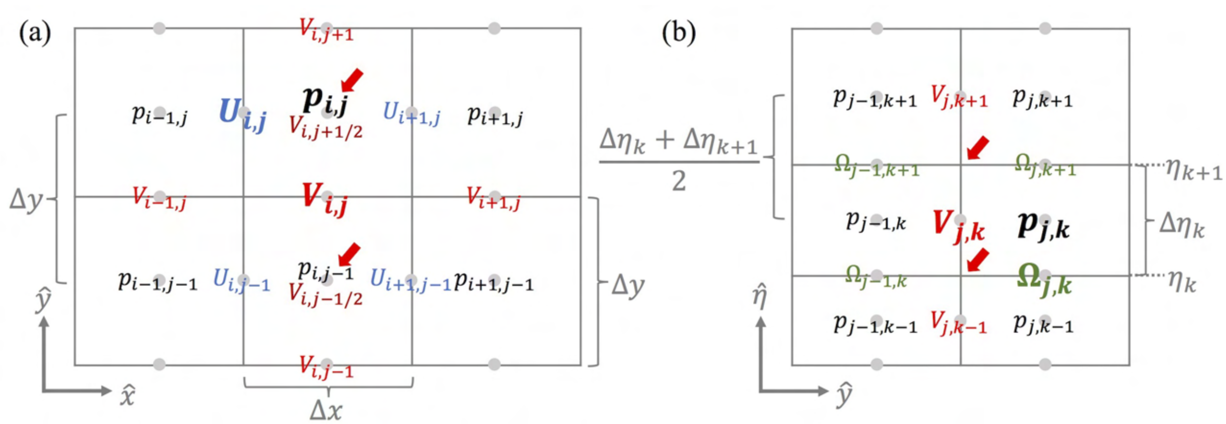


**Fig. 3.6**: (a) Horizontal and (b) vertical C staggering grids for different variables in the WRF model. Note that variables $\phi$ and $W$ are allocated on the same grid as $\Omega$; $u$, $\alpha$, and $q_*$ are on grid same as $p$. The red arrows indicate the grids that would be used to calculate the second-order spatial derivative term for the $V$ momentum at the $V$ grid $(i, j, k)$.

all the associated forcing terms involving the spatial derivatives should be performed on the $V$ grid. More specifically, to calculate the PGF term for the $V$ tendency equation, the term $\frac{\partial p}{\partial y}$ and the term $\frac{\partial p}{\partial \eta}$ in (3.1) should be calculated on the $V$ grid but not the pressure grid ($p$ grid). Applying (3.9) for $\frac{\partial p}{\partial y}$, the $V$ grid with location indices of $(i, j - \frac{1}{2}, k)$ and $(i, j + \frac{1}{2}, k)$ falls exactly on the $p$ grid and hence no interpolation is required (red arrows in Fig. 3.6a). However, for $\frac{\partial p}{\partial \eta}$, the pressures on the $V$ grid with indices of $(i, j, k - \frac{1}{2})$ and $(i, j, k + \frac{1}{2})$ must be obtained (red arrows in Fig. 3.6b) through linear interpolation using their surrounding closest four pressure values, e.g.,

$$\begin{aligned} P_{V-grid(i,j,k+\frac{1}{2})} = & \frac{\frac{1}{2}\left(P_{p-grid(i,j-1,k)} + P_{p-grid(i,j,k)}\right)\frac{\Delta\eta_{k+1}}{2}}{\frac{1}{2}(\Delta\eta_k + \Delta\eta_{k+1})} \\ & + \frac{\frac{1}{2}\left(P_{p-grid(i,j-1,k+1)} + P_{p-grid(i,j,k+1)}\right)\frac{\Delta\eta_k}{2}}{\frac{1}{2}(\Delta\eta_k + \Delta\eta_{k+1})}, \end{aligned} \tag{3.10}$$

which is weighted by the irregular (stretched) vertical grid-lengths (Fig. 3.6b).

If the C-grid staggering is not considered during the post-processing analysis, i.e., all the variables have been interpolated on the universal grids before carrying out the budget calculation, in addition to the potential errors brought on by the interpolation method, the term $\frac{\partial p}{\partial y}$, for example, would essentially involve pressure differences over a larger grid interval of $2 \times \Delta y$ instead of $\Delta y$, with larger associated truncation errors.

**(c) Advection operators** For advection, higher-order operators for finite differencing are provided as the default WRF setup. Taking the $y$ component of the flux-form advection for $V$ momentum in (3.3) as an example, with a fifth-order operator as selected in the present simulation, it is written as

$$-\left.\frac{\partial(Vv)}{\partial y}\right|_{i,j,k} \approx -\frac{1}{\Delta y}\left(V_{i,j+\frac{1}{2},k}v^{5th}_{i,j+\frac{1}{2},k} - V_{i,j-\frac{1}{2},k}v^{5th}_{i,j-\frac{1}{2},k}\right), \tag{3.11}$$

where $V$ and $v$ are the mass-coupled and mass-uncoupled velocities, respectively:

$$v^{5th}_{i,j-\frac{1}{2},k} = v^{6th}_{i,j-\frac{1}{2},k} - \mathrm{sign}(V_{i,j-\frac{1}{2},k})\frac{1}{60}[(v_{i,j+1,k} - v_{i,j-3,k}) - 5(v_{i,j+1,k} - v_{i,j-2,k}) + 10(v_{i,j,k} - v_{i,j-1,k})]$$

and

$$v^{6th}_{i,j-\frac{1}{2},k} = \frac{1}{60}[37(v_{i,j,k} - v_{i,j-1,k}) - 8(v_{i,j+1,k} + v_{i,j-2,k}) + 1(v_{i,j+2,k} + v_{i,j-3,k})].$$

The odd-order advection operators include a spatially centered even-order operator and an upwind diffusion term. A detailed discussion on the advection scheme in the WRF model with different-order operators can be found in Wicker and Skamarock (2002) and Skamarock et al. (2008). Simplifying the advection estimation using an operator with an order that differs from the numerical setup would contribute to errors in the ADV estimation.

**(d) Forward or backward Euler method** Conceptually, the WRF model can be considered more of a forward scheme, i.e., using the known variables from the current state to calculate the forcing and then advancing the variables forward until reaching the prediction time. However, there are a few implicit components during the integration. For example, as discussed in Section 3.2.1, the large-step forcings are updated using a predictor–corrector method in the second and third RK3 steps. In addition, the $W$ equation is coupled with the geopotential tendency equation and includes a forward-in-time weighting that utilizes predicted states of the geopotential and temperature in solving the $W$ (Eq. (3.11), (3.12), and (3.19) in Skamarock et al., 2008).

In numerical analysis for solving ordinary differential equations, the (explicit) forward Euler method approximates the change of a system from $t$ to $t+\Delta t$ using the current states ($t$), while the (implicit) backward Euler method finds the solution using the predicted states

$(t + \Delta t)$:

$$\frac{\partial \Phi^{t+\Delta t}}{\partial t} \approx F(\Phi^{t}) \quad \text{forward Euler method,} \tag{3.12}$$

$$\frac{\partial \Phi^{t+\Delta t}}{\partial t} \approx F(\Phi^{t+\Delta t}) \quad \text{backward Euler method.} \tag{3.13}$$

Consistent with this concept, the rhs forcing terms of a budget equation can be estimated using two different instantaneous states in analogous ways. However, we emphasize that the post-processed budget analysis does not solve the tendency equation per se but only diagnoses the relationship between the two sides of the equation. Note that for post-processing analyses, the availability of the data depends on the output time interval ($\Delta t_{\text{output}}$), which is often much larger than the integration time step ($\Delta t$). Thus, for the tendency at a given time $t + \Delta t$, when applying the forward Euler method to estimate the associated rhs forcings, the "current states" one can use are the most recent prior output at $t + \Delta t - \Delta t_{\text{output}}$ (see Fig. 3.7):

$$\frac{\partial \Phi^{t+\Delta t}}{\partial t} \approx F(\Phi^{t+\Delta t-\Delta t_{\text{output}}}) \quad \text{forward Euler method for post-processing.} \tag{3.14}$$

If $\Delta t_{\text{output}}$ is the same as $\Delta t$, (3.14) reverts to (3.12). If $\Delta t_{\text{output}}$ is much larger than $\Delta t$, the backward Euler method using predicted states at $t+\Delta t$ may better estimate the true model forcing terms as they are calculated using variables at a closer time to the real integration window in the model (Fig. 3.7).

The above two diagnostic methods estimate the forcing terms using instantaneous states. However, as mentioned in Section 3.3.2(a), the diagnosed lhs tendency depends on two successive model output times. Thus, an average between forcings diagnosed explicitly and implicitly are often considered. For a post-processed analysis, this translates into estimating the forcings using both predicted states and the most recent prior available current states:

$$\left.\frac{\partial \Phi^{t+\Delta t}}{\partial t}\right|_{\text{diagnosed}} \approx \frac{1}{2}[F(\Phi^{t+\Delta t - t+\Delta t_{\text{output}}}) + F(\Phi^{t+\Delta t})]. \tag{3.15}$$

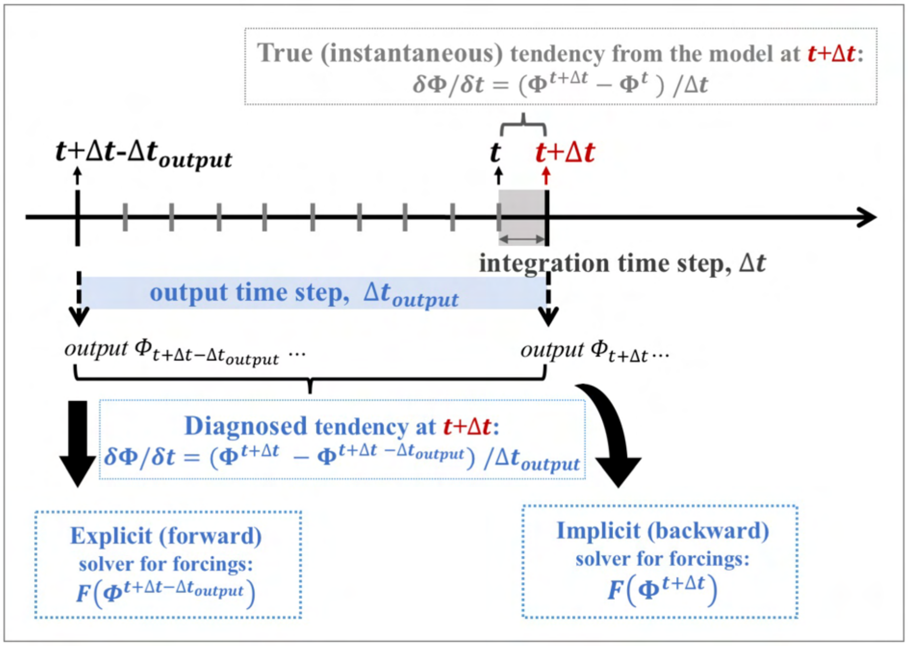


**Fig. 3.7**: Schematic plot showing the explicit (forward) and implicit (backward) solvers for the rhs forcing terms, as well as the diagnosed and the true (calculated in-line during the integration of the model) lhs tendency term defined in this study.

**(e) Flux or advective form of equation** While the momentum equations solved in the WRF model are in flux form, their corresponding advective forms can be derived and are often used for post-processed budget analyses for convenience. To derive the advective form, the flux-form $V$ momentum equation [(3.1) excluding residual] is first multiplied by a factor of $\frac{1}{\mu_\text{d}}$ and $V$ is rewritten as $\mu_\text{d} v$:

$$\underbrace{\frac{1}{\mu_\mathrm{d}}\frac{\partial(\mu_\mathrm{d} v)}{\partial t}}_{V\text{ tendency}} = \underbrace{-\frac{1}{\mu_\mathrm{d}}\nabla\cdot(\mu_\mathrm{d}\boldsymbol{v}v)}_{\substack{\text{advection}\\ \text{ADV}}} + \underbrace{\frac{1}{\mu_\mathrm{d}}\left[-\alpha\frac{\partial p}{\partial y} - \frac{\alpha}{\alpha_\mathrm{d}}\frac{\partial p}{\partial \eta}\frac{\partial \phi}{\partial y}\right]}_{\substack{\text{horizontal pressure gradient force}\\ \text{PGF}}} \underbrace{-\frac{1}{\mu_\mathrm{d}}fU}_{\substack{\text{Coriolis}\\ \text{COR}}} \underbrace{-\frac{1}{\mu_\mathrm{d}}(\frac{vW}{r_\mathrm{e}})}_{\substack{\text{curvature}\\ \text{CUV}}} \underbrace{+\frac{1}{\mu_\mathrm{d}}P_V}_{\substack{\text{remaining}\\ \text{(parameterized)}\\ \text{physics}}} \quad . \tag{3.16}$$

Then, by adding the mass continuity equation in WRF (multiplied by a factor of $\frac{v}{\mu_\mathrm{d}}$):

$$\frac{v}{\mu_\mathrm{d}}\left[\frac{\partial \mu_\mathrm{d}}{\partial t} + \nabla\cdot(\mu_\mathrm{d}\boldsymbol{v})\right] = 0$$

to the rhs of (3.16), we obtain

$$\begin{aligned}\underbrace{\frac{1}{\mu_\mathrm{d}}\frac{\partial(\mu_\mathrm{d} v)}{\partial t}}_{V\text{ tendency}} =& \frac{v}{\mu_\mathrm{d}}\frac{\partial \mu_\mathrm{d}}{\partial t} + \frac{v}{\mu_\mathrm{d}}\nabla\cdot(\mu_\mathrm{d}\boldsymbol{v}) \underbrace{-\frac{1}{\mu_\mathrm{d}}\nabla\cdot(\mu_\mathrm{d}\boldsymbol{v}v)}_{\substack{\text{advection}\\ \text{ADV}}} + \underbrace{\frac{1}{\mu_\mathrm{d}}\left[-\alpha\frac{\partial p}{\partial y} - \frac{\alpha}{\alpha_\mathrm{d}}\frac{\partial p}{\partial \eta}\frac{\partial \phi}{\partial y}\right]}_{\substack{\text{horizontal pressure gradient force}\\ \text{PGF}}} \\ & \underbrace{-\frac{1}{\mu_\mathrm{d}}fU}_{\substack{\text{Coriolis}\\ \text{COR}}} \underbrace{-\frac{1}{\mu_\mathrm{d}}\left(\frac{vW}{r_\mathrm{e}}\right)}_{\substack{\text{curvature}\\ \text{CUV}}} \underbrace{+\frac{1}{\mu_\mathrm{d}}P_V}_{\substack{\text{remaining}\\ \text{(parameterized)}\\ \text{physics}}} \quad .\end{aligned} \tag{3.17}$$

Moving the first term on the rhs of (3.17) to the lhs, the second rhs term can be combined with the flux-form advection using the vector identity $\nabla\cdot(\mu_\mathrm{d}\boldsymbol{v}) = \mu_\mathrm{d}(\nabla\cdot\boldsymbol{v}) + \boldsymbol{v}\cdot(\nabla\mu_\mathrm{d})$. Then, the advective form of the horizontal momentum equation is obtained as

$$\underbrace{\frac{\partial v}{\partial t}}_{\substack{v\text{tendency}\\ \text{in advective form}}} = \underbrace{-\boldsymbol{v}\cdot\nabla v}_{\substack{\text{advection ADV}\\ \text{in advective form}}} \underbrace{+\frac{1}{\mu_\mathrm{d}}\left[-\alpha\frac{\partial p}{\partial y} - \frac{\alpha}{\alpha_\mathrm{d}}\frac{\partial p}{\partial \eta}\frac{\partial \phi}{\partial y}\right]}_{\substack{\text{horizontal pressure gradient force}\\ \text{PGF}}} \underbrace{-\frac{1}{\mu_\mathrm{d}}fU}_{\substack{\text{Coriolis}\\ \text{COR}}} \underbrace{-\frac{1}{\mu_\mathrm{d}}\left(\frac{vW}{r_\mathrm{e}}\right)}_{\substack{\text{curvature}\\ \text{CUV}}} \underbrace{+\frac{1}{\mu_\mathrm{d}}P_V}_{\substack{\text{remaining}\\ \text{(parameterized)}\\ \text{physics}}} \quad . \tag{3.18}$$

### (2) Results of horizontal momentum budget

Table 3.1 summarizes all the post-processed budget analyses tested in this study. In the present section, we first present the results one by one, and then a qualitative intercomparison among them and the in-line retrieval method is discussed. The first post-processed method (POST10min-E) for $V$ budget follows all the approaches in the model as closely as possible using the 10 min output data. The flux-form equation, C staggering grids, and the same orders of advection operators as the experimental setup are used. The diagnosis of the large-step forcing is applied directly to the model outputs on $\eta$ levels using the explicit or forward Euler method as shown in (3.14). The diagnosed forcing terms are compared

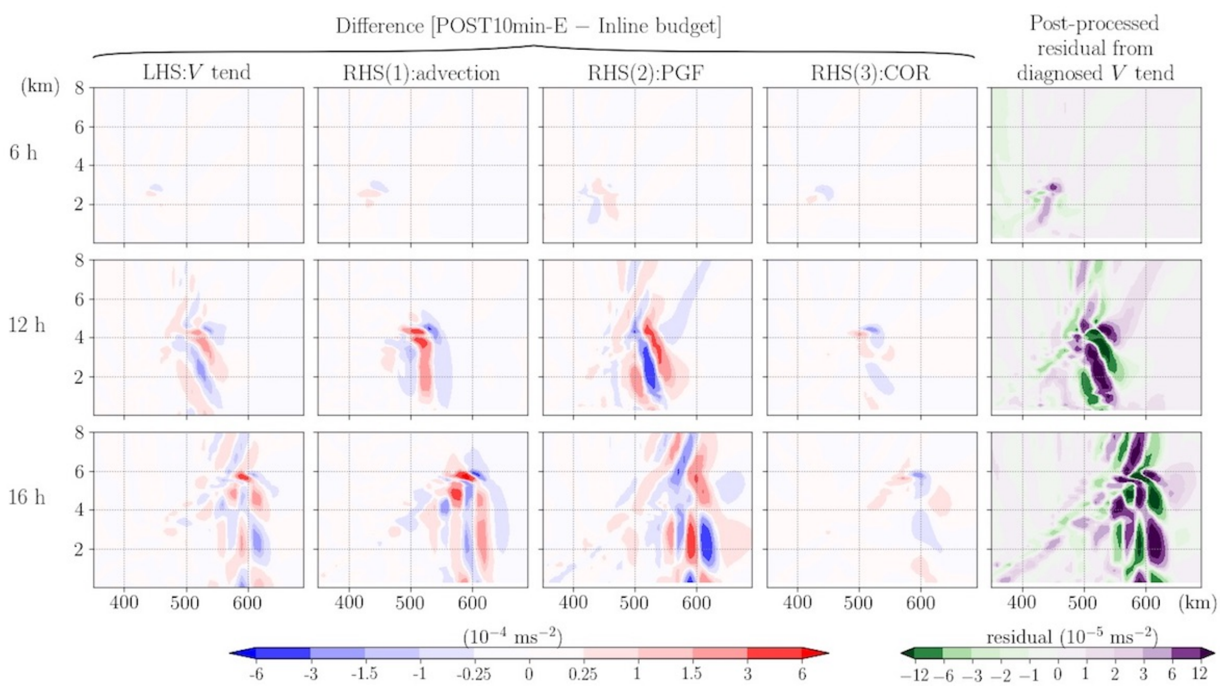


**Fig. 3.8**: The difference between the post-processed (POST10min-E; with an explicit or forward method on 10 min output) and in-line budget analysis for the horizontal momentum, $V$. All terms have been divided by $\mu_d$ and thus have a uniform unit of meters per second squared. In each row, from left to right indicates the difference for $V$ tendency, ADV, PGF, and COR. The rightmost column indicates the residual term obtained in the post-processed budget analysis. Each row from top to bottom shows the results at 6, 12, and 16 h, respectively.

with their corresponding true values from the in-line retrieval (Fig. 3.8). Errors smaller than, but on the same order of $10^{-4}$ m s$^{-2}$ as the $V$ tendency, are observed in all terms including the diagnosed tendency term. These errors grow in magnitude and areal coverage with the growth of the disturbance. Aside from COR, the absolute errors in the tendency, ADV and PGF can exceed $6 \times 10^{-4}$ m s$^{-2}$, the former two of which are more than 50% of the magnitude of their true (instantaneous) values locally.

The second post-processed analysis (POST1min-E) is done following the same approach but applied to the 1 min (same as the integration time step for this simulation) output data, and the results show strongly reduced errors in all terms (Fig. 3.9). The errors that remain are mostly in the PGF term and likely stem from the fact that the small-step modes and the RK3 integration scheme are not considered in the post-processed budget. These inherent errors result in a small residual term with a general order of $10^{-5}$ m s$^{-2}$, 1 to 2 order(s)

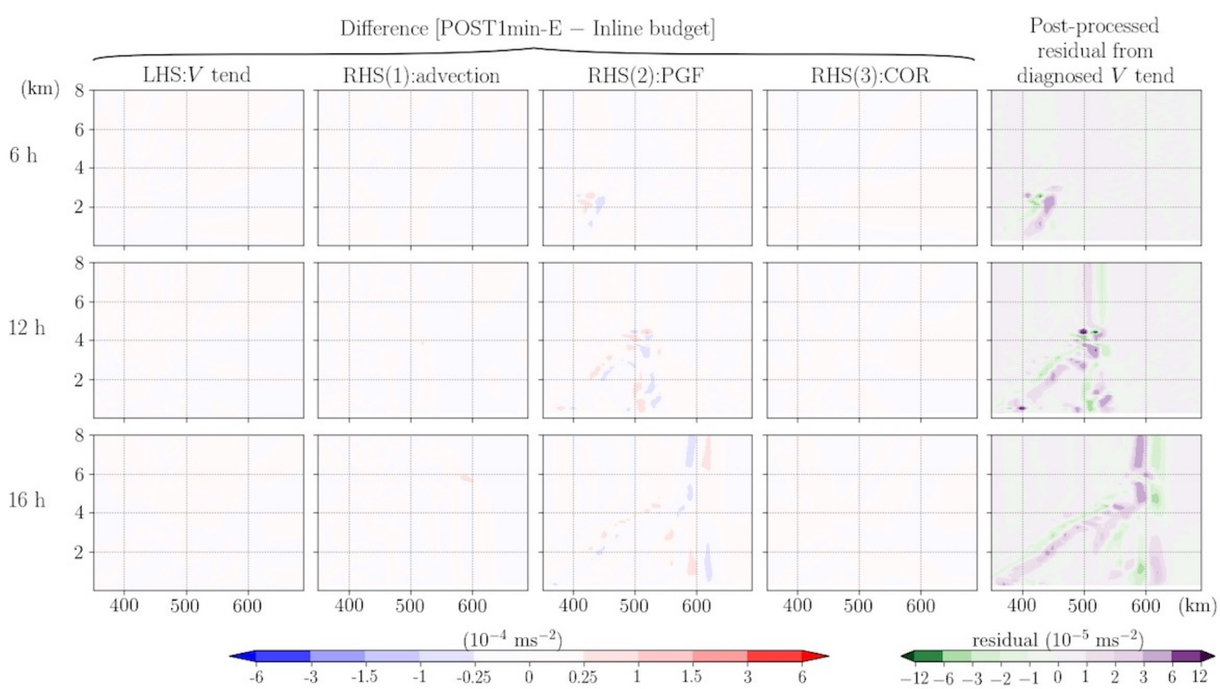


**Fig. 3.9**: Same as Fig. 3.8, but the post-processed budget analysis is applied to the data with an output time interval of 1 min (POST1min-E).

smaller than the maximum $V$ tendency. In terms of local maxima, the 99th percentile magnitude of the residual obtained in POST1min-E gives a relative magnitude of about 7% of the 99th percentile $v$ tendency during the peak intensifying stage of the convection at around 15 h (Figs. 3.2b and 3.5). Although reducing the model output interval to be close to the integration time step helps to balance the budget without the need for in-line diagnoses, it is computationally expensive especially for large, data-intensive simulations.

Given that computational cost is often a major consideration, we also test whether the implicit or backward Euler method (POST10min-I) can improve the estimation of instantaneous forcing terms relative to the explicit method for the same 10 min output data (POST10min-E). POST10min-I follows the same strategy as POST10min-E except that all the rhs terms, following (3.13), are diagnosed with the predicted states instead of the previous output states. As depicted in Fig. 3.10, POST10min-I does indeed better

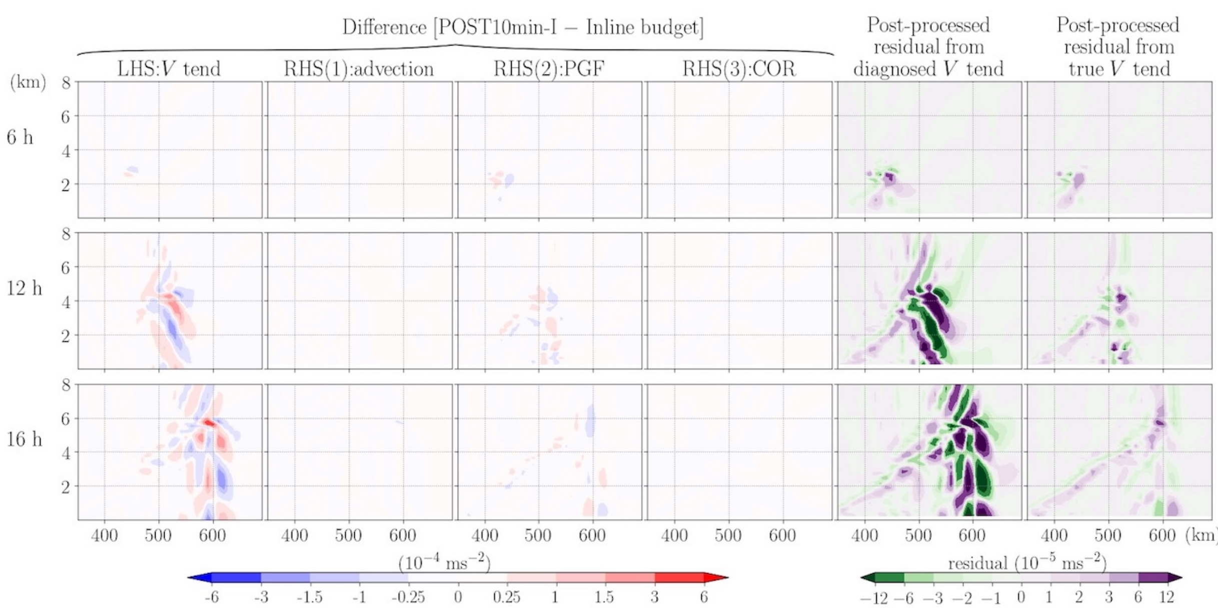


**Fig. 3.10**: Same as Fig. 3.8, but the post-processed rhs terms are diagnosed using the implicit or backward method (POST10min-I) and an extra column is added on the rightmost showing the residual from the true tendency (i.e., the instantaneous value obtained from the model).

capture the true model estimated forcing values as errors in all the rhs forcing terms diminish greatly to an accuracy similar to POST1min-E. However, as these forcings are calculated at a given instant, the imbalance of the budget would remain if the diagnosed tendency term is not calculated instantaneously (the second column from the right in Fig. 3.10). Therefore, if budget analysis at an instant of time is desired, we recommend adding the tendency calculation within the model as a standard output and diagnosing the forcing terms implicitly, which yields a residual term on a similar order to the one obtained in POST1min-E (the rightmost column in Fig. 3.10 and Fig. 3.5a).

For the more common situation, the post-processed analyses diagnose rhs terms using two successive outputs over an output time interval, i.e., taking the averages of the explicitly and implicitly calculated forcings using (3.15) on the 10 min output (POST10min-(E+I)/2). Comparing the averaged rhs forcings with the analogously diagnosed lhs momentum tendency (3.8) gives a small residual to a similar accuracy level as POST1min-E and POST10min-I (the rightmost column in Fig. 3.11 and Fig. 3.5b).

We now investigate the impact of other common simplifications on top of the reference experiment, POST10min-(E+I)/2. The first such simplification is to approximate the flux-form advection term using the second-order operator (3.9) for both vertical and horizontal components (POST2oadv-(E+I)/2) instead of the third- and fifth-order operators as used in the model setup. In our simulation, such inconsistency of advection operators introduced errors in the ADV term with a maximum value $> 3 \times 10^{-4}$ m s$^{-2}$, more than 50% of its true magnitude along the slantwise convective band (Fig. 3.12). Next, we repeated POST10min-(E+I)/2 but the calculation is applied after all the model output variables have been interpolated to the universal or un-staggered grid (pressure grid) (POSTnonstag-(E+I)/2). This is a common way to post-process model output data for plotting purposes. As mentioned earlier, this approach would reduce the accuracy when solving the spatial differential terms, and indeed, the results do indicate significant errors over a large area in

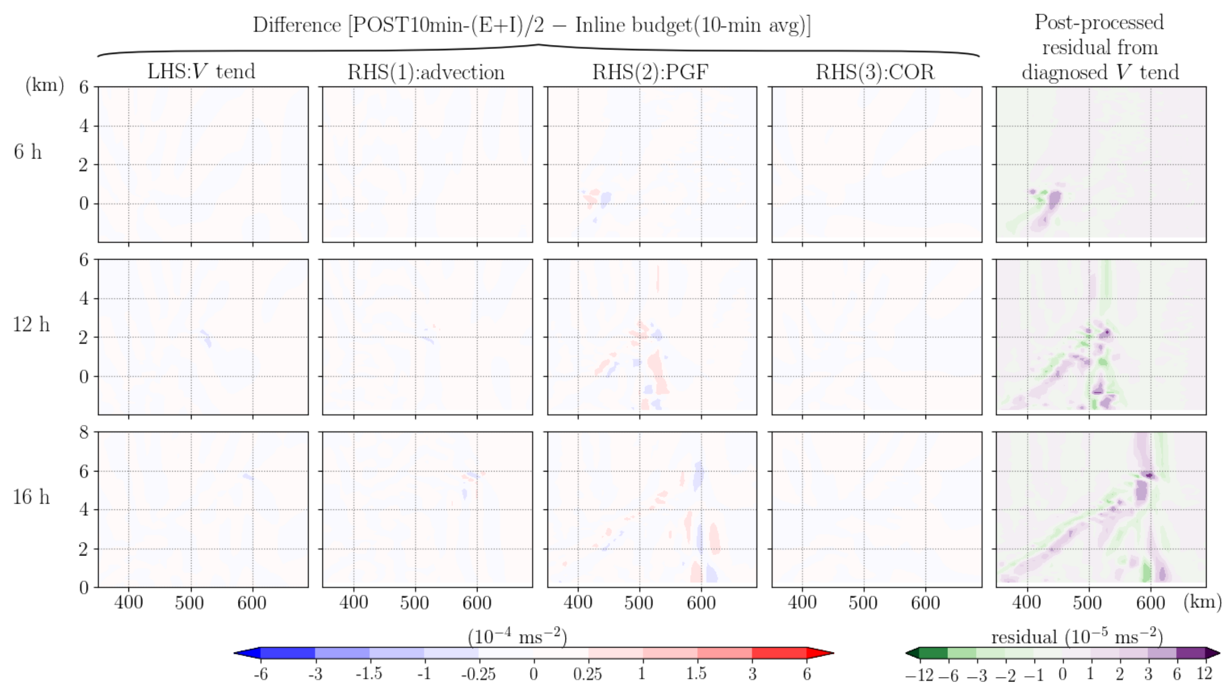


**Fig. 3.11**: Same as Fig. 3.8, but the forcing terms diagnosed in the post-processed budget analysis are the averages of explicit and implicit methods (POST10min-(E+I)/2). To represent the same time window as the post-processed analysis, the in-line budget results used here for the difference calculation are the 10 min averages (corresponding to the output interval) instead of the instantaneous values.

both ADV and PGF (Fig. 3.13). Their combined errors result in widespread residual values $> 3 \times 10^{-5}$ m s$^{-2}$ even over the area where the tendency term is smaller than $> 1 \times 10^{-4}$ m s$^{-2}$ (error is at least of 30% magnitude of the tendency term over a wide area and is reaching 100% over the band head).

Finally, a different format of the $V$ equation, the advective form, is used for post-processed analysis (POSTadvF- (E+I)/2). Mathematically, the flux-from momentum equation can be rewritten in the advective form without making any additional approximation, only with the aid of the conservation law of dry-air mass in the WRF model as shown in (3.16)–(3.18). However, during the interchange of the expression for the tendency and advection terms, truncation errors may be introduced. We reiterate that the tendency term in the advective form is not equivalent to the one in the flux form divided by $\mu_{\rm d}$; however,

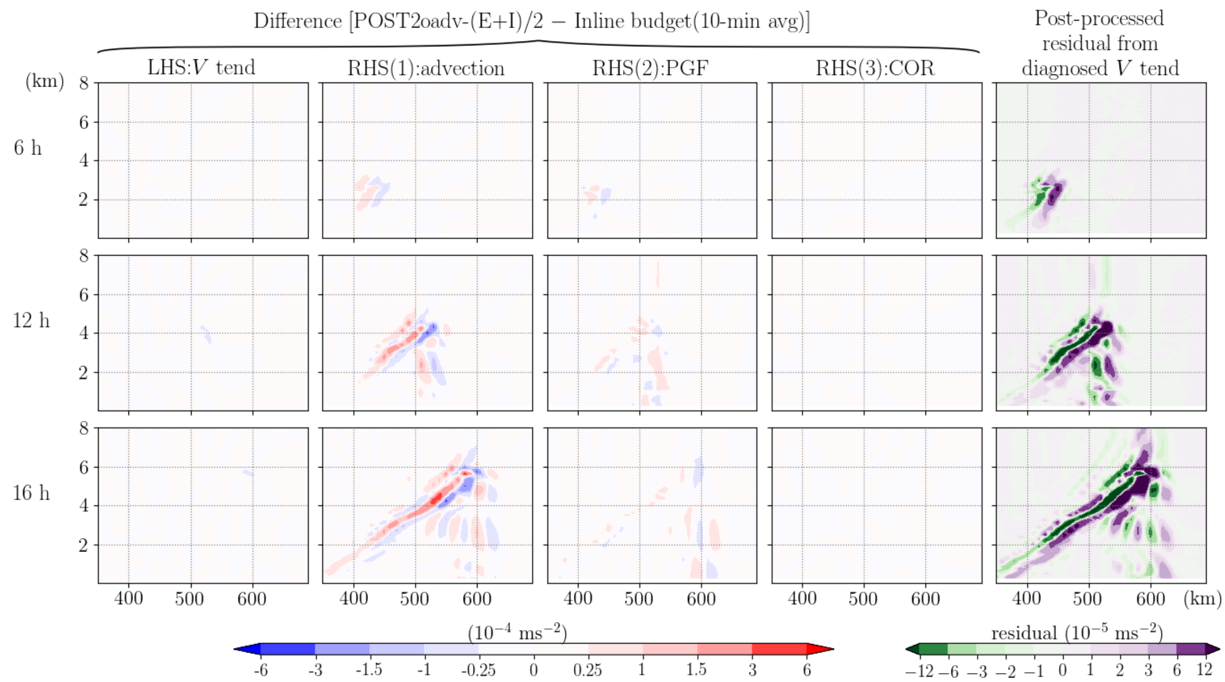


**Fig. 3.12**: Same as Fig. 3.11, but the post-processed analysis uses a second-order operator for advection calculation (POST2oadv-(E+I)/2).

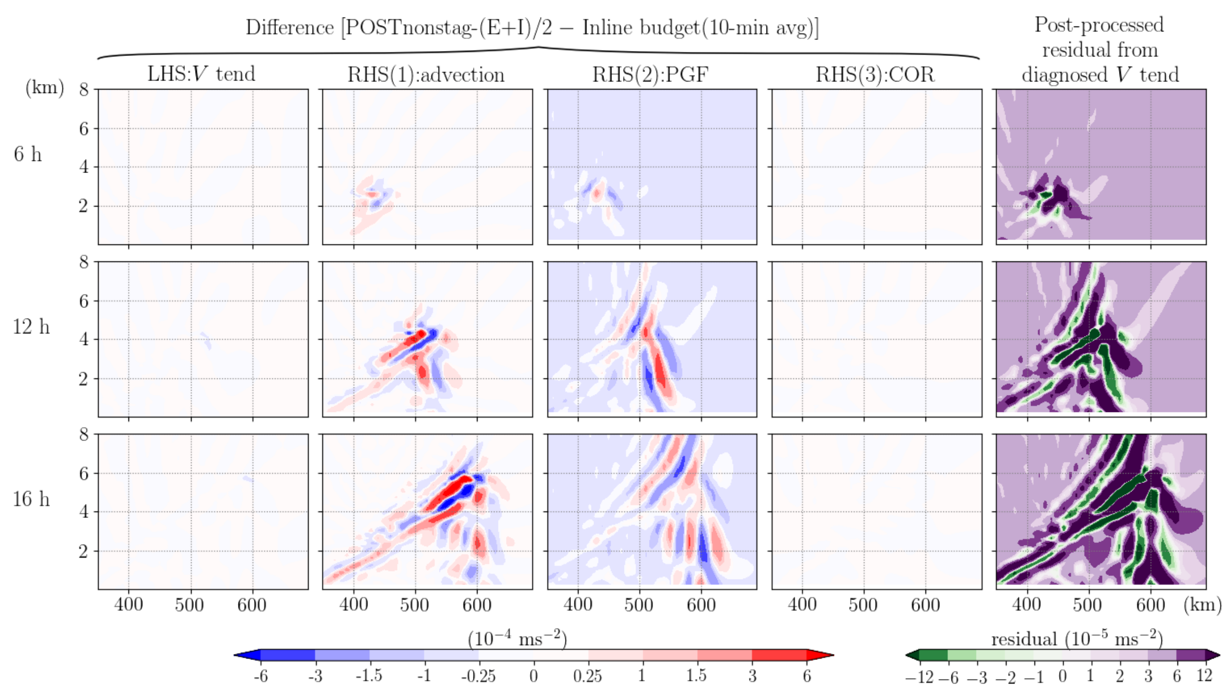


**Fig. 3.13**: Same as Fig. 3.11, but the post-processed analysis does not consider C staggering grids (POSTnonstag-(E+I)/2).

calculation suggests that they are approximately equal, i.e.,

$$\frac{1}{\mu_{\mathrm{d}}}\frac{\partial(\mu_{\mathrm{d}}v)}{\partial t} \approx \frac{\partial v}{\partial t},$$

with a maximum error that is on the order of $10^{-7}$ $10^{-8}$ m s$^{-2}$ (3 orders of magnitude smaller than the simulated $v$ tendency) in our study. The summation of the tendency term and advection term in these two forms of the momentum equation should be mathematically identical, so we would expect to see a small difference in the advection term as in the tendency term. However, we find that the advection term in the advective form has a strong positive bias compared to that in the flux form (Fig. 3.14). The residual term in the POSTadvF-(E+I)/2 is thus negatively biased over the entire convective band with a magnitude exceeding $1.2 \times 10^{-4}$ m s$^{-2}$ (reaching 100% error near the upper half of the convective band). If the residual is neglected or not shown, authors and/or readers may

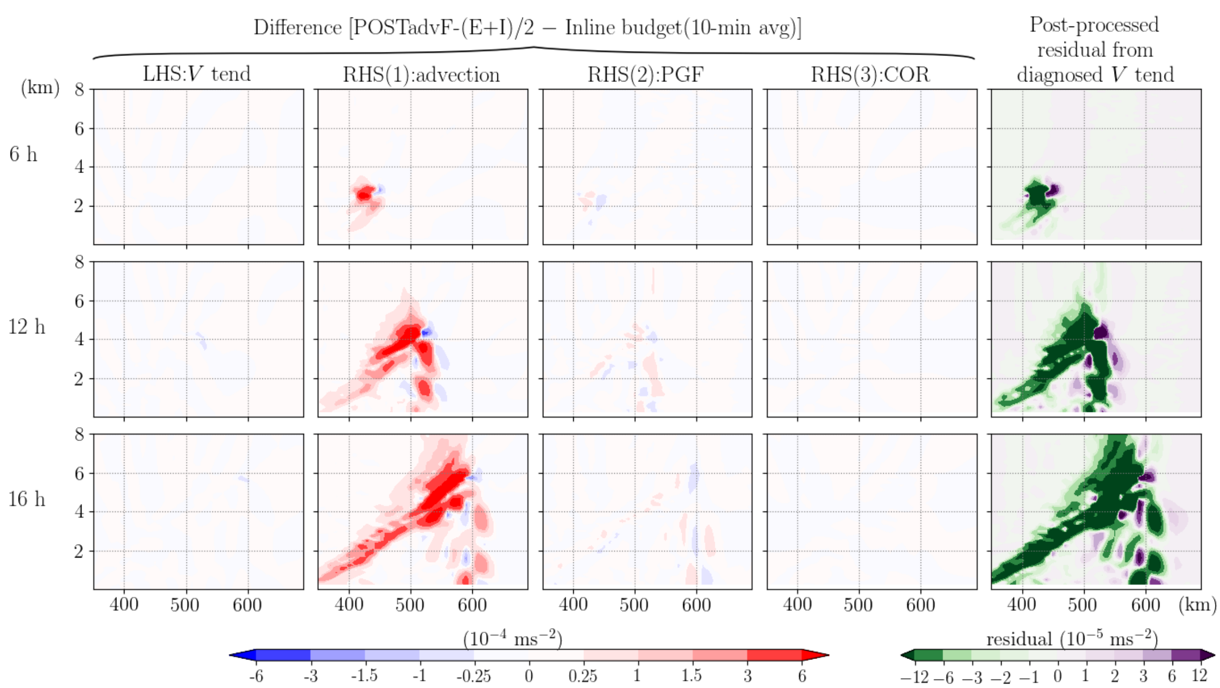


**Fig. 3.14**: Same as Fig. 3.11, but the post-processed analysis is applied using the advective-form equation (POSTadvF-(E+I)/2).

falsely consider the advection process to be the dominant term governing the evolution of the slantwise updraft.

A quantitative comparison of the 99th percentile of the magnitude of the residual term in the domain (excluding the boundaries) among different analysis methods is shown in Fig. 3.5. The residuals between the instantaneously diagnosed forcings and the true model tendency term (calculated in-line) are shown in Fig. 3.5a while the ones between the averaged forcings of two consecutive outputs and the diagnosed tendency term are shown in Fig. 3.5b. The evolution of the 99th percentile residual shows generally larger magnitudes when the momentum tendency is larger (Fig. 3.2b), suggesting that these errors may amplify in stronger convection cases. While the post-processed budget analysis in POST1min-E, POST10min-I, and POST10min-(E+I)/2 can achieve a relatively small 99th percentile residual (peak at $5 \times 10^{-5}$ m s$^{-2}$ or about 7% of the concurrent 99th percentile $v$ tendency), the in-line budget analysis always gives a much smaller magnitude ($< 10^{-8}$ m s$^{-2}$, or 0.001% of the tendency, during the entire simulation). Figure 3.5 also shows that any simplification that is inconsistent with the model solver can severely degrade the accuracy of the post-processed budget analysis. Both POSTnonstag-(E+I)/2 and POSTadvF- (E+I)/2 can lead to a 99th percentile of the residual magnitude peaking at around $4 \times 10^{-4}$ m s$^{-2}$ or more, which corresponds to $> 50\%$ of their concurrent 99th percentile simulated $v$ tendency, respectively. Generally, a higher relative magnitude of residual to $v$ tendency is reached if the maximum instead of the 99th percentile is examined (despite larger fluctuation with time).We also examined the 95th percentile of the residual magnitude and obtained qualitatively similar results although the relative magnitudes of such chosen residuals among the three post-processing methods with simplifications (POST2oadv-(E+I)/2, POSTnonstag-(E+I)/2, and POSTadvF-(E+I)/2) vary due to their different error distributions.

### (3) Results of vertical momentum budget

For the $W$ equation, the closure of the post-processed budget appears not to be practicable even when the output time interval is reduced to the integration time step (Fig. 3.15). One partial reason is that the spatially noisy small-step modes, neglected in the off-line budget analysis, are surprisingly large with a general order of $10^{-4}$ m s$^{-2}$ over the growing band, which is 1 order of magnitude larger than the $W$ tendency (see the blue and red contours overlapped on the residual subplots in Fig. 3.4). These high-frequency modes not only include vertically propagating sound waves but also some gravity wave modes (Klemp et al., 2007). Furthermore, as indicated in (3.6) and mentioned in Section 3.3.1, the $W$ equation solved in the WRF model is implicit, coupled with geopotential tendency equation

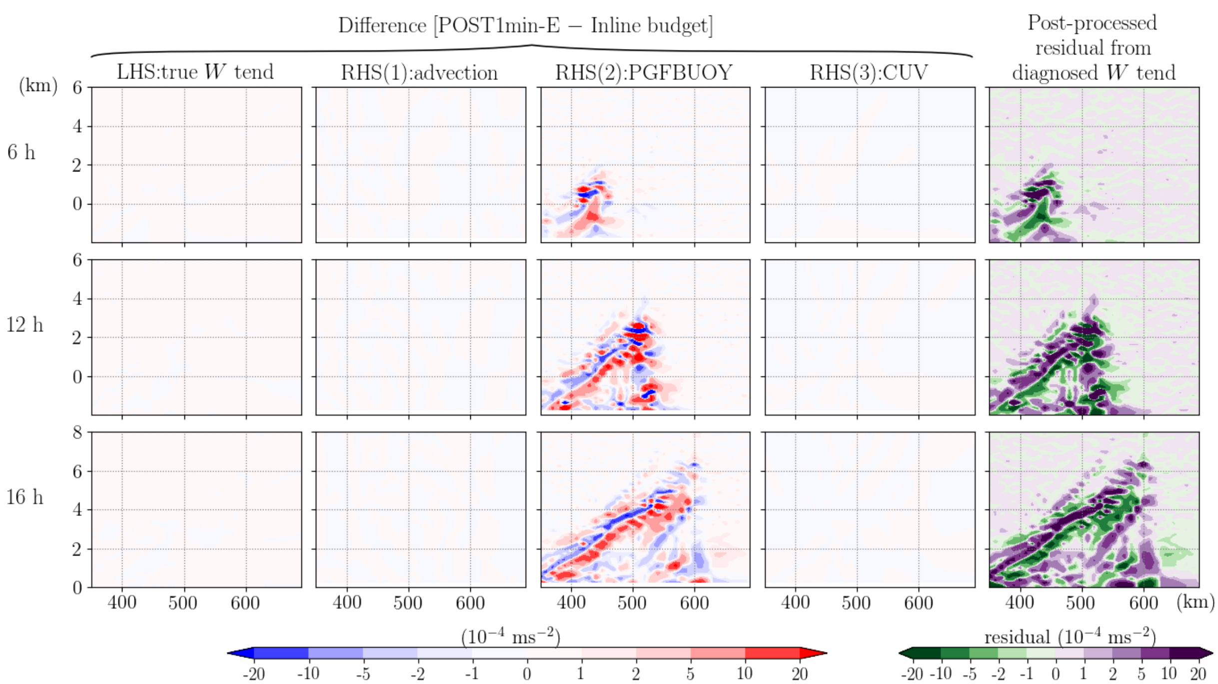


**Fig. 3.15**: The difference between the post-processed (POST1min-E) and the in-line budget analysis for vertical momentum $W$. All terms have been divided by $\mu_\mathrm{d}$ and thus have a uniform unit of meters per second squared. In each row, the subplots from left to right indicate the difference of true $W$ tendency, ADV, PGFBUOY, and CUV. The rightmost subplot indicates the residual term obtained in the post-processed budget analysis. Each row from top to bottom shows the results at 6, 12, and 16 h, respectively.

and includes a forward-in-time averaging operator that is applied to the small-step modes:

$$\overline{(\mathrm{ACOUS})}^{\tau} = \frac{1+\beta}{2}(\mathrm{ACOUS})^{\tau+\Delta\tau} + \frac{1-\beta}{2}(\mathrm{ACOUS})^{\tau},$$

where $\beta$ is a user-specified parameter and $\Delta\tau$ indicates the small time step in the acoustic scheme. This means that the small-step modes at a current small step, $\overline{(\mathrm{ACOUS})}^{\tau}$, are calculated using information (e.g., geopotential, potential temperature and density) at the forecast time $\tau + \Delta\tau$ (see Eq. (3.11) and (3.12) in Skamarock et al., 2008). All these components are not feasible for an off-line budget calculation.

The application of POST1min-E for the $W$ tendency shows that this method accurately estimates most of the processes, but large errors $> 2\times10^{-3}$ m s$^{-2}$ remain in the PGFBUOY term resulting in a widespread residual that reaches the same magnitude of the peak $W$ tendency term (Fig. 3.15). The fact that these errors exceed the small-step modes of PGFBUOY (shown in the right most column in Fig. 3.4) suggests that such imbalance does not solely come from the neglect of the small-step modes. A close comparison of the post-processed and the in-line PGFBUOY shows that our estimation is close to the in-line value to an accuracy of at least three significant figures at the first RK3 step before the acoustic contribution is considered (not shown). However, this large-step forcing term adjusts rapidly, sometime even with a sign change, from step to step within the RK3 integration. Although it is feasible to estimate $F(\Phi^t)$ via post-processing, it is however impossible to retrieve $F(\Phi^{**})$ in (3.4), leading to the poor estimation of vertical pressure gradient and buoyancy force in the $W$ budget. This result also suggests that the budget closure for vertical velocity is difficult by nature due to its rapid variation on small scales.

## 3.4 Tests on different cases or with different horizontal resolutions

The growth of the residual as the convection intensifies (Fig. 3.5) motivates a test for a different case with stronger momentum tendencies. A WRF idealized 2D squall line test case (em_squall2d_y; Skamarock et al., 2008) is selected with a horizontal resolution of 250 m and 3 s integration time step, and the simulation is integrated for 1 h. A subgrid turbulence scheme based on the prognostic turbulent kinetic energy equation is activated (diff_opt=2 and km_opt=2; Chapter 4.2.4 in Skamarock et al., 2008). The simulated $v$ tendency in this case is 2 orders of magnitude stronger than the one in the slantwise convection case. The in-line retrieval budget tool works well with 99th percentile residuals generally 2 orders smaller than the tendency terms in the domain during this simulation. However, as compared to the slantwise convection case, this case features a larger relative magnitude of 99th percentile residual to the 99th percentile tendency term of about 0.1%. Furthermore, the post-processed budget analysis applied to the output data with an output interval the same as the integration time step (analogous to POST1min-E but in this case, it is termed POST3sec-E; Fig. 3.16), with no simplification made, does not work as well as in the slantwise convection case. POST3sec-E shows that the largest error appears in the PGF term with a magnitude of 50% of its true value at a given instant. The error in diffusion only accounts for about 10% of the error at the same time. One possible reason is that unlike the case of slantwise convection where the PGF exhibits a horizontally rather uniform structure with almost the same sign (Fig. 3.3), the PGF term in this case has a more complex spatial structure with several sign changes over a horizontal distance of 10–15 km. Thus, large errors appear at the edge of these positive or negative patches where the sign changes. Despite the small spatial scales of these errors, the large error magnitude would render accurate interpretation of the physical process difficult based on such post-processed budget analysis. This result suggests that the post-processed budgets, even when done with care, do not always work well, and that the associated residual or errors might be sensitive to the intensity of the simulated system, the spatial or temporal resolution, and the nature of the physical processes governing the different systems.

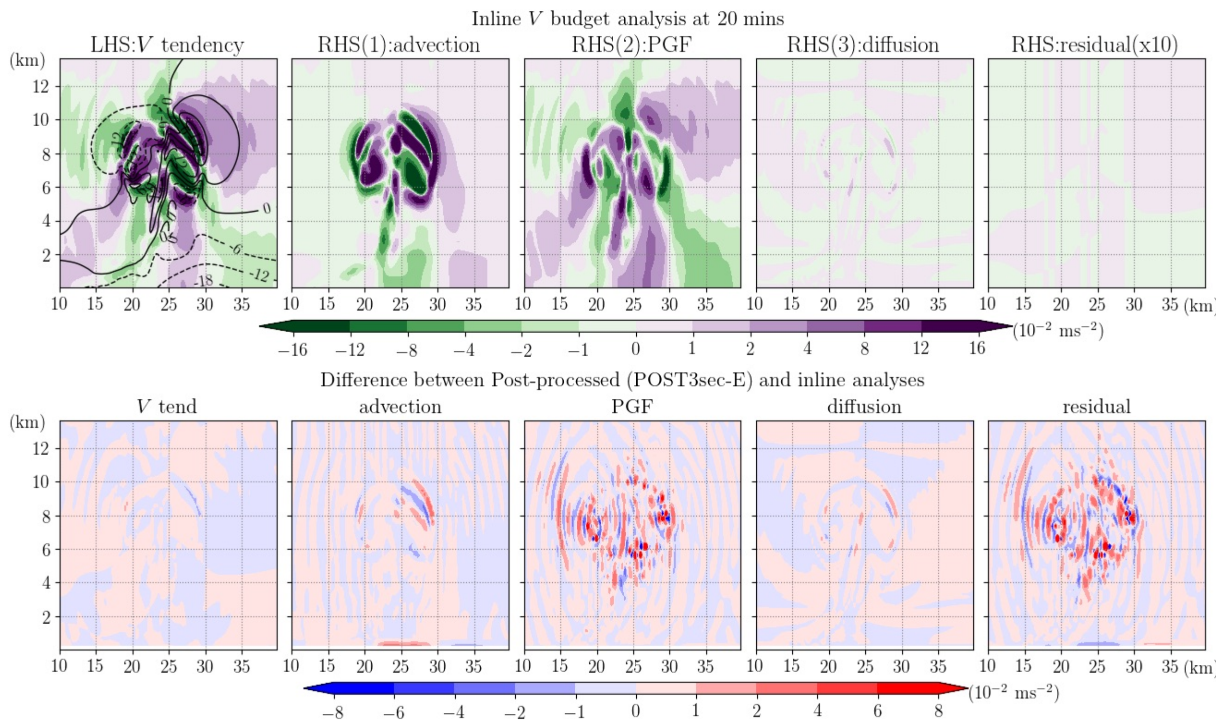


**Fig. 3.16**: Upper row shows the in-line budget analysis of horizontal momentum, $V$, for the WRF ideal test case of 2D squall line at 20 min of simulation time. Shading in subplots from left to right represents the term of $V$ tendency, advection (ADV), horizontal pressure gradient force (PGF), diffusion, and residual (multiplied by 10 to emphasize its small magnitude as compared to the other terms). All terms are divided by $\mu_{\mathrm{d}}$ and thus have units of meters per second squared. The black contours show the velocity, $v$, with an interval of 6 m s$^{-1}$. The bottom row shows the difference between the post-processed (POST3sec-E) and the in-line budget analysis.

While an increase in spatial resolution often requires a shorter integration time step for numerical stability and may result in stronger simulated convection, it is almost impossible to separate all these factors. We can, however, conduct the same slantwise convection simulation with a higher resolution of 2 km (and a shorter integration time step of 10 s) to exclude the effect of different physical processes in different systems and discuss the changes in the accuracy of the budget analysis when spatial resolution is increased from 10 km. As shown in Fig. 3.2b, in the 2 km simulation the maximum of the simulated 99th percentile $v$ tendency is $1.2 \times 10^{-3}$ m s$^{-2}$, almost twice the magnitude in the 10 km run. The magnitude of the residual from the in-line budget analysis also becomes larger with the 99th percentile value almost 1 order larger than that in the 10 km simulation (Fig. 3.5). However, its relative magnitude is still small and amounts to about 0.005% of the tendency in the 2 km case. For the post-processed budget analysis applied to the 2 km simulation, the 99th percentile residual with the instantaneous calculation of POST10min-I-2km appears only slightly larger yet sometimes smaller than those in its 10 km case (Fig. 3.5a). For the method using two model outputs for both diagnosed tendency and forcing terms, the peak 99th percentile residual in POST10min-(E+I)/2-2km is about 4 times larger than that in its 10 km counterpart (POST10min-(E+I)/2). This is likely due to the larger deviation caused by the longer diagnosed window (10 min) with respect to the integration time step (10 s) in the 2 km case. In addition, it appears that the simulated fields adjust more rapidly with more complex structures on smaller scales in the 2 km simulation as compared to the 10 km simulation (not shown). If the same analysis is performed using the 1 min output (POST1min-(E+I)/2-2km) as opposed to the 10 min output, the residual can be greatly reduced to be similar to that obtained in POST10min-(E+I)/2 (Fig. 3.5b).

The results presented above suggest that the relative magnitude of errors in budget analysis vary with different systems or cases. Furthermore, while the absolute errors in the in-line momentum budget analyses do indeed increase with increasing horizontal resolution, the relative magnitude with respect to the simulated tendency does not increase substantially. The accuracy of the post-processed budget analysis using the averages of two consecutive model outputs is highly dependent on the ratio of the output interval and the integration time step. A ratio of 10 as used in the POST10min-(E+I)/2 results in an acceptable accuracy (99th percentile residual of about 7% of the tendency), while a lower value of 6 is required for high-resolution simulations (e.g., the 2 km case) to reach a similar accuracy. For cases with a more complex physical process like the squall line test case, the in-line budget retrieval appears necessary for adequate budget closure.

## 3.5 Discussion and summary

Budget analysis is a commonly employed tool in numerical studies to understand the underlying mechanisms for certain simulated features of interest. However, many studies still have difficulties in achieving a balanced or closed budget especially when a full-physics model is used and when the budget is calculated instantaneously over a local area. Aside from the complexity of various (some implicit) parameterization schemes, the main challenge in closing the budget involves the analysis of post-processed data using algorithms that are inconsistent with the model solver. In this study, an in-line momentum budget retrieval tool is developed for the WRF model, and its advantages for momentum budget analysis are demonstrated. The 99th percentile residual obtained from this in-line retrieval is always smaller than or about 0.1% of the actual tendency term in all the tested cases, which include idealized, 2D simulations of slantwise convection and squall lines. Taking the results from the in-line retrieval as "truth", we investigate the potential errors in each term and the resultant residual for post-processed budget analyses under different assumptions.

The comparison among different post-processed diagnoses is focused on the horizontal momentum ($V$) budget. The reason is that post-processed vertical momentum ($W$) budget analysis fails to produce reasonably accurate results due to the noisy vertical pressure gradient and buoyancy forces that are tied closely to the small time-step modes and the implicit scheme used for the vertical momentum integration. Thus, in-line retrieval is necessary for an accurate $W$ budget analysis. The errors in the post-processed $V$ budget arise from both the left-hand-side tendency term and the right-hand-side (rhs) forcing terms. To improve the accuracy of the diagnosed momentum tendency estimation, one can reduce the output interval to the model integration time step, which incurs a large computational cost and consumes a large amount of disk space. An alternative and cheaper solution is to add the tendency calculation within the model as a standard output. Our test case of slantwise convection shows that the diagnosed tendency using two successive model outputs with a 10 min interval to approximate the instantaneous true tendency (with an integration time step of 1 min) could create an error exceeding 50%, which greatly limits the effectiveness of such a budget for physical interpretation.

For the rhs forcing terms in the $V$ equation, errors can be limited if the post-diagnosis is done with care using the same form of the model equation, the same spatial discretization, and the same order of the advection operators and performing the calculation on the original (e.g., C staggering and vertically stretched) model grids. However, these steps are necessary but not necessarily sufficient for the closure of the budget, as the forcing term diagnosis also largely depends on the selected input states. If the budget at an instant of time is desired, the explicit or forward Euler method using the previous states (POST10min-E)) might result in large and widespread errors in the advection and horizontal pressure gradient terms (local peak errors are about 50% and 25% of their true values in our simulation, respectively) unless the output interval is reduced to the integration time step. In the latter case (POST1min-E), an error $< 5\%$ for each individual term and a residual generally 1 to 2 order(s) smaller than the maximum tendency can be achieved (the 99th percentile residual is about 7% of the 99th percentile $v$ tendency). An alternative way to reach a similar level of accuracy for instantaneous fields without compromising the computational cost is to diagnose the rhs forcings using the implicit or backward Euler method (POST1min-I). This method diagnoses the forcings using the predicted states and thus can better capture the true model forcings by using inputs at a closer time to the model integration window.

Instead of performing the calculation using model output at one given instant, a more general post-processed budget analysis can use two successive model outputs (POST10min-(E+I)/2). This method seems to work well with the 99th percentile percentile residual being about 7% of the 99th percentile $v$ tendency in our 10 km slantwise convection case with 10 min output intervals. However, the accuracy of this method varies among the test cases of different systems and is sensitive to the ratio of the output interval to the integration time step. Among the tests conducted in this study, an upper limit of 10 for this ratio is suggested, and it should be even smaller for high-resolution simulations of high-amplitude weather systems, as rapid adjustments occur on the small scales.

Three other common assumptions in post-processing analysis are made on top of the POST10min-(E+I)/2 to examine their potential impacts on the accuracy of the horizontal momentum budget analysis. First, utilizing an advection operator with a lower order than the one used in the model setup degrades the accuracy of the advection term with up to 50% error over the area where the advection is the strongest (POST2oadv-(E+I)/2). Second, the neglect of the staggering grids would negatively impact the estimation of all the spatial differential terms, leading to a widespread residual of at least 30% of the local tendency (POSTnonstag-(E+I)/2). Last, when the advective form of the momentum equation is used for post-diagnosis rather than the flux form, although it is mathematically equivalent to the flux form solved in the model solver, a strong negatively biased residual results (POSTadvF-(E+I)/2). Both POSTnonstag-(E+I)/2 and POSTadvF-(E+I)/2 give a peak 99th percentile residual of about $> 50\%$ of the concurrent 99th percentile of the $v$ tendency. All the above errors do not just appear randomly; rather, they are spread over the area where the dynamics are the most active, thus undermining the physical interpretation of the dynamics of the simulated system. We thus emphasize the importance of revealing the magnitude of the residual (relative to the tendency term) in publications on budget analysis, to enable readers to gauge the validity of the results.

While the post-processed $V$ budget analysis can reach an acceptable accuracy in some cases, the resultant residual may vary from case to case even when the same analysis method is adopted. Our test of an idealized squall line case with strong momentum tendencies shows that the application of the post-processed budget analysis method without any simplification using the 3 s (same as the model integration time step) output data nevertheless results in a large relative error magnitude ($\sim 50\%$) in the horizontal pressure gradient force, with very small-scale error structures.

In summary, different assumptions or simplifications made in a post-processed budget analysis may severely impact the estimation of each forcing term and result in a large imbalance of the budget. Based on our experiments, we conclude that the in-line retrieval method like that developed herein is the most reliable one for budget analysis in numerical studies. While the budget analyses shown in this study are only for $V$ and $W$ momentum under the 2D idealized configurations, this newly developed budget tool also retrieves budget terms for $U$ momentum and potential temperature. It can be applied to 3D idealized and real cases as the map projection is also considered, following the original governing equations as shown in Skamarock et al.'s (2008) Eq. (2.23)–(2.25) with map factors, which are equal to 1 for an idealized setup on the Cartesian coordinate. We also stress that in some budget studies where a coordinate transformation is necessary (e.g., from Cartesian to polar), some errors are unavoidable. In such cases, it is best to perform the budget calculation using the in-line retrieval method on the model grid and then transform the budget to a new coordinate (e.g., Zhang et al., 2000). Finally, in situations where the in-line coding cannot be done, this study also provides general guidance to minimize the error in the budget. Thus, our results are beneficial to budget analyses in numerical studies in general and are not limited to the WRF model.

# Appendix A

To our knowledge, there are at least three other similar in-line budget retrieval works that have been done in the WRF model:

1. Lehner (2012) applied to v3.2.1:

   Lehner (2012) provides a very detailed instruction of how an in-line budget retrieval is done for the WRF model. The method or code was utilized in Lehner and David Whiteman (2014) to study the mechanisms of the thermally driven cross-basin circulation. However, the code was never made publicly available. From the document, it appears that Lehner's (2012) general procedure of retrieving the rhs budget terms during the model integration is essentially the same as our approach, which considers both the large time-step and the small or acoustic time-step contributions. Furthermore, the individual contribution from different parameterization schemes that are activated in her study was also separately retrieved. While the general method appears highly similar to our code, the momentum budget retrieval in Lehner (2012) only applies to the horizontal momentum ($U$ and $V$) whereas our tool includes the budget retrieval for the vertical momentum ($W$) as well.

2. Moisseeva (2014) and Moisseeva and Steyn (2014) with v3.4.1:

   The code is publicly available. The developed budget retrieval is also for the horizontal momentum equations only. The method is simpler than Lehner (2012) as it does not include the acoustic or small-step correction terms. Furthermore, while the large time-step, non-parameterized terms (e.g., pressure gradient terms, advection, Coriolis terms) are individually retrieved, their modified registry file only outputs one (summarized) term for all the parameterized physics.

3. Potter et al. (2018) with v3.8.1:

   The code is publicly available. This budget retrieval uses the code adapted from Moisseeva (2014), taking references from Lehner (2012), and is applied to the same version of the WRF model as used in this study (v3.8.1). More components are added from the version used in Moisseeva (2014), including the potential temperature budget, vertical velocity budget, the sixth-order diffusion term, the parameterized physics term decomposed to boundary layer, and radiation schemes. A major difference from our retrieval tools exists in that the small-step components are neglected in Potter et al. (2018). Comparing the budget analysis results using our retrieval tool with those using theirs for the same idealized test case of the 2D squall line, the largest differences appear in terms that involve the small-step contributions (e.g., PGF and PGFBUOY), which result in larger residual terms with Potter et al.'s (2018) retrieval method (not shown). While the relative magnitudes of such residuals to the tendency term still appear small for the horizontal momentum budget, they become larger for the vertical momentum budget. This is consistent with our result that the small-step modes are more important in the $W$ budget equation than in the $V$ budget equation, and thus ignoring them results in larger errors.

Furthermore, calculations of the lhs tendency terms are added as new variables in our tool while the tendency terms used in the above studies are the pre-existing model variables ru_tend, rv_tend, rw_tend, etc., which only represent the summation of all the large-step forcings to their corresponding fields (can be directly outputted via changing the WRF registry file) instead of their true local changes with time.

# Appendix B

To construct an initial condition that contains conditional symmetric instability (CSI) but to avoid dry symmetric instability and dry and conditional (gravitational) instability is a challenging task (Persson and Warner, 1995). Therefore, the initial profile in our test case is decided by a trial-and-error method and follows the following steps.

1. We first prescribe a horizontally uniform Brunt– Väisäilä frequency, $N^2 = \frac{g}{\theta_v}\frac{\partial \theta_v}{\partial z}$ with a vertical profile of

$$N^2 = \begin{cases} 1.25 \times 10^{-4}\ \mathrm{s}^{-2} & z < 0.5\ \mathrm{km} \\ 9 \times 10^{-5}\ \mathrm{s}^{-2} & 5\ \mathrm{km} \leq z < 10.5\ \mathrm{km}, \\ 5 \times 10^{-4}\ \mathrm{s}^{-2} & z \geq 13.5\ \mathrm{km} \end{cases} \tag{B1}$$

   where $z$ is the height and there is a linear transition for the layers $0.5$ km $\leq z < 5$ km and $10.5$ km $\leq z < 13.5$ km using the specified values beneath and above the layers.

2. A constant geostrophic vertical zonal wind shear is given: $\frac{\partial U_g}{\partial z} = 5.8 \times 10^{-3}\ \mathrm{s}^{-1}$. Thermal wind balance gives

$$\frac{\partial U_g}{\partial z} = -\frac{g}{f\theta_v}\frac{\partial \theta_v}{\partial y}. \tag{B2}$$

3. Based on (B1) and (B2), we can specify the value of $\theta_v$ at any point and then derive the $\theta_v$ for the entire domain. In this case, $\theta_v(y_0, z_0) = 287.5$ K, where $(y_0, z_0)$ indicates the grid point at the surface on the southern boundary.

4. The relative humidity (RH) field is constructed by specifying a horizontally uniform background profile ($\mathrm{RH_{background}}$) with some enhancement ($\mathrm{RH_{bubble}}$) over an elliptical area where the initial perturbation will be later added. The enhanced humidity over a limited area hastens the release of CSI and avoids convection developing near the

southern boundary.

$$\mathrm{RH}_{\mathrm{background}}(z) = \begin{cases} 0.81 & \text{for } z \leq 5 \text{ km} \\ \min\left[0.81, 1 - 0.9\left(\frac{z-5}{7.5}\right)^{0.8}\right] \text{ for} & 5 \text{ km} \leq z < 12.5 \text{ km}, \\ 0.1 & \text{z} \geq 12.5 \text{ km} \end{cases}$$

$$\mathrm{RH}_{\mathrm{bubble}}(y, z) = \mathrm{RH}_{\mathrm{background}}(z) \times f_{\mathrm{enhancement}}(y, z),$$

where

$$f_{\mathrm{enhancement}}(y, z) = \begin{cases} 1.22 & e \leq 1 \\ 1.22 - 0.11(\mathrm{e}{-}1) \text{ for} & 1 < e \leq 3, \\ 1 & e > 3 \end{cases}$$

where $e = \left(\frac{y-410}{e_{\mathrm{b}}}\right)^2 + \left(\frac{z-1}{e_{\mathrm{z}}}\right)^2$, $e_{\mathrm{b}} = 100$, $e_{\mathrm{a}} = 3$, and $y$ and $z$ are the horizontal distance from the southern boundary and height, respectively, with units of kilometers. The constructed initial profile has a maximum RH of 98.82% over an elliptical area centered at $y = 410$ km and $z = 1$ km.

5. A constant surface pressure is specified: $p_{\mathrm{sfc}} = 1000$ hPa.

6. We then iteratively solve for the hydrostatically balanced pressure, water vapor mixing ratio, potential temperature, dry and full (moist) air density, and geostrophic zonal wind for the entire domain.

The constructed initial environment contains some CSI, which is identified by the presence of negative saturated geostrophic potential vorticity (Chen et al., 2018). In this test case, CSI only exists over the southern half of the domain and never extends higher than 5 km.

To initiate convection, a 2D bubble of potential temperature and zonal wind perturbations is inserted in the area where RH is maximized and where the saturated geostrophic potential vorticity has a value of about $-0.2 \sim -0.1$ pvu. The center of the bubble, located at $y_c = 400$ km and $z_c = 1.5$ km, has a maximum potential temperature perturbation $\Delta\theta_{\max} = 0.5$ K and zonal wind perturbation $\Delta u_{\max} = -6$ m s$^{-1}$. Both perturbation fields decrease to 0 with radius, following $\Delta\theta = \Delta\theta_{\max}\cos^2(0.5\pi r)$ and $\Delta u = \Delta u_{\max}\cos^2(0.5\pi r)$ for $r \leq 1$, where $r = \sqrt{(\frac{y-y_c}{R})^2 + (\frac{z-z_c}{H})^2}$, $R = 50$ km is the horizontal radius, and $H = 1.5$ km is the vertical radius.

**Code availability.** The standard version of WRF v3.8.1 is publicly available at http://www2.mmm.ucar.edu/wrf/users/download/get_sources.html (last access: 6 June 2019; National Center for Atmospheric Research, 2016). The in-line budget retrieval tool in the WRF v3.8.1 described in this study can be found at https://doi.org/10.5281/zenodo.3373872 (Chen, 2019). In this repository, all the files that remain unchanged from the defaults are tagged as "Initial commit". The modified files for the budget retrieval include the Registry.EM_COMMON within the directory registry; module_diag_misc.F, module_diagnostic_driver.F, and module_physics_addtendc.F within the directory phys; module_after_all_rk_steps.F, module_em.F, module_big_step_utilities_em.F, module_first_rk_step_par2.F, module_small_step_em.F, and solve_em.F within the directory dyn_em. The current version includes retrieval for terms of local tendency, advection, horizontal pressure gradient force, net force resulting from vertical pressure gradient and buoyancy, Coriolis force, curvature, upper damping (damp_opt = 2 and 3), turbulence or diffusion (diff_opt = 2), vertical-velocity damping (w_damping = 1) and parameterized physics from the planetary boundary layer scheme (bl_pbl_physics), the radiation scheme (ra_lw_physics and ra_sw_physics), the cumulus scheme (cu_physics), and the shallow cumulus scheme (shcu_physics).

**Author contributions.** TCC designed and performed the numerical experiments under the supervision of MKY and DJK. MKY proposed the idea of comparing the in-line and post-processed budget analyses. TCC developed the code of the in-line budget retrieval tool in the WRF v3.8.1 model and the post-processed analyses. DJK provided useful suggestions to improve the work. TCC prepared the paper and all co-authors contributed to the writing and editing of the paper.

**Competing interests.** The authors declare that they have no conflict of interest.

**Acknowledgments.** We thank Patrick Hawbecker, Ian Dragaud, and one anonymous reviewer for their valuable comments and suggestion that helped to improve this study.

**Financial support.** This research has been supported by the NSERC/Hydro-Quebec Industrial Research Chair program and the Fonds de recherche du Québec – Nature et technologies (FRQNT) doctoral research scholarship grant.

**Review statement.** This paper was edited by Chiel van Heerwaarden and reviewed by Patrick Hawbecker and one anonymous referee.

# Chapter 4

# Numerical modeling: sensitivity to model grid spacing

This chapter focuses on the physical interpretation of simulating the unforced, pure slantwise convection (i.e., the process of CSI release) using the 2D idealized, non-hydrostatic version of WRF model. This work investigates how the explicit representation of slantwise circulation and its important large-scale feedbacks differ when the horizontal model grid spacing varies from 1 to 40 km. The goal is to find out at which resolution can pure slantwise convection be adequately resolved and how the failure to do so would impact its environment? With the in-line retrieval tool for momentum budget analysis introduced in Chapter 3, we can identify the critical dynamics that govern the evolution of slantwise convection and examine their sensitivities to the horizontal model grid spacing.

This work consists of the following published article:

Chen, T.-C., Yau, M.-K., Kirshbaum, D. J. Sensitivities of slantwise convection dynamics to model grid spacing under an idealized framework. *Q. J. R. Meteorol. Soc.* 2021; 1– 19. https://doi.org/10.1002/qj.4003

Footnotes with a numerical superscript are from the original published article, while the ones with a superscript "†" are editorial notes added for clarifications in this thesis.

# Sensitivities of slantwise convection dynamics to model grid spacing under an idealized framework

TING-CHEN CHEN, MAN-KONG YAU, AND DANIEL J. KIRSHBAUM

*Department of Atmospheric and Oceanic Sciences, McGill University, Montreal, Quebec, Canada*



## Abstract

Although the release of conditional symmetric instability (CSI) by slantwise convection is recognized as an important baroclinic process, the basic dynamics of these circulations and their representation in numerical models remain inadequately understood. To address this issue, a series of 2D idealized experiments of pure slantwise convection are performed in an initially statically stable environment using the non-hydrostatic Weather Research and Forecasting Model, with the horizontal grid lengths varying between 1 to 40 km. The results show that the larger-scale feedbacks of the slantwise convection converge numerically when a cross-band grid length ($\Delta y$) of 5 km is reached. The differences between the non-converged and converged results tie closely to the release of a shallow layer of conditional instability that inevitably accompanies the early development of the slantwise circulation due to differential advection of saturation equivalent potential temperature ($\theta_e^*$). The resolved small-scale upright convection embedded within the slantwise band can energize the horizontal acceleration of the slantwise band at mid-to-upper levels by transporting low geostrophic momentum upward that results in localized inertial instability. The convective cell also enhances the large-scale CSI neutralization by advecting high $\theta_e^*$ downward with

strong downdrafts that orient more vertically than coarser-gridded runs. Moreover, $\Delta y \leq$ 5 km also better resolves the horizontal pressure gradients for cross-band motions. This work suggests that global/climate numerical weather prediction models may not adequately resolve important characteristics of slantwise convection. As most cumulus schemes target only upright convection, the inclusion of parameterized slantwise convection may improve their performance.

## 4.1 Introduction

The importance of moist symmetric instability in the atmosphere, in particular conditional symmetric instability (CSI), has been extensively studied since the pioneering work of Bennetts and Hoskins (1979), who proposed it to be one of the mechanisms for frontal rain bands in baroclinic environments. Since then, numerous observational studies have provided evidence of slantwise convection, the process by which CSI is released, often in the form of single or multiple quasi-linear bands (e.g., Bennetts and Sharp, 1982; Emanuel, 1988; Reuter and Yau, 1990, 1993). Moreover, moist symmetric neutrality (but conditional stability) is often observed in the trailing precipitation regions of squall lines (e.g., Zhang and Cho, 1992; Jiang and Raymond, 1995) and in the ascent regions within cyclones (e.g., Emanuel, 1988). Emanuel (1988) suggested that such findings indicate that slantwise convective adjustment occurs continuously on a smaller time-scale than larger-scale baroclinic processes (e.g., frontogenesis) that generate CSI. In addition to its direct impact on precipitation, slantwise convection may drive the formation of sting jets (e.g., Gray et al., 2011; Baker et al., 2014; Schultz and Browning, 2017) and enhance moist frontogenesis to spin up cyclones in the midlatitudes (e.g., Kuo et al., 1991; Balasubramanian and Yau, 1994a,b, 1995).

Despite numerous theoretical (e.g., Ooyama, 1966; Hoskins, 1974; Emanuel, 1983a), numerical (e.g., Innocentini and Neto, 1992 (hereafter IC92); Thorpe and Rotunno, 1989; Persson and Warner, 1991, 1993, 1995 (hereafter PW91, PW93, PW95, respectively); Seman, 1994) and observational (e.g., Reuter and Yau, 1990, 1993; Thorpe and Clough, 1991; Browning et al., 2001a) studies on symmetric instability, only recently have the climatological aspects of CSI and its association with midlatitude weather systems been explored using global reanalysis data (e.g., Ma, 2000; Glinton et al., 2017; Chen et al., 2018). (Chen et al., 2018; see Chapter 2 of this thesis) examined all the Northern Hemisphere cyclones over the period 1979–2008 and found that the chance of slantwise convection occurrence increases with the coincident intensification rate of the cyclones. Furthermore, larger slantwise convective available potential energy (SCAPE or slantwise CAPE) but smaller CAPE are found for explosive cyclones than for non-explosive cyclones. Whereas SCAPE drops significantly during explosive intensification, it does not change notably over the lifetime of non-explosive cyclones. This result provides supporting (albeit indirect) evidence that slantwise convection may contribute to rapid cyclone intensification, as hypothesized by Kuo et al. (1991), Reuter and Yau (1993), and Balasubramanian and Yau (1994a,b, 1995).

Given its potential importance for the midlatitude climate, one may ask whether slantwise convection can be reasonably resolved in global climate models (or general circulation models: GCMs) and what resolution is required to capture its important features and larger-scale feedbacks. A typical slantwise convective band has a time-scale of a few hours and a width of tens to hundreds of kilometres in the cross-band direction (e.g., Reuter and Yau, 1990; Schultz and Schumacher, 1999). Nonetheless, smaller-scale embedded processes might meaningfully affect its evolution. Most GCMs have horizontal grid lengths of O(10–100 km), for which parametrization of upright convection is needed. However, most cumulus parametrization schemes do not consider slantwise convection. While the impacts of horizontal grid spacing on simulated frontal bands in cyclones (e.g., Lean and Clark, 2003) or squall lines (e.g., Bélair and Mailhot, 2001) have been addressed, few studies have examined the grid-resolution sensitivity of pure slantwise convection. Thus, the resolution at which slantwise convection can be adequately (explicitly) resolved, and how significantly the failure to do so would impact the large-scale environment, remain unclear.

PW93 is one of a few studies to investigate the effects of model grid spacing on the unforced/free (with no external forcings applied) slantwise convective band in an environment that is stable to upright convection. They performed idealized simulations with a hydrostatic and viscous two-dimensional (2D) version of the MM4 mesoscale model (developed by the Pennsylvania State University–National Center for Atmospheric Research) with horizontal grid spacings ($\Delta y$) ranging from 6 to 40 km. Their results show that the model simulates a slower and weaker development of slantwise convection with increasing $\Delta y$, but this sensitivity is less noticeable for $\Delta y \leq 15$ km. They thus concluded that one should strongly consider parametrization for slantwise convection for a horizontal grid spacing larger than 15 km, and possibly for even finer resolution in environments where the symmetric instability is weak. To understand such a grid-spacing sensitivity, PW93 solved the linear growth rate as a function of the updraught width (Xu, 1986) and found that when the updraught width of the most unstable mode cannot be reasonably resolved in the model (i.e. the width is smaller than about four grid lengths), a less unstable mode might be triggered. This results in a weaker growth rate of slantwise convection than that simulated at a finer grid spacing. Another study is Knight and Hobbs's (1988) numerical simulation of frontal development in an Eady wave, in which they reached a similar conclusion that hydrostatic slantwise convections were poorly resolved at a horizontal grid spacing of 40 km but reasonably resolved at a horizontal grid spacing of 10 km.

The purpose of this article is to extend the work of PW93 on the sensitivity of pure and unforced slantwise convection to horizontal grid spacing to a non-hydrostatic framework, with the finest grid spacing reduced to 1 km to resolve smaller-scale and non-hydrostatic processes that could potentially affect band development. Another justification for revisiting the CSI problem is that many numerical studies in the 1980s and 1990s, including PW93 and IC92, intended to investigate CSI but actually examined potential symmetric instability (PSI) instead. This was a common misnomer pointed out by Schultz and Schumacher (1999). PSI is assessed using wet-bulb or equivalent potential temperature ($\theta_e$) and such instability is created only if a potentially unstable layer first undergoes a finite vertical displacement to reach saturation. On the other hand, CSI is assessed with saturation equivalent potential temperature and the instability is called "conditional" because it exists locally only if the condition of saturation is met. The distributions of PSI and CSI may be substantially different, and they are equivalent only if the flow is saturated everywhere (Bennetts and Hoskins, 1979; Schultz and Schumacher, 1999).

The dynamics of slantwise convection are analysed here using an in-line momentum budget retrieval tool that accurately captures the tendencies associated with different forcing terms during the model integration (Chen et al., 2020; see Chapter 3). These analyses aid investigation of the main dynamical processes that are responsible for the grid-spacing sensitivity. We then examine how such sensitivities in momentum fields affect other thermodynamic fields and the associated larger-scale feedbacks. The organization of the article is as follows. In Section 4.2, the basic principles and assessment of CSI are introduced. The governing equations, configuration, and set-up of the numerical model are presented in Section 4.3. Section 4.4 presents the model results, including investigation of the dynamics governing the evolution of slantwise circulation and their sensitivities to the horizontal grid spacing. In Section 4.5, we provide some additional sensitivity tests. Finally, Section 4.6 presents the conclusions.

## 4.2 Identification of CSI and slantwise convection

The basic principles of symmetric instability are discussed in Emanuel (1994), Schultz and Schumacher (1999), and Markowski and Richardson (2010). The term "symmetric" refers to its 2D nature, assuming no variation along the thermal wind direction. Conceptually, symmetric instability is a mixture of static and inertial instabilities. Notably, although Ooyama's (1966) theoretical necessary and sufficient condition for symmetric instability[1] does not exclude static and inertial instabilities, "pure" symmetric instability is often considered to occur within environments that are both statically and inertially stable (e.g., Emanuel, 1983a,b; Dixon et al., 2002; Chen et al., 2018). Pure symmetric instability involves both vertical and horizontal driving forces, resulting in a tilting structure with height toward the cool side of the baroclinic zone.

In a dry atmosphere, the environment is considered statically stable to infinitesimal upward movements if $\frac{\partial\overline{\theta}}{\partial z} > 0$, where $\theta$ is the potential temperature and the overbar indicates the hydrostatically balanced component. Defining the $y$-axis as 90° counterclockwise to the geostrophic wind $\boldsymbol{V}_{\mathrm{g}}$, the environment is considered inertially stable to infinitesimal horizontal displacements in $y$ if $\frac{\partial M_{\mathrm{g}}}{\partial y} < 0$, where

$$M_{\mathrm{g}} = u_{\mathrm{g}} - fy$$

is the geostrophic absolute/pseudo-angular momentum, $u_{\mathrm{g}}$ is the geostrophic ("zonal"; here along the $x$-axis) wind and $f$ is the Coriolis parameter. Pure dry symmetric instability exists in the above environment if $\overline{\theta}$ surfaces slope more steeply in the vertical than $M_{\mathrm{g}}$ surfaces in the $y$-$z$ cross-section. A slantwise displacement of the air tube (of infinite extent in $x$) at an angle between the slopes of these two surfaces would result in positive accelerations

[1] The determinant or the trace (or possibly both) of the stability tensor in a meridional plane is negative. The stability tensor is defined as $\mathfrak{m} = \begin{pmatrix} F^2 & B \\ B & N^2 \end{pmatrix}$, where $F^2$ and $N^2$ are inertial stability and static stability, respectively, and $B$ is the measure of baroclinicity.

in both horizontal (along $y$) and vertical directions.

The concept of symmetric instability can be extended to a moist atmosphere by replacing $\theta$ with the saturation equivalent potential temperature $\theta_e^*$. The resulting dynamical instability is termed conditional symmetric instability (CSI). CSI can be viewed as conditional instability along an $M_{\mathrm{g}}$ surface, that is, $\frac{\partial\overline{\theta}}{\partial z}|_{M_{\mathrm{g}}} < 0$, which is mathematically equivalent to negative saturation geostrophic potential vorticity in the Northern Hemisphere (e.g., Chen et al., 2018):

$$f\mathrm{MPV}_{\mathrm{g}}^* < 0, \quad \text{where} \quad \mathrm{MPV}_{\mathrm{g}}^* = \frac{1}{\rho}[\nabla \times \boldsymbol{V}_{\mathbf{g}} + f\hat{\boldsymbol{z}}] \cdot \nabla\overline{\theta_e^*}, \tag{4.1}$$

where $\rho$ is the air density. Note that (4.1) does not guarantee pure CSI as both pure conditional and inertial instabilities can each contribute to negative $\mathrm{MPV}_{\mathrm{g}}^*$.

Another measure of the degree of CSI is the SCAPE, which has proven useful for studying developing frontal bands and cyclones (e.g., Shutts, 1990b; Gray and Thorpe, 2001; Glinton et al., 2017). Sherwood (2000) argued that SCAPE is more appropriate for establishing a meaningful slantwise instability than the lapse-rate criterion ($\frac{\partial\overline{\theta_{\mathrm{e}}^*}}{\partial z}|_{M_{\mathrm{g}}} < 0$). SCAPE is calculated analogously to CAPE but by lifting a hypothetical air tube (rather than parcel) along a slanted $M_{\mathrm{g}}$ surface instead of vertically (Emanuel, 1983b):

$$\mathrm{SCAPE} = {}_{M_{\mathrm{g}}}\int_{\mathrm{LFSC}}^{\mathrm{LSNB}} [R_{\mathrm{d}}(T_{\mathrm{vt}} - T_{\mathrm{ve}})]d(-\ln p) \tag{4.2}$$

where $T_{\mathrm{vt}}$ and $T_{\mathrm{ve}}$ are the virtual temperatures of the lifted air and the environment, respectively, $p$ is the pressure, and $R_{\mathrm{d}}$ is the gas constant for dry air. Here we confine the integral to the layer over which positive buoyancy is attained by the air tube. LFSC stands for the level of free slantwise convection and LSNB is the level of slantwise neutral buoyancy. SCAPE represents the maximum amount of potential energy available for conversion to kinetic energy and is not proportional to $\mathrm{MPV}_{\mathrm{g}}^{*}$. It should be noted that, as in upright convection where positive buoyancy can extend above the conditionally unstable layer, the buoyancy can remain positive above the negative $\mathrm{MPV}_{\mathrm{g}}^{*}$ layer until the LSNB is reached (e.g., Stull, 1991). Therefore, one should not downplay the role of CSI merely because the convective band extends into a positive $\mathrm{MPV}_{\mathrm{g}}^{*}$ region (e.g., Zhang and Cho, 1992). Many CSI studies approximated $\overline{\theta_{\mathrm{e}}^{*}}$ with $\theta_{\mathrm{e}}^{*}$ and $M_{\mathrm{g}}$ with $M$ (e.g., Emanuel, 1988; Shutts, 1990b; Gray and Thorpe, 2001). While the former is generally valid, the latter can introduce large error when significant ageostrophy is present (Schultz and Schumacher, 1999). Thus, in the current study, we use $\theta_{\mathrm{e}}^{*}$ and $M_{\mathrm{g}}$ to assess CSI.

## 4.3 Methodology

### 4.3.1 Model and numerical set-up

The numerical model used in this study is the compressible, non-hydrostatic, and idealized version of the Advanced Research Weather Research and Forecasting (WRF) model, version 3.8.1 (Skamarock et al., 2008). The model is run in 2D, with a domain size of 1,600 and 16 km in the $y$ and $z$ directions, respectively. The lateral boundaries are open in $y$ and the lower boundary is free slip. The only subgrid parametrization scheme in use is the Thompson microphysics scheme (Thompson et al., 2008). Implicit Rayleigh damping for vertical velocity is activated over the uppermost 4 km of the domain to absorb vertically propagating internal gravity waves (Klemp et al., 2008). Six simulations with different horizontal grid spacings ($\Delta y$) of 40, 20, 10, 5, 2 and 1 km are conducted. The simulations are all carried out with a total of 130 vertical layers (stretched with an averaged vertical grid spacing of around 125 m; see more discussion in Section 4.5.1). Although no subgrid turbulence scheme is used for simplicity, the selected third- and fifth-order vertical and horizontal advection, respectively, contain implicit diffusion (Wicker and Skamarock, 2002; Skamarock et al., 2008).

### 4.3.2 Governing equations and the in-line budget retrieval

The WRF governing equations are formulated in flux form (Skamarock et al., 2008). The momentum components, coupled with the dry air mass in the column, $\mu_\mathrm{d}$, are defined as

$$U = \mu_\mathrm{d} u,\ V = \mu_\mathrm{d} v,\ W = \mu_\mathrm{d} w,\ \Omega = \mu_\mathrm{d} \frac{d\eta}{dt},$$

where $\eta = (p_\mathrm{dh} - p_\mathrm{dh\_top})/\mu_\mathrm{d}$ is the terrain-following vertical coordinate, in which $p_\mathrm{dh}$ stands for the hydrostatic pressure and $p_\mathrm{dh\_top}$ is the $p_\mathrm{dh}$ at the top of the dry atmosphere, $u$, $v$ and $w$ are the velocity components parallel to the Cartesian $x$, $y$ and $z$ axes, respectively, and $\frac{d\eta}{dt}$ is the vertical velocity on the $\eta$-coordinate. For our idealized set-up on an $f$-plane, where $f = 1 \times 10^{-4}\ s^{-1}$, these equations are written as

$$\underbrace{\frac{\partial U}{\partial t}}_{u \text{ tendency}} = \underbrace{-\nabla \cdot (\boldsymbol{V} u)}_{\substack{\text{advection} \\ \mathrm{ADV}_u}} \underbrace{-\mu_\mathrm{d} \alpha \frac{\partial p}{\partial x} - \frac{\alpha}{\alpha_\mathrm{d}} \frac{\partial p}{\partial \eta} \frac{\partial \phi}{\partial x}}_{\substack{\text{horizontal pressure gradient force} \\ \mathrm{PGF}_u}} \underbrace{+ fV}_{\substack{\text{Coriolis} \\ \mathrm{COR}_u}} \underbrace{-(\frac{uW}{r_\mathrm{e}})}_{\substack{\text{curvature} \\ \mathrm{CUV}_u}}, \tag{4.3}$$

$$\underbrace{\frac{\partial V}{\partial t}}_{v \text{ tendency}} = \underbrace{-\nabla \cdot (\boldsymbol{V} v)}_{\substack{\text{advection} \\ \mathrm{ADV}_v}} \underbrace{-\mu_\mathrm{d} \alpha \frac{\partial p}{\partial y} - \frac{\alpha}{\alpha_\mathrm{d}} \frac{\partial p}{\partial \eta} \frac{\partial \phi}{\partial y}}_{\substack{\text{horizontal pressure gradient force} \\ \mathrm{PGF}_v}} \underbrace{- fU}_{\substack{\text{Coriolis} \\ \mathrm{COR}_v}} \underbrace{-(\frac{vW}{r_\mathrm{e}})}_{\substack{\text{curvature} \\ \mathrm{CUV}_v}}, \tag{4.4}$$

$$\underbrace{\frac{\partial W}{\partial t}}_{w \text{ tendency}} = \underbrace{-\nabla \cdot (\boldsymbol{V} w)}_{\substack{\text{advection} \\ \mathrm{ADV}_w}} \underbrace{+g(\frac{\alpha}{\alpha_\mathrm{d}} \frac{\partial p}{\partial \eta} - \mu_\mathrm{d})}_{\substack{\text{net vertical pressure gradient} \\ \text{and buoyancy force} \\ \mathrm{PGBUOY}_w}} \underbrace{+(\frac{uU + vV}{r_\mathrm{e}})}_{\substack{\text{curvature} \\ \mathrm{CUV}_w}}, \tag{4.5}$$

where

$$-\nabla \cdot (\boldsymbol{V} a) = -\frac{\partial (Ua)}{\partial x} - \frac{\partial (Va)}{\partial y} - \frac{\partial (\Omega a)}{\partial \eta},$$

$p$ is the full pressure with inclusion of water vapour, $\phi$ is the geopotential, $r_\mathrm{e}$ is the mean Earth radius, and $\alpha$ and $\alpha_\mathrm{d}$ are the full and dry-air specific volumes, respectively. For the horizontal momentum equations, the right-hand-side (r.h.s.) forcing terms include the flux-form advection ($\mathrm{ADV}_{u,v}$), horizontal pressure gradient force ($\mathrm{PGF}_v$; $\mathrm{PGF}_u = 0$ because $\frac{\partial}{\partial x} = 0$ in the 2D set-up), Coriolis force ($\mathrm{COR}_{u,v}$), and Earth-surface curvature ($\mathrm{CUV}_{u,v}$). For the $w$ tendency in (4.5), the r.h.s. forcings include the flux-form advection ($\mathrm{ADV}_w$), net force between the vertical pressure gradient and buoyancy ($\mathrm{PGBUOY}_w$), curvature effect ($\mathrm{CUV}_w$) and the implicit Rayleigh damping for the vertical velocity (D), which can be neglected except at upper levels. Other parametrized terms may appear in these equations depending on the set-up.

Budget analysis for (4.4) and (4.5) is conducted with an in-line retrieval tool that strictly follows the model solver and thus has high accuracy with the 99th percentile of the residual always less than 0.1% of the concurrent tendency term (Chen et al., 2020). To demonstrate in a common physical unit (m $\mathrm{s}^{-2}$), every term in the flux-form budget equation shown herein is divided by the dry-air mass $\mu_\mathrm{d}$. To facilitate CSI assessment, the geostrophic wind is diagnosed from the in-line-retrieved $\mathrm{PGF}_v$. However, the geostrophic wind field often appears noisier than the total wind, especially for small $\Delta y$ (e.g., Shutts, 1990b). Thus, we applied the cowbell spectral filter (Barnes et al., 1996; Stoelinga, 2009) to filter out gravity-wave-induced variations with a cut-off wavelength of 40 km on the $u_\mathrm{g}$ and $M_\mathrm{g}$ fields for simulations with $\Delta y \leq 10$ km.

### 4.3.3 Initial conditions

An ideal design for a clean experiment for CSI is to construct an initial condition with uniform negative $\mathrm{MPV}^*_\mathrm{g}$ or SCAPE in the domain. However, such a set-up does not guarantee the absence of dry symmetric instability, conditional (static) or inertial instabilities.

Moreover, a moisture field that satisfies these requirements may not be realistically distributed and would serve as an extra parameter affecting the flow dynamics. Thus, as in IC92 and PW95, we choose an iterative method to construct an initial flow by prescribing a constant zonal wind shear, $\frac{\partial u_{\mathrm{g}}}{\partial z} = 5.8 \times 10^{-3}$ s$^{-1}$, a constant surface pressure of 1,000 hPa, and horizontally uniform vertical profiles of Brunt–Väisälä frequency ($N^2 = \frac{g}{\theta_{\mathrm{v}}} \frac{\partial \theta_{\mathrm{v}}}{\partial z}$) and relative humidity (RH). By specifying the virtual potential temperature $\theta_{\mathrm{v}} = 287.5$ K at the surface on the southern boundary, we then solve for the hydrostatically balanced $p$, $\alpha$, $\alpha_{\mathrm{d}}$, $q_{\mathrm{v}}$, $\theta$ and $u_{\mathrm{g}}$ for the entire domain. The resulting initial state contains horizontally uniform static stability ($N^2 > 0$) and baroclinicity ($f \frac{\partial u_{\mathrm{g}}}{\partial z} > 0$), a constant inertial stability ($\frac{\partial M_{\mathrm{g}}}{\partial y} < 0$), and decreasing CSI (in terms of the thickness of the MPV$_{\mathrm{g}}^{*} < 0$ layer in the lowest 4 km and SCAPE) from south to north (Fig. 4.1). CAPE is zero everywhere in the domain. The initial flow ($u$, $v$, $w$)=($u_{\mathrm{g}}$, 0, 0) is in thermal wind balance.

To initiate a single slantwise convective band, positive $\theta$ perturbations and negative $u$ perturbations are added to the initial flow to provide locally positive buoyancy and inertial forces in the vertical and horizontal directions, respectively. Perturbations assume a bubble of the form

$$\Delta\varphi = \Delta\varphi_{\max}\cos^2(0.5\pi r) \text{ for } r \leq 1, \tag{4.6}$$

where $\varphi$ represents $\theta$ or $u$, $r = \sqrt{(\frac{y-y_{\mathrm{c}}}{R})^2 + (\frac{z-z_{\mathrm{c}}}{H})^2}$, where $R = 50$ km and $H = 1.5$ km are the horizontal and vertical radii, respectively, and the centre is located at $y_{\mathrm{c}} = 400$ km and $z_{\mathrm{c}} = 1.5$ km. The values of $\Delta\theta_{\max} = 0.5$ K and $\Delta u_{\max} = -6$ m s$^{-1}$ are chosen empirically to give just enough amplitude to trigger the release of CSI. This bubble is located where MPV$_{\mathrm{g}}^{*}$ is about $-0.2$ pvu (potential vorticity units) and SCAPE is around 400 J kg$^{-1}$ (Fig. 4.1b,c). This SCAPE value might seem small compared to characteristic values of CAPE during severe weather events, but it is reasonable in the context of the SCAPE climatology of Chen et al. (2018, shown in Chapter 2). To hasten CSI release while avoiding widespread slantwise convection developing in the domain, we also add an RH perturbation (to a maximum RH of 98.8%) over the area where the initial bubble is inserted (Fig. 4.1a). The step-by-step construction and the specified vertical profiles of $N^2$ and RH can be found in Appendix B of Chen et al. (2020, shown in Chapter 3).

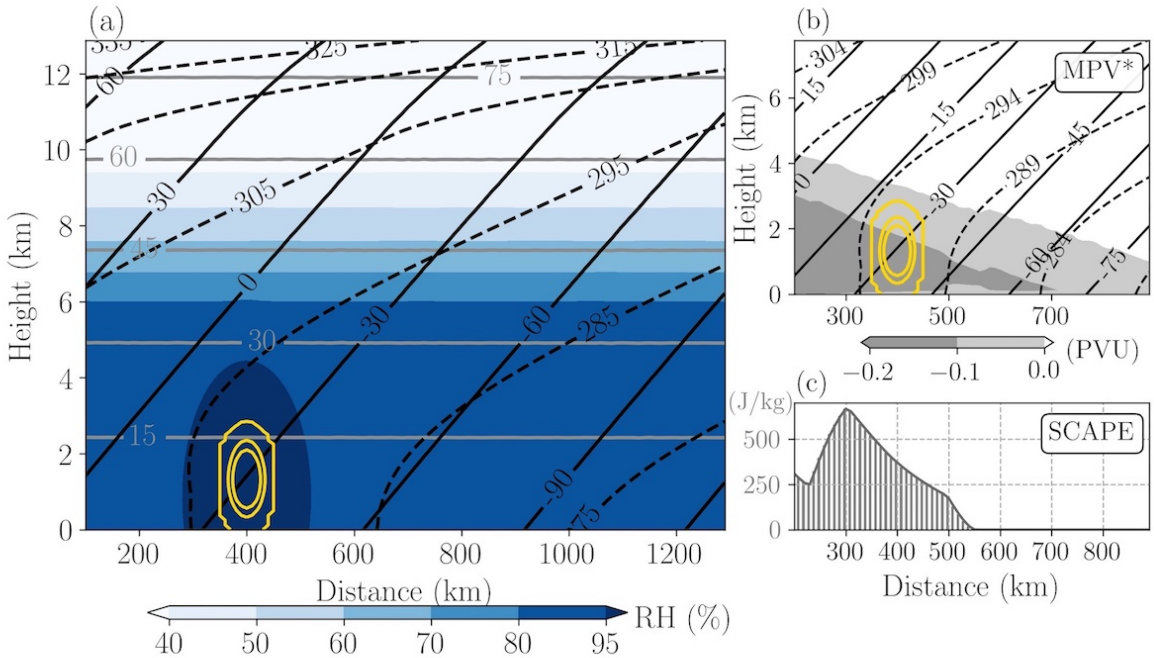


**Fig. 4.1**: Initial conditions: (a) relative humidity (shading; %), geostrophic wind (grey solid; m s$^{-1}$), $\theta_e^*$ surfaces (black dashed; K), $M_g$ surfaces (black solid; m s$^{-1}$), and (b) saturation geostrophic potential vorticity, MPV$_g^*$ [shading; pvu; see (4.1)]. The yellow contours of 0, 0.2 and 0.4 K indicate the initial potential temperature perturbation. (c) The initial SCAPE [bar; J kg$^{-1}$; see(4.2)] at the location where the corresponding $M_g$ surface intersects the ground.

## 4.4 Results

### 4.4.1 Overview of horizontal grid-spacing sensitivity

We first provide an overview of the $\Delta y = 10$ km simulation to draw a comparison with past CSI studies using similar horizontal grid spacings. After the slantwise transverse circulation ($v$, $w$) is initiated, a slantwise band extends upward and northward with time (Fig. 4.2). The peak $v$ and $w$ are around 10 m s$^{-1}$ and 20 cm s$^{-1}$, respectively. To avoid providing a misleading picture by outliers, the evolutions of their 99th percentiles are shown. These values peak at 5.3 m s$^{-1}$ and 8.5 cm s$^{-1}$ at around 21 and 17 hr[†], respectively (Fig. 4.2a). Compared to PW91's numerical study with a similar initial MPV$_{\rm g}$ of $\sim -0.2$ pvu (but calculated using the wet-bulb potential temperature instead of $\theta_{\rm e}^*$) and the same $\Delta y =$ 10 km, our maximum ($v$, $w$) and the time-scale are slightly larger and a few hours faster. However, the overall band evolution and life cycle are consistent. The simulated longer lifetime than the observed ∼3 hr CSI adjustment time-scale in Reuter and Yau (1990) is possibly due to the lack of continuous external forcing in the idealized set-up. The return flow is much more intense and deeper in the lower flank of the slantwise band than the upper side, consistent with PW91, PW95, and IC92 (Fig. 4.2b,c). During its development, the lower part of the band slowly drifts southward at a speed of about 1.2 m s$^{-1}$, similar in magnitude to that noted in IC92. The saturated band has a local width of several tens of km to 100 km, with the entire circulation extending over 400–500 km horizontally and from near the surface up to 8 km height at its peak intensity. SCAPE is reduced to nearly zero at some grid points where the return downdraught nearly reaches the surface (Fig. 4.2c). Since the initial condition is only weakly symmetrically unstable and the band develops in an unforced environment, the accumulated precipitation is modest with a local maximum of less than 2 mm over 20 hr.

Figure 4.3 shows snapshots of the simulated slantwise circulation for all the experiments at 16 hr. For $\Delta y = 40$ km, the model fails to maintain the slantwise convection as the initial perturbation decays quickly, with almost no consequent reduction in SCAPE. Meanwhile, $\Delta y = 20$ km only marginally resolves the band, resulting in a weak and slow growth.[2] The

[†]for $v$ and $w$, respectively.

[2]Even with a wider initial perturbation, that is, doubled $R$ in (4.6), we obtain similar results. $\Delta y = 40$ km still fails to maintain the band while $\Delta y = 20$ km simulates a slower growth of slantwise band than the

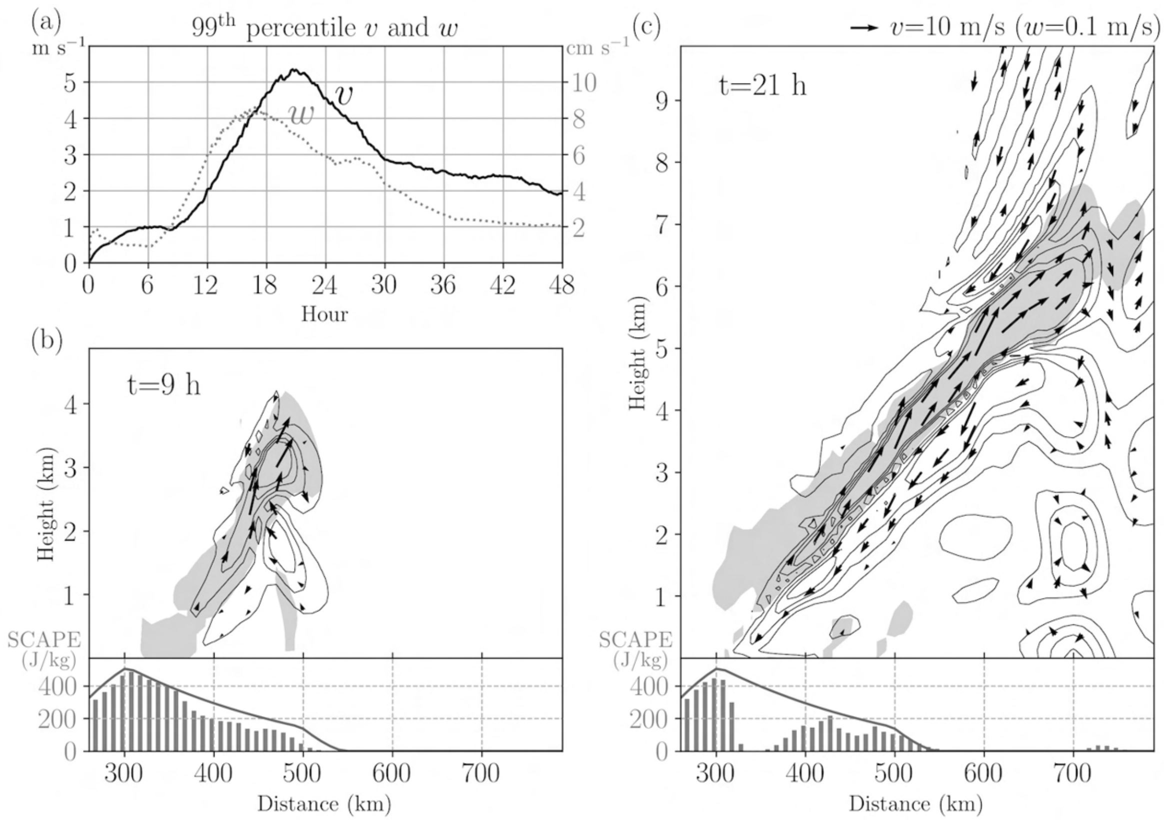


**Fig. 4.2**: Results for $\Delta y = 10$ km. (a) The time evolution of the 99th percentile $v$ (black; m s$^{-1}$) and $w$ (grey; cm s$^{-1}$) over the entire domain. (b) The slantwise transverse circulation ($v$, $w$) (vectors), wind speed (contours starting from 0 m s$^{-1}$ with an interval of 1 m s$^{-1}$), RH≥100% (light grey shading) at 9 hr. The lower panel shows the SCAPE (grey bar shows the current value while the solid grey line shows the initial value; J kg$^{-1}$), recorded at the location where the sloped $M_g$ surface intersects the ground. (c) Same as (b) but for 21 hr.

horizontal and vertical extents of the slantwise updraught are similar for $\Delta y = 1$, 2, 5 and 10 km. However, one obvious difference exists: instead of having one linearly tilted band in $\Delta y = 10$ km, an embedded quasi-upright cell develops at $y \sim 450$ km and $z = 1.5$–4 km for $\Delta y \leq 5$ km, breaking the slantwise band into two segments. Above this cell, the slantwise band continues to ascend with a gentler slope.

While the transient 99th percentile vertical velocity increases with finer horizontal grid

finer-gridded simulations (not shown). Moreover, despite the doubled width of the initial perturbations, the developed slantwise band has similar width and thickness to the one with original $R$.

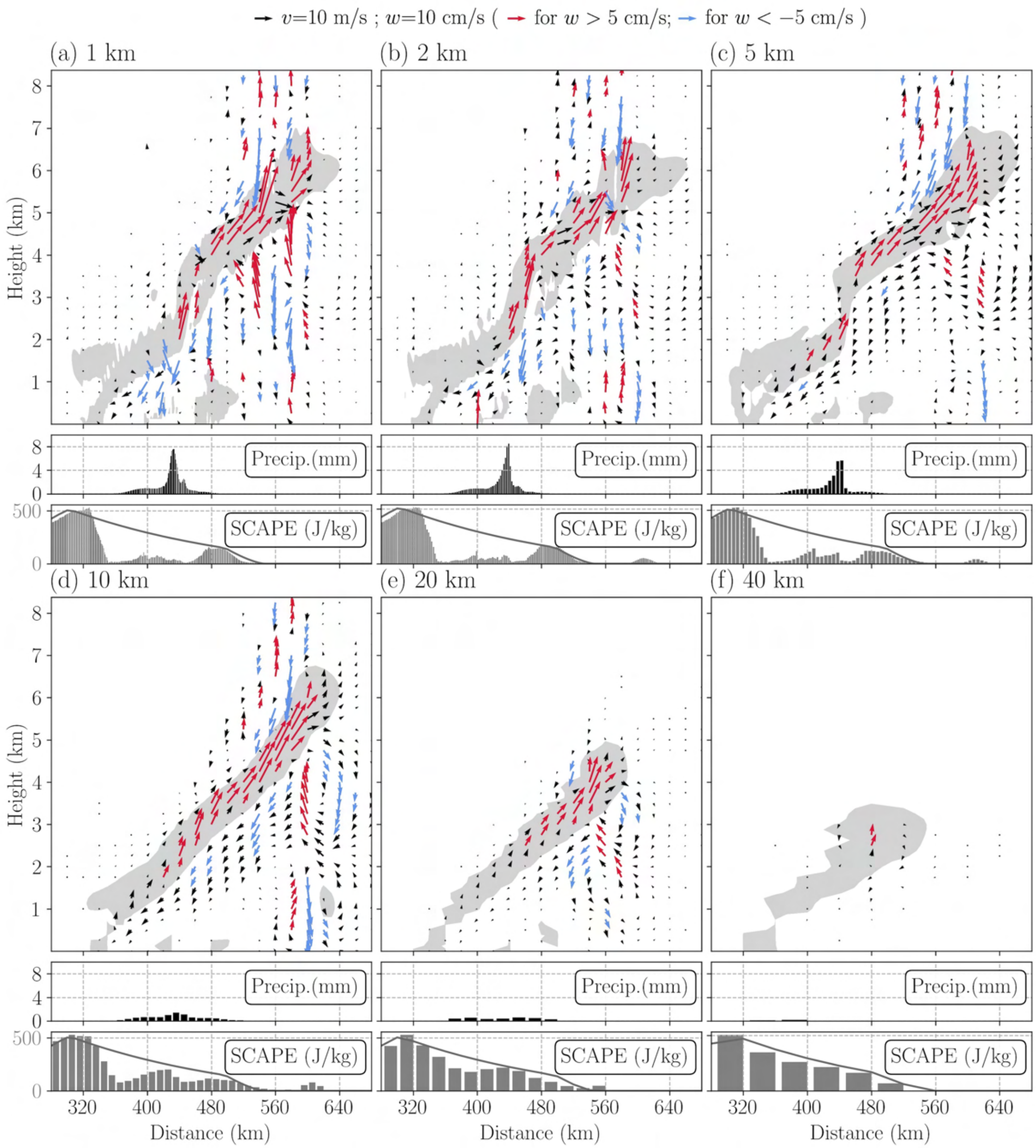


**Fig. 4.3**: The slantwise convection for $\Delta y$ of (a) 1 km, (b) 2 km, (c) 5 km, (d) 10 km, (e) 20 km and (f) 40 km, at 16 hr. The uppermost panel shows areas with RH $\leq$ 100% (light grey shading) and the transverse circulation ($v$, $w$) (vectors; strong ascent with $w > 5$ cm $s^{-1}$ and descent with $w < -5$ cm $s^{-1}$ are marked in red and blue, respectively). The lower two panels show the accumulated precipitation (black bars; mm) and SCAPE (grey bars; J $kg^{-1}$), respectively, and the latter is shown at the location where the $M_g$ intersects the ground.

spacing (Fig. 4.4a), the bulk features converge numerically at $\Delta y \leq 5$ km. These include the SCAPE consumption, accumulated precipitation and 48-hour averaged upward zonal momentum flux (Fig. 4.4b–d). For $\Delta y \leq 5$ km, around 100 J kg$^{-1}$ of averaged SCAPE is consumed by 24 hr, and the domain-averaged accumulated precipitation reaches 0.4 mm by 30 hr. In contrast, the 10 km simulation shows much smaller effects (50 J kg$^{-1}$ of SCAPE consumption and 0.2 mm of precipitation by 24 and 30 hr, respectively; Fig. 4.4b,c). The vertical profile of zonal momentum flux reflects an important large-scale feedback of the slantwise convection in baroclinic environments (Fig. 4.4d); the generally negative values indicate upward transport of the low zonal momentum and downward transport of high zonal momentum by the slantwise circulation. Simulations with coarser grid spacings exhibit a peak momentum flux at lower altitudes with smaller magnitudes than the finer-gridded runs. As numerical bulk convergence is reached at $\Delta y = 5$ km, a robust peak magnitude of momentum flux of around $-1.5 \times 10^{-2}$ kg m$^{-1}$ s$^{-2}$ forms at $z = 4.5$ km. The above results suggest that while $\Delta y = 10$ km is sufficient to simulate the general structure of the slantwise convection, the embedded quasi-upright convective cell that initiates at around 5 hr for finer grid spacings may have significant impacts on the larger-scale environment, thus affecting whether or not the bulk properties numerically converge. Below we present evidence showing how the convective cell develops in an initially moist statically stable environment, how it then affects the slantwise band and the larger-scale environment differently between $\Delta y = 10$ km and $\leq 5$ km runs.

### 4.4.2 Dynamical origin of the upright convection

The air parcel (tube) theory indicates that CSI can be released only if a finite-amplitude forcing is applied along a gentler angle than the sloped $\theta_e^*$ surfaces. Thus, positive $\theta_e^*$ advection must accompany the early initiation of the slantwise updraught. Although $\theta_e^*$ is not

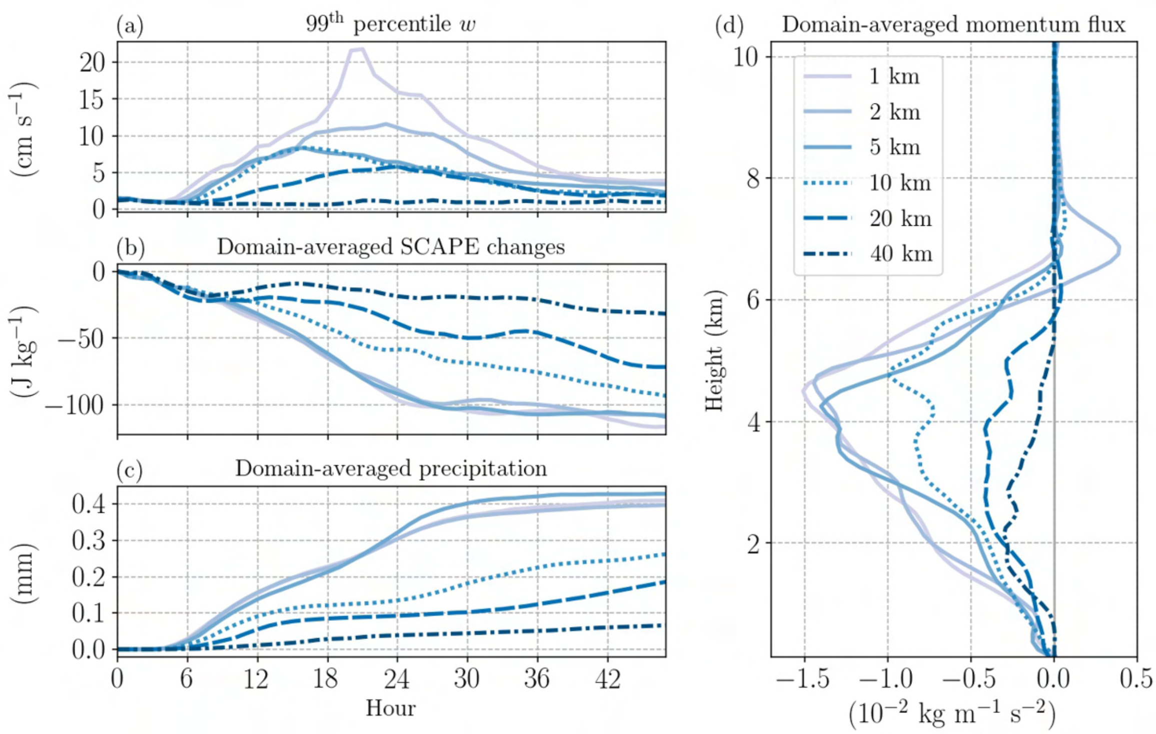


**Fig. 4.4**: The time evolution of the (a) 99th percentile vertical velocity of the domain, (b) domain-averaged SCAPE difference from the initial time, and (c) domain-averaged precipitation. (d) The 48 hr and domain-averaged zonal momentum flux for experiments with different horizontal grid spacings as indicated in the legend. The area used for these calculations is bounded by $y = 200$ and 1,000 km.

a prognostic variable, we have added an in-line calculation for $\theta_e^*$ to WRF so that the $\theta_e^*$ advection can be estimated using the model's advection operator and the local $\theta_e^*$ tendency can be calculated in-line (Chen et al., 2020). Because $\theta_e^*$ is only conserved for reversible moist adiabatic process in a saturated flow, irreversible processes (e.g., precipitation, mixing, etc.) and diabatic processes can regulate its distribution. Nevertheless, Fig. 4.5 shows that the advection still dominates the local tendency, at least in the vicinity of the slantwise band.

During the early development of the slantwise convection, the differential advection of $\theta_e^*$ between the updraught and the surrounding environment renders $\theta_e^*$ surfaces buckled (i.e. distorted) locally (Fig. 4.5c,d), leading to the formation of conditional instability (i.e. $\frac{\partial \theta_e^*}{\partial z} <$

0) (e.g., Bennetts and Hoskins, 1979; Bennetts and Sharp, 1982; IC92; PW95). A shallow layer of conditional instability develops above the maximum ascent by 5 hr (Fig. 4.5c-d). As the slantwise band extends upward, the updraught penetrates this conditionally unstable layer, which splits into two at about 7 hr (not shown). While the conditionally unstable layer remains intact for $\Delta y = 10$ km at later times, it breaks up into small scattered patches in $\Delta y \leq 5$ km with stronger $w$, indicating a stronger release of conditional instability in the latter (Fig. 4.5g-h; similar features shown for $\Delta y = 5$ km are also observed for $\Delta y < 5$ km). Note that at 9 hr, strong $\theta_e^*$ tendencies with opposite signs stacking below the head of the slantwise band likely reflect the inertia-gravity waves triggered by the slantwise convection,

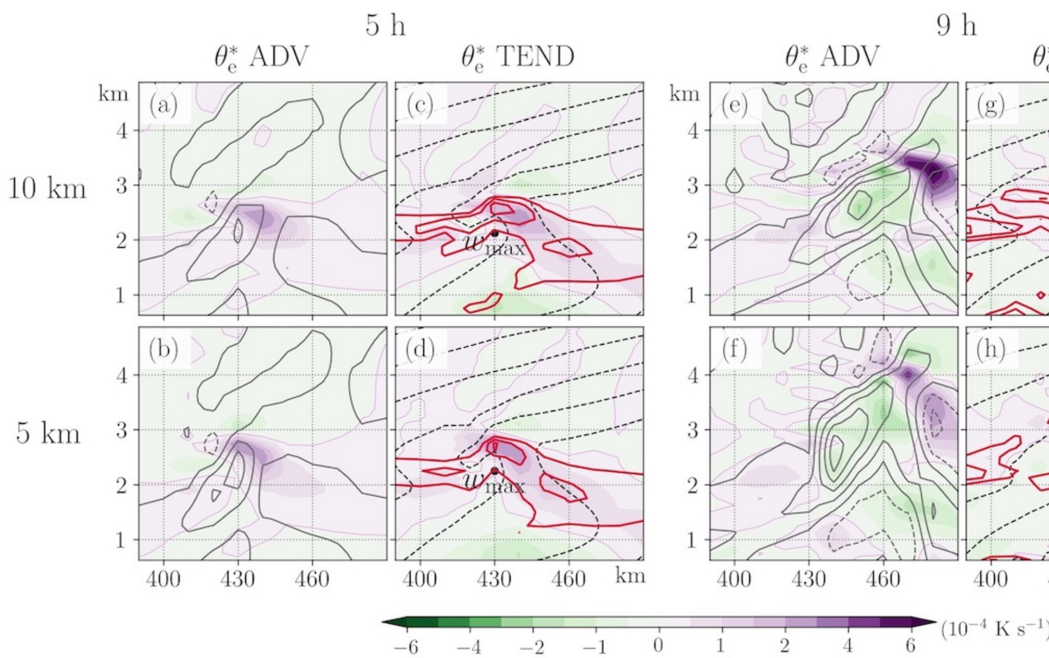


**Fig. 4.5**: The estimated $\theta_e^*$ advection (shading) and $w$ (grey solid and dashed lines indicate the positive and negative values with an interval of 5 cm s$^{-1}$, respectively) for (a) $\Delta y =$ 10 km and (b) $\Delta y = 5$ km, at 5 hr. The concurrent local $\theta_e^*$ tendency (shading), $\theta_e^*$ (black dashed contours) and the conditional instability, that is, $\frac{\partial \theta_e^*}{\partial z} < 0$, (red solid contours with an interval of -1 $\times 10^{-3}$ K m$^{-1}$) are shown in (c) for $\Delta y = 10$ km and in (d) for $\Delta y = 5$ km. The location ofmaximum w is also noted. (e–h) The same as (a–d), respectively, but at 9 hr. For $\Delta y = 5$ km, all fields are averaged onto the same 10 km grid to smooth out the smaller-scale noise.

forming in response to weak ageostrophy in a sheared environment (Fig. 4.5g-h; PW95; Huang, 1991). Despite the transient large magnitudes, these waves do not have long-lasting impacts locally as the environment recovers after they propagate away (not shown).

The in-line budget analysis of $w$ tendency (4.5) shows that the positive $\mathrm{PGBUOY}_w$ along the slantwise ascent is already slightly stronger and wider for $\Delta y \leq 5$ km than for $\Delta y = 10$ km at 5 hr (not shown). This term represents the transient imbalance between the buoyancy and vertical gradient of pressure perturbation, indicating the non-hydrostatic forcing. While the $\mathrm{PGBUOY}_w$ is maximized at about 1.5 $\times 10^{-5}$ m s$^{-2}$ for $\Delta y = 10$ km, $\Delta y \leq 5$ km exhibits peak values of above 6.5 $\times 10^{-5}$ m s$^{-2}$ at 7 hr (Fig. 4.6d–f; note that the budget analysis for $\Delta y = 2$ km is also presented to help access the degree of numerical convergence for $\Delta y \leq 5$ km). By 9 hr, the maximum $\mathrm{PGBUOY}_w$ in $\Delta y \leq 5$ km is 10 times larger than that in $\Delta y = 10$ km over the area where conditional instability previously existed (not shown). It is a well-known relationship that stronger $\mathrm{PGBUOY}_w$ develops at smaller $\Delta y$ because, for a given buoyancy, the opposing vertical PGF weakens as the scale of the circulation contracts, leading to stronger non-hydrostatic acceleration. This can be inferred from the linear dispersion relation (Orlanski, 1981), which shows that given the same degree of convective instability, the growth rate of the unstable waves increases with reducing $\Delta y$ in the mesoscale for $H/\Delta y \lesssim 1$, where $H$ is the vertical scale of the motion. In the present case, although $\Delta y = 10$ km captures the overturning of $\theta_e^*$ surfaces [Fig. 4.5c; also for $\Delta y =$ 20 km (not shown)], such $\Delta y$ is too coarse to allow the instability to grow at a realistic rate. Notably, even without adequately resolving the transient non-hydrostatic forcing for the embedded convective cell, $\Delta y = 10$ km still reasonably captures the overall feature of the slantwise band (Fig. 4.3d). This indicates that the hydrostatic forcing (buoyancy) is still highly dominant for the general slantwise convection, with buoyancy [O($10^{-2}$ m s$^{-2}$); not shown] being three orders of magnitude larger than the non-hydrostatic forcing even for $\Delta y \leq 5$ km. The non-hydrostatic forcing is weak, as one would expect given the shallow and weak conditional instability, but is nevertheless responsible for accelerating the embedded convective cell differently between fine-gridded and coarse-gridded simulations.

For $\Delta y \leq 5$ km, the major upright convection persists until $\sim 24$ hr but is confined to low levels even at later stages of the slantwise convection development (not shown). This is because the layer with $\mathrm{MPV}_{\mathrm{g}}^{*} < 0$, that is, where $\theta_{\mathrm{e}}^{*}$ surfaces are steeper than $M_{\mathrm{g}}$ surfaces,

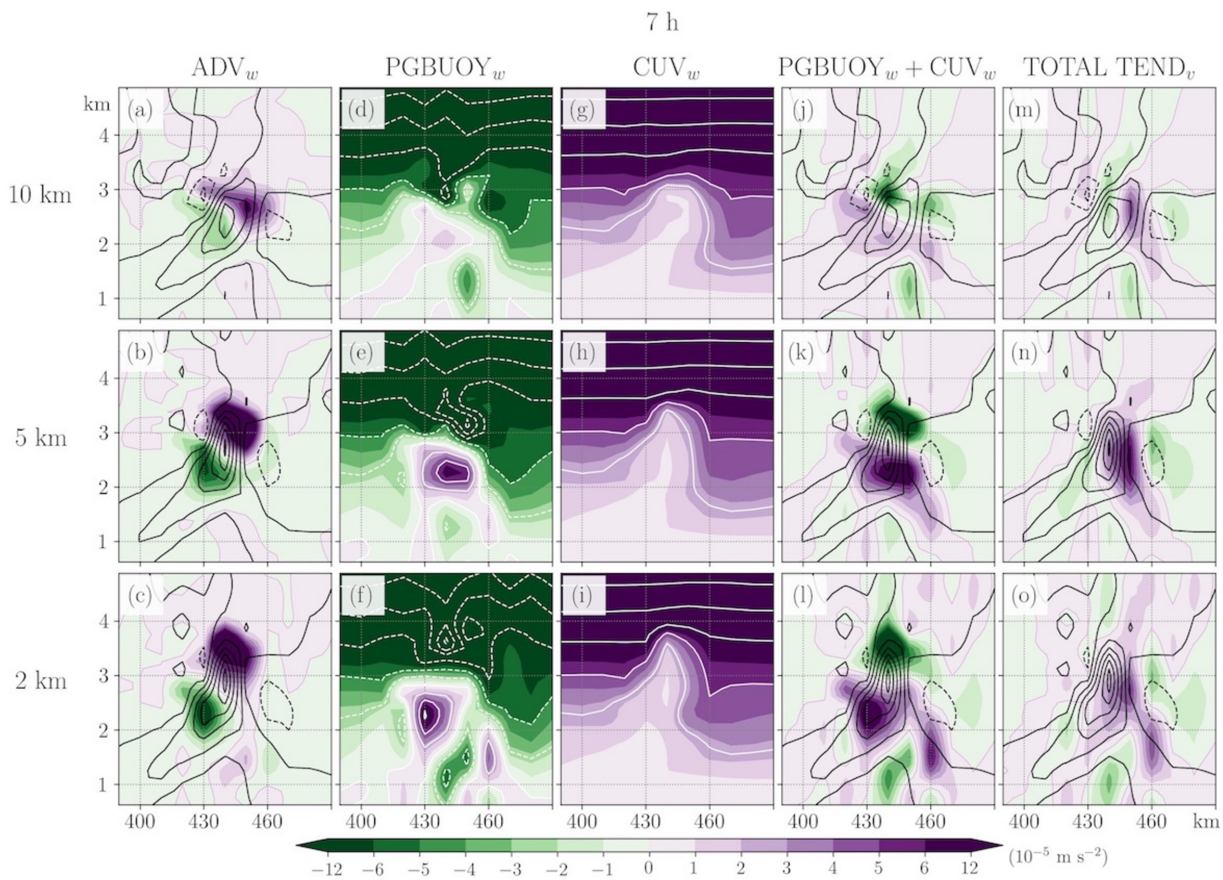


**Fig. 4.6**: In-line budget analysis of $w$ at 7 hr. Each shaded panel from left to right shows the (a–c) advection ($\mathrm{ADV}_w$), (d–f) net vertical pressure gradient and buoyancy force ($\mathrm{PGBUOY}_w$), (g–i) curvature ($\mathrm{CUV}_w$) (solid and dashed white contours indicate positive and negative values, respectively, with an interval of 2.5 $\times 10^{-5}$ m s$^{-2}$), (j–l) the net force of $\mathrm{PGBUOY}_w$ and $\mathrm{CUV}_w$ [ (4.5); the damping term is small and thus not shown], and (m–o) the total tendency. All terms have a uniform unit of m s$^{-2}$. The top, mid- and bottom rows are for runs with $\Delta y = 10$, 5 and 2 km, respectively. The black contours indicate w with an interval of 5 cm s$^{-1}$ (positive and negative values shown in solid and dashed lines, respectively). For $\Delta y \leq 5$ km, all fields are averaged onto the same 10 km grid.

does not extend beyond 4 km (Fig. 4.1b). Thus, although the slantwise band continues to grow upward at the expense of SCAPE, the slope of the ascent becomes parallel and even steeper than the surrounding $\theta_e^*$ surfaces, and thus the associated $\theta_e^*$ advection does not lead to strongly buckled/overturned $\theta_e^*$ contours at upper levels.

### 4.4.3 Early-staged evolution of the slantwise circulation

To obtain a more comprehensive picture of the evolution of $w$ in slantwise convection, other contributing processes in (4.5) must also be examined (Fig. 4.6). This section focuses on the early stage of the slantwise development before 9 hr. While strongly positive $\mathrm{PGBUOY}_w$ mainly occurs over the upright convective core, the Earth-surface curvature ($\mathrm{CUV}_w$) is positive everywhere with increasing values with height. $\mathrm{CUV}_w$ is dominated by the (re-)distribution of zonal momentum, and so areas with small values extend upward as the growing slantwise band, which do not show an obvious sensitivity to $\Delta y$ (Fig. 4.6g–i). Meanwhile, the advection term ($\mathrm{ADV}_w$) shows differences as early as 4 hr, with the $\Delta y = 10$ km case exhibiting generally weaker magnitudes and a maximum located more northward rather than upward than for $\Delta y \leq 5$ km (e.g., Fig. 4.6a–c). These differences increase with time as the updraught core intensifies more strongly with a more vertically tilted axis, leading to stronger horizontal gradient of $w$ and thus stronger $\mathrm{ADV}_w$ for $\Delta y \leq 5$ km. $\mathrm{ADV}_w$ generally reaches the same order of magnitude but with opposite signs as the net driving force of $\mathrm{PGBUOY}_w + \mathrm{CUV}_w$ (Fig. 4.6a–c, j–l). The combined total tendency thus has peak values shifted northward and upward from where the $\mathrm{PGBUOY}_w + \mathrm{CUV}_w$ is largest, indicating the upward and northward propagation of the developing slantwise band (Fig. 4.6m–o).

The dynamical sensitivities to the grid spacing are also reflected in the meridional motions, in which the inertial force ($\mathrm{PGF}_v$+$\mathrm{COR}_v$) is crucial in driving slantwise convection.

In the initially geostrophically balanced background flow, $\mathrm{PGF}_v$ and $\mathrm{COR}_v$ point north (i.e. positive) and south (i.e. negative), respectively (Fig. 4.7d–i). The initial introduction of a negative $u$ perturbation causes $\mathrm{COR}_v$ to no longer fully oppose $\mathrm{PGF}_v$, which gives rise to a positive acceleration to the north. During the continuous release of CSI, such positive inertial forces are sustained over time, expand in area, and strengthen locally, fuelling the $v$ circulation for several hours (Fig. 4.7j–l). This is largely owing to the slantwise ascent transporting smaller $u$ from lower levels upward and thus locally reducing the magnitude of $\mathrm{COR}_v$ (i.e. $fu$) along the sloped updraught (Fig. 4.7g–i). Such a self-maintainingmechanism has been documented in past studies (e.g., IC92; PW93).

Although the evolution of $\mathrm{PGF}_v$ in slantwise convection has not been extensively studied, it shows a larger sensitivity to $\Delta y$ than does $\mathrm{COR}_v$ (Fig. 4.7d–f). IC92 considered that warming via positive $\theta_e^*$ advection and the condensational heating would lead to a local hydrostatic pressure drop maximized in the central part of the updraught. This pressure change would result in a pair of $\mathrm{PGF}_v$ anomalies that act in the opposite direction, slightly reducing and reinforcing the northward acceleration on the northern and southern half of the band, respectively. They view this pair of $\mathrm{PGF}_v$ anomalies as responsible for the observed slow drift of the slantwise updraught toward the warmer side of the domain while the parcels themselves move toward the north. However, our in-line-budget-retrieval results show a much more complicated quantitative picture than the conceptual one in IC92.

Generally speaking, $\mathrm{PGF}_v$ contributes negatively to the evolution of inertial force as the area with weakening (i.e. less positive) $\mathrm{PGF}_v$ extends upward as the band grows (Fig. 4.7d–f). Comparing the distribution of $\mathrm{COR}_v$ and $\mathrm{PGF}_v$ suggests that the sustaining positive inertial force over the slantwise ascent is mainly due to the less-negative $\mathrm{COR}_v$ overpowering the less-positive $\mathrm{PGF}_v$ (Fig. 4.7d–l). However, the broadly distributed $\mathrm{PGF}_v$ can have dominant effects outside of the slantwise ascent. Specifically, $\mathrm{PGF}_v$ exhibits weaker values over a wide isosceles-triangular region covering from the top of slantwise band to the surface, and so a negatively tilted patch of negative inertial force develops below the band (e.g., Fig. 4.7d–f, j–l). This explains the deeper and more intense return flow in the lower flank than the upper side of the slantwise convection (Fig. 4.2). To the north of the triangular top, strong $\mathrm{PGF}_v$ overpowers $\mathrm{COR}_v$, leading to positive inertial force enhancement that helps the upper-northern part of the slantwise band accelerate

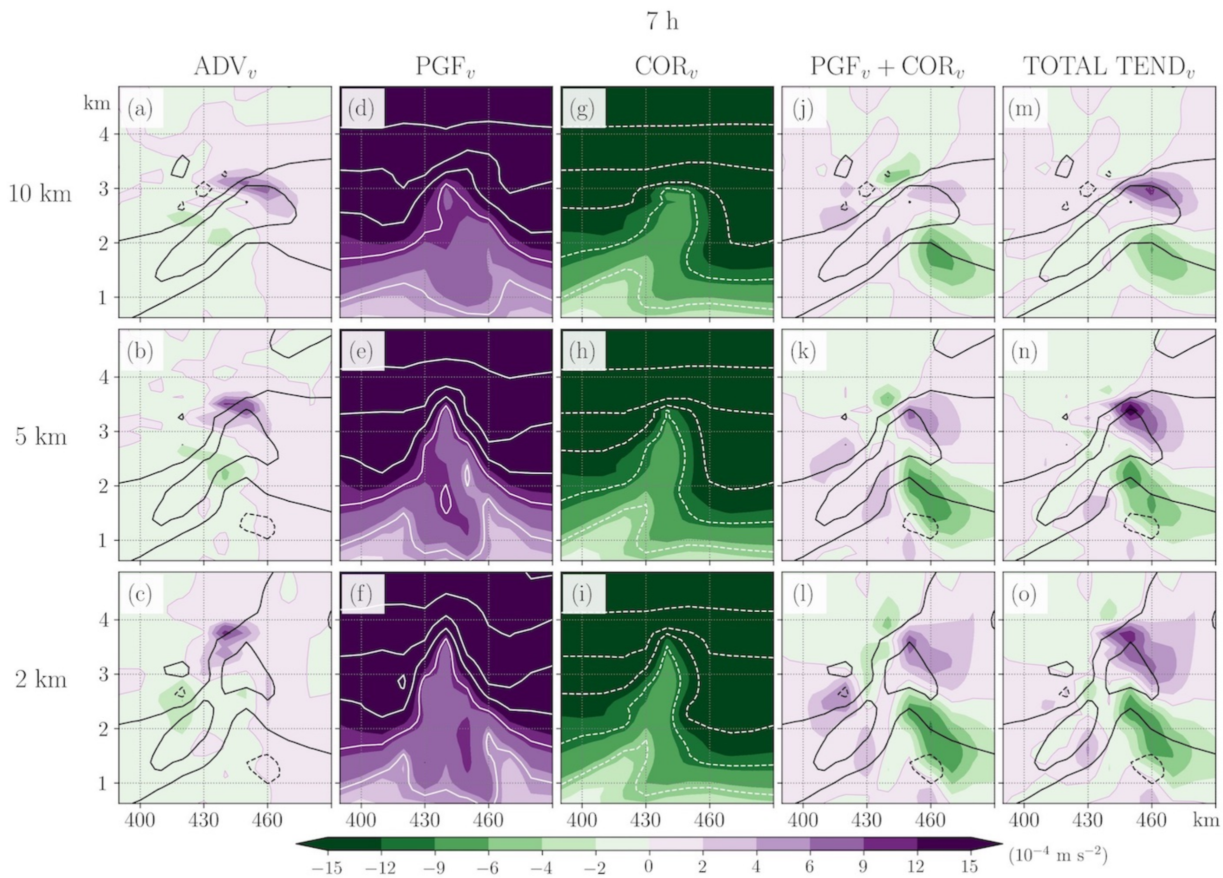


**Fig. 4.7**: In-line budget analysis of $v$ at 7 hr. Each shaded panel from left to right shows the (a–c) advection ($\mathrm{ADV}_v$), (d–f) horizontal pressure gradient force ($\mathrm{PGF}_v$), (g–i) Coriolis force ($\mathrm{COR}_v$) (solid and dashed white contours indicate positive and negative values, respectively, with an interval of 5 $\times 10^{-4}$ m s$^{-2}$), (j–l) the net force of $\mathrm{PGF}_v$ and $\mathrm{COR}_v$ [(4.4); the curvature term ($\mathrm{CUV}_v$) is small and thus not shown], and (m–o) the total tendency. All terms have a uniform unit of m s$^{-2}$. The top, mid- and bottom rows are for runs with $\Delta y = 10$, 5 and 2 km, respectively. The black contours indicate $v$ with an interval of 2 m s$^{-2}$ (positive and negative values shown in solid and dashed lines, respectively). For $\Delta y \leq 5$ km, all fields are averaged onto the same 10 km grid.

northward.

Compared to $\Delta y = 10$ km, the $\text{PGF}_v$ feature in $\Delta y \leq 5$ km is more pronounced, exhibiting a more vertically oriented spatial distribution with smaller values reaching higher altitudes and a slightly stronger $\text{PGF}_v$ to its north (Fig. 4.7d–f). On one hand, the negatively tilted negative inertial force can penetrate the $v$ core, tending to break the $v$ contours into two segments across the convective cell. This results in a detached instead of linearly tilted slantwise band at finer grids (Fig. 4.3). On the other hand, the locally stronger $\text{PGF}_v$ accelerates $v$ of the detached upper band much more so for $\Delta y \leq 5$ km than for $\Delta y = 10$ km (Fig. 4.7j–l). To sum up, the weakening of the south-pointing $\text{COR}_v$ is critical for sustaining and accelerating the northward motion over the slantwise ascent region as the north-pointing $\text{PGF}_v$ is generally weakening there. Meanwhile, the localized strengthening $\text{PGF}_v$, especially to the north of the $w$ core (Figs. 4.6a–c and 4.7d–f), accelerates and extends the upper-northern part of the slantwise band northward. While the $\text{COR}_v$ evolution does not show a significant grid-spacing sensitivity at the early stage, the $\text{PGF}_v$ effect becomes more pronounced at finer grids.

### 4.4.4 Maintenance of the slantwise band and its large-scale feedbacks

As upright convection lasts, it transports more low zonal momentum upwards and thus increases the imbalance between $\text{PGF}_v$ and $\text{COR}_v$ at upper levels while the inertial force weakens at lower levels (Fig. 4.8). A locally strengthened inertial force above the upright convection has been observed over both squall lines and frontal regions (Zhang and Cho, 1992; Browning et al., 2001a). Here, the apparently stronger inertial force over the upper slantwise band in $\Delta y \leq 5$ km (relative to the $\Delta y = 10$ km case) lasts until 20 hr, causing $v$ contours with gentler slopes there.

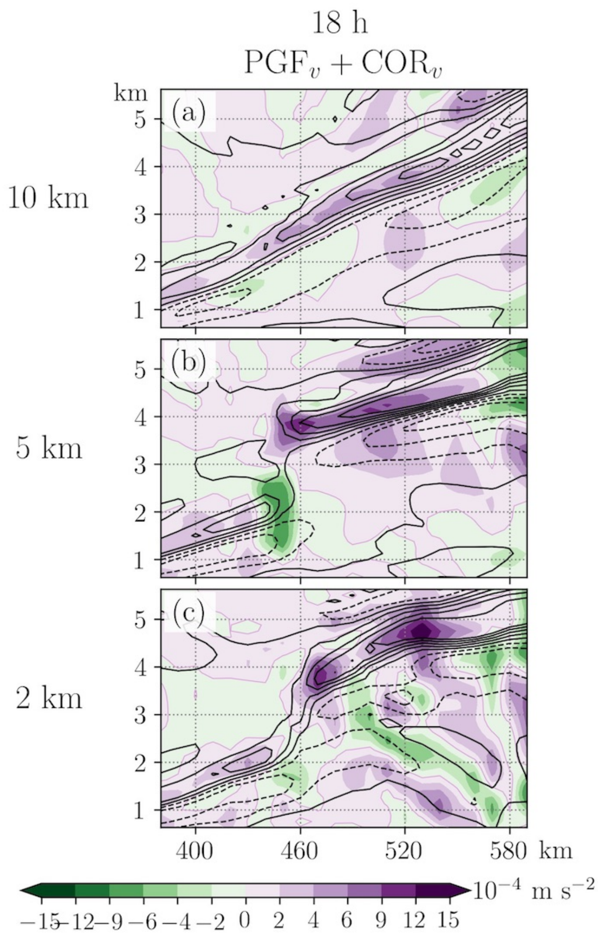


**Fig. 4.8**: The net force of $\mathrm{PGF}_v$ and $\mathrm{COR}_v$ (shading) for $\Delta y =$ (a) 10 km, (b) 5 km, and (c) 2 km runs at 18 hr. The black contours indicate $v$ with an interval of 2 m s$^{-1}$ (solid for positive and dashed for negative values). For $\Delta y \leq 5$ km, all fields are averaged onto the same 10 km grid.

Having examined the detailed dynamics during the evolution of slantwise convection, we return to their links to the large-scale feedbacks. Recalling Fig. 4.4, a question remains as to how exactly does the better-resolved upright-convection-associated features in $\Delta y \leq$ 5 km contribute to the faster and stronger neutralization of CSI, that is, larger release of environmental SCAPE, hence leading to larger precipitation and vertical momentum fluxes than the coarser-gridded simulations. Although both $\theta_e^*$ and $M_g$ surfaces become buckled locally during the development, the later state when the CSI circulation is about to cease shows that the slopes of the $\theta_e^*$ surfaces change more than those of the $M_g$ surfaces from their initial states (Fig. 4.9). The $\theta_e^*$ surfaces become flattened not only over the region traversed by the slantwise band but also in the column below. In the example given in Fig. 4.9, for an air tube lifted from the surface at $y \sim 400$ km, the flattened $\theta_e^*$ surfaces become increasingly parallel to the $M_g$ surfaces over time and lower the LSNB by 1–2 km by 24 hr. These factors lead to a smaller surface integral between the $\theta_e^*$ and $M_g$ surfaces at the later time, and thus smaller SCAPE for air tubes initialized at the same near-surface location.

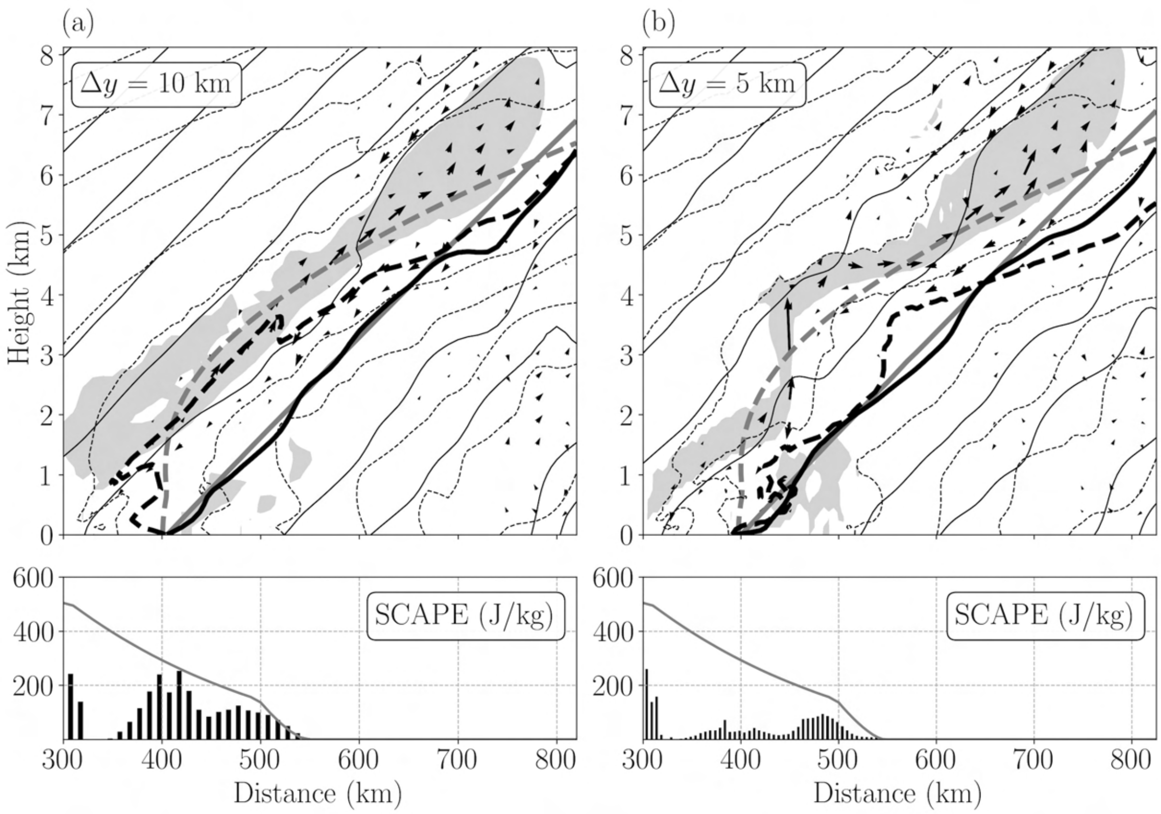


**Fig. 4.9**: Conditions after the CSI adjustment at 24 hr for $\Delta y =$ (a) 10 km, (b) 5 km. The upper panel shows the transverse circulation $(v, w)$ (vectors), the $M_g$ (solid) and $\theta_e^*$ surfaces (dashed), RH≥100% (light grey shading). Thick solid and dashed lines in the upper panel indicate the $M_g$ and $\theta_e^*$ surfaces corresponding to air tubes lifted from near the surface at $y$ ∼400 km at the initial time (dark grey) and 24 hr (black), respectively. The lower panel shows the SCAPE (bar indicates the current value while solid line shows the initial value; J kg$^{-1}$) at the location where the $M_g$ intersects the ground.

The more parallel $\theta_e^*$ and $M_g$ surfaces in $\Delta y \leq 5$ km than $\Delta y = 10$ km are especially noticeable at low levels. While both $\Delta y \leq 5$ km and $\Delta y = 10$ km capture the strong $\theta_e^*$ increase over the lower flank of the slantwise band as some cross-$\theta_e^*$ return flow brings the higher-$\theta_e^*$ downward, enhanced low-level warming only occurs in $\Delta y \leq 5$ km (Fig. 4.10). This warming is caused by the continuous positive vertical $\theta_e^*$ advection due to the descending flow associated with the resolved upright convection (Fig. 4.10d-e). Meanwhile, for $\Delta y = 10$ km, the sloped downdraught becomes mostly parallel to the surrounding $\theta_e^*$ surfaces at low-to-middle levels (Fig. 4.10a-b). While the evaporative cooling of precipitation partially offsets the warming in the lowest 2 km, a patch of positive $\theta_e^*$ anomaly

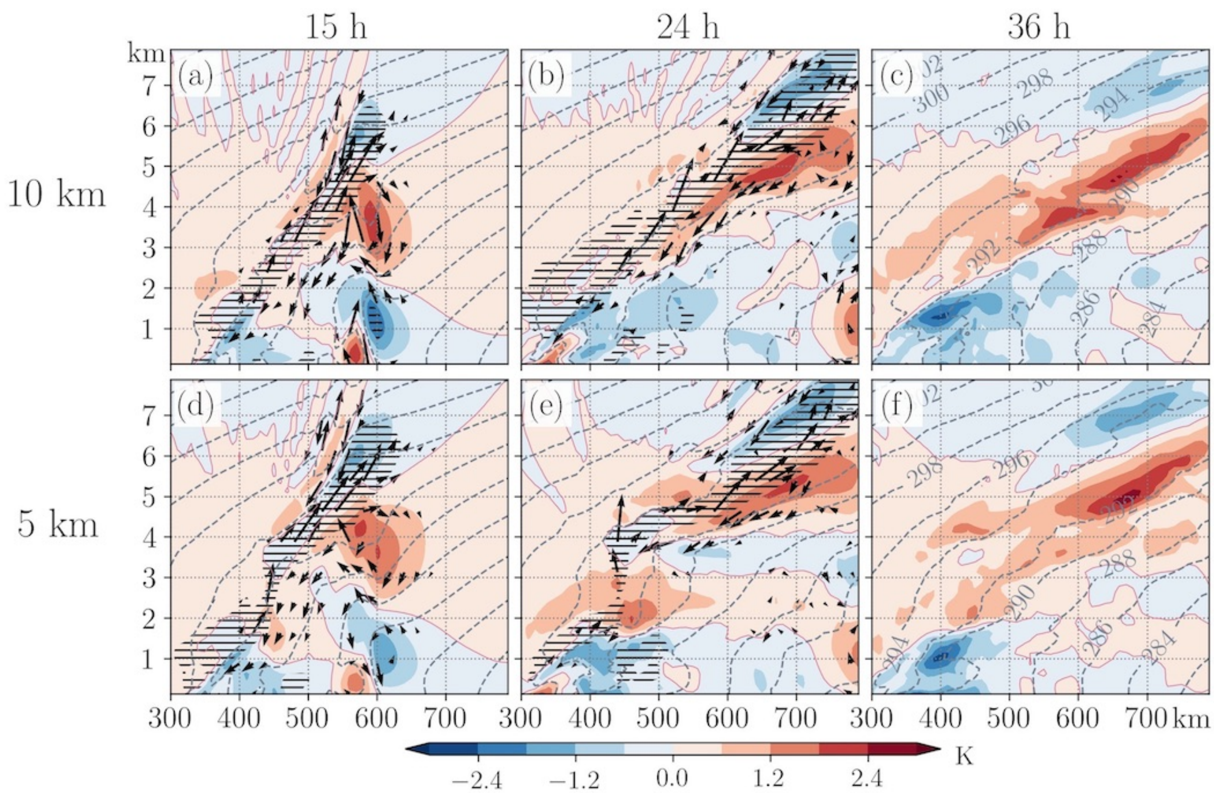


**Fig. 4.10**: The $\theta_e^*$ (dashed contours) and the $\theta_e^*$ deviation from its initial field (shading) at (a) 15 hr, (b) 24 hr and (c) 36 hr, for $\Delta y = 10$ km. For earlier times (a–b), the transverse circulation ($v$, $w$) is also shown (vectors). Areas with RH≥100% are hatched with horizontal black lines. (d–f) The same as (a–c) but for $\Delta y = 5$, whose fields shown here are averaged onto the same 10 km grid.

persists between 1.5∼3 km in $\Delta y \leq 5$ km even after the upright convection weakens (Fig. 4.10e-f). Thus, adequately resolving upright convection formed by the early-stage slantwise motion can have a major impact on the CSI release and corresponding moist-symmetric stabilization.

## 4.5 Additional sensitivity tests and potential limitations

### 4.5.1 Vertical grid spacing

Because the local thickness of the slantwise band can be small in a convectively stable environment (as shown here and in PW93), a high vertical resolution is needed to adequately resolve it. PW93 suggested $\Delta z \leq 170$ m and we used $\Delta z \leq 125$ m for all simulations. Another issue worthy of consideration is that when the horizontal and vertical grid spacings are not changed consistently, spurious gravity waves, appearing as short-wavelength variations, might be generated (PW91). This is particularly important for simulating a narrow sloping thermal feature because resolving the slope depends on the ratio of $\Delta y$ and $\Delta z$, which may result in a discontinuous "stairs-like" feature that introduces perturbations into the mass field (Lindzen and Fox-Rabinovitz, 1989). Huang's (1991) numerical study on slantwise convection with a fixed $\Delta y = 10$ km but different vertical grid spacings also supports this finding. PW91 proposed the following guideline to mitigate such effects:

$$\mathrm{AS} \leq 1 \quad \text{where} \quad \mathrm{AS} \equiv \frac{\Delta p/\Delta y}{s}, \tag{4.7}$$

$\Delta p$ and $\Delta y$ are the vertical (in pressure coordinates) and horizontal grid lengths, respectively, and $s$ is the slope of the slantwise/frontal structure on ($p$, $y$) coordinates. In our simulations, (4.7) is satisfied for all the simulations with $\Delta y \geq 5$ km.

To test whether our finer-gridded simulations are affected by the inconsistent horizontal and vertical grid lengths, we carried out additional simulations with an increased vertical resolution to 320 and 640 levels for $\Delta y = 2$ and 1 km, respectively (both result in an AS ∼0.96, as in the 5 km run). In those simulations, the convective features within the slantwise updraught do not change significantly and the fields sometimes appear even noisier outside of the primary band than for their coarser vertically gridded counterparts. The inconsistency between this result and those of PW91 and Huang (1991) may be caused by other factors (physical and/or spurious) that were absent in both past studies with a horizontal resolution of 10 km, namely increased upright convection owing to the buckling of $\theta_e^*$ surfaces and the presence of non-hydrostatic dynamics.

### 4.5.2 Tests with cumulus parametrization schemes

Our results suggest that the ability to resolve embedded upright convection has important impacts on the CSI neutralization process. It is therefore of interest to know whether the inclusion of available parametrization schemes for upright convection can bring the $\Delta y = 10$ km simulation closer to the converged results for $\Delta y \leq 5$ km. Two different convective schemes are tested. In a 10 km-simulation with the Kain–Fritsch scheme (Kain, 2004), the deep convection parametrization is never activated due to the shallowness of the convective layer. Another test for $\Delta y$ =10 km uses the Tiedtke scheme (Zhang et al., 2011), which shows a minor enhancement in the total precipitation starting from the beginning of the simulation, but it does not appear to be physically associated with the slowly developing slantwise band as simulated in $\Delta y = 5$ km (not shown). The rest of the bulk properties (i.e. SCAPE and upward momentum flux) also do not change significantly (not shown). These results suggest that, although the upright convective cell is the key feature differentiating the coarser- and finer-gridded simulations, the use of existing upright convective parametrizations at coarser resolution does not necessarily improve the representation of this feature.

### 4.5.3 Generality of the embedded upright convection

Although the results presented herein are derived from a single idealized set-up, embedded upright convective cells are believed to be general features during the development of slantwise convection. The parcel (tube) theory guarantees that CSI release must be accompanied by some degree of positive $\theta_e^*$ advection. Whether this advection can induce the overturning of $\theta_e^*$ surfaces, i.e. $\frac{\partial \theta_e^*}{\partial z} < 0$, depends on the environmental stability and the strength and vertical slope of the circulation. For weaker stabilities and stronger ascent rates, both of which are associated with more intense and meteorologically significant slantwise bands, the probability of this overturning is particularly high. The formation of convective instability above a developing slantwise band has been extensively documented in both observational and numerical studies (e.g., Bennetts and Hoskins, 1979; Bennetts and Sharp 1982; Thorpe and Clough 1991; IC92; PW95).

### 4.5.4 Limitations of the 2D framework

Strictly speaking, symmetric instability theory is applicable only to two-dimensional flow. However, real-world slantwise bands have 3D structures such as a finite length and some variability along the direction of symmetry (the thermal wind direction; $x$), partially due to the chaotic nature of atmosphere with turbulence, non-symmetric environmental conditions, etc. Jones and Thorpe (1992) investigated the 3D nature of slantwise band by considering two possible situations in a 3D model: (a) the region with CSI is assumed 2D, that is, extending infinitely along $x$, but the trigger to release the instability occurs only locally, or (b) the region that contains CSI has a finite length in $x$. Both scenarios result in circulations that gradually become more elongated in $x$, forming the quasi-linear but finite-length banded structure with some degrees of horizontal tilt/orientation from $x$. They found that the magnitude and direction of this tilt are associated with the viscous properties of the flow. Interestingly, the growth rate in scenario (b) depends on a ratio of the length of the CSI region in $x$ and the horizontal wavelength of the circulations in $y$ (along temperature gradient). The longer the CSI region is in $x$, the larger the corresponding slantwise growth rate. Thus, for CSI to occur in the 3D world, there exist minimum thresholds in both the width and length of the CSI region.

Other caveats in the 2D framework could arise from the deficiency of the 2D model in representing the realistic 3D physics. One example is that 2D models generally provide a poor representation of 3D atmospheric turbulence. Zhang and Cho (1995) conducted a 3D simulation of an Eady wave, building on an earlier 2D study of Knight and Hobbs (1988). They documented the differences introduced by the inclusion of the third spatial dimension, such as the curving features of the quasi-linear rain bands and their $8-10°$ deviations from the along-front (i.e. $x$) direction. Moreover, 2D models tend to simulate updraughts that lean downshear, leading to weaker growth of the slantwise band. They associated this problem to the unrealistic representation of divergence, vortex stretching, and tilting in 2D models when environmental wind shears are strong. Nevertheless, as in Jones and Thorpe (1992), their 3D simulated results conformed in many aspects to the CSI theory and its 2D interpretations.

## 4.6 Conclusions

Recent climatological studies have reinforced the potential global importance of slantwise convection, raising questions about whether large-scale models can resolve slantwise convection and under what conditions it should be parametrized. To address these questions, the present study simulates isolated free moist slantwise convection (the process by which conditional symmetric instability, or CSI, is released without continuous external forcings) in a baroclinic environment that is initially unstable to slantwise displacements but inertially and conditionally stable. The simulations are conducted in an idealized, non-hydrostatic, 2D ($y$–$z$ plane) framework with the Weather Research and Forecasting (WRF) model. The sensitivities of the slantwise convection to the horizontal (cross-band; along the temperature gradient) grid spacing ($\Delta y$; varied from 40, 20, 10, 5, 2 to 1 km) are examined to determine the necessary grid spacing to robustly capture the band dynamics and larger-scale feedbacks. While $\Delta y = 40$ and 20 km are too coarse to sustain the slantwise circulation, $\Delta y = 10$ km can reasonably capture its general feature, including the spatial extent (i.e. 400–500 km horizontally and 8 km vertically) and the time-scale to reach peak intensity. However, the slantwise-convection-associated large-scale impacts are found to converge numerically at $\Delta y \leq 5$ km. We utilize an in-line momentum-budget retrieval method to identify the dynamical processes that account most for the grid-spacing sensitivity.

We found that the key feature that differentiates the converged and non-converged bulk properties is closely related to a major upright convective cell that emerges within the slantwise band at low levels only for $\Delta y \leq 5$ km. The upright cell develops when the growing sloped updraught enters a shallow conditionally unstable layer, which forms at around 4–5 hr due to the strong positive $\theta_e^*$ advection by the developing slantwise ascent itself. The $w$-budget shows that $\Delta y \leq 5$ km can resolve the localized convective cell better, releasing conditional instability with an order-of-magnitude stronger non-hydrostatic force (i.e. imbalance between the vertical pressure gradient and buoyancy; $\mathrm{PGBUOY}_w$) than $\Delta y = 10$ km.

As for the horizontal flow of the slantwise band, the $v$ acceleration depends on the inertial force, that is, imbalance between the horizontal pressure gradient force ($\mathrm{PGF}_v$; initially positive toward the north) and the Coriolis force ($\mathrm{COR}_v$; initially negative toward the south). $\mathrm{COR}_v$ plays a self-sustaining role in the slantwise convection evolution as it becomes less negative with slantwise ascent transporting lower zonal momentum $u$ upward. While $\mathrm{COR}_v$ shows a relatively small grid-spacing sensitivity at the early stage, the changes of $\mathrm{PGF}_v$ exhibit a more complicated spatial distribution that becomes more distinctive at finer grids. On one hand, the widespread weakening $\mathrm{PGF}_v$ leads to a reversed inertial force extending to the surface which is responsible for the deep and intense return flow over the lower flank of the slantwise ascent. The weakening $\mathrm{PGF}_v$ at low levels can penetrate the slantwise ascent and break the $v$ contours across the embedded convective cell for $\Delta y \leq$ 5 km. On the other hand, the localized strengthening of $\mathrm{PGF}_v$ to the north of maximum updraught becomes more pronounced at finer grids, leading to a stronger northward acceleration and extension of the upper-level (detached) band than the coarser-gridded runs.

The resolved upright convection promotes a faster release of CSI. The embedded upright convective cell in finer-gridded simulations continuously transports more air with low $u$ upward, leading to a stronger inertial force that enhances the northward accelerations at upper levels. Moreover, the descending cross-$\theta_e^*$ flow associated with the upright convective cell strengthens the positive $\theta_e^*$ advection beneath the slantwise updraught, causing additional warming of $\theta_e^*$ at low levels for $\Delta y \leq 5$ km. This warming helps flatten $\theta_e^*$ surfaces to be closer to geostrophic absolute momentum ($M_\mathrm{g}$) surfaces and lower the level of slantwise neutral buoyancy, resulting in a larger consumption of slantwise convective available potential energy (SCAPE), that is, larger adjustment toward a slantwise-neutral state. Therefore, accumulated precipitation and the domain-averaged vertical momentum flux both increase in magnitude with decreasing $\Delta y$ until 5 km is reached. While this study shows that the smaller-scale upright convective processes can have significant impacts on the larger-scale environments, we reiterate that slantwise convection itself is still dominantly driven by the hydrostatic forcing (buoyancy; which is three orders of magnitude larger than the non-hydrostatic forcing), and therefore $\Delta y = 10$ km can still reasonably capture its general feature.

The current findings suggest that numerical models may not adequately resolve critical properties associated with the development of slantwise convection with a horizontal grid spacing coarser than around 5 km. Because slantwise convection can exist in an environment without CAPE (as shown herein), existing parametrizations for upright convection may not properly capture it. Thus, either these schemes should be adapted to account for slantwise convection and its larger-scale feedbacks, or new schemes for pure slantwise convection should be developed (e.g., Emanuel, 1983a; PW93; Schultz and Schumacher, 1999). A few studies (e.g., Lindstrom and Nordeng, 1992; Balasubramanian and Yau, 1995; Ma, 2000) have shown that inclusion of slantwise convective parametrization in numerical models improves forecasts of precipitation, jet, and/or cyclone intensity, but these schemes have not been commonly employed. Chang et al. (2013) and Zappa et al. (2013) compared the historical simulations from phases 3 and 5 of the Coupled Model Intercomparison Project (CMIP3 and CMIP5) with the reanalysis data, respectively, and both found significant biases in extratropical storm-track properties. Considering that slantwise convection is climatologically important in the midlatitudes (e.g., Glinton et al., 2017), particularly for rapidly deepening cyclones (Chen et al., 2018), implementing a slantwise convection parametrization in climate models may be beneficial for their general forecast skill.

# Chapter 5

# Parameterization of slantwise convection

The results from Chapter 4 suggest that models with a horizontal grid spacing coarser than 5 km may not adequately resolve important features associated with slantwise convection and may benefit from the parameterization of slantwise convection.

In this chapter, we implement a parameterization scheme for slantwise convection in the WRF model and evaluate its potential benefits for the coarse-gridded simulations. This slantwise convective parameterization scheme is based on Ma (2000), but we add some modifications to improve its physics to yield a better consistency with the high-resolution simulations. Two different cases are tested, including the same 2D idealized simulation for the pure CSI release shown in Chapter 4 and a 3D real-data case along a cold-frontal region that contains both CSI and conditional (static) instability (CI).

This chapter consists of a manuscript submitted to *Journal of Atmospheric Sciences*: Chen, T.-C., M. K. Yau, and D. J. Kirshbaum, 2021: A parameterization of slantwise convection in the WRF model. *J. Atmos. Sci.*, submitted.

# A parameterization of slantwise convection in the WRF model

TING-CHEN CHEN, MAN-KONG YAU, AND DANIEL J. KIRSHBAUM

*Department of Atmospheric and Oceanic Sciences, McGill University, Montreal, Quebec, Canada*

## Abstract

In this study, a parameterization scheme for slantwise convection (SC) is proposed and implemented in the Weather Research and Forecasting (WRF) model to supplement the existing cumulus parameterization schemes for upright convection. The SC scheme primarily applies momentum adjustments to render the environment symmetrically neutral by removing positive slantwise convective available potential energy within a prescribed adjustment timescale. Condensational heating caused by the slantwise updraft and the associated moisture loss are also parameterized. Unlike most of the cumulus parameterizations acting locally in 1D, the SC scheme acts on a 2D cross-section perpendicular to the local column-averaged thermal winds. We test the performance of the SC scheme using two different numerical setups: a 2D idealized, unforced simulation of the release of conditional symmetric instability (CSI) in an initially conditionally stable environment and a 3D real-data simulation of a banded precipitation event that contains both CSI and conditional instability along the cold front of the October 2000 storm near the UK. Both cases show significant improvements for the coarse-gridded (40-km) simulations when parameterizing slantwise convection. By comparing the runs with only the upright cumulus scheme and the one with both the upright and slantwise convection schemes, it is shown that the latter

exhibits a larger extent of CSI neutralization, generates a stronger grid-resolved slantwise circulation, and produces greater amounts of precipitation, all in better agreement with the fine-gridded reference simulations.

## 5.1 Introduction

The representation of convection is one of the most critical problems in numerical weather prediction (NWP). Although increasing computational capacity has allowed regional NWP systems toward convective scale (with a model grid spacing of a few kilometers or less), convection parameterization remains a necessary component, especially in global and climate models (Arakawa, 2004; Stensrud, 2007). Even with a grid spacing that is generally considered sufficient for explicit convection representation, e.g., 1-3 km, some operational NWP systems still employ convective/cumulus parameterizations schemes (CPS) to reduce bias in precipitation forecast (e.g., Milbrandt et al., 2016). Most of the commonly-employed CPS target deep vertical convection. Although additional components for different types of clouds (e.g., boundary-layer, shallow, and mid-level/elevated) are sometimes utilized, an often-missing element is slantwise convection. Because slantwise convection can occur in the absence of conditional instability (e.g., Emanuel, 1983b) with zero convective available potential energy (CAPE), CPS with a CAPE-based trigger and/or closure function may fail to trigger and/or underestimate the convective activity.

Slantwise convection results from conditional symmetric instability (CSI) being released in a baroclinic environment and is often observed near frontal regions (e.g., Thorpe and Clough, 1991; Browning et al., 2001a). It is one of the physical mechanisms for precipitation bands (Bennetts and Hoskins, 1979; Reuter and Yau, 1990, 1993) and may be related to sting jet formation (e.g., Gray et al., 2011; Baker et al., 2014; Schultz and Browning, 2017) and explosive cyclone development (e.g., Kuo et al., 1991; Reuter and Yau, 1993;

Balasubramanian and Yau, 1994a,b, 1995). Numerical studies suggested a lower limit of grid spacing of 5-15 km to properly capture the cross-band (mesoscale) features associated with slantwise convection and the need to parameterize them in coarser-gridded models (e.g., Seltzer et al., 1985; Persson and Warner, 1995; Chen et al., 2021). In practice, however, the application of slantwise convection parameterization is scarce. Recently, some climatological studies reinforced the importance of slantwise convection in midlatitudes. Glinton et al. (2017) showed that regions where CSI is likely to be released, existing in layers over 1 km deep, occurs about 20% of the total time over the Gulf Stream region in winter. Chen et al. (2018) indicated an averaged 30% probability of potential slantwise convection occurrence within cyclones at any given time. This probability increases with the concurrent intensification rate of the cyclones, e.g., it reaches 57% for storms undergoing rapid intensification.

To date, there are only a few parameterization schemes developed for slantwise convection (e.g., Thorpe, 1986; Nordeng, 1987, 1993; Chou and Thorpe, 1993; Ma, 2000). All the above schemes are built on the same concept that the environment will transition to a slantwise neutral state after undergoing a period of slantwise convection. CSI is identified by the presence of negative and positive saturation geostrophic potential vorticity ($\mathrm{MPV}_{\mathrm{g}}^{*}$) in the Northern and Southern Hemisphere, respectively. An alternative measure of the potential for slantwise convection is slantwise CAPE (SCAPE), representing the maximum work done by positive buoyancy for an air tube (of infinite extent in $x$) if it ascends along a surface of constant geostrophic pseudo-angular/absolute momentum $M_{\mathrm{g}}$, where

$$M_{\mathrm{g}} = U_{\mathrm{g}} - fy, \tag{5.1}$$

$y$ is defined as 90 degrees counterclockwise of the direction of geostrophic winds with magnitudes of $U_{\mathrm{g}}$ (Emanuel, 1983b). A moist, symmetrically neutral state should contain nearly zero $\mathrm{MPV}_\mathrm{g}^*$ and/or zero SCAPE, but there is no unique way to adjust a slantwise-unstable flow into slantwise-neutral.

Based on some frontal observations, Nordeng (1987) adjusts the temperature and moisture fields along the $M_\mathrm{g}$ surfaces to remove negative $\mathrm{MPV}_\mathrm{g}^*$. On the other hand, the Lagragian parcel dynamics indicate that the free motion of unstable air tubes in a pure CSI case (conditionally unstable for slantwise displacements but stable for vertical movements) tends to ascent along the neutral buoyancy surface (with constant potential temperature $\theta$ and saturation equivalent potential temperature $\theta_\mathrm{e}^*$ for dry and saturated flow, respectively) (Emanuel, 1983a). Nonlinear simulations also showed that slantwise circulation often has updrafts nearly in parallel to the neutral buoyancy surfaces (e.g., Thorpe, 1986; Thorpe and Rotunno, 1989). Such trajectories suggest that momentum transport is predominant in slantwise convection. As such, schemes like Chou and Thorpe (1993) and Ma (2000) adjust the $M_\mathrm{g}$ ($U_\mathrm{g}$) field to achieve symmetric neutrality. There are different formulations used in these schemes, but all of them are extensions from an established CPS. For example, Nordeng's (1987) scheme is based on the Kuo-type scheme, in which the onset of convection is controlled by the net moisture convergence into the grid column (Kuo, 1965). Chou and Thorpe's (1993) scheme follows the European Centre for Medium-Range Weather Forecasts's mass flux formulations, and Ma's (2000) scheme is extended from the Betts and Miller scheme (Betts, 1986; Betts and Miller, 1986). All these schemes take into account the potential shifts to neighboring grid columns when slantwise convection is expected to span over a distance larger than the model grid spacing horizontally.

Benefits of parameterizing slantwise convection have been reported in both idealized and real-data case studies. In dry idealized flows, Chou and Thorpe (1993) showed that their slantwise convection scheme effectively reduces the symmetric instability in initially unstable, unforced conditions and reaches an equilibrium state in conditions with a large-scale forcing that continuously produces instability. In numerical studies of polar lows using the

Norwegian operational mesoscale model, Nordeng (1987) found some clear improvements on the simulated frontal structure in one of the two cases (the other case shows limited impacts) when parameterizing slantwise convection. In his simulation with both upright and slantwise convection parameterized, the leading front becomes nearly neutral to slantwise overturnings, whereas the simulation with only upright convection parameterized still contains symmetric instability yet no significant convective activity. Lindstrom and Nordeng (1992) utilized a similar slantwise convection scheme to Nordeng (1987) as an addition to a vertical convective scheme (Anthes, 1977) in the PSU-NCAR Mesoscale Model and studied a wintertime rain band over the US. They found that the slantwise convective scheme helps to mitigate the model spin-up problem by generating the secondary convective circulation more quickly than without the scheme. This leads to a greater precipitation amount over a narrower region in better agreement with observations than the simulation with only the upright convection parameterization.

The impacts of parameterizing slantwise convection are not limited to the regional scale. Ma (2000) implemented his scheme in a Canadian general circulation model (GCM) and conducted a 5-year simulation over the entire globe, finding that the additional slantwise convection scheme has significant impacts on the simulated climate. With the parameterized momentum tendency, generally a source of westerly momentum at low-levels and a sink at high-levels, the Ma (2000) scheme acts to reduce the zonal wind shear and induces a direct secondary mean meridional circulation over the midlatitudes (Eliassen, 1951; Kuo, 1956). The adiabatic cooling over the ascending branch of the induced circulation in lower latitudes and the adiabatic warming over the descending branch at higher latitudes further weaken the meridional temperature gradient and baroclinicity. The poleward transient eddy transports of heat and zonal momentum are therefore also weakened. While the above effects bring the simulated climate into closer agreement with observations in the Southern Hemisphere, the improvement is mixed and can be negative for the Northern

Hemisphere in some situations. Ma (2000) noted that this is likely because the GCMs are often tuned to yield a good climate result for Northern Hemisphere, and so readjustment of other parameters may be required when a new scheme is introduced.

The above slantwise convection schemes have only been tested in a few studies. The issue of whether parameterizing slantwise convection benefits the performance of weather forecast requires more investigation. We present here a modified slantwise convection (SC) parameterization scheme based on Ma (2000). The SC scheme is implemented in the Weather Research and Forecasting (WRF) model and tested first under a 2D idealized setting that allows us to evaluate it for a pure initial CSI problem while excluding other common mechanisms for convective activity. Then, we test the SC scheme in a real-data simulation for precipitation bands forming along the cold frontal system of a storm in October 2000. The organization of the paper is as follows. Section 5.2 provides an introduction of this modified SC scheme, the implementation of which into WRF is described in Section 5.3. In Sections 5.4 and 5.5, we show test results for the idealized and real-data experiments, respectively. Finally, Section 5.6 presents the summary and suggestions for future application.

## 5.2 Description of the slantwise convective parameterization scheme

The Ma (2000) scheme is a static scheme and, as opposed to dynamic schemes, does not concern the detailed physical processes involved in convection but what the environmental state would be after a period of convective activity (Stensrud, 2007). There are two key elements: the reference state ($\psi^{\mathrm{R}}$, where $\psi$ can be any prognostic variable of the resolved scale) and the adjustment timescale ($\tau_{\mathrm{SC}}$), the latter of which estimates how long it takes to reach the reference state. Therefore, the convective eddy fluxes associated with subgrid slantwise convection are parameterized as

$$\left(\frac{\partial \psi}{\partial t}\right)_{\mathrm{SC}} = \frac{\psi^{\mathrm{R}} - \psi}{\tau_{\mathrm{SC}}}. \tag{5.2}$$

### 5.2.1 Reference state

For a given vertical displacement of an air tube, the change of its potential energy is maximized if it is displaced along the $M_{\mathrm{g}}$ surfaces (Emanuel, 1983b). This describes the definition of SCAPE, i.e.,

$$\mathrm{SCAPE}(T, q_v, M_{\mathrm{g}}) =_{M_{\mathrm{g}}} \int_{\mathrm{LFSC}}^{\mathrm{LSNB}} [R_{\mathrm{d}}(T_{\mathrm{vt}} - T_{\mathrm{ve}})] d(-\ln p), \tag{5.3}$$

where $T_{\mathrm{vt}}$ and $T_{\mathrm{ve}}$ are the virtual temperatures of the air tube and environment, respectively, and $R_{\mathrm{d}}$ is the gas constant for dry air. The $M_{\mathrm{g}}$ surface is defined on a 2D cross-section that aligns along the local temperature gradient (hereafter the CSI plane) as defined in (5.1). The LFSC and LSNB denote the level of free slantwise convection and the level of slantwise neutral buoyancy along the $M_{\mathrm{g}}$ surface. Note that as done in Chapter 2, the integral is confined to where the $(T_{\mathrm{vt}} - T_{\mathrm{ve}})$ along the $M_{\mathrm{g}}$ surface is positive. For a barotropic environment where $M_{\mathrm{g}}$ surfaces are vertical, (5.3) reduces to the formula for CAPE. Generally, SCAPE is equal to or larger than CAPE, especially in subtropics (Chen et al., 2018).

For computational efficiency, Ma (2000) adopted Emanuel's (1983b) 1D formula for SCAPE estimation, in which $T_{\mathrm{ve}}$ along the $M_{\mathrm{g}}$ surface is approximated locally using the first-order Taylor expansion and thermal wind balance assumption, i.e.,

$$T_{\mathrm{ve}}|_{M_{\mathrm{g}}} \approx T_{\mathrm{ve}} - \frac{1}{2R_{\mathrm{d}}}\frac{f}{\overline{\eta}}\frac{d(U_{\mathrm{g}} - U_{\mathrm{g0}})^2}{d(-\ln p)},$$

and

$$\mathrm{SCAPE}(T, q_v, M_\mathrm{g}) = \int_{\mathrm{LFSC}}^{\mathrm{LSNB}} \left[ R_\mathrm{d}(T_\mathrm{vt} - T_\mathrm{ve}) + \frac{1}{2}\frac{f}{\overline{\eta}}\frac{d(U_\mathrm{g} - U_\mathrm{g0})^2}{d(-\ln p)} \right] d(-\ln p), \tag{5.4}$$

where $U_{\mathrm{g0}}$ is the $U_\mathrm{g}$ of the lifted air tube, $\eta$ represents the absolute geostrophic vorticity on pressure levels, $\eta = f - \partial U_\mathrm{g}/\partial s$, where $\boldsymbol{s}$ is the horizontal axis of the CSI plane, and the overbar means the layer average. Such a 1D approximation is generally applicable for systems that are nearly two-dimensional and non(slowly)-evolving with respect to the unstable air tube ascent but may lead to biases otherwise (e.g., Gray and Thorpe, 2001). Within the generally two-dimensional frontal zones, Chen et al. (2018) noted that the approximated formula (5.4) gives reasonably consistent results with Glinton et al. (2017), in which the original equation (5.3) was used.

Ma (2000) assumed that in the pure CSI condition, the neutralization is achieved by redistributing pseudo-angular momentum along a fixed neutral buoyancy surface, and the reference state (with a superscript R) is characterized by

$$\mathrm{SCAPE}^\mathrm{R}(T, q_v, M_\mathrm{g}^\mathrm{R}) = \int_{\mathrm{LFSC}}^{\mathrm{LSNB}} \left[ R_\mathrm{d}(T_\mathrm{vt} - T_\mathrm{ve}) + \frac{1}{2}\frac{f}{\overline{\eta}}\frac{d(U_\mathrm{g}^\mathrm{R} - U_\mathrm{g0}^\mathrm{R})^2}{d(-\ln p)} \right] d(-\ln p) = 0. \tag{5.5}$$

Because SCAPE is an integrated quantity, additional assumptions are required to obtain unique solutions. Ma (2000) obtained a first guess solution of $U_\mathrm{g}^\mathrm{R}$ (denoted as $U_\mathrm{g}^{\mathrm{R}'}$) with the concept that positive buoyancy along the $M_\mathrm{g}$ surface at every vertical layer will be diminished. Assuming $U_\mathrm{g}$ remains unchanged for levels below the LFSC ($U_\mathrm{g}^{\mathrm{R}'} = U_\mathrm{g}$ there), we can obtain a height function for $U_\mathrm{g}^{\mathrm{R}'}$ as

$$U_\mathrm{g}^{\mathrm{R}'}(m+1) = U_\mathrm{g0} + \sqrt{\left(U_\mathrm{g}^{\mathrm{R}'}(m) - U_\mathrm{g0}\right)^2 - \frac{2\overline{\eta}}{fp} R_\mathrm{d}(T_\mathrm{vt} - T_\mathrm{ve}) d(-\ln p)}, \quad m = 1, ...N, \tag{5.6}$$

where $m$ represents the model level index starting from LFSC to LSNB. Ma (2000) solved

(5.6) iteratively from $m = 1$ upward.

Conceptually, this first-guess solution corresponds to adjusting the environmental $M_{\mathrm{g}}$ surface to overlap with the $\theta_{\mathrm{e}}^{*}$ surface (both of which have the constant values same as the lifted air tube, respectively) between LFSC and LSNB in the CSI plane (Fig. 5.1a). However, this indicates entirely negative geostrophic momentum adjustment. There must exist some momentum increases elsewhere to ensure momentum conservation for the entire column, i.e.,

$$\int_{\mathrm{surface}}^{\mathrm{top}} \left(U_{\mathrm{g}} - U_{\mathrm{g}}^{\mathrm{R}}\right) dp = 0. \tag{5.7}$$

To do so, Ma (2000) horizontally shifted a segment of the $U_{\mathrm{g}}^{\mathrm{R}'}$ surface, i.e., between the surface to LSNB, by a uniform distance to fulfill (5.7) (Fig. 5.1b). This is mathematically done by subtracting a constant, given by the mean difference between the first guess $U_{\mathrm{g}}^{\mathrm{R}'}$ and the original $U_{\mathrm{g}}$, and the final $U_{\mathrm{g}}^{\mathrm{R}}$ is derived:

$$U_{\mathrm{g}}^{\mathrm{R}}(k) = U_{\mathrm{g}}^{\mathrm{R}'}(k) - \frac{\sum [U_{\mathrm{g}}^{\mathrm{R}'}(k) - U_{\mathrm{g}}(k)] dp}{\sum dp}, \tag{5.8}$$

where $k$ is the model level index from the surface. Although $\mathrm{SCAPE}^{\mathrm{R}}$ does not necessarily equal zero after applying (5.8), our test shows that on average, about 90% of the original SCAPE has vanished in the reference state.

While we generally follow Ma's (2000) method for solving the reference state, two minor modifications are made. First, we notice that real solutions may not be found when the values within the square root of (5.6) become negative. This often occurs when conditional instability is also present in the layer, i.e., $R_{\mathrm{d}}(T_{\mathrm{vt}} - T_{\mathrm{ve}})d(-\ln p) > 0$, and to eliminate positive buoyancy along the $M_{\mathrm{g}}$ surface, $U_{\mathrm{g}}^{\mathrm{R}'}$ should decrease with height such that $[U_{\mathrm{g}}^{R'}(m+1) - U_{\mathrm{g0}}]^2 < [U_{\mathrm{g}}^{R'}(m) - U_{\mathrm{g0}}]^2$. However, Ma's (2000) upward iterative solution with fixed value beneath the layer is inadequate to obtain such a solution and he simply assumed

$$U_{\mathrm{g}}^{R'}(m+1) = U_{\mathrm{g0}}$$

for those layers. In the modified SC scheme, after using the upward iterative method (5.6) to obtain $U_{\mathrm{g}}^{R'}(m+1)$, we recalculate $U_{\mathrm{g}}^{R'}(m)$ iteratively downward from the upper-most layer, in which the value inside the square root of (5.6) is negative, by

$$U_{\mathrm{g}}^{\mathrm{R}'}(m) = U_{\mathrm{g0}} + \sqrt{\left(U_{\mathrm{g}}^{\mathrm{R}'}(m+1) - U_{\mathrm{g0}}\right)^2 + \frac{2\overline{\eta}}{fp} R_{\mathrm{d}}(T_{\mathrm{vt}} - T_{\mathrm{ve}}) d(-\ln p)}.$$

This solution can then describe a possible reference state that contains a layer of overturning geostrophic momentum ($U_{\mathrm{g}}^{\mathrm{R}'}$ decreases with height). Another modification is regarding the horizontal shift to conserve momentum. Instead of moving the segment of $U_{\mathrm{g}}^{\mathrm{R}'}$ from the

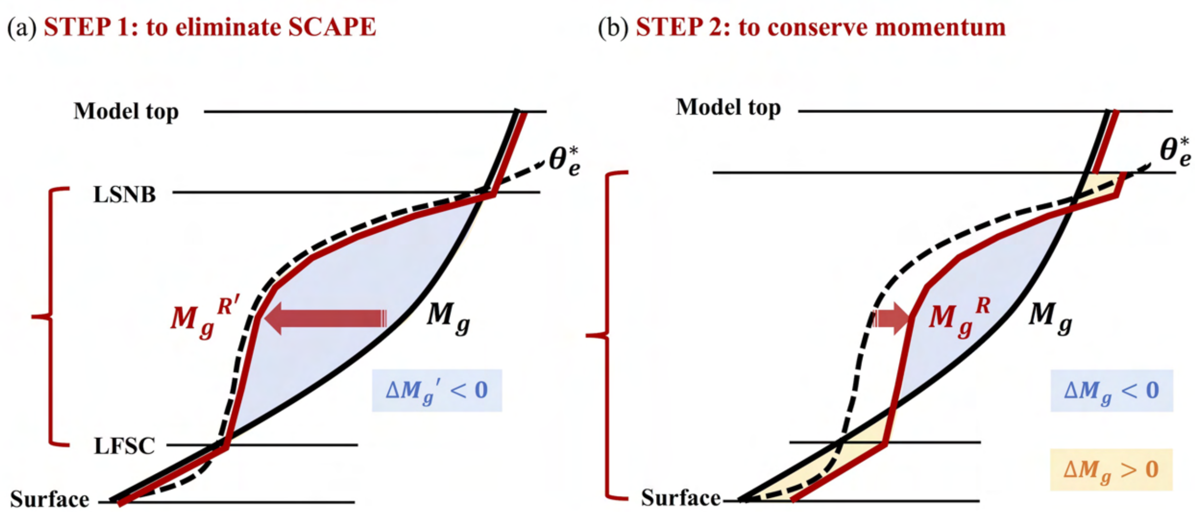


**Fig. 5.1**: The reference profile of the geostrophic momentum defined in the SC scheme. The black dashed and solid lines represent the $\theta_{\mathrm{e}}^*$ and $M_{\mathrm{g}}$ surfaces, respectively, indicating the presence of CSI. (a) The first guess of the reference profile is solved by adjusting the geostrophic momentum to diminish SCAPE at every level between LFSC and LSNB (denoted as $M_{\mathrm{g}}^{R'}$ in dark red). (b) Then, to ensure momentum conservation, a segment of $M_{\mathrm{g}}^{R'}$ surface is shifted horizontally by a constant distance to reach the final $M_{\mathrm{g}}^{R}$ (dark red curve). The total layer-integrated momentum decrease (blue shading) is equivalent to momentum increase (yellow shading). Adapted from Ma (2000).

surface to LSNB whenever the SC scheme is activated, we move only the segment from the surface to an estimated height (see LSAT defined in Section 5.2.3), which can be lower than LSNB if we expect that convection has not developed to upper-levels or higher than LSNB if overshooting is assumed to exist.

### 5.2.2 Adjustment timescale

Reuter and Yau (1990) analyzed seven banded precipitation events associated with winter cyclones near Nova Scotia in Canada. They examined the evolution of regions that exhibited CSI, noting that the environment remains slantwise unstable when moisture is lacking. Once saturation has been achieved due to lifting of the boundary layer air, the region transitions to a state of conditional slantwise neutrality in about $<3$ hours, consistent with Emanuel's (1983b) theoretical timescale characterizing slantwise convection of $f^{-1}$. Using a Lagrangian parcel model, Ma (2000) showed that when conditional instability and CSI coexist in the low-level, there exists two separable relaxation timescales for the nearly vertical ascent (buoyancy mode) and the slantwise ascent (inertial mode) above, respectively. His numerical results showed that the relaxation timescale for the buoyancy mode ranges from $0.98N_{\mathrm{m}}^{-1} \sim 1N_{\mathrm{m}}^{-1}$, where $N_{\mathrm{m}}^{-1}$ is the low-level moist Brunt–Väisälä frequency, and the inertial mode has a timescale of $0.94(f\eta)^{-1/2} \sim 2.2(f\eta)^{-1/2}$, which is about 3-6 hours for typical midlatitude conditions. Consistent results were also obtained by Chou and Thorpe (1993) for dry idealized flows that CSI adjustment time is about 3-4 hours for a single column cloud but a few hours longer for a whole cloud domain due to the interactive effects of the population of clouds. Considering that the life cycle of slantwise convection is generally longer in an unforced setting (e.g., Persson and Warner, 1995; Chen et al., 2021), we specify a constant $\tau_{\mathrm{SC}} = 5$ hours for the idealized experiment and $\tau_{\mathrm{SC}} = 3$ hours for the real-data simulation.

### 5.2.3 CSI plane and the adjustment path

With the reference state and the adjustment timescale, the parameterized momentum tendency is derived with (5.2). A remaining problem is where to apply it. In the scheme Ma (2000) implemented in the GCM, it is assumed that the CSI plane is always parallel to the meridional direction. Moreover, instead of considering a slantwise path, Ma (2000) applied the adjustment to the entire local and neighboring columns within an estimated horizontal (cross-band) scale, $L = \frac{U_{\mathrm{gLSNB}} - U_{\mathrm{g0}}}{\overline{\eta}}$, where $U_{\mathrm{gLSNB}}$ is the $U_{\mathrm{g}}$ at the height of LSNB. This method may result in unphysical SCAPE release over regions/layers where subgrid slantwise convection is absent.

We improve the above two issues in the modified SC scheme by locally defining the CSI plane and a sloped adjustment path. For an air tube lifted from the model grid point $(i,\ j)$ in the model Cartesian horizontal coordinates, the corresponding CSI plane is the vertical cross-section with transformed coordinates $(s,\ k)$, where $\boldsymbol{k}$ is the vertical axis, and $\boldsymbol{s}$ points from $s_0 = (i, j)$ to the negative horizontal temperature gradient averaged from the surface to the thermal tropopause (Fig. 5.2a-b). The geostrophic wind $U_{\mathrm{g}}$ is assumed to be the horizontal wind component perpendicular to $\boldsymbol{s}$ and is interpolated from the surrounding model grid points to the $(s,\ k)$ coordinates with a grid length $\Delta s$. For the SCAPE calculation in (5.4), we estimate $\eta$ using forward differencing, $\eta \approx f - [U_{\mathrm{g}}(s_0 + \Delta s, k) - U_{\mathrm{g}}(s_0, k)]/\Delta s$.

The slantwise path is parameterized by

$$\Delta s_{\mathrm{AD}}(k) = \alpha \Delta s_{M_{\mathrm{g}}}(k) + (1 - \alpha)\Delta s_{\theta_{\mathrm{e}}^*}(k), \tag{5.9}$$

where $\Delta s_{\mathrm{AD}}(k)$, $\Delta s_{M_{\mathrm{g}}}(k)$ and $\Delta s_{\theta_{\mathrm{e}}^*}(k)$ represent the horizontal shifts of the adjustment path, constant $M_{\mathrm{g}}$ and $\theta_{\mathrm{e}}^*$ surfaces (that have same values as the lifted air tube) along $\boldsymbol{s}$ at level $k$, respectively (Fig. 5.2b). The tunable parameter $\alpha \in [0, 1]$, indicating that the slantwise path is always bounded by the $M_\mathrm{g}$ and $\theta_\mathrm{e}^*$ surfaces, as suggested by the parcel theory for CSI triggering. The $\Delta s_{M_\mathrm{g}}$ and $\Delta s_{\theta_\mathrm{e}^*}$ are approximated with (Emanuel, 1983b):

$$\Delta s_{M_\mathrm{g}}(k) = -\frac{\partial M_\mathrm{g}/\partial z}{\partial M_\mathrm{g}/\partial s} z(k), \quad \Delta s_{\theta_\mathrm{e}^*}(k) = -\frac{\partial \theta_\mathrm{e}^*/\partial z}{\partial \theta_\mathrm{e}^*/\partial s} z(k).$$

The slopes, e.g., $\frac{\partial \theta_\mathrm{e}^*/\partial z}{\partial \theta_\mathrm{e}^*/\partial s}$, are calculated at every $k$, and then two separate layer averages are taken below and above the level where the local buoyancy for a slantwise ascent is maximized, respectively. Therefore, the estimated $M_\mathrm{g}$ and $\theta_\mathrm{e}^*$ surfaces retain some degree of vertical variation but are not severely discontinuous in height.

We assume that below LFSC, $\Delta s_\mathrm{AD}(k) = 0$. For layers high above LFSC where

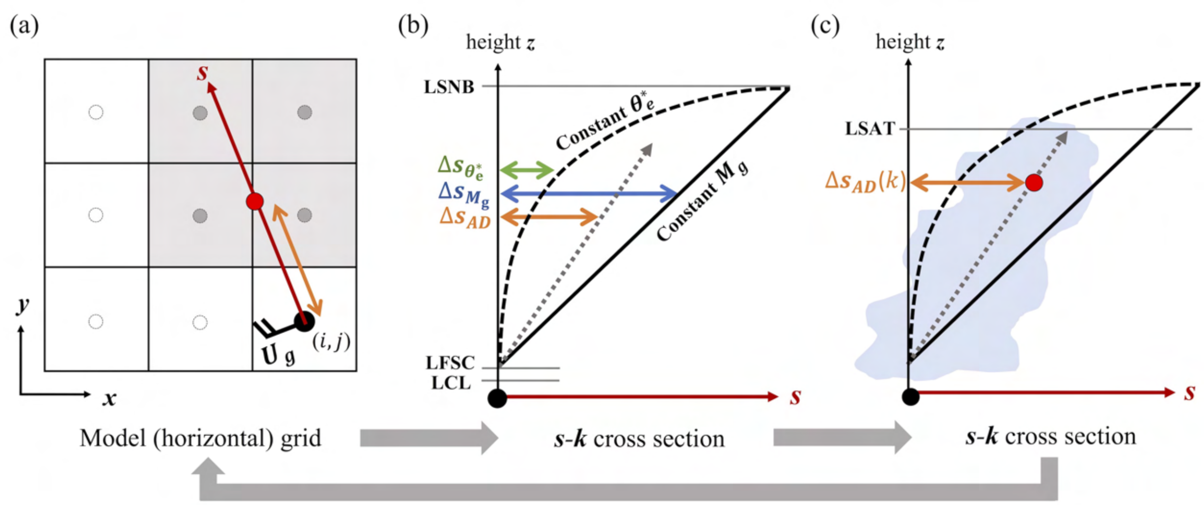


**Fig. 5.2**: Schematic illustration of the SC scheme. (a) For a low-level mixed-layer air mass originated from $(i,\ j)$ in the model horizontal plane, the scheme first decides the direction (along temperature gradient) for CSI. The environmental variables on the model coordinates are interpolated into the transformed $s$-$k$ cross-section. (b) The horizontal shifts of $\theta_\mathrm{e}^*$ and $M_\mathrm{g}$ surfaces and the adjustment path on this cross-section are estimated ($\Delta s_{\theta_\mathrm{e}^*}$, $\Delta s_{M_\mathrm{g}}$, and $\Delta s_\mathrm{AD}$, respectively) at each $k$. (c) The adjustment is limited to near-saturated (light blue shading) levels below LSAT. Finally, for every height, the SC-parameterized tendencies on the adjustment path are distributed to the four horizontally closest model grid points (e.g., the red circle on the $s$-$k$ cross-section corresponds the light-gray-shaded model grid boxes in (a) at the same $k$).

$\Delta s_{\theta_e^*}(k) > \Delta s_{M_g}(k)$, the local $\mathrm{MPV}_g^* > 0$ but the air tube still obtains positive buoyancy and generally ascends along the $M_g$ surface, and so we set $\alpha = 1$ in (5.9). As for the local unstable layers above LFSC where $\Delta s_{\theta_e^*}(k) < \Delta s_{M_g}(k)$, it is assumed that the path lies halfway between the $M_g$ and $\theta_e^*$ surfaces, so an initial guess of $\alpha = 0.5$ is used. During the testing in our idealized experiment, the estimation of adjustment path is found critical to the performance of the scheme. Bias of a few tens kilometers might release SCAPE at the wrong location and worsen the model verification. We found that including information of the grid-resolved relative humidity (RH) may aid the path estimation, on condition that models are operating at a resolution where the saturated slantwise band can be partially resolved. Specifically, if the grid-resolved RH drops to below 90% along the initial-guessed path before reaching LSNB, the scheme then readjusts $\alpha$ with an increment of 0.1 iteratively until $\alpha = 1$ to find the best path along which RH$\geq$ 90% extends to the highest altitude. If all $\alpha$ gives the same height for the upper bounds of RH$\geq$ 90%, which may be the case when the subgrid saturation is fully unresolved, $\alpha = 0.5$ is used. Note that most of the operational NWP models and GCMs are currently at or transitioning to the numerical gray zone for convection in the mesoscale range (e.g., Jeworrek et al., 2019), and so such an additional grid-scale RH indicator is likely to be generally beneficial.

Another issue to be considered is that it may take several hours for the free slantwise convection to develop in height in the real world. In other words, the associated CSI neutralization effects starting from LFSC do not extend to LSNB within one time step. If the scheme adjusts momentum for the entire path whenever it is triggered, the mid-to-upper levels may go through a too-rapid neutralization when slantwise convection has only developed in the low levels. Following a similar concept for the path estimation, we add another upper-limit constraint to where the adjustment should be applied, that is, the level where the grid-resolved RH drops to below 90% for a depth of at least 1 km (noted as the level of near saturation; LSAT in Fig. 5.2c). If LSAT is higher than LSNB, we assumed an overshooting cloud top.

Finally, the tendencies defined in the CSI plane are converted back to the model grid points (Fig. 5.2a, c). Specifically, the scheme distributes the tendency $\left[\frac{\partial U_{\mathrm{g}}(k)}{\partial t}\right]_{\mathrm{SC}}$ along the slantwise path at $s = s_0 + \Delta s_{\mathrm{AD}}(k)$ to its four closest model grid points at the same $k$, weighted by the inverse of each of their distance to $s = s_0 + \Delta s_{\mathrm{AD}}(k)$ (Nordeng, 1987). For every air tube lifted from the location $(i, j)$, the scheme repeats the same process from the surface upward until LSAT. Note that for a 3D model grid point at $(i, j, k)$, it is possible that the SC scheme assigns momentum tendencies more than once for different air tubes lifted from different low-level locations at the same time step. The final output tendency is the summation of all such contributions.

### 5.2.4 Condensational heating, moisture loss, and precipitation

If an environment is saturated, ascending motion can result in supersaturation and may produce condensates. In addition to the momentum adjustment to eliminate SCAPE, Ma (2000) also parameterized the condensational latent heating and the associated moisture loss by first estimating the vertical velocity of the slantwise updraft. Based on parcel theory, the maximum speed that a rising tube can obtain due to the energy conversion is $\sqrt{2\mathrm{SCAPE}}$. We parameterize the vertical component of the slantwise ascent to have a maximum value of

$$w_{\mathrm{SCmax}} = (\sin\alpha)\mu\sigma f_s\sqrt{2\mathrm{SCAPE}}, \tag{5.10}$$

where $\alpha$ is the averaged angle between the sloped adjustment path and $\boldsymbol{s}$, and $\mu = \frac{z(\mathrm{LSAT}-z(\mathrm{LFSC})}{z(\mathrm{LSNB}-z(\mathrm{LFSC})}$ is introduced as SCAPE is unlikely to be released fully within one time step. Considering that the slantwise cloud may cover only a fraction of the grid box, the cloud fraction $\sigma$ is included to represent the averaged subgrid characteristics, and

$$f_s = \frac{\text{SCAPE} - \text{CAPE}}{\text{SCAPE}} \tag{5.11}$$

gauges the relative dominance between upright and slantwise convection when their associated instabilities coexist (Ma, 2000; Chen et al., 2018). Unlike assuming a vertically uniform ascent for the entire cloud layer as in Ma (2000), the modified scheme, inspired by other parameterizations that relate heating to vertical velocity (e.g., Mak, 1994; Haualand and Spengler, 2019), assumes a parabolic profile for the vertical velocity:

$$w_{\text{SC}}(k) = \begin{cases} 0 & z(k) \leq z_{\text{LCL}}, \\ \epsilon w_{\text{LCL}} w_{\text{SCmax}} \left\{ 1 - \frac{[z(k) - z_{\text{mid}}]^2}{[z_{\text{LCL}} - z_{\text{mid}}]^2} \right\} & z_{\text{LCL}} < z(k) \leq z_{\text{mid}}, \\ \epsilon w_{\text{LCL}} w_{\text{SCmax}} \left\{ 1 - \frac{[z(k) - z_{\text{mid}}]^2}{[z_{\text{LSAT}} - z_{\text{mid}}]^2} \right\} & z_{\text{mid}} < z(k) \leq z_{\text{LSAT}}, \\ 0 & z_{\text{LSAT}} < z(k), \end{cases} \tag{5.12}$$

where $\epsilon$ is a nondimensional intensity parameter, $w_{\text{LCL}}$ is the grid-resolved vertical velocity at the lifting condensation level (LCL), $z_{\text{LCL}}$ is the height of LCL, $z_{\text{mid}}$ is the mid-level between LFSC and LSNB, and the $z_{\text{LSAT}}$ is the height of LSAT.

The condensation rate at a given level is

$$\frac{d\chi}{dt} = \frac{Q_1}{Q_2} w_{\text{SC}},$$

where $\chi$ is the mixing ratio of condensates, $Q_1 = \frac{gL_v}{C_p R_v T^2} - \frac{g}{R_d T}$ and $Q_2 = \frac{p}{\varepsilon e_s} - \frac{{L_v}^2}{C_p R_v T^2}$ (Rogers and Yau, 1989). The total condensate production rate is $R_{\text{SC}} = \int_{\text{LCL}}^{\text{LSAT}} \frac{d\chi}{dt} \rho dz$, which must be accompanied by moisture loss somewhere in the column to conserve the total water:

$$R_{\mathrm{SC}} = -\int \left(\frac{\partial q_v}{\partial t}\right)_{\mathrm{SC}} \rho dz,$$

where $q_v$ is the water vapor mixing ratio. Considering that the main source for moisture is the low-level convergent flow, we parameterize a profile of negative $q_v$ tendency focusing in the subcloud layer. We prescribe weights maximized (equal to one) at the half height of LCL and dropped parabolically to zero down to the surface and upward to 500 m above the LFSC, respectively. With $R_{\mathrm{SC}}$ and the weight distribution, a height function of $\left(\frac{\partial q_v}{\partial t}\right)_{\mathrm{SC}}$ is derived. Note that care must be given to avoid $q_v < 0$ after applying $\left(\frac{\partial q_v}{\partial t}\right)_{\mathrm{SC}}$ to the total $q_v$ tendency equation.

Assuming the advection of condensates is negligible, the latent heating is parameterized as

$$\left[\frac{\partial T}{\partial t}(k)\right]_{\mathrm{SC}} = \frac{L_v}{C_p}\frac{d\chi}{dt}(k), \tag{5.13}$$

where the total integrated enthalpy is conserved, i.e.,

$$\int -L_v \left[\frac{\partial q_v}{\partial t}(k)\right]_{\mathrm{SC}} \rho dz = \int C_p \left[\frac{\partial T}{\partial t}(k)\right]_{\mathrm{SC}} \rho dz.$$

Note that unlike a vertically uniform latent heating in Ma (2000), the modified heating profile is more physically reasonable and qualitatively consistent to that observed/used in midlatitude cyclones studies (e.g., Dearden et al., 2016; Haualand and Spengler, 2019).

If all condensates precipitate out immediately without evaporation, the accumulated precipitation over the integration time step ($\Delta t$) is $R_{\mathrm{SC}}\Delta t$. Since the slantwise band is tilted, the precipitation does not always fall to where the air tube is originally lifted from. The modified SC scheme assumes that precipitation falls out from the sloped path at the height of $z_{\mathrm{mid}}$ (with the level index $k_{\mathrm{mid}}$), therefore reaching to the ground at $s_0+\Delta s_{\mathrm{AD}}(k_{\mathrm{mid}})$ on the CSI-plane.

### 5.2.5 Trigger function

Ma's (2000) trigger function only considers the presence and dominance of CSI. According to the ingredients-based methodology for deep convection (e.g., Doswell, 1987), we add two other necessary components, i.e., moisture and lift, in the modified trigger function. The SC scheme is activated when the lowest 50-hPa mixed-layer air tube, which is searched from the surface to a level 300 hPa above, satisfies:

(1) Presence of high relative humidity at the tube's LCL, i.e., $\mathrm{RH_{LCL}} \geq 85\%$.

(2) $\begin{cases} \text{SCAPE-CAPE} > 100 \text{ J kg}^{-1} \text{ and } f_s > 0.1 \\ \text{or} \\ \text{SCAPE-CAPE} > 50 \text{ J kg}^{-1} \text{ and } f_s > 0.5 \end{cases}$, where $f_s$ is defined in (5.11).

(3) Presence of triggering forces at the tube's LCL: $w_{\mathrm{LCL}} > 1$ cm s$^{-1}$ and $v_{s\mathrm{LCL}} > 0$ m s$^{-1}$, where $v_s$ is the horizontal component of the wind in parallel with $\boldsymbol{s}$.

(4) Cloud depth exceeding a minimum threshold, i.e., $z(\mathrm{LSNB}) - z(\mathrm{LFSC}) \geq 2$ km.

The fourth criterion is added to exclude situations when the seemingly large SCAPE is attributed to the small-scale momentum noises over a shallow layer.

## 5.3 Implementation in the WRF model

We implement this modified SC scheme in the fully compressible, non-hydrostatic version of the Advanced Research WRF model (both version 3.8.1 and version 4.1.5). For practical considerations, the slantwise convection scheme is implemented as an addition to the existing CPS schemes. In this study, we select the Kain-Fritsch (KF) cumulus scheme (Kain, 2004) for upright convection, given its CAPE-removal closure assumption. Lindstrom and Nordeng (1992) and Nordeng (1987) activated their SC scheme only when CPS is not triggered at the same location at the same time considering the larger growth rate and shorter timescale of conditional instability than CSI (minutes vs. hours; e.g. Schultz and Schumacher, 1999). We have tested the same strategy and another one that allows the concurrent activation of KF and SC schemes. For the real-data case presented here (shown in Section 5.5), we found that the former strategy results in little difference between experiments with and without the additional SC scheme. This is because CSI regions are often also conditionally unstable in this case, and deactivating the SC scheme when KF is in effect results in a 90%-drop in the total number of SC scheme calls. Therefore, this study only presents the experiments that allow the co-activation of KF and SC schemes.

In WRF, tendencies due to different physics are not added to the prognostic variables right away after calling each parameterization (Chapter 8.7 in Skamarock et al., 2008), so even with a calling order of CPS before SC scheme, we need to internally introduce the output from CPS to the SC scheme before identifying CSI. In so doing, we assume that in situations with positive CAPE, CPS acts to advance the environment toward a conditionally neutral state, and if high susceptibility to slantwise convection remains afterward, the SC scheme then adjusts the flow to be conditionally symmetrically neutral. The larger adjustments are presumably taken care by the CPS, given its shorter neutralization timescale than the SC scheme.

For computational efficiency, not all the parameterizations are called at the same frequency as the integration time step. For regional climate simulations, a 5-minute frequency is suggested for the usage of the KF scheme in WRF. Unlike the KF scheme operating in each local column, the 2D SC scheme is more costly to run, and so we call the SC scheme every 10 minutes to update its parameterized tendencies, which are kept constant between calls. Note that because slantwise convection evolves more slowly than upright convection, such a lower calling frequency is considered physically reasonable.

To summarize, the SC scheme outputs height-dependent tendencies, $(\frac{\partial U_g}{\partial t})_{\mathrm{SC}}$, $(\frac{\partial q_v}{\partial t})_{\mathrm{SC}}$, and $(\frac{\partial T}{\partial t})_{\mathrm{SC}}$ along the adjustment path defined in Section 5.2.3. The tendencies of $U_{\mathrm{g}}$ and $T$ are transformed to those of the prognostic variables in WRF, i.e.,

$$\begin{cases} \frac{\partial u(k)}{\partial t}_{\mathrm{SC}} = \frac{\partial U_{\mathrm{g}}(k)}{\partial t}_{\mathrm{SC}} \cos(\delta - \frac{\pi}{2}) \\ \frac{\partial v(k)}{\partial t}_{\mathrm{SC}} = \frac{\partial U_{\mathrm{g}}(k)}{\partial t}_{\mathrm{SC}} \sin(\delta - \frac{\pi}{2}) \\ \frac{\partial \theta(k)}{\partial t}_{\mathrm{SC}} = \frac{\partial T(k)}{\partial t}_{\mathrm{SC}} \left(\frac{p_0}{p(k)}\right)^{\kappa} \end{cases},$$

where $\delta$ is the angle between $\boldsymbol{s}$ and the $\boldsymbol{x}$ axis of the model Cartesian coordinate, $p$ is the pressure, whose tendency is neglected here, and $\kappa$ is the Poisson constant.

## 5.4 Results: 2D idealized pure slantwise convection

We first test the performance of the SC scheme for a 2D idealized simulation of a pure CSI release process where the $\boldsymbol{y}$ axis equals to $\boldsymbol{s}$ (i.e., the negative temperature gradient) using the WRF (v3.8.1) model, same as in Chapter 4. A major slantwise band is kicked off in an initially conditionally stable environment that contains a uniform zonal wind shear. Chen et al. (2021) investigated the explicit representation of this process with varying model grid spacings. It is shown that the simulated bulk features, such as the accumulated precipitation, upward momentum transport, and SCAPE evolutions, converge numerically when the grid spacing is reduced to $\leq 5$ km.

Here, we utilize the same numerical setup and present three experiments: the control simulation is taken from Chapter 4 that has a grid spacing of 2 km with neither the upright nor the slantwise convection parameterization (CTL); two other simulations both have a grid spacing of 40 km, but one with only the KF cumulus scheme turned on (40KF), and the other with both the KF and SC schemes activated (40KFSC). For the SC scheme, the parameters in (5.12) are determined empirically with $\sigma = 0.5$ and $\epsilon = 1.15$. Note that to avoid complication, the shallow cloud component in the KF scheme, with a different closure from CAPE removal, is disabled in the presented idealized experiments[1].

We first check the tendencies generated by the SC scheme (Fig. 5.3). Figure 5.3a shows the vertical profile of $\left(\frac{\partial U_g}{\partial t}\right)_{SC}$ at an integration time of 21 h. The distribution of positive tendency at low-to-mid levels and negative values above is consistent with Emanuel (1983a) that moist symmetric instability depletes the upper-level momentum and deposits

[1]If this component is enabled,the slantwise band slightly intensifies and reaches a higher altitude than when it is disabled in 40KF. However, the strengthening $w$ is constrained in shallow layers instead of extending over a deep layer.

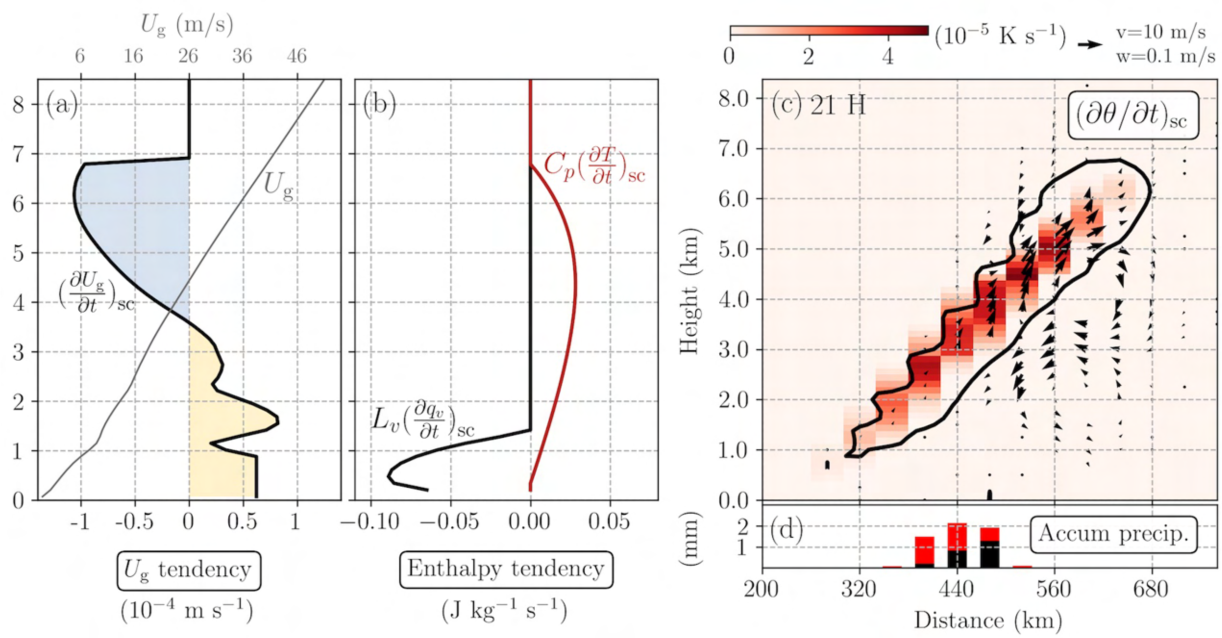


**Fig. 5.3**: The parameterized tendencies generated by the SC scheme for 40KFSC at 21 h. Panel (a) shows the vertical profile of $\left(\frac{\partial U_g}{\partial t}\right)_{SC}$ (black) and $U_g$ (gray) for an air tube lifted from $y = 320$ km. Yellow and blue shadings represent the integrated regions with positive and negative $\left(\frac{\partial U_g}{\partial t}\right)_{SC}$, respectively. Panel (b) is the same as (a) but for the enthalpy tendencies associated with the parameterized $\left(\frac{\partial T}{\partial t}\right)_{SC}$ (dark red) and $\left(\frac{\partial q_v}{\partial t}\right)_{SC}$ (black), respectively. Panel (c) shows the distribution of $\left(\frac{\partial \theta}{\partial t}\right)_{SC}$ (shaded, $10^{-5}$ K s$^{-1}$) on the CSI plane, along with the resolved-scale transverse circulation ($v$, $w$) (vectors) and RH = 100% (black contours). (d) shows the accumulated precipitation (black and red are from the microphysics and the SC scheme, respectively) along $y$.

it at lower levels. The momentum tendency acts to reduce the vertical geostrophic wind shear, rendering the environment less susceptible to CSI. The enthalpy profiles associated with $(\frac{\partial q_v}{\partial t})_{\text{SC}}$ and $(\frac{\partial T}{\partial t})_{\text{SC}}$ are shown in Fig. 5.3b, exhibiting latent heating over a deep layer and drying in the subcloud layer. In the CSI plane, the applied tendencies coincide nicely with the tilted saturated ascent (e.g., Fig. 5.3c), indicating that the adjustment path is well estimated by the SC scheme. The diagnosed precipitation shows comparable magnitudes to the large-scale (explicitly resolved) precipitation from the microphysics scheme accumulated up to 21 h (Fig. 5.3d).

Figure 5.4 shows the simulated results for all experiments at 25 h. For CTL, a major slantwise convective band grows upward and toward the cooler side of the domain at the expense of SCAPE, reaching $y = 800$ km and $z = 9$ km by 25 h (Fig. 5.4a). Despite exhibiting a gentler slope at upper levels than at low-mid levels, the ascent is uniformly strong with $w$ exceeding 10 cm s$^{-1}$ throughout the band. The precipitation spans horizontally over ∼200 km with a peak accumulated value of $>$ 10 mm locally. SCAPE with an initial value of ∼500 J kg$^{-1}$ has been consumed almost entirely at some grid points. Compared to CTL, the slantwise convection in 40KF is remarkably weaker. Upward motion decays in the lower half of the saturated band while weak ascent with $w$ of $<$ 5 cm s$^{-1}$ remains only at its upper part. The band reaches a height of only 4.5 km after 25 h (Fig. 5.4b). Little precipitation is produced, and almost no SCAPE has been removed.

With the addition of SC scheme (40KFSC), the simulated slantwise circulation intensifies significantly compared to 40KF (Fig. 5.4c). The updraft exceeds 6 cm s$^{-1}$ over a deep layer (with a maximum $w$ of $\sim$ 10 cm s$^{-1}$), and the band reaches a similar height as in CTL. Although the saturated band appears wider due to the coarse horizontal grid spacing, important large-scale impacts associated with the slantwise convection, such as accumulated precipitation and SCAPE, are in close agreement with CTL. Even the near-surface shallow convections that emerge later beneath the primary slantwise band at $y =$

400-500 km in CTL are partially captured in 40KFSC.

It is also of interest to examine the impact of the SC scheme if it only parameterizes the momentum adjustment but not the condensation-associated effects (hereafter 40KFSC-

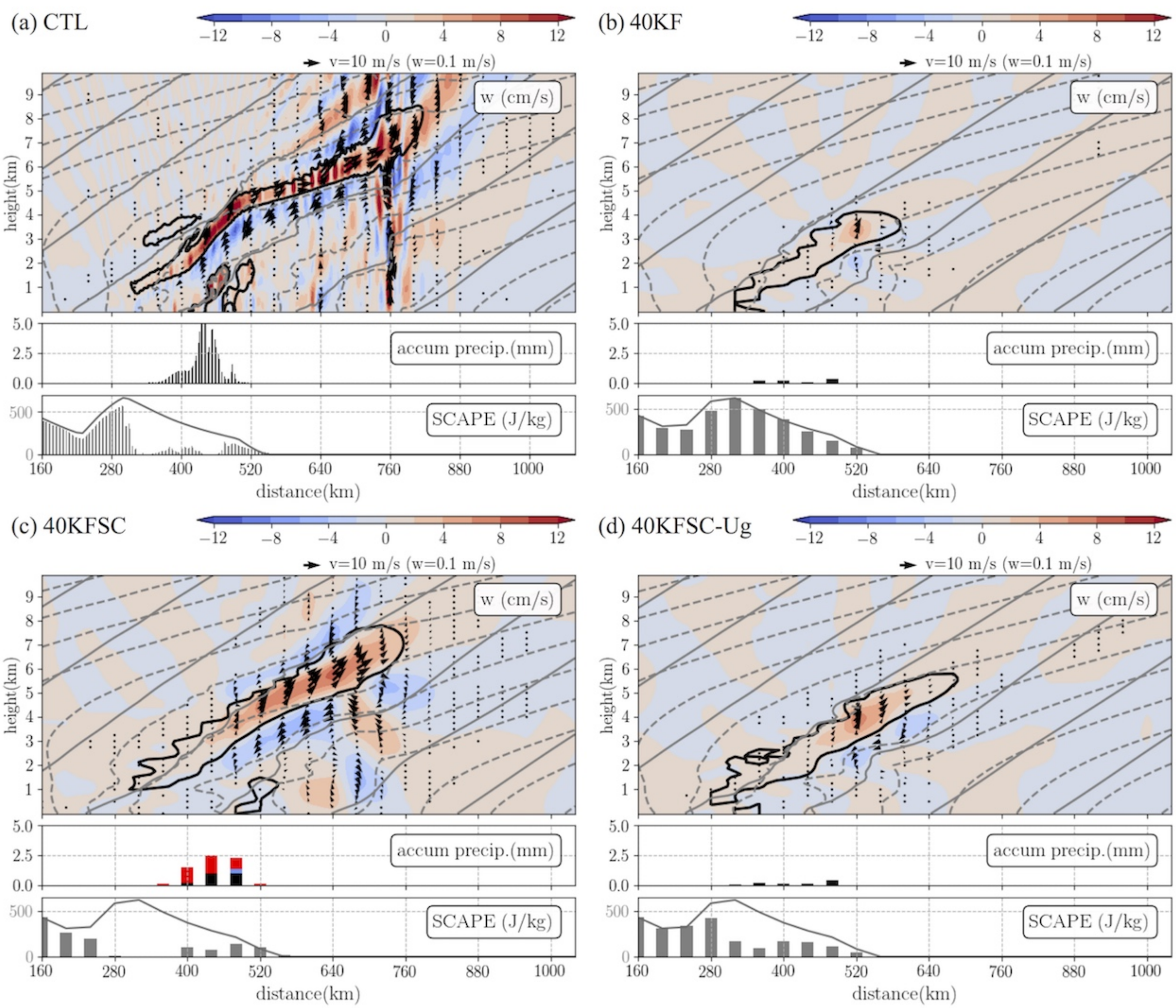


**Fig. 5.4**: 2D idealized simulation of free slantwise convection for (a) CTL, (b) 40KF, (c) 40KFSC, and (d) 40KFSC-Ug at 25 h. The uppermost subpanel shows the vertical velocity (shaded; cm s$^{-1}$), constant surfaces of $\theta_e^*$ (gray dashed contours) and $M_g$ (gray solid contours), RH= 100% (black contours), and the transverse circulation ($v$, $w$) (vectors). The lower two subpanels show the accumulated precipitation (black, blue, and red bars are from microphysics, KF, and the SC schemes, respectively; mm) and SCAPE (gray bars shows the current values while the solid line shows the initial values; J kg$^{-1}$ ), respectively. SCAPE is recorded at the location where the $M_g$ surfaces intersect the ground.

Ug; Fig. 5.4d). The results show that 40KFSC-Ug indeed consumes more SCAPE than 40KF. Moreover, because the momentum tendencies tend to destroy the local thermal-wind balance, the dynamics will act to restore it by generating unstable motions. A stronger slantwise ascent (peak $w \sim 8$ cm s$^{-1}$) than 40KF is therefore produced, but these effects are less pronounced than 40KFSC. The precipitation in 40KFSC-Ug is still mininmal, suggesting that parameterizing the latent heating effects is critical to bring the coarse-gridded simulation closer to CTL.

The overall time evolution of some horizontally averaged convective properties also supports the above findings (Fig. 5.5). Compared to 40KF, 40KFSC-Ug exhibits slightly stronger conditionally averaged $w$ and the diabatic heating, with both peak values extending to a higher altitude (Fig. 5.5b, f). However, the total precipitation increases only by $\sim 10\%$ if the SC scheme adjusts only the momentum. When the condensational effects are included (40KFSC), the $w$, diabatic heating and precipitation all intensify remarkably (Fig. 5.5c, g, k). One may question that $w$ appears too strong in 40KFSC with respect to CTL, but note that the calculation is taken wherever $w$ is positive, which includes many small-scale regions scattered outside of the primary slantwise band in CTL. The total domain-averaged precipitation in 40KFSC (0.327 mm) becomes four to five times larger than that in 40KF (0.06 mm) and 40KFSC-Ug (0.07 mm), closer to the value in CTL (0.397 mm).

It is worth noting that in 40KFSC, while the diagnosed precipitation from the SC scheme accounts for 60% of the total precipitation, the precipitation from the microphysics scheme also increases by about 55% from that in 40KFSC-Ug. In other words, the parameterized heating over a deep layer also strengthens the resolvable slantwise circulation. The KF scheme produces some precipitation ($\sim$0.02 mm) in 40KFSC versus none in 40KF. This is because, during the evolution of the slantwise convection, a shallow-layer of conditional instability emerges due to the differential advection by the slantwise circulation (see Chapter 4). Comparing 40KFSC with CTL, although there is still a few hours of time lag during the initial spin-up, similar slopes of the maximum convective properties on the height-time plot indicate similar growth rates in height once the convection is kicked off.

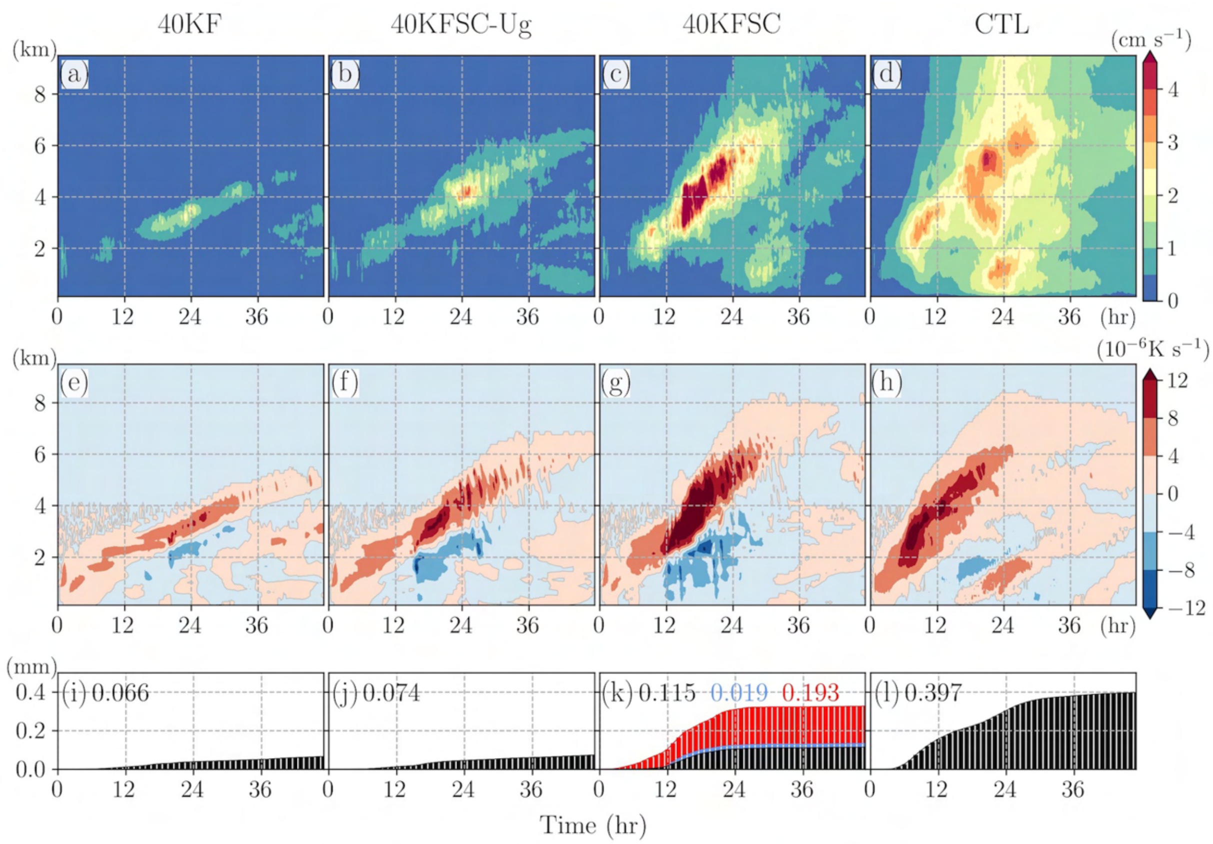


**Fig. 5.5**: Time-height distribution of the horizontally-averaged (a)-(d) $w$ over the ascent region (shaded, cm s$^{-1}$) and (e)-(h) diabatic heating (shaded, $10^{-6}$ K s$^{-1}$) for experiments from left to right: 40KF, 40KFSC-Ug, 40KFSC, and CTL. (i)-(l) present the domain-averaged precipitation (mm) accumulated over time, and the numbers note the total values at the end of the 48-h simulations. The black, blue, and red bars indicate the precipitation from the microphysics, KF, and SC schemes, respectively.

## 5.5 Results: a real case study

The excellent performance of the SC scheme in the idealized experiments motivates us to test it in a real-data simulation. We chose a banded precipitation event near a cold front over the United Kingdom from Browning et al. (2001b) and Morcrette (2004). According to Browning et al. (2001b), the cold front is associated with a surface low-pressure centre that deepened by 36 hPa in 12 hours from 1800 on Oct 29, 2000, to 958 hPa over the UK Midlands (Fig. 5.6a). The Met Office surface site at Camborne recorded a 3 degree C drop in temperature within 10 minutes when the surface cold front passed by, and the radar observation suggested that the rainfall intensity could be as high as 32 mm $h^{-1}$ (Fig. 5.6b). Using the Doppler wind-profiling radar, Browning et al. (2001b) examined the cross-band structures of this cold-frontal system. Although the focus was placed on the boundary-layer convergence features and the associated intense line convection at low levels, it was observed that they partially feed a deep layer of rearward-sloping ascent above. The same case was later revisited by Morcrette (2004). His diagnosis using the global version of the Met Office Unified Model output (with a grid spacing of around 60 km over the study region) showed that SCAPE is two times more than CAPE along the cold frontal region. Additionally, another diagnostic called "Vertically-integrated extent of Realisable conditional Symmetric instability (VRS)" that identifies the air thickness where CSI, moisture and lift coexist, is also remarkably higher than the similar diagnostic but for conditional instability (see his Fig. 2.15). Therefore, there is evidence of a high likelihood of slantwise convection in this event.

We conduct 24-hour stimulations initialized at 1200 UTC on Oct 29, 2000, using the WRF (v4.1.5) model. Three experiments all cover a geographic domain of 4800 km by 4800 km (D1 in Fig. 5.6c). For the initialization and lateral boundaries, we use the NCEP FNL Operational Global Analysis data. The coarse-gridded simulation, 40KFr, is run at a grid spacing of 40 km. The parameterized physics include the Thompson microphysics scheme (Thompson et al., 2008), RRTMG (Rapid Radiative Transfer Model for GCMs) scheme for both longwave and shortwave radiation (Iacono et al., 2008), MYJ (Mellor-Yamada-Janjic) planetary boundary layer scheme (Janjić, 1994), and the KF cumulus scheme. Experiment

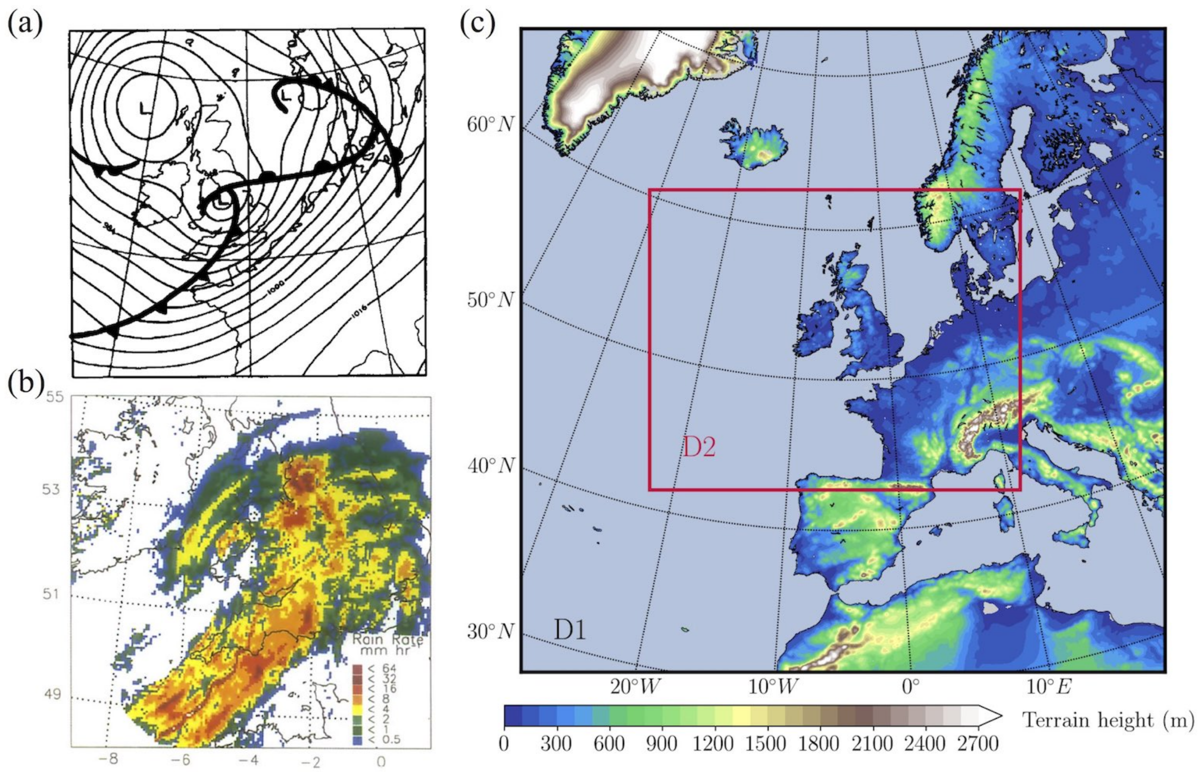


**Fig. 5.6**: (a) Met Office surface analysis at 0600 UTC on Oct 30, 2000. (b) Weather radar network display at 0400 UTC, showing the estimated rainfall intensities (shaded; mm $h^{-1}$). Both (a)-(b) are taken from Browning et al. (2001b). (c) The domain configuration for the WRF simulations conducted in this study. D1 and D2 represent domains with 10- and 3.333-km grid spacing, respectively, for the CTLr experiment. For the experiments 40KFr and 40KFSCr, only D1 is used with a grid spacing of 40 km.

40KFSCr is the same as 40KFr but with the addition of SC scheme. The reference simulation, CTLr, contains another nested two-way interactive inner domain D2 ($2760\times2240$ km) within D1 (Fig. 5.6c). For CTLr, D1 is run with the same parameterized physics as 40KFr but a grid spacing of 10 km, and D2 is run with a grid spacing of 3.333 km and the KF scheme deactivated. All simulations contain 66 vertical levels. The comparison among CRLr, 40KFr, and 40KFSCr focuses on hours 6-18 of the integration.

CTLr shows that before the precipitation period of interest, the research area contains widely-distributed rich SCAPE residual (SCAPE-CAPE) at 1800 UTC on Oct 29 (Fig.

5.7a). A nearly west-east-oriented low-level cold front, indicated by the positive 1-km Petterssen frontogenesis (Schultz and Blumen, 2015) and compressed isotherms, is observed along 50°N. The frontal system intensifies with time and extends to the south of Ireland and southern England, while its orientation changing to southwest-northeast (Fig. 5.7d-f). The most intense precipitation occurs over the elongated narrow zone where strong frontogenesis is present, and SCAPE residual of over 400 J kg$^{-1}$ drops significantly within 9∼12 hours, correlating with weak to moderate precipitation over a wide region (Fig. 5.7a-c, g-i). While the low-level frontogenesis remains active at 0400 UTC on Oct 30, the surrounding areas, especially over Ireland and southern England, have been rendered nearly slantwise neutral by this time (Fig. 5.7c, f). The significant release of SCAPE could be triggered by the strengthening frontogenetical forcing, as suggested in the observational study of Emanuel (1988). Dynamically, it is difficult to separate frontogenesis and the pure release of CSI due to their similar circulation responses and operating timescales (Schultz and Schumacher, 1999). Moreover, CSI often coincides with frontal zones as it is favored in strongly baroclinic environments, and the release of CSI may enhance frontogenesis via mass convergence (Emanuel, 1983a) or the vertical tilting term (Balasubramanian and Yau, 1994a). We emphasize that the purpose of this study is not to identify the dominant process in CTLr but to evaluate the performance of the SC scheme on the coarse-gridded simulation.

The spatial distribution of SC calls generally agrees with the simulated precipitation, suggesting that our trigger function is physically reasonable (Fig. 5.8). During the 12-hour period of interest, the total SC calls have a peak number of 50, equivalent to an effective time of 8 hours, to the south of England. The simulated precipitation for different experiments is displayed in Fig. 5.9. 40KFr reasonably captures the curved band(s) but the peak value (∼50 mm) is underestimated and located some distance away from that observed in CTLr (86.7 mm). While the precipitation distribution in 40KFr exhibits two separated

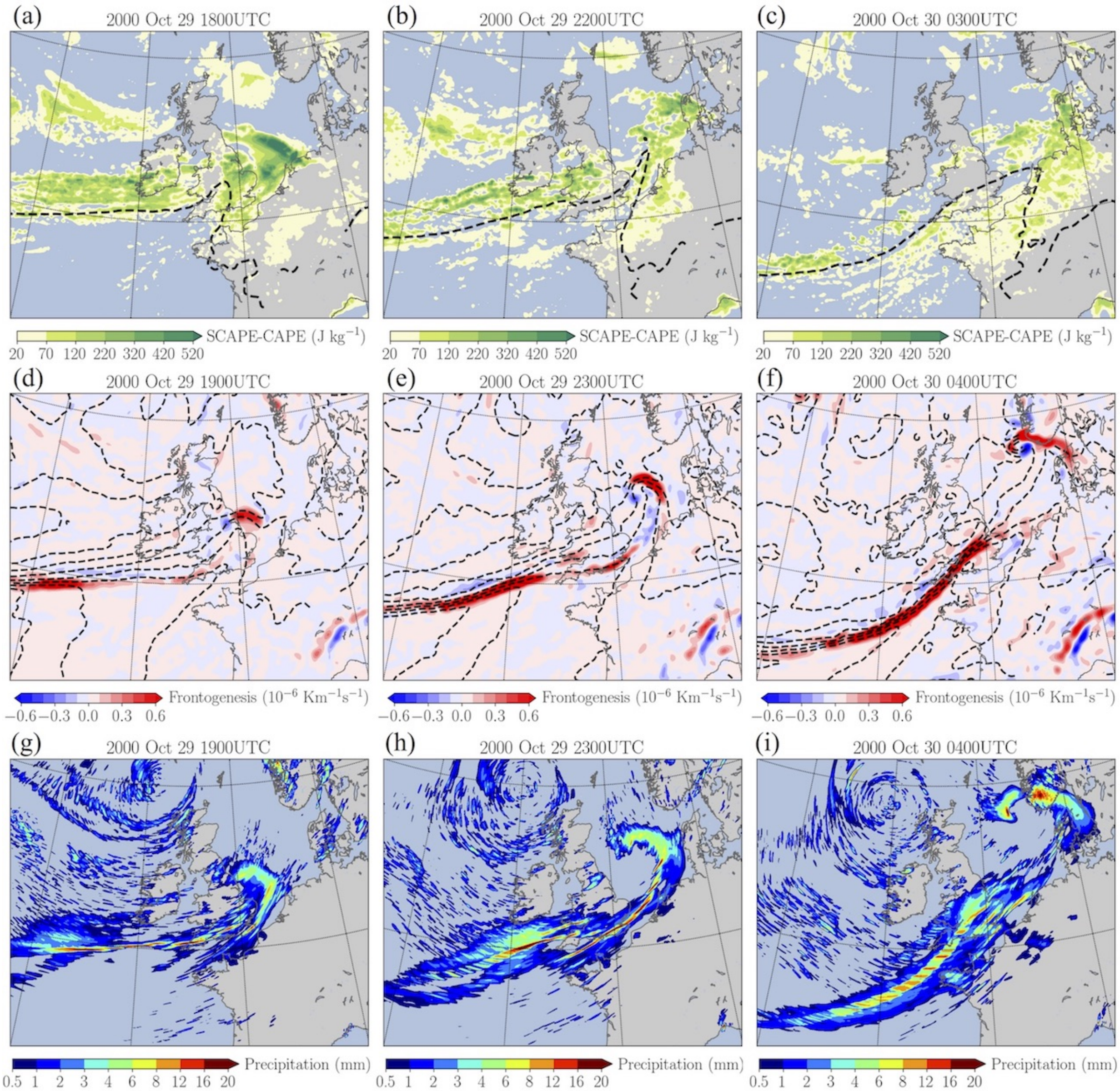


**Fig. 5.7**: Simulated results for CTLr: (a)-(c) SCAPE residual (SCAPE-CAPE; shaded; J kg$^{-1}$) and the 900-hPa isotherm of 288 K. (d)-(f) Pettersen frontogenesis for 3D flows at 1 km (shaded; K m$^{-1}$ s$^{-1}$) and 900-hPa potential temperature (dashed contours with an interval of 1.5 K). (g)-(i) Hourly precipitation (shaded; mm). (a)-(c) are shown at Oct 29, 18 UTC, 22 UTC, and Oct 30, 03 UTC, respectively, and (d)-(f), (g)-(i) are shown one hour later than (a)-(c), respectively. Precipitation is displayed using the 3.333-km data, but the rests are shown using the 10-km data.

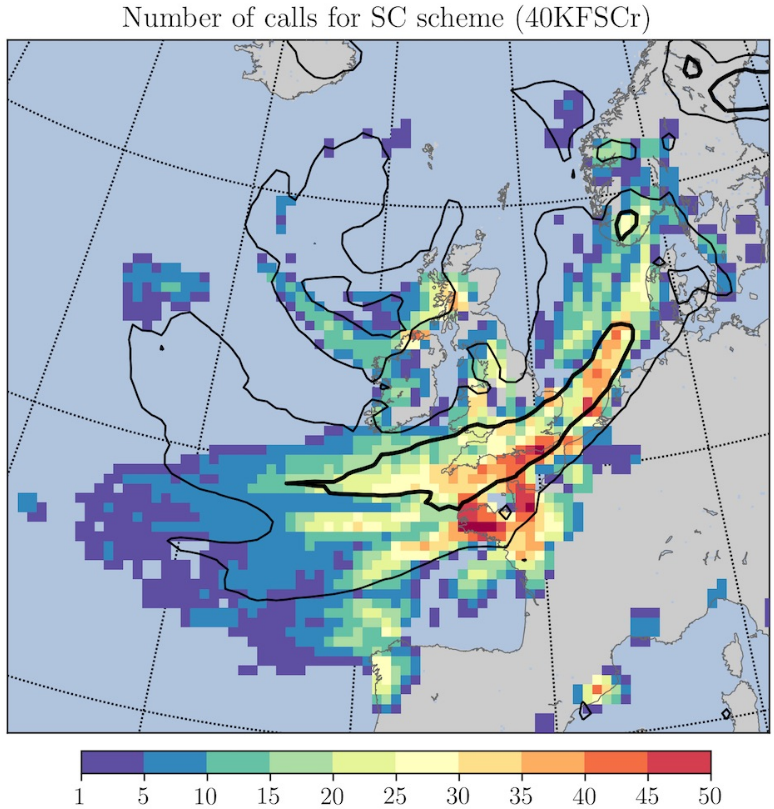


**Fig. 5.8**: Total number of calls for the SC scheme (shaded) and accumulated precipitation (black contours; thin and thick for 5 and 20 mm, respectively) during a 12-hour period from 1800 UTC on Oct 29 for 40KFSCr.

narrow lines, 40KFSCr shows precipitation focused over one major band. The location of the peak precipitation in 40KFSCr is in better agreement with CTLr. To quantitatively compare the precipitation forecast between 40KFr and 40KFSCr, the equitable threat score (ETS; e.g., Schaefer, 1990) is calculated over the domain shown in Fig. 5.9a-c. The 12-h precipitation in 40KFr and 40KFSCr are first bilinearly interpolated to the 3.333-km grid, and CTLr is considered as the truth. Over a range from 0 to 1, a larger ETS indicates a higher consistency with CTLr and therefore a better quantitative precipitation forecast skill. Whereas 40KFr has a slightly higher ETS than 40KFSCr for weak rainfall, the difference is small. A notably higher ETS is found in 40KFSCr than 40KFr for moderate to large rainfall thresholds (25 to 45 mm; Fig. 5.9d).

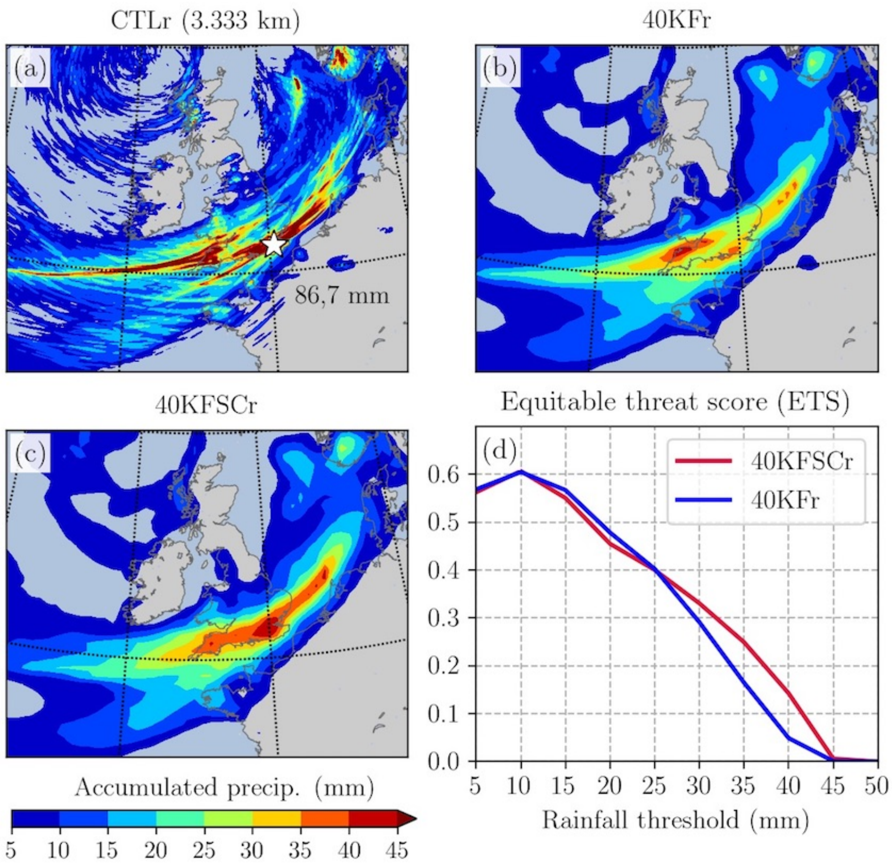


**Fig. 5.9**: Accumulated precipitation (shaded; mm) over 12 hours starting from 1800 UTC on Oct 29 for (a) CTLr (with 3.333-km grid), (b) 40KFr, and (c) 40KFSCr. The star in (a) indicates the maximum of 86.7 mm. (d) The equitable threat score at different rainfall thresholds for 40KFr (blue) and 40KFSCr (red) calculated over the domain in (b)-(c).

Contribution from different schemes to the total precipitation difference between 40KFSCr and 40KFr is examined (Fig. 5.10). As the SC scheme acts to adjust the environment toward CSI neutral, which is conditionally stable, it is not surprising to see that the KF scheme produces less precipitation in 40KFSCr. Although the significant reduction in the cumulus scheme spreads over the entire precipitation band, it is largely offset by the increase in large-scale precipitation due to the enhanced grid-scale updrafts with the addition of SC scheme. Combining with the additional SC-parameterized precipitation over some local regions, the net difference is mostly positive along the elongated band with a maximum difference of > 10 mm coinciding with the peak in CTLr.

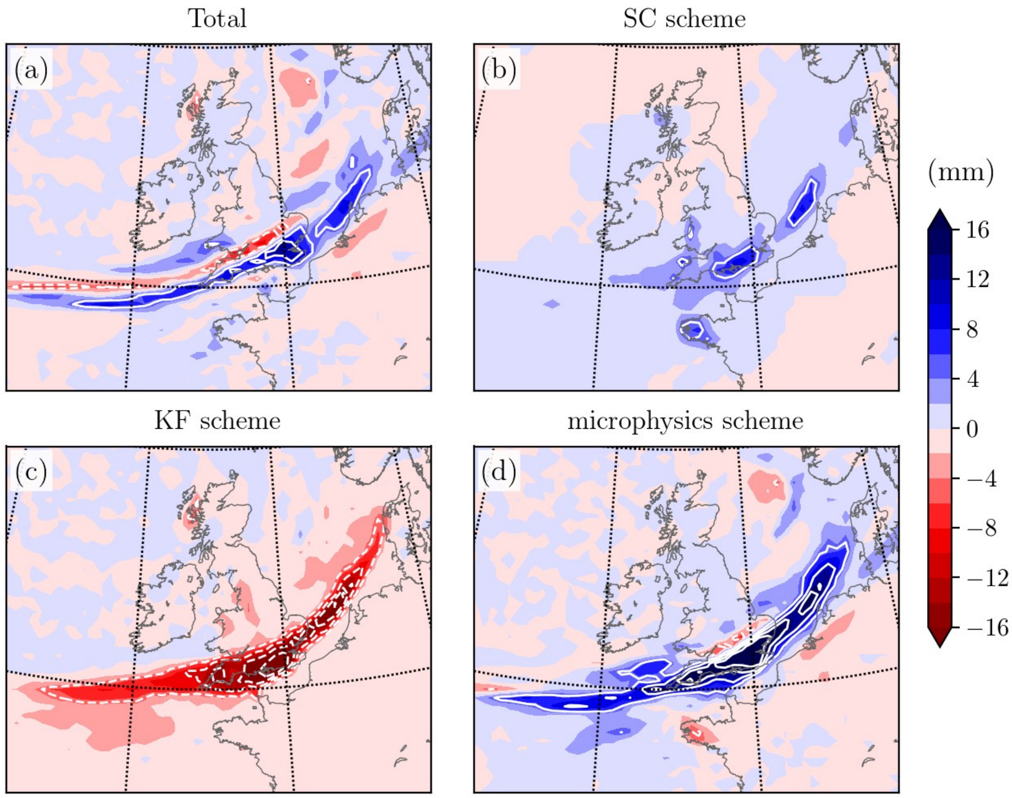


**Fig. 5.10**: The difference of 12-h accumulated precipitation between 40KFSCr and 40KFr (shaded; white contours indicate $\pm$ 5, 10, 15, 20 mm). Each panel shows differences in (a) total, (b) SC scheme, (c) KF scheme, and (d) microphysics (grid-resolved) scheme.

A closer examination at a given time when 40KFSCr exhibits notably stronger precipitation rates than 40KFr shows that the former has lower SCAPE (Fig. 5.11). This feature resembles the SCAPE distribution in CTLr, indicating that the SC scheme successfully helps release SCAPE over a KF-only simulation. Cross-sections through a precipitating band, perpendicular to the mid-level horizontal winds (from A to B in Fig. 5.11) are constructed to provide more insights. Figure 5.12 shows a low-level southwesterly flow on the warmer side of the band, consistent with the reported warm conveyor layer belt that feeds the moist ascending air in Browning et al. (2001b). In CTLr, the strong updraft has its base in close proximity to strong frontogenesis over the lowest 2 km, where conditional instability is also present (Figs. 5.12a-b). Whereas $w$ is peaked at around 2 km, the upward motion with $w$ >15 cm s$^{-1}$ and saturation extend upward beyond 8 km, penetrating to upper levels where the environment is conditionally stable. The $M_g$ surfaces are generally parallel to the $\theta_e^*$ surfaces on the cooler and lower frank of the tilted updraft. Regions with CSI are small and scattered.

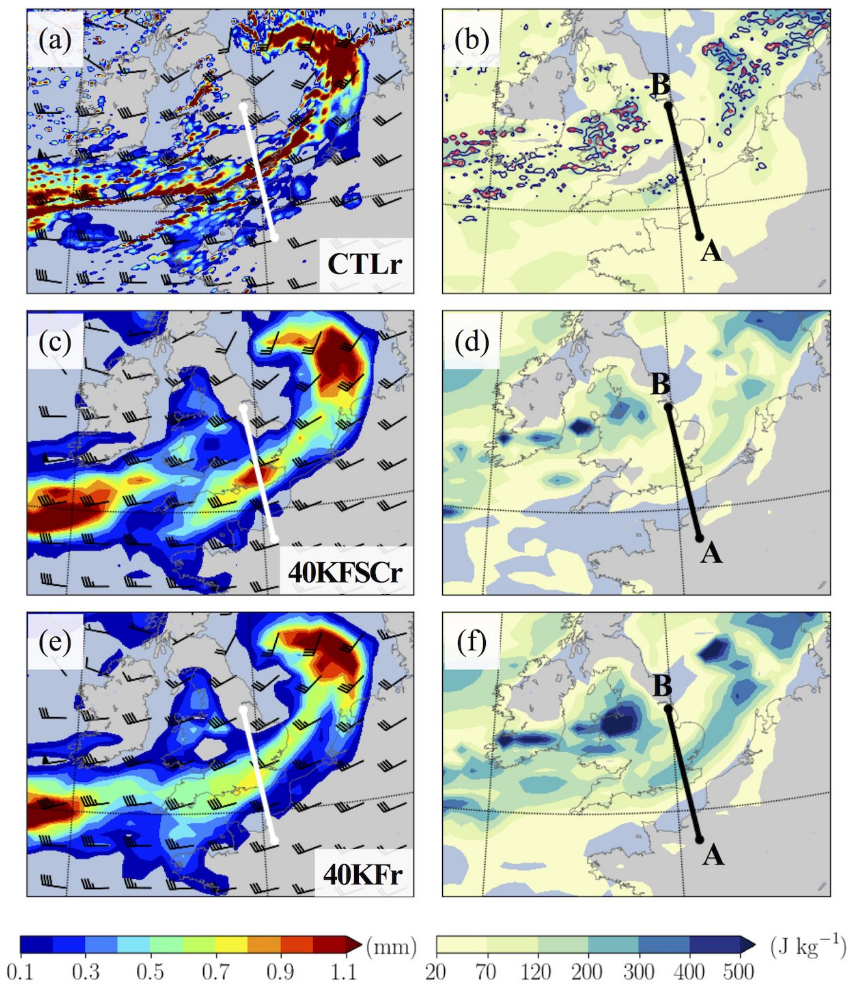


**Fig. 5.11**: (a) Hourly precipitation (shaded; mm), 500-hPa winds (barbs; m s$^{-1}$) and (b) SCAPE (shaded; J kg$^{-1}$) for CTLr at 2215 UTC. (c)-(d) And (e)-(f) are same as (a)-(b), respectively, but for 40KFSCr and 40KFr, respectively. In (b), the shading shows SCAPE averaged onto the 40-km grid. Dark blue and red contours indicate SCAPE of 200 and 400 J kg$^{-1}$, respectively, on the original 3.333-km grid.

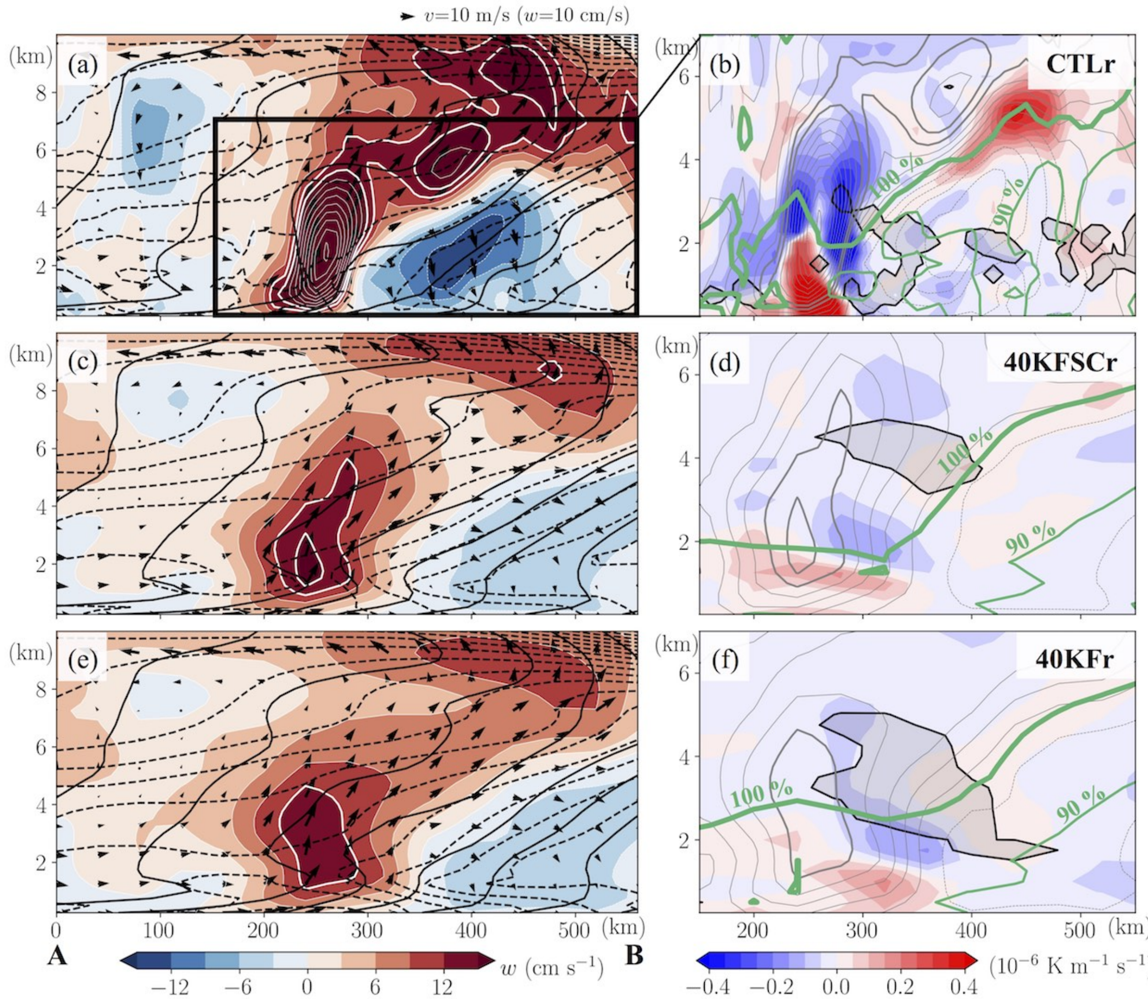


**Fig. 5.12**: A cross-section taken along line A-B in Fig. 5.11 for (a) vertical velocity (shaded; cm $s^{-1}$; white contours shows interval of 3 cm $s^{-1}$; thick white contours indicate 12 and 15 cm $s^{-1}$), constant $\theta_e^*$ (black dashed) and $M_g$ (black solid) surfaces, and transverse circulation ($v$, $w$) (vectors). (b) Same as (a) but zoom in for Petterssen frontogenesis (shaded; $10^{-6}$ K $m^{-1}$ $s^{-1}$), vertical velocity (gray contours), RH=90, 100% (green contours), and regions with CSI (gray shades). (c)-(d) And (e)-(f) are the same as (a)-(b), respectively, but for 40KFSCr and 40KFr, respectively.

Comparing the coarse-gridded runs 40KFSCr and 40KFr, the former exhibits a stronger updraft that extends to a higher altitude and has a tilt that more resembles CTLr (Fig. 5.12a, c, e). The $\theta_e^*$ and $M_g$ surfaces on the lower and cooler side of the updraft are more parallel in 40KFSCr than in 40KFr, the latter of which has a larger region of CSI remaining at a lower altitude than the former (Fig. 5.12d, f). Lindstrom and Nordeng (1992) noted a greater frontogenetic response in their simulation with slantwise convection parameterized than the one without. However, in this case, the near-surface frontogenetic forcing appears weaker with the SC scheme. This difference may be associated with case-to-case variability or the fact that our SC scheme is designed to reduce the vertical wind shear and therefore overall counteracts frontogenesis on the large scales. Emanuel's (1985) theoretical model and Sanders and Bosart's (1985) observational study showed that in a saturated frontal region where slantwise convection has occurred leaving small conditional symmetric stability, an intense response in vertical motion might ensue on the warmer side of maximum forcing when the flow is subjected to a given large-scale frontogenesis. This feature may explain the stronger and deeper updraft in 40KFSCr, which has gone through a larger extent of slantwise convective adjustment than in 40KFr.

## 5.6 Conclusions and suggestion for future work

In this study, a modified parameterization scheme for slantwise convection (SC) based on Ma (2000) is proposed. We implement the SC scheme in the Weather Research and Forecasting (WRF) model and evaluate its performance for two different test cases. The first test case is the 2D idealized, unforced simulation of releasing pure conditional symmetric instability (CSI) in an initially conditionally stable environment. The second case is a real-data simulation of precipitation band(s) along a cold front on Oct 29-30, 2000, near the UK, where the environment contains both CSI and conditional instability.

The modified SC scheme works as a supplement to the existing cumulus parameterization scheme (CPS) for upright convection. The central concept of this SC scheme is to remove positive slantwise convective available potential energy (SCAPE) by adjusting the momentum field to render the environment toward slantwise neutrality given a prescribed adjustment timescale (5 and 3 hours for the unforced idealized and real-data simulations, respectively). Condensational heating and moisture loss associated with the upward motion are also parameterized. Unlike most of the CPS acting locally as a 1D scheme, the SC scheme performs on a 2D cross-section perpendicular to the local thermal winds.

The performance of the SC scheme is tested using the 40-km horizontal grid spacing. Note that this is the range where mesoscale features, including slantwise convection, may be partially resolved. As opposed to parameterizing the fully unresolved subgrid processes, the cases presented here involve the parametrization for slantwise convection in its gray zone [e.g., O(10 km)-O(100 km)], where most of the general circulation models are currently at or entering in the near future. Both test cases show that the addition of SC scheme helps to release more SCAPE and produces stronger, deeper updrafts and larger precipitation than the same 40-km CPS-only simulation, yielding improved agreement with the fine-gridded reference simulation.

Between the two test cases, the benefits of parameterizing slantwise convection are more significant in the idealized pure CSI case with no external forcings. The upright CPS [Kain-Fritsch (KF) scheme] is not active regardless of the activation of SC scheme because the environment is initially stable in the vertical direction and becomes only weakly unstable at a later time. The additional SC scheme releases SCAPE, which the KF scheme fails to do, and the total domain-averaged precipitation becomes four to five times larger than the KF-only run. The SC itself contributes to 60% of the total precipitation, and the microphysics scheme increases by 55%. As for the real-data case, the precipitation difference between two 40-km runs (KF-only and KF+SC) is smaller than that for the pure CSI idealized case. This is because the precipitation increase by the SC and microphysics schemes is largely offset by the precipitation reduction in the KF scheme as the slantwise neutral state that the SC scheme adjusts toward is conditionally stable. Nevertheless, by releasing more SCAPE over the KF-only run, the run with both KF and SC schemes still has a net precipitation increase with a maximum of $> 10$ mm coinciding with the peak precipitation in the fine-gridded run. Therefore, whereas for weak rainfall, the quantitative precipitation forecast skill (equitable threat score; ETS) does not differ much between the KF-only and KF+SC runs, the latter has a notably higher ETS for moderate to large rainfall thresholds (25-55 mm).

While the modified SC scheme is largely built based on testing in the idealized pure CSI simulation, more investigation is required to validate the parameters used here and to test its performance in different environmental conditions. For example, the competing effect between the KF and microphysics schemes with the inclusion of SC scheme are worthy of detailed examinations. Some improvements in the SC scheme itself may be considered, such as unifying the momentum and thermodynamic adjustments using a consistent algorithm. Another example is the estimation of adjustment path. While we utilize the grid-resolved relative humidity as a simple indicator to aid the estimation, this may not be optimal if the environment is nearly saturated everywhere or the subgrid saturation is unresolved. A more theory-consistent formulation may be derived, taking into consideration the localized conditional stability, inertial stability, and low-level ascent direction. Nevertheless, this study exhibits two cases in which parameterizing slantwise convection is notably beneficial in 40-km-gridded simulations, especially in improving the precipitation forecasts. Given the importance of slantwise convection in high-impact weather events (e.g., Reuter and Yau, 1990; Gray et al., 2011; Glinton et al., 2017; Chen et al., 2018), parameterizing slantwise convection in global circulation models may improve the accuracy of climate projection as well as the initial/boundary conditions used for the short-term regional forecast in operational models.

# Chapter 6

# Concluding summary and future directions

## 6.1 Summary

While the importance of convection representation in numerical weather/climate modeling is well recognized, most of the attention has been placed on upright convection. Slantwise convection, resulting from the release of conditional symmetric instability (CSI), is often overlooked. This dissertation aims to fill important gaps in this problem by studying slantwise convection following three major steps.

The first question we attempt to answer is whether, and where, slantwise convection is climatologically significant. Chapter 2 analyzes the 37-yr global ERA-Interim reanalysis data set to calculate two indices for assessing the potential for slantwise convection: slantwise convective available potential energy (SCAPE) and vertically integrated extent of realizable symmetric instability (VRS). Their long-term-averaged distributions show that the air over the midlatitude westernmost oceans (i.e., storm-track regions) is the most susceptible to slantwise convection due to strong baroclinicity and abundant moisture. It is also found that SCAPE, accommodating both upright convection and slantwise convection, correlates with precipitation more strongly than CAPE over subtropical and midlatitude areas. Moreover, for the average cyclones, the probability of slantwise convection (with positive VRS) within a 300-km radius of the storm center is about 30% at any given time. This probability increases to 57% for a rapid deepening cyclone. Furthermore, it is found that while there are no sharp SCAPE and VRS changes during the lifetime of non-explosive cyclones, a notable drop of SCAPE and VRS, indicating a significant slantwise convective adjustment, coincides with the rapid intensification of the explosive storms.

The above results indicating the importance of slantwise convection motivates the second part of the study: to investigate the numerical model grid spacing at which slantwise convection can be adequately resolved. We conduct 2D idealized simulations for a pure CSI release process in an unforced, conditionally (vertically) stable environment using the Weather Research and Forecasting (WRF) model. The simulated results with different horizontal (cross-band) grid spacings from 1 to 40 km are compared. While momentum budget analysis helps identify the critical flow dynamics, we find that post-processing methods often lead to significant error (residual) and may hinder an accurate interpretation of the momentum budget. An in-line retrieval tool is therefore implemented in WRF, as described in Chapter 3. The in-line retrieval method is highly accurate with the 99th percentile residual of the budget equation always smaller than 0.1% of the local tendency term.

In Chapter 4, we return to the physical discussion on the sensitivity of explicit slantwise convection representation to horizontal grid spacing ($\Delta y$). It is shown that the larger-scale feedbacks associated with slantwise convection converge numerically when $\Delta y$ of 5 km or below is reached. This grid spacing is required not only to properly resolve the pressure gradients for horizontal acceleration but to realistically release a shallow layer of conditional instability (CI) that inevitably develops via the differential advection of saturation equivalent potential temperature ($\theta_e^*$) by the slantwise updraft. The resolved, embedded small-scale upright convection can energize the upper-level slantwise band by transporting low momentum air upward, increasing the localized inertial instability aloft and releasing the remaining SCAPE. The convective cell also enhances the large-scale CSI neutralization via strong downward transport of high $\theta_e^*$ as its descending flow is oriented more vertically than the slantwise returning downdraft. Therefore, simulations with $\Delta y \leq$ 5 km exhibit a faster and larger SCAPE consumption, producing a greater amount of precipitation and stronger upward momentum transports that peak at a higher altitude than the coarse-gridded runs.

Finally, in Chapter 5, we implement and test a modified slantwise convection (SC) parameterization scheme based on Ma (2000) in the WRF model. The scheme, when triggered, adjusts the momentum field to remove positive SCAPE given a prescribed adjustment timescale. To identify where to apply the adjustment, it requires a local coordinate transformation to a cross-section in which CSI operates, i.e., along the horizontal temperature gradient. Then, an adjustment path in this cross-section is parameterized. The impacts of the additional SC scheme to the existing convective/cumulus parameterization scheme (Kain-Fritsch scheme) for upright convection are evaluated in two test cases: the idealized CSI simulation from Chapter 4 and a real-data simulation in which the environment contains both CSI and CI. Both cases show improvements in the quantitative precipitation forecast for the coarse-gridded runs with the SC scheme. The parameterized momentum tendency, typically a source and a sink in the low- and mid/upper- levels, respectively, reduces the vertical wind shear along the slantwise path, rendering the flow less susceptive to CSI while indirectly seeding the grid-resolved slantwise circulation. The additionally parameterized cloud-layer latent heating due to condensation further strengthens the slantwise updraft, producing significantly more precipitation, all of which bring the coarse-gridded runs to be in better agreement with the fine-gridded reference runs.

## 6.2 Avenues for future work

While the results from Chapter 5 are promising, the SC scheme requires more testing to verify its utility for different environmental conditions. In particular, our real-data simulation suggests that, when CI and CSI coexist, the additional SC scheme may significantly offset the CPS parameterized effects. Therefore, the interactive feedback between the SC scheme and the CPS, and whether it may lead to unphysical results (e.g., "double counting"), require careful investigation. In this regard, a suggestion for future work is to conduct simulations for flows with both CI and CSI using an idealized setting to better examine the SC-CPS compatibility. Additional complexities, such as large-scale forcings, can then be included one by one to investigate how the SC scheme performs differently. Moreover, the present study tests the SC scheme with a fixed $\Delta y = 40$ km and there is the need to evaluate the performance of the SC scheme at a wide range of $\Delta y$ from finer to coarser than 40 km.

As for the SC scheme itself, while we have made several modifications to the scheme originally developed by Ma (2000), there is still substantial room for improving its physics. For example, in all the existing slantwise convective parameterization schemes, including the one presented here, there is the assumption that the CSI-neutral reference state is achieved by adjusting either $\theta_e^*$ or geostrophic absolute momentum ($M_g$) for simplicity. A more realistic transition could involve both fields and is an area worthy of testing. Another SC component that is highly simplified is its precipitation. The current SC assumes that precipitation for a rising air tube falls out entirely to one location below its slantwise path at any given time. Although the total accumulated SC precipitation from our 40-km idealized run still exhibits a broad distribution (because the fall-out location evolves with time and there may exist more than one unstable air tube at the same time), a more physical choice is to assume precipitation falling from the entire slantwise path, possibly weighted by the vertical velocity at different heights.

Finally, after the SC scheme has been well validated, it is desirable to test it in the global circulation climate models. Its application may be beneficial not only for climate studies but also for providing improved initial/boundary conditions for downscaling to regional simulations.

# Bibliography

Abarca, S. F., and M. T. Montgomery, 2013: Essential dynamics of secondary eyewall formation. *Journal of the Atmospheric Sciences*, **70 (10)**, 3216–3230, doi:10.1175/JAS-D-12-0318.1.

Adler, R. F., and Coauthors, 2003: The version-2 global precipitation climatology project (GPCP) monthly precipitation analysis (1979–Present). *Journal of Hydrometeorology*, **4 (6)**, 1147–1167, doi:10.1175/1525-7541(2003)004⟨1147:TVGPCP⟩2.0.CO;2.

Andersen, J. A., and Z. Kuang, 2012: Moist static energy budget of MJO-like disturbances in the atmosphere of a zonally symmetric aquaplanet. *Journal of Climate*, **25 (8)**, 2782–2804, doi:10.1175/JCLI-D-11-00168.1.

Anthes, R. A., 1977: A cumulus parameterization scheme utilizing a one-dimensional cloud model. *Monthly Weather Review*, **105 (3)**, 270 – 286, doi:10.1175/1520-0493(1977)105⟨0270:ACPSUA⟩2.0.CO;2.

Arakawa, A., 1993: *Closure Assumptions in the Cumulus Parameterization Problem*, 1–15. American Meteorological Society, Boston, MA, doi:10.1007/978-1-935704-13-3_1.

Arakawa, A., 2004: The cumulus parameterization problem: Past, present, and future. *Journal of Climate*, **17 (13)**, 2493 – 2525, doi:10.1175/1520-0442(2004)017⟨2493:RATCPP⟩2.0.CO;2.

Arakawa, A., J.-H. Jung, and C.-M. Wu, 2011: Toward unification of the multiscale modeling of the atmosphere. *Atmospheric Chemistry and Physics*, **11 (8)**, 3731–3742, doi:10.5194/acp-11-3731-2011.

Arakawa, A., and V. R. Lamb, 1977: Computational design of the basic dynamical processes of the UCLA general circulation model. **17**, 173 – 265, doi:10.1016/B978-0-12-460817-7.50009-4.

Arakawa, A., and W. H. Schubert, 1974: Interaction of a cumulus cloud ensemble with the large-scale environment, part i. *Journal of Atmospheric Sciences*, **31 (3)**, 674 – 701, doi:10.1175/1520-0469(1974)031⟨0674:IOACCE⟩2.0.CO;2.

Arnault, J., R. Knoche, J. Wei, and H. Kunstmann, 2016: Evaporation tagging and atmospheric water budget analysis with WRF: a regional precipitation recycling study for West Africa. *Water Resources Research*, **52 (3)**, 1544–1567, doi:10.1002/2015WR017704.

Baker, L. H., S. L. Gray, and P. A. Clark, 2014: Idealised simulations of sting-jet cyclones. *Quarterly Journal of the Royal Meteorological Society*, **140 (678)**, 96–110, doi:10.1002/qj.2131.

Balasubramanian, G., and M. K. Yau, 1994a: Baroclinic instability in a two-layer model with parameterized slantwise convection. *Journal of the Atmospheric Sciences*, **51 (7)**, 971–990, doi:10.1175/1520-0469(1994)051⟨0971:BIIATL⟩2.0.CO;2.

Balasubramanian, G., and M. K. Yau, 1994b: The effects of convection on a simulated marine cyclone. *Journal of Atmospheric Sciences*, **51 (16)**, 2397 – 2417, doi:10.1175/1520-0469(1994)051⟨2397:TEOCOA⟩2.0.CO;2.

Balasubramanian, G., and M. K. Yau, 1995: Explosive marine cyclogenesis in a three-layer model with a representation of slantwise convection: A sensitivity study. *Journal of Atmospheric Sciences*, **52 (5)**, 533 – 550, doi:10.1175/1520-0469(1995)052⟨0533:EMCIAT⟩2.0.CO;2.

Barnes, S. L., F. Caracena, and A. Marroquin, 1996: Extracting synoptic-scale diagnostic information from mesoscale models: The eta model, gravity waves, and quasigeostrophic diagnostics. *Bulletin of the American Meteorological Society*, **77 (3)**, 519 – 528, doi:10.1175/1520-0477(1996)077⟨0519:ESSDIF⟩2.0.CO;2.

Bengtsson, L., K. I. Hodges, and E. Roeckner, 2006: Storm tracks and climate change. *Journal of Climate*, **19 (15)**, 3518–3543, doi:10.1175/JCLI3815.1.

Bennetts, D. A., and B. J. Hoskins, 1979: Conditional symmetric instability - a possible explanation for frontal rainbands. *Quarterly Journal of the Royal Meteorological Society*, **105 (446)**, 945–962, doi:10.1002/qj.49710544615.

Bennetts, D. A., and J. C. Sharp, 1982: The relevance of conditional symmetric instability to the prediction of mesoscale frontal rainbands. *Quarterly Journal of the Royal Meteorological Society*, **108 (457)**, 595–602, doi:10.1002/qj.49710845707.

Betts, A. K., 1986: A new convective adjustment scheme. part i: Observational and theoretical basis. *Quarterly Journal of the Royal Meteorological Society*, **112 (473)**, 677–691, doi:10.1002/qj.49711247307.

Betts, A. K., and M. J. Miller, 1986: A new convective adjustment scheme. Part II: single column tests using GATE wave, BOMEX, ATEX and Arctic air-mass data sets. *Quarterly Journal of the Royal Meteorological Society*, **112 (473)**, 693–709, doi:10.1002/qj.49711247308.

Bromwich, D. H., J. P. Nicolas, and A. J. Monaghan, 2011: An assessment of precipitation changes over Antarctica and the Southern Ocean since 1989 in contemporary global reanalyses. *Journal of Climate*, **24 (16)**, 4189–4209, doi:10.1175/2011JCLI4074.1.

Brooks, H. E., J. W. Lee, and J. P. Craven, 2003: The spatial distribution of severe thunderstorm and tornado environments from global reanalysis data. *Atmospheric Research*, **67-68**, 73 – 94, doi:10.1016/S0169-8095(03)00045-0, european Conference on Severe Storms 2002.

Browning, K. A., D. Chapman, and R. S. Dixon, 2001a: Stacked slantwise convective circulations. *Quarterly Journal of the Royal Meteorological Society*, **127 (578)**, 2513–2536, doi:10.1002/qj.49712757803.

Browning, K. A., R. S. Dixon, C. Gaffard, and C.-G. Wang, 2001b: Wind profiler measurements in the storm of 30 October 2000. *Weather*, **56 (10)**, 367–373.

Bryan, G. H., and J. M. Fritsch, 2002: A benchmark simulation for moist nonhydrostatic numerical models. *Monthly Weather Review*, **130 (12)**, 2917–2928, doi:10.1175/1520-0493(2002)130⟨2917:ABSFMN⟩2.0.CO;2.

Bélair, S., and J. Mailhot, 2001: Impact of horizontal resolution on the numerical simulation of a midlatitude squall line: Implicit versus explicit condensation. *Monthly Weather Review*, **129 (9)**, 2362 – 2376, doi:10.1175/1520-0493(2001)129⟨2362:IOHROT⟩2.0.CO;2.

Chang, E. K. M., Y. Guo, X. Xia, and M. Zheng, 2013: Storm-track activity in IPCC AR4/CMIP3 model simulations. *Journal of Climate*, **26 (1)**, 246 – 260, doi:10.1175/JCLI-D-11-00707.1.

Chen, T.-C., 2019: WRFv3.8.1_inline_budget_retrieval: Inline budget retrieval tool for 3D momentum components and potential temperature. doi:10.5281/zenodo.3373872.

Chen, T.-C., M. K. Yau, and D. J. Kirshbaum, 2018: Assessment of conditional symmetric instability from global reanalysis data. *Journal of the Atmospheric Sciences*, **75 (7)**, 2425–2443, doi:10.1175/JAS-D-17-0221.1.

Chen, T.-C., M.-K. Yau, and D. J. Kirshbaum, 2020: Towards the closure of momentum budget analyses in the wrf (v3.8.1) model. *Geoscientific Model Development*, **13 (3)**, 1737–1761, doi:10.5194/gmd-13-1737-2020.

Chen, T.-C., M.-K. Yau, and D. J. Kirshbaum, 2021: Sensitivities of slantwise convection dynamics to model grid spacing under an idealized framework. *Quarterly Journal of the Royal Meteorological Society*, doi:10.1002/qj.4003.

Chou, S. C., and A. J. Thorpe, 1993: *A Parameterization Scheme for Symmetric Instability: Tests for an Idealized Flow*, 203–217. American Meteorological Society, Boston, MA, doi: 10.1007/978-1-935704-13-3_21.

Dearden, C., G. Vaughan, T. Tsai, and J.-P. Chen, 2016: Exploring the diabatic role of ice microphysical processes in two North Atlantic summer cyclones. *Monthly Weather Review*, **144 (4)**, 1249 – 1272, doi:10.1175/MWR-D-15-0253.1.

Dee, D. P., and Coauthors, 2011: The ERA-Interim reanalysis: configuration and performance of the data assimilation system. *Quarterly Journal of the Royal Meteorological Society*, **137 (656)**, 553–597, doi:10.1002/qj.828.

Dixon, R. S., K. A. Browning, and G. J. Shutts, 2002: The relation of moist symmetric instability and upper-level potential-vorticity anomalies to the observed evolution of cloud heads. *Quarterly Journal of the Royal Meteorological Society*, **128 (581)**, 839–859, doi:10.1256/0035900021643719.

Doswell, C. A., 1987: The distinction between large-scale and mesoscale contribution to severe convection: A case study example. *Weather and Forecasting*, **2 (1)**, 3 – 16, doi:10.1175/1520-0434(1987)002⟨0003:TDBLSA⟩2.0.CO;2.

Duran, P., and J. Molinari, 2019: Tropopause evolution in a rapidly intensifying tropical cyclone: A static stability budget analysis in an idealized axisymmetric framework. *Journal of the Atmospheric Sciences*, **76 (1)**, 209–229, doi:10.1175/JAS-D-18-0097.1.

Eady, E. T., 1949: Long waves and cyclone waves. *Tellus*, **1 (3)**, 33–52, doi:10.3402/tellusa.v1i3.8507.

Eliassen, A., 1951: Slow thermally or frictionally controlled meridional circulation in a circular vortex. *Astrophysica Norvegica*, **5**, 19.

Emanuel, K. A., 1983a: The Lagrangian parcel dynamics of moist symmetric instability. *Journal of the Atmospheric Sciences*, **40 (10)**, 2368–2376, doi:10.1175/1520-0469(1983)040⟨2368:TLPDOM⟩2.0.CO;2.

Emanuel, K. A., 1983b: On assessing local conditional symmetric instability from atmospheric soundings. *Monthly Weather Review*, **111 (10)**, 2016–2033, doi:10.1175/1520-0493(1983)111⟨2016:OALCSI⟩2.0.CO;2.

Emanuel, K. A., 1985: Frontal circulations in the presence of small moist symmetric stability. *Journal of Atmospheric Sciences*, **42 (10)**, 1062 – 1071, doi:10.1175/1520-0469(1985)042⟨1062:FCITPO⟩2.0.CO;2.

Emanuel, K. A., 1988: Observational evidence of slantwise convective adjustment. *Monthly Weather Review*, **116 (9)**, 1805–1816, doi:10.1175/1520-0493(1988)116⟨1805:OEOSCA⟩2.0.CO;2.

Emanuel, K. A., 1991: A scheme for representing cumulus convection in large-scale models. *Journal of Atmospheric Sciences*, **48 (21)**, 2313 – 2329, doi:10.1175/1520-0469(1991)048⟨2313:ASFRCC⟩2.0.CO;2.

Emanuel, K. A., 1994: *Atmospheric Convection*. Oxford University Press.

Gallus, J., William A., and R. H. Johnson, 1992: The momentum budget of an intense midlatitude squall line. *Journal of the Atmospheric Sciences*, **49 (5)**, 422–450, doi:10.1175/1520-0469(1992)049⟨0422:TMBOAI⟩2.0.CO;2.

Glinton, M. R., 2013: The role of conditional symmetric instability in numerical weather prediction. Ph.D. thesis, University of Reading, 251 pp.

Glinton, M. R., S. L. Gray, J. M. Chagnon, and C. J. Morcrette, 2017: Modulation of precipitation by conditional symmetric instability release. *Atmospheric Research*, **185**, 186 – 201, doi:10.1016/j.atmosres.2016.10.013.

Gray, S. L., O. Martínez-Alvarado, L. H. Baker, and P. A. Clark, 2011: Conditional symmetric instability in sting-jet storms. *Quarterly Journal of the Royal Meteorological Society*, **137 (659)**, 1482–1500, doi:10.1002/qj.859.

Gray, S. L., and A. J. Thorpe, 2001: Parcel theory in three dimensions and the calculation of SCAPE. *Monthly Weather Review*, **129 (7)**, 1656–1672, doi:10.1175/1520-0493(2001)129⟨1656:PTITDA⟩2.0.CO;2.

Grell, D. J., G. A., and D. Stauffer, 1994: A description of the fifth-generation Penn State/NCAR Mesoscale Model (MM5). Ncar tech. note ncar/tn-398+str, 121 pp. doi:10.5065/D60Z716B.

Haualand, K. F., and T. Spengler, 2019: How does latent cooling affect baroclinic development in an idealized framework? *Journal of the Atmospheric Sciences*, **76 (9)**, 2701 – 2714, doi:10.1175/JAS-D-18-0372.1.

Hawcroft, M. K., L. C. Shaffrey, K. I. Hodges, and H. F. Dacre, 2016: Can climate models represent the precipitation associated with extratropical cyclones? *Climate Dynamics*, **47**, 679–695.

Hodur, R. M., and J. S. Fein, 1977: A vorticity Budget over the Marshall Islands During the Spring and Summer Months. *Monthly Weather Review*, **105 (12)**, 1521–1526, doi:10.1175/1520-0493(1977)105⟨1521:AVBOTM⟩2.0.CO;2.

Holton, J., 2004: *An Introduction to Dynamic Meteorology*. No. v. 1, An Introduction to Dynamic Meteorology, Elsevier Science.

Hoskins, B. J., 1974: The role of potential vorticity in symmetric stability and instability. *Quarterly Journal of the Royal Meteorological Society*, **100 (425)**, 480–482, doi:10.1002/qj.49710042520.

Huang, J., 1991: A numerical study of slantwise convection. M.S. thesis, Dept. of Meteorology, McGill University, 73 pp.

Huang, W. C.-C., Y.-H., and M. T. Montgomery, 2018: Concentric eyewall formation in Typhoon Sinlaku (2008), Part III: horizontal momentum budget analyses. *Journal of the Atmospheric Sciences*, **75**, 3541–3563, doi:10.1175/JAS-D-18-0037.1.

Iacono, M. J., J. S. Delamere, E. J. Mlawer, M. W. Shephard, S. A. Clough, and W. D. Collins, 2008: Radiative forcing by long-lived greenhouse gases: calculations with the AER radiative transfer models. *Journal of Geophysical Research: Atmospheres*, **113 (D13)**, doi:10.1029/2008JD009944.

Innocentini, V., and E. D. S. C. Neto, 1992: A numerical study of the role of humidity in the updraft driven by moist slantwise convection. *Journal of Atmospheric Sciences*, **49 (13)**, 1092 – 1106, doi:10.1175/1520-0469(1992)049⟨1092:ANSOTR⟩2.0.CO;2.

Janjić, Z. I., 1994: The step-mountain eta coordinate model: Further developments of the convection, viscous sublayer, and turbulence closure schemes. *Monthly Weather Review*, **122 (5)**, 927 – 945, doi:10.1175/1520-0493(1994)122⟨0927:TSMECM⟩2.0.CO;2.

Jeworrek, J., G. West, and R. Stull, 2019: Evaluation of cumulus and microphysics parameterizations in WRF across the convective gray zone. *Weather and Forecasting*, **34 (4)**, 1097 – 1115, doi:10.1175/WAF-D-18-0178.1.

Jiang, H., and D. J. Raymond, 1995: Simulation of a mature mesoscale convective system using a nonlinear balance model. *Journal of Atmospheric Sciences*, **52 (2)**, 161 – 175, doi:10.1175/1520-0469(1995)052⟨0161:SOAMMC⟩2.0.CO;2.

Jones, S. C., and A. J. Thorpe, 1992: The three-dimensional nature of 'symmetric' instability. *Quarterly Journal of the Royal Meteorological Society*, **118 (504)**, 227–258, doi:10.1002/qj.49711850404.

Kain, J. S., 2004: The Kain–Fritsch convective parameterization: an update. *Journal of Applied Meteorology*, **43 (1)**, 170–181, doi:10.1175/1520-0450(2004)043⟨0170:TKCPAU⟩2.0.CO;2.

Kain, J. S., and J. M. Fritsch, 1990: A one-dimensional entraining/detraining plume model and its application in convective parameterization. *Journal of Atmospheric Sciences*, **47 (23)**, 2784 – 2802, doi:10.1175/1520-0469(1990)047⟨2784:AODEPM⟩2.0.CO;2.

Kallberg, P. W., 2011: Forecast drift in era-interim. ERA Report Series 10, ECMWF. Available at: https://www.ecmwf.int/sites/default/files/elibrary/2011/10381-forecast-drift-era-interim.pdf.

Kanamitsu, M., and S. Saha, 1996: Systematic tendency error in budget calculations. *Monthly Weather Review*, **124 (6)**, 1145–1160, doi:10.1175/1520-0493(1996)124⟨1145:STEIBC⟩2.0.CO;2.

Kiranmayi, L., and E. D. Maloney, 2011: Intraseasonal moist static energy budget in reanalysis data. *Journal of Geophysical Research: Atmospheres*, **116 (D21)**, doi:10.1029/2011JD016031.

Kirshbaum, D. J., T. M. Merlis, J. R. Gyakum, and R. McTaggart-Cowan, 2018: Sensitivity of idealized moist baroclinic waves to environmental temperature and moisture content. *Journal of the Atmospheric Sciences*, **75 (1)**, 337–360, doi:10.1175/JAS-D-17-0188.1.

Kistler, R., and Coauthors, 2001: The NCEP–NCAR 50-Year reanalysis: monthly means CD-ROM and documentation. *Bulletin of the American Meteorological Society*, **82 (2)**, 247 – 268, doi:10.1175/1520-0477(2001)082⟨0247:TNNYRM⟩2.3.CO;2.

Klemp, J. B., J. Dudhia, and A. D. Hassiotis, 2008: An upper gravity-wave absorbing layer for NWP applications. *Monthly Weather Review*, **136 (10)**, 3987 – 4004, doi:10.1175/2008MWR2596.1.

Klemp, J. B., W. C. Skamarock, and J. Dudhia, 2007: Conservative split-explicit time integration methods for the compressible nonhydrostatic equations. *Monthly Weather Review*, **135 (8)**, 2897–2913, doi:10.1175/MWR3440.1.

Knight, D. J., and P. V. Hobbs, 1988: The mesoscale and microscale structure and organization of clouds and precipitation in midlatitude cyclones. Part XV: a numerical modeling study of frontogenesis and cold-frontal rainbands. *Journal of Atmospheric Sciences*, **45 (6)**, 915 – 931, doi:10.1175/1520-0469(1988)045⟨0915:TMAMSA⟩2.0.CO;2.

Kornegay, F. C., and D. G. Vincent, 1976: Kinetic energy budget analysis during interaction of Tropical Storm Candy (1968) with an extratropical frontal system. *Monthly Weather Review*, **104 (7)**, 849–859, doi:10.1175/1520-0493(1976)104⟨0849:KEBADI⟩2.0.CO;2.

Korty, R. L., and T. Schneider, 2007: A climatology of the tropospheric thermal stratification using saturation potential vorticity. *Journal of Climate*, **20 (24)**, 5977–5991, doi:10.1175/2007JCLI1788.1.

Kuo, H.-L., 1956: Forced and free meridional circulations in the atmosphere. *Journal of Atmospheric Sciences*, **13 (6)**, 561 – 568, doi:10.1175/1520-0469(1956)013⟨0561:FAFMCI⟩2.0.CO;2.

Kuo, H. L., 1965: On formation and intensification of tropical cyclones through latent heat release by cumulus convection. *Journal of Atmospheric Sciences*, **22 (1)**, 40 – 63, doi:10.1175/1520-0469(1965)022⟨0040:OFAIOT⟩2.0.CO;2.

Kuo, Y.-H., and R. A. Anthes, 1984: Accuracy of Diagnostic Heat and Moisture Budgets Using SESAME-79 Field Data as Revealed by Observing System Simulation Experiments. *Monthly Weather Review*, **112 (8)**, 1465–1481, doi:10.1175/1520-0493(1984)112⟨1465:AODHAM⟩2.0.CO;2.

Kuo, Y.-H., M. A. Shapiro, and E. G. Donall, 1991: The interaction between baroclinic and diabatic processes in a numerical simulation of a rapidly intensifying extratropical marine cyclone. *Monthly Weather Review*, **119 (2)**, 368–384, doi:10.1175/1520-0493(1991)119⟨0368:TIBBAD⟩2.0.CO;2.

Lean, H. W., and P. A. Clark, 2003: The effects of changing resolution on mesocale modelling of line convection and slantwise circulations in FASTEX IOP16. *Quarterly Journal of the Royal Meteorological Society*, **129 (592)**, 2255–2278, doi:https://doi.org/10.1256/qj.02.57.

Lee, C.-S., 1984: The bulk effects of cumulus momentum transports in tropical cyclones. *Journal of the Atmospheric Sciences*, **41 (4)**, 590–603, doi:10.1175/1520-0469(1984)041⟨0590:TBEOCM⟩2.0.CO;2.

Lehner, M., 2012: Observations and large-eddy simulations of the thermally driven cross-basin circulation in a small, closed basin. Ph.D. thesis, University of Utah.

Lehner, M., and C. David Whiteman, 2014: Physical mechanisms of the thermally driven cross-basin circulation. *Quarterly Journal of the Royal Meteorological Society*, **140 (680)**, 895–907, doi:10.1002/qj.2195.

Lilly, D. K., and B. F. Jewett, 1990: Momentum and kinetic energy budgets of simulated supercell thunderstorms. *Journal of the Atmospheric Sciences*, **47 (6)**, 707–726, doi:10.1175/1520-0469(1990)047⟨0707:MAKEBO⟩2.0.CO;2.

Lindstrom, S. S., and T. E. Nordeng, 1992: Parameterized slantwise convection in a numerical model. *Monthly Weather Review*, **120 (5)**, 742–756, doi:10.1175/1520-0493(1992)120⟨0742:PSCIAN⟩2.0.CO;2.

Lindzen, R. S., and M. Fox-Rabinovitz, 1989: Consistent vertical and horizontal resolution. *Monthly Weather Review*, **117 (11)**, 2575 – 2583, doi:10.1175/1520-0493(1989)117⟨2575:CVAHR⟩2.0.CO;2.

Liu, L., Y.-L. Lin, and S.-H. Chen, 2016: Effects of landfall location and approach angle of an idealized tropical cyclone over a long mountain range. *Frontiers in Earth Science*, **4**, 14, doi:10.3389/feart.2016.00014.

Ma, L., 2000: On the parameterization of slantwise convection in general circulation models. Ph.D. thesis, McGill University, 175 pp.

Mak, M., 1994: Cyclogenesis in a conditionally unstable moist baroclinic atmosphere. *Tellus A: Dynamic Meteorology and Oceanography*, **46 (1)**, 14–33, doi:10.3402/tellusa.v46i1.15424.

Manabe, S., J. Smagorinsky, and R. F. Strickler, 1965: Simulated climatology of a general circulation model with a hydrologic cycle. *Monthly Weather Review*, **93 (12)**, 769 – 798, doi:10.1175/1520-0493(1965)093⟨0769:SCOAGC⟩2.3.CO;2.

Markowski, P., and Y. Richardson, 2010: *Mesoscale Instabilities*, 41–70. John Wiley and Sons, Ltd, doi:10.1002/9780470682104.ch3.

Marsh, P. T., H. E. Brooks, and D. J. Karoly, 2007: Assessment of the severe weather environment in North America simulated by a global climate model. *Atmospheric Science Letters*, **8 (4)**, 100–106, doi:10.1002/asl.159.

Milbrandt, J. A., S. Bélair, M. Faucher, M. Vallée, M. L. Carrera, and A. Glazer, 2016: The pan-Canadian high resolution (2.5 km) deterministic prediction system. *Weather and Forecasting*, **31 (6)**, 1791 – 1816, doi:10.1175/WAF-D-16-0035.1.

Moisseeva, N., 2014: Dynamical analysis of sea breeze hodograph rotation in Sardinia. Available at: http://hdl.handle.net/2429/46069 (last access: 18 December 2019).

Moisseeva, N., and D. G. Steyn, 2014: Dynamical analysis of sea-breeze hodograph rotation in Sardinia. *Atmospheric Chemistry and Physics*, **14 (24)**, 13 471–13 481, doi:10.5194/acp-14-13471-2014.

Monkam, D., 2002: Convective available potential energy (CAPE) in Northern Africa and Tropical Atlantic and study of its connections with rainfall in Central and West Africa during summer 1985. *Atmospheric Research*, **62 (1)**, 125 – 147, doi:10.1016/S0169-8095(02)00006-6.

Morcrette, C. J., 2004: Radar and modelling studies of upright and slantwise convection. Ph.D. thesis, University of Reading, 172 pp.

National Center for Atmospheric Research, 2016: WRF-ARW Code Version 3.8.1. Available at: https://www2.mmm.ucar.edu/wrf/users/download/get_sources.html (last access: 6 June 2019).

NCEP/National Weather Service/NOAA/U.S. Department of Commerce, 1994: NCEP/NCAR Global Reanalysis Products, 1948-continuing. Updated monthly. Research Data Archive at NOAA/PSL:/data/gridded/data.ncep.reanalysis.html.

Nordeng, T. E., 1987: The effect of vertical and slantwise convection on the simulation of polar lows. *Tellus A: Dynamic Meteorology and Oceanography*, **39 (4)**, 354–375, doi:10.3402/tellusa.v39i4.11765.

Nordeng, T. E., 1993: *Parameterization of Slantwise Convection in Numerical Weather Prediction Models*, 195–202. American Meteorological Society, Boston, MA, doi:10.1007/978-1-935704-13-3_20.

O'Neill, M. E., and Y. Kaspi, 2016: Slantwise convection on fluid planets. *Geophysical Research Letters*, **43 (20)**, 10,611–10,620, doi:10.1002/2016GL071188.

Ooyama, K., 1966: On the stability of the baroclinic circular vortex: a sufficient criterion for instability. *Journal of Atmospheric Sciences*, **23 (1)**, 43 – 53, doi:10.1175/1520-0469(1966)023⟨0043:OTSOTB⟩2.0.CO;2.

Orlanski, I., 1981: The quasi-hydrostatic approximation. *Journal of Atmospheric Sciences*, **38 (3)**, 572 – 582, doi:10.1175/1520-0469(1981)038⟨0572:TQHA⟩2.0.CO;2.

Persson, P. O. G., and T. T. Warner, 1991: Model generation of spurious gravity waves due to inconsistency of the vertical and horizontal resolution. *Monthly Weather Review*, **119 (4)**, 917 – 935, doi:10.1175/1520-0493(1991)119⟨0917:MGOSGW⟩2.0.CO;2.

Persson, P. O. G., and T. T. Warner, 1993: Nonlinear hydrostatic conditional symmetric instability: Implications for numerical weather prediction. *Monthly Weather Review*, **121 (6)**, 1821 – 1833, doi:10.1175/1520-0493(1993)121⟨1821:NHCSII⟩2.0.CO;2.

Persson, P. O. G., and T. T. Warner, 1995: The nonlinear evolution of idealized, unforced, conditional symmetric instability: A numerical study. *Journal of the Atmospheric Sciences*, **52 (20)**, 3449–3474, doi:10.1175/1520-0469(1995)052⟨3449:TNEOIU⟩2.0.CO;2.

Pielke, R. A., and Coauthors, 1992: A comprehensive meteorological modeling system—rams. *Meteorology and Atmospheric Physics*, **49**, 69–91, doi:10.1007/BF01025401.

Potter, E. R., A. Orr, I. C. Willis, D. Bannister, and F. Salerno, 2018: Dynamical drivers of the local wind regime in a Himalayan valley. *Journal of Geophysical Research: Atmospheres*, **123 (23)**, 13,186–13,202, doi:10.1029/2018JD029427.

Powers, J. G., and Coauthors, 2017: The weather research and forecasting model: overview, system Efforts, and future directions. *Bulletin of the American Meteorological Society*, **98 (8)**, 1717–1737, doi:10.1175/BAMS-D-15-00308.1.

Prein, A. F., and Coauthors, 2015: A review on regional convection-permitting climate modeling: Demonstrations, prospects, and challenges. *Reviews of Geophysics*, **53 (2)**, 323–361, doi:10.1002/2014RG000475.

Reuter, G. W., and M. K. Yau, 1990: Observations of slantwise convective instability in winter cyclones. *Monthly Weather Review*, **118 (2)**, 447–458, doi:10.1175/1520-0493(1990)118⟨0447:OOSCII⟩2.0.CO;2.

Reuter, G. W., and M. K. Yau, 1993: Assessment of slantwise convection in erica cyclones. *Monthly Weather Review*, **121 (2)**, 375–386, doi:10.1175/1520-0493(1993)121⟨0375:AOSCIE⟩2.0.CO;2.

Riemann-Campe, K., K. Fraedrich, and F. Lunkeit, 2009: Global climatology of convective available potential energy (CAPE) and convective inhibition (CIN) in ERA-40 reanalysis. *Atmospheric Research*, **93 (1)**, 534 – 545, doi:10.1016/j.atmosres.2008.09.037, 4th European Conference on Severe Storms.

Rios-Berrios, R., R. D. Torn, and C. A. Davis, 2016: An ensemble approach to investigate tropical cyclone intensification in sheared environments. Part I: Katia (2011). *Journal of the Atmospheric Sciences*, **73 (1)**, 71–93, doi:10.1175/JAS-D-15-0052.1.

Rogers, R., and M. Yau, 1989: *A Short Course in Cloud Physics*. 3rd ed., Oxford: Pergamon Press.

Sanders, F., and L. F. Bosart, 1985: Mesoscale structure in the megalopolitan snowstorm of 11–12 February 1983. Part I: frontogenetical forcing and symmetric instability. *Journal of Atmospheric Sciences*, **42 (10)**, 1050 – 1061, doi:10.1175/1520-0469(1985)042⟨1050:MSITMS⟩2.0.CO;2.

Sanders, F., and K. A. Emanuel, 1977: The momentum budget and temporal evolution of a mesoscale convective system. *Journal of the Atmospheric Sciences*, **34 (2)**, 322–330, doi:10.1175/1520-0469(1977)034⟨0322:TMBATE⟩2.0.CO;2.

Sanders, F., and J. R. Gyakum, 1980: Synoptic-dynamic climatology of the “bomb”. *Monthly Weather Review*, **108 (10)**, 1589–1606, doi:10.1175/1520-0493(1980)108⟨1589:SDCOT⟩2.0.CO;2.

Satoh, M., 2002: Conservative scheme for the compressible nonhydrostatic models with the horizontally explicit and vertically implicit time integration scheme. *Monthly Weather Review*, **130 (5)**, 1227–1245, doi:10.1175/1520-0493(2002)130⟨1227:CSFTCN⟩2.0.CO;2.

Schaefer, J. T., 1990: The critical success index as an indicator of warning skill. *Weather and Forecasting*, **5 (4)**, 570 – 575, doi:10.1175/1520-0434(1990)005⟨0570:TCSIAA⟩2.0.CO;2.

Schultz, D. D., and W. Blumen, 2015: Synoptic meteorology — fronts. *Encyclopedia of Atmospheric Sciences (Second Edition)*, G. R. North, J. Pyle, and F. Zhang, Eds., second edition ed., Academic Press, Oxford, 337–343, doi:10.1016/B978-0-12-382225-3.00039-6.

Schultz, D. M., and K. A. Browning, 2017: What is a sting jet? *Weather*, **72 (3)**, 63–66, doi:10.1002/wea.2795.

Schultz, D. M., and P. N. Schumacher, 1999: The use and misuse of conditional symmetric instability. *Monthly Weather Review*, **127 (12)**, 2709–2732, doi:10.1175/1520-0493(1999)127⟨2709:TUAMOC⟩2.0.CO;2.

Seltzer, M. A., R. E. Passarelli, and K. A. Emanuel, 1985: The possible role of symmetric instability in the formation of precipitation bands. *Journal of the Atmospheric Sciences*, **42 (20)**, 2207–2219, doi:10.1175/1520-0469(1985)042⟨2207:TPROSI⟩2.0.CO;2.

Seman, C. J., 1994: A numerical study of nonlinear nonhydrostatic conditional symmetric instability in a convectively unstable atmosphere. *Journal of Atmospheric Sciences*, **51 (11)**, 1352 – 1371, doi:10.1175/1520-0469(1994)051⟨1352:ANSONN⟩2.0.CO;2.

Serreze, M., 1995: Climatological aspects of cyclone development and decay in the Arctic. *Atmosphere-Ocean*, **33 (1)**, 1–23, doi:10.1080/07055900.1995.9649522.

Serreze, M., 2009: Northern hemisphere cyclone locations and characteristics from NCEP/NCAR reanalysis data, version 1. Boulder, Colorado USA. NSIDC: national snow and ice data center. Available at: https://nsidc.org/data/NSIDC-0423/versions/1 (last access: 25 October 2016).

Serreze, M., F. Carse, R. G. Barry, and J. C. Rogers, 1997: Icelandic low cyclone activity: climatological features, linkages with the NAO, and relationships with recent changes in the Northern Hemisphere circulation. *Journal of Climate*, **10 (3)**, 453–464, doi:10.1175/1520-0442(1997)010⟨0453:ILCACF⟩2.0.CO;2.

Sherwood, S. C., 2000: On moist instability. *Monthly Weather Review*, **128 (12)**, 4139 – 4142, doi:10.1175/1520-0493(2000)129⟨4139:OMI⟩2.0.CO;2.

Shutts, G. J., 1990a: SCAPE charts from numerical weather prediction model fields. *Monthly Weather Review*, **118 (12)**, 2745–2751, doi:10.1175/1520-0493(1990)118⟨2745:SCFNWP⟩2.0.CO;2.

Shutts, G. J., 1990b: The dynamical structure of some North Atlantic depressions simulated by the fine-mesh model. Tech. Rep. 17, Met Office: Bracknell, UK.

Simmons, A. J., K. M. Willett, P. D. Jones, P. W. Thorne, and D. P. Dee, 2010: Low-frequency variations in surface atmospheric humidity, temperature, and precipitation: Inferences from reanalyses and monthly gridded observational data sets. *Journal of Geophysical Research: Atmospheres*, **115 (D1)**, doi:10.1029/2009JD012442.

Skamarock, W. C., J. B. Klemp, J. Dudhia, D. O. Gill, D. M. Barker, W. Wang, and J. G. Powers, 2008: A description of the advanced research wrf version 3. Tech. rep., NCAR/TN-475+STR.

Stensrud, D., 2007: *Parameterization Schemes: Keys to Understanding Numerical Weather Prediction Models*. Cambridge University Press, 459 pp.

Stoelinga, M., 2009: A users guide to RIP version 4.6: a program for visualizing mesoscale model output. Available at: https://a.atmos.washington.edu/~ovens/ripug_uw.html (last access: 17 July 2020).

Stone, P. H., 1966: On non-geostrophic baroclinic stability. *Journal of the Atmospheric Sciences*, **23 (4)**, 390–400, doi:10.1175/1520-0469(1966)023⟨0390:ONGBS⟩2.0.CO;2.

Stone, P. H., 1967: An application of baroclinic stability theory to the dynamics of the jovian atmosphere. *Journal of the Atmospheric Sciences*, **24 (6)**, 642–652, doi:10.1175/1520-0469(1967)024⟨0642:AAOBST⟩2.0.CO;2.

Stone, P. H., 1971: The symmetric baroclinic instability of an equatorial current. *Geophysical Fluid Dynamics*, **2 (1)**, 147–164, doi:10.1080/03091927108236055.

Stull, R. B., 1991: Static stability—an update. *Bulletin of the American Meteorological Society*, **72 (10)**, 1521 – 1530, doi:10.1175/1520-0477(1991)072⟨1521:SSU⟩2.0.CO;2.

Subrahmanyam, K. V., K. K. Kumar, and A. Narendra Babu, 2015: Phase relation between CAPE and precipitation at diurnal scales over the Indian summer monsoon region. *Atmospheric Science Letters*, **16 (3)**, 346–354, doi:10.1002/asl2.566.

Tamarin, T., and Y. Kaspi, 2017: Mechanisms controlling the downstream poleward deflection of midlatitude storm tracks. *Journal of the Atmospheric Sciences*, **74 (2)**, 553–572, doi:10.1175/JAS-D-16-0122.1.

Thompson, G., P. R. Field, R. M. Rasmussen, and W. D. Hall, 2008: Explicit forecasts of winter precipitation using an improved bulk microphysics scheme. part ii: Implementation of a new snow parameterization. *Monthly Weather Review*, **136 (12)**, 5095–5115, doi:10.1175/2008MWR2387.1.

Thorpe, A., 1986: Parameterization of mesoscale processes. *Proceedings of Seminar on Physical Parameterization for Numerical Models of the Atmosphere*, ECMWF, Shinfield Park, Reading, UK, 205–233.

Thorpe, A. J., and S. A. Clough, 1991: Mesoscale dynamics of cold fronts: Structures described by dropsoundings in fronts 87. *Quarterly Journal of the Royal Meteorological Society*, **117 (501)**, 903–941, doi:https://doi.org/10.1002/qj.49711750103.

Thorpe, A. J., and K. A. Emanuel, 1985: Frontogenesis in the presence of small stability to slantwise convection. *Journal of the Atmospheric Sciences*, **42 (17)**, 1809–1824, doi: 10.1175/1520-0469(1985)042⟨1809:FITPOS⟩2.0.CO;2.

Thorpe, A. S., and R. Rotunno, 1989: Nonlinear aspects of symmetric instability. *Journal of Atmospheric Sciences*, **46 (9)**, 1285 – 1299, doi:10.1175/1520-0469(1989)046⟨1285: NAOSI⟩2.0.CO;2.

Tiedtke, M., 1989: A comprehensive mass flux scheme for cumulus parameterization in large-scale models. *Monthly Weather Review*, **117 (8)**, 1779 – 1800, doi:10.1175/ 1520-0493(1989)117⟨1779:ACMFSF⟩2.0.CO;2.

Trier, S. B., M. A. LeMone, and W. C. Skamarock, 1998: Effect of three-dimensional structure on the stormwide horizontal accelerations and momentum budget of a simulated squall line. *Monthly Weather Review*, **126 (10)**, 2580–2598, doi:10.1175/1520-0493(1998) 126⟨2580:EOTDSO⟩2.0.CO;2.

Undén, P., and Coauthors, 2002: HIRLAM-5 scientific documentation. Available at: http://www.hirlam.org/ (last access: 9 August 2019), 144 pp.

Wang, B., and Q. Ding, 2008: Global monsoon: Dominant mode of annual variation in the tropics. *Dynamics of Atmospheres and Oceans*, **44 (3)**, 165–183, doi:10.1016/j.dynatmoce.2007.05.002.

Wicker, L. J., and W. C. Skamarock, 2002: Time-splitting methods for elastic models using Forward time schemes. *Monthly Weather Review*, **130 (8)**, 2088–2097, doi:10.1175/1520-0493(2002)130⟨2088:TSMFEM⟩2.0.CO;2.

Xie, P., and P. A. Arkin, 1997: Global precipitation: A 17-year monthly analysis based on gauge observations, satellite estimates, and numerical model outputs. *Bulletin of the American Meteorological Society*, **78 (11)**, 2539–2558, doi:10.1175/1520-0477(1997)078⟨2539:GPAYMA⟩2.0.CO;2.

Xu, Q., 1986: Conditional symmetric instability and mesoscale rainbands. *Quarterly Journal of the Royal Meteorological Society*, **112 (472)**, 315–334, doi:10.1002/qj.49711247203.

Xue, M., K. K. Droegemeier, and V. Wong, 2000: The advanced regional prediction system (ARPS) – a multi-scale nonhydrostatic atmospheric simulation and prediction model. Part I: Model dynamics and verification. *Meteorology and Atmospheric Physics*, **75**, 161–193, doi:10.1007/s007030070003.

Xue, M., and Coauthors, 2001: The advanced regional prediction system (ARPS) – a multi-scale nonhydrostatic atmospheric simulation and prediction tool. Part II: Model physics and applications. *Meteorology and Atmospheric Physics*, **76**, 143–165, doi:10.1007/s007030170027.

Zamora, R. A., R. L. Korty, and M. Huber, 2016: Thermal stratification in simulations of warm climates: A climatology using saturation potential vorticity. *Journal of Climate*, **29 (14)**, 5083–5102, doi:10.1175/JCLI-D-15-0785.1.

Zappa, G., L. C. Shaffrey, and K. I. Hodges, 2013: The ability of CMIP5 models to simulate North Atlantic extratropical cyclones. *Journal of Climate*, **26 (15)**, 5379 – 5396, doi:10.1175/JCLI-D-12-00501.1.

Zhang, C., Y. Wang, and K. Hamilton, 2011: Improved Representation of Boundary Layer Clouds over the Southeast Pacific in ARW-WRF Using a Modified Tiedtke Cumulus Parameterization Scheme. *Monthly Weather Review*, **139 (11)**, 3489 – 3513, doi:10.1175/MWR-D-10-05091.1.

Zhang, D.-L., and H.-R. Cho, 1992: The development of negative moist potential vorticity in the stratiform region of a simulated squall line. *Monthly Weather Review*, **120 (7)**, 1322 – 1341, doi:10.1175/1520-0493(1992)120⟨1322:TDONMP⟩2.0.CO;2.

Zhang, D.-L., and H.-R. Cho, 1995: Three-dimensional simulation of frontal rainbands and conditional symmetric instability in the Eady-wave model. *Tellus A: Dynamic Meteorology and Oceanography*, **47 (1)**, 45–61, doi:10.3402/tellusa.v47i1.11493.

Zhang, D.-L., Y. Liu, and M. K. Yau, 2000: A multiscale numerical study of Hurricane Andrew (1992). Part III: dynamically induced vertical motion. *Monthly Weather Review*, **128 (11)**, 3772–3788, doi:10.1175/1520-0493(2001)129⟨3772:AMNSOH⟩2.0.CO;2.

Zhao, M., 2014: An investigation of the connections among convection, clouds, and climate sensitivity in a global climate model. *Journal of Climate*, **27 (5)**, 1845 – 1862, doi:10.1175/JCLI-D-13-00145.1.

Zhao, M., and Coauthors, 2016: Uncertainty in model climate sensitivity traced to representations of cumulus precipitation microphysics. *Journal of Climate*, **29 (2)**, 543 – 560, doi:10.1175/JCLI-D-15-0191.1.

Zhou, T., and Coauthors, 2016: GMMIP (v1.0) contribution to CMIP6: Global monsoons model inter-comparison project. *Geoscientific Model Development*, **9 (10)**, 3589–3604, doi:10.5194/gmd-9-3589-2016.